Surface, Emitter and Bulk Recombination in Silicon and Development of Silicon Nitride Passivated Solar Cells

Mark John Kerr

June 2002



A thesis submitted for the degree of Doctor of Philosophy of The Australian National University

HANWHA 1034

Declaration

I certify that this thesis does not incorporate, without acknowledgement, any material previously submitted for a degree or diploma in any university, and that, to the best of my knowledge, it does not contain any material previously published or written by another person except where due reference is made in the text. The work in this thesis is my own, except for the contributions made by others as described in the Acknowledgements.

Mark Kerr

Acknowledgments

I would like to express indebted gratitude to my supervisor Dr Andres Cuevas. He has always been extremely generous with his time, knowledge and ideas and allowed me great freedom in this research. His enthusiastic approach to research, his endless excitement for solar cells and his effervescent personality have made this experience all the more enjoyable and I am greatly appreciative. I would also like to thank Prof. Andrew Blakers for forming part of my supervisory panel, for helpful discussions and for establishing the PV labs at the ANU, they are a tremendous place to work and study. I am also grateful to Dr Matt Stocks and Dr Rob Elliman for their advice as members of my supervisory panel.

I would like to thank Dr Daniel Macdonald for many hours of useful banter, as a source and a sounding board for many ideas, and for his in-depth knowledge on gettering multicrystalline silicon. I am also extremely grateful to Chris Samundsett for his assistance in the labs, for showing me the ropes and for his endless help with various samples, even the ones that got dropped on the floor. Equally important, I am grateful for his keen sense of wit and balanced perspective on life.

I am very appreciative of Dr Jan Schmidt for introducing me to the world of PECVD SiN and for a wealth of useful discussions and contributions. I would also like to thank Dr Ron Sinton for developing such wonderful tools for studying recombination and for all the helpful advice he provided, especially in the art of lifetime measurements and for the work in Chapter 2 on the generalised $QssV_{oc}$ technique.

I would also like to thank the many people who have collaborated with me and contributed to various parts of this research, in particular to Prof. C. Jagadish and Dr H. Tan of EME for use of the PECVD reactor. Dr Jan Bultman of ECN organised the stripping Hall measurements of emitter profiles and I am grateful to Dr Pietro Altermatt of UNSW for discussion and data on Auger recombination. Many thanks to Dr D. Ruby of Sandia National Laboratories, Dr K. Emery of NREL and Dr Stefan Glunz of the Fraunhofer ISE for quantum efficiency data and for I-V measurements of solar cells under standard conditions. Dr D. Ruby also performed the texturing of mulitcrystalline cells by RIE. Thanks to Dr Stefan Glunz and Stefan Rein of the Fraunhofer ISE for the solar cell used in Figure 2.18. Dr Patrick Campbell of UNSW performed the montecarlo simulations of photon recycling in silicon and Prof. Martin Green provided useful discussion on modeling the limiting efficiency of silicon solar cells. Francesca Ferrazza kindly supplied the Eurosolare multicrystalline silicon material and the assistance of Dr Saul Winderbaum and Tony Leo of BP Solar is gratefully acknowledged for fabricating large area multicrystalline silicon solar cells.

Abstract

Recombination within the bulk and at the surfaces of crystalline silicon has been investigated in this thesis. Special attention has been paid to the surface passivation achievable with plasma enhanced chemical vapour deposited (PECVD) silicon nitride (SiN) films due to their potential for widespread use in silicon solar cells. The passivation obtained with thermally grown silicon oxide (SiO_2) layers has also been extensively investigated for comparison.

Injection-level dependent lifetime measurements have been used throughout this thesis to quantify the different recombination rates in silicon. New techniques for interpreting the effective lifetime in terms of device characteristics have been introduced, based on the physical concept of a net photogeneration rate. The converse relationships for determining the effective lifetime from measurements of the open-circuit voltage (V_{oc}) under arbitrary illumination have also been introduced, thus establishing the equivalency of the photoconductance and voltage techniques, both quasi-static and transient, by allowing similar possibilities for all of them.

The rate of intrinsic recombination in silicon is of fundamental importance. It has been investigated as a function of injection level for both *n*-type and *p*-type silicon, for dopant densities up to ~$5x10^{16}cm^{-3}$. Record high effective lifetimes, up to 32ms for high resistivity silicon, have been measured. Importantly, the wafers where commercially sourced and had undergone significant high temperature processing. A new, general parameterisation has been proposed for the rate of band-to-band Auger recombination in crystalline silicon, which accurately fits the experimental lifetime data for arbitrary injection level and arbitrary dopant density. The limiting efficiency of crystalline silicon solar cells has been re-evaluated using this new parameterisation, with the effects of photon recycling included.

Surface recombination processes in silicon solar cells are becoming progressively more important as industry drives towards thinner substrates and higher cell efficiencies. The surface recombination properties of well-passivating SiN films on *p*-type and *n*-type silicon have been comprehensively studied, with S_{eff} values as low as 1cm/s being unambiguously determined. The well-passivating SiN films optimised in this thesis are unique in that they are stoichiometric in composition, rather than being silicon rich, a property which is attributed to the use of dilute silane as a process gas. A simple physical model, based on recombination at the Si/SiN interface being determined by a high fixed charge density within the SiN film (even under illumination), has been proposed to explain the injection-level dependent S_{eff} for a variety of differently doped wafers. The passivation obtained with the optimised SiN films has been compared to that obtained with high temperature thermal oxides (FGA and alnealed) and the limits imposed by surface recombination on the efficiency of SiN passivated solar cells investigated. It is shown that the optimised SiN films show little absorption of UV photons from the solar spectrum and can be easily patterned by photolithography and wet chemical etching.

The recombination properties of n^+ and p^+ emitters passivated with optimised SiN films and thermal SiO_2 have been extensively studied over a large range of emitter sheet resistances. Both planar and random pyramid textured surfaces were studied for n^+ emitters, where the optimised SiN films were again found to be stoichiometric in composition. The optimised SiN films provided good passivation of the heavily doped n^+-Si/SiN interface, with the surface recombination velocity increasing from 1400cm/s to 25000cm/s as the surface concentration of electrically active phosphorus atoms increased from $7.5x10^{18}cm^{-3}$ to $1.8x10^{20}cm^{-3}$. The optimised SiN films also provided reasonable passivation of industrial n^+ emitters formed in a belt-line furnace. It was found that the surface recombination properties of SiN passivated p^+ emitters was poor and was worst for sheet resistances of ~150Ω/□. The hypothesis that recombination at the Si/SiN interface is determined by a high fixed charge density within the SiN films was extended to explain this dependence on sheet resistance. The efficiency potential of SiN passivated n^+p cells has been investigated, with a sheet resistance of 80-100Ω/□ and a base resistivity of 1-2Ωcm found to be optimal. Open-circuit voltages of 670-680mV and efficiencies up to ~20% and ~23% appear possible for SiN passivated planar and textured cells respectively. The recombination properties measured for emitters passivated with SiO_2, both n^+ and p^+, were consistent with other studies and found to be superior to those obtained with SiN passivation.

Stoichiometric SiN films were used to passivate the front and rear surfaces of various solar cell structures. Simplified PERC cells fabricated on 0.3Ωcm *p*-type silicon, with either a planar or random pyramid textured front surface, produced high V_{oc}'s of 665-670mV and conversion efficiencies up to 19.7%, which are amongst the highest obtained for SiN passivated solar cells. Bifacial solar cells fabricated on planar, high resistivity *n*-type substrates (20Ωcm) demonstrated V_{oc}'s up to 675mV, the highest ever reported for an all-SiN passivated cell, and excellent bifaciality factors. Planar PERC cells fabricated on gettered 0.2Ωcm multicrystalline silicon have also demonstrated very high V_{oc}'s of 655-659mV and conversion efficiencies up to 17.3% using a single layer anti-reflection coating. Short-wavelength internal quantum efficiency measurements confirmed the excellent passivation achieved with the optimised stoichiometric SiN films on n^+ emitters, while long-wavelength measurements show that there is a loss of short-circuit current at the rear surface of SiN passivated *p*-type cells. The latter loss is attributed to parasitic shunting, which arises from an inversion layer at the rear surface due to the high fixed charge (positive) density in the SiN layers. It has been demonstrated that that a simple way to reduce the impact of the parasitic shunt is to etch away some of the silicon from the rear contact dots. An alternative is to have locally diffused p^+ regions under the rear contacts, and a novel method to form a rear structure consisting of a local Al-BSF with SiN passivation elsewhere, without using photolithography, has been demonstrated.

Table of Contents

CHAPTER 1: INTRODUCTION 1

1.1 MARKET OVERVIEW 1

1.2 THESIS MOTIVATION 5

1.3 THESIS OUTLINE 6

CHAPTER 2: QUANTIFYING AND MEASURING RECOMBINATION IN CRYSTALLINE SILICON 9

2.1 RECOMBINATION MECHANISMS 10

2.1.1 Radiative Recombination 11

2.1.2 Auger Recombination 12

2.1.3 Bulk Recombination Through Defects 14

2.1.4 Surface Recombination Through Defects 16

2.1.5 Emitter Recombination 18

2.2 THE EFFECTIVE LIFETIME 20

2.3 MEASURING THE EFFECTIVE LIFETIME 22

2.3.1 Introduction 22

2.3.2 Photoconductance Based Techniques 24

2.3.3 Calibration Functions for Determining the Photoconductance 25

2.4 DETERMINING DEVICE CHARACTERISTICS FROM THE EFFECTIVE LIFETIME 28

2.4.1 Determination of Implied V_{oc} vs. Light Intensity Curves 28

2.4.2 Determination of Photovoltaic I-V Curves 30

2.5 GENERALISATION OF OPEN-CIRCUIT VOLTAGE MEASUREMENTS 32

2.5.1 Introduction 33

2.5.2 Experimental Illustration of the General Analysis 34

2.5.3 Determination of the Lifetime from V_{oc} 37

2.5.4 Determination of the Photovoltaic I-V Curve from V_{oc} 38

2.5.5 Determination of the Lifetime from the J_{sc}-V_{oc} Curve 40

2.6 DISCUSSION 42

2.7 CHAPTER SUMMARY 47

CHAPTER 3: LIFETIME AND EFFICIENCY LIMITS OF CRYSTALLINE SILICON SOLAR CELLS 49

3.1 INTRODUCTION 49

3.2 LIMITS FOR THE EFFECTIVE LIFETIME 50
3.2.1. Previous Work 50
3.2.2 Experimental Details 51
3.2.3 Results and Discussion 53
3.2.4 Conclusions 55
3.3 COULOMB-ENHANCED AUGER RECOMBINATION 56
3.3.1 Introduction 56
3.3.2 Existing Analytical Models 57
3.3.2.1 Low Injection Models 57
3.3.2.2 High Injection Models 58
3.3.2.3 Complete Models 59
3.3.3 A New Auger Parameterisation 60
3.3.3.1 The Low Injection Auger Lifetime 60
3.3.3.2 The High Injection Auger Lifetime 62
3.3.3.3 A General Parameterisation 64
3.3.3.4 Validation of the New Parameterisation 64
3.3.3.5 Discussion 66
3.3.4 Estimate of the SRH Lifetime in Silicon 71
3.3.5 Auger Recombination in Multicrystalline Silicon 72
3.3.6 Conclusions 74
3.4 LIMITING EFFICIENCY OF SILICON SOLAR CELLS 74
3.4.1 Solar Cell I-V Characteristics 75
3.4.2 Effect of Coulomb-Enhanced Auger Recombination 77
3.4.3 Effect of Dopant Density and Dopant Type 79
3.4.4 Effect of Emitter and Surface Recombination 81
3.4.5 Effect of Additional Bulk Recombination 84
3.4.6 Comparison with Experimental Devices 84
3.4.7 Conclusions 86
3.5 CHAPTER SUMMARY 87

CHAPTER 4: SURFACE RECOMBINATION OF *p*-TYPE AND *n*-TYPE SILICON PASSIVATED WITH PECVD SILICON NITRIDE 89

4.1 INTRODUCTION 89
4.2 OPTIMISATION OF THE PECVD DEPOSITION PARAMETERS 91
4.2.1 Process Variables and Experimental Details 91
4.2.2 Results and Discussion 93
4.2.2.1 Effect of Gas Flow Ratio and Rate 93

4.2.2.2 Effect of Deposition Temperature, Process Pressure and Process Power 94
4.2.2.3 Effect of Deposition Time 97
4.2.2.4 Optimal Parameters for 0.3Ωcm *p*-type Silicon 98
4.2.3 Comparison with Previous Work 100
4.2.3.1 Effect of Deposition Temperature 100
4.2.3.2 Effect of Other Process Variables and Correlation with the Refractive Index 100
4.2.3.3 Effect of SiN Film Thickness 102
4.2.4 Conclusions 103
4.3 SURFACE RECOMBINATION PROPERTIES 104
4.3.1 Review of Previous Work 104
4.3.1.1 Low-Frequency Direct PECVD SiN Films 104
4.3.1.2 Remote and High-Frequency Direct PECVD SiN Films 105
4.3.2 Experimental Details 107
4.3.3 Results 109
4.3.4 Discussion 113
4.3.4.1 Comparison with Literature Data for $S_{eff}(\Delta n)$ 113
4.3.4.2 Physical Mechanisms for Recombination at the Si/SiN Interface 114
4.3.5 Comparison of Stoichiometric SiN and Thermal SiO_2 118
4.3.6 Limiting Efficiency of SiN Passivated Solar Cells 121
4.3.7 Conclusions 123
4.4 CHARACTERISATION AND THERMAL STABILITY OF THE OPTIMAL SIN FILMS 125
4.4.1 Absorption Coefficient 125
4.4.2 Etch Rates 126
4.4.3 Thermal Stability 128
4.5 CHAPTER SUMMARY 130

CHAPTER 5: PASSIVATING DIFFUSED EMITTERS 133

5.1 INTRODUCTION 133
5.2 n^+ EMITTERS 135
5.2.1 Previous Work 135
5.2.2 Experimental Details 136
5.2.3 PECVD SiN Deposition Parameters 137
5.2.3.1 Effect of Deposition Temperature and Gas Flow Ratio 137
5.2.3.2 Effect of Process Power and Process Pressure 137
5.2.3.3 Comparison with Previous Work 138
5.2.4 Passivation Results and Discussion 139
5.2.4.1 J_{oE} measurements for planar SiN passivated samples 139

5.2.4.2 J_{oE} measurements for planar thin oxide passivated samples 141
5.2.4.3 J_{oE} measurements for textured samples 141
5.2.4.4 J_{oE} measurements for planar unpassivated samples 143
5.2.4.5 Electrically active phosphorus profiles 144
5.2.4.6 Band gap narrowing (BGN) parameters for PC1D 145
5.2.4.7 Extracted S_p for passivated emitters 146
5.2.5 Industrial Phosphorus Emitters 148
5.2.5.1 Experimental Details 149
5.2.5.2 Results and Discussion 149
5.2.6 Conclusions 151
5.3 p^+ EMITTERS 152
5.3.1 Introduction 152
5.3.2 Previous Work 153
5.3.3 Experimental Details 155
5.3.4 Results and Discussion 155
5.3.4.1 J_{op+} measurements for planar oxide passivated samples 155
5.3.4.2 J_{op+} measurements for planar SiN passivated samples 156
5.3.4.3 Degradation of the bulk lifetime during boron diffusion 160
5.3.5 Conclusions 160
5.4 EFFICIENCY POTENTIAL OF SIN PASSIVATED n^+p CELLS 161
5.5 CHAPTER SUMMARY 166

CHAPTER 6: SOLAR CELL STRUCTURES PASSIVATED WITH STOICHIOMETRIC PECVD SILICON NITRIDE 169

6.1 INTRODUCTION 169
6.2 PREVIOUS WORK 170
6.2.1 *p*-type Float-Zone Silicon Solar Cells 170
6.2.1.1 Front and Rear SiN Passivated Cells 170
6.2.1.2 Rear SiN Passivated Cells 171
6.2.1.3 Cells Incorporating SiN at the Front Surface 172
6.2.2 *p*-type Multicrystalline Silicon Solar Cells 172
6.2.3 *n*-type Silicon Solar Cells 173
6.3 DEVELOPMENT OF SIMPLIFIED PERC CELLS WITH SIN PASSIVATION 174
6.3.1 Cell Design 174
6.3.2 Cell Fabrication 174
6.3.3 Cell Results and Discussion 176
6.3.3.1 Planar Float-Zone Silicon Solar Cells 176

6.3.3.2 Planar SiN Passivated Multicrystalline Silicon Solar Cells 179
6.3.3.3 Random-Pyramid Textured Float-Zone Silicon Solar Cells 181
6.3.3.4 Alternative Rear Contact Schemes 184
6.3.3.5 Local BSF Type Rear Contact Without Photolithography 186
6.3.3.6 Conclusions 187
6.4 *n*-TYPE CELLS WITH SIN PASSIVATION 188
6.5 SOLAR CELLS WITH AN INDUSTRIAL BELT-LINE EMITTER DIFFUSION 192
6.5.1 Large Area Planar Float-Zone Silicon Cells 192
6.5.2 Large Area Screen-Printed Multicrystalline Silicon Cells 194
6.5.3 Large Area Fire-Through Multicrystalline Silicon Cells 195
6.5.4 Conclusions 198
6.6 CHAPTER SUMMARY 199

CHAPTER 7: SUMMARY AND FURTHER WORK 201

7.1 MEASURING RECOMBINATION IN CRYSTALLINE SILICON 202
7.2 LIFETIME AND EFFICIENCY LIMITS OF SILICON SOLAR CELLS 203
7.3 PASSIVATION OF *n*-TYPE AND *p*-TYPE SILICON WITH PECVD SILICON NITRIDE 204
7.4 PASSIVATION OF DIFFUSED SURFACES 205
7.5 SOLAR CELL STRUCTURES PASSIVATED WITH PECVD SIN 207

LIST OF PUBLICATIONS 211

BIBLIOGRAPHY 215

CHAPTER 1

Introduction

Solar cells convert sunlight directly into electricity using the *photovoltaic effect*. They are a promising technology for satisfying current and future energy demands in a sustainable and environmentally friendly way. The first commercial use of solar cells was in space applications for powering satellites in the late 1950's. Today, the terrestrial market for solar cells greatly exceeds that for space applications, with a variety of end uses including grid connected systems, consumer products and for remote area power supply. This rapidly expanding market calls for advanced technologies and devices capable of yielding a higher performance at lower cost.

1.1 Market Overview

The market for solar cells has benefited significantly from government based subsidy programs over recent years. Figure 1.1 shows the annual worldwide shipments of photovoltaic (PV) modules over the last 25 years [1, 2]. Worldwide production at the end of 2000 was 288 MW of which 287.3 MW was for terrestrial applications. In the period from 1977-1983 the market was operating from a very small base and grew at a very high rate. The following decade was characterised by a relatively constant growth rate of around 12%pa. In the last four years,

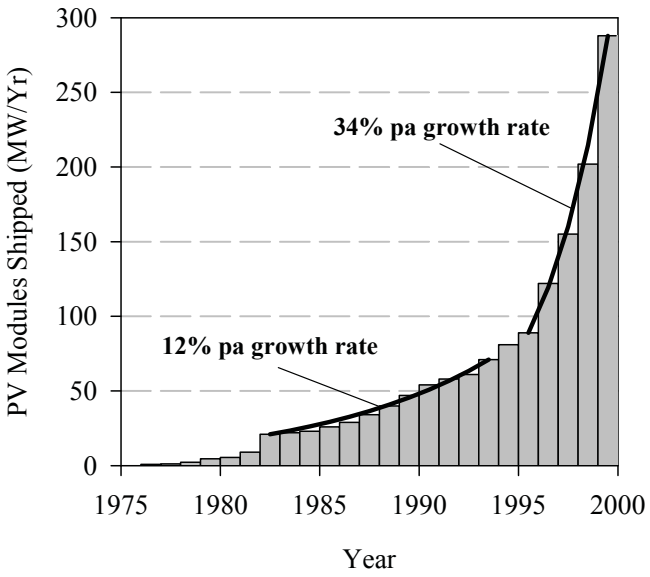


Figure 1.1: Worldwide shipments of PV modules over the last 25 years.

the market for PV modules has undergone tremendous growth at an annual rate of 34%. The resulting average growth rate since 1983 is then 16.6%pa.

Based on the above growth rates, projections of the future market size for PV modules are given in Figure 1.2 for the period up to 2010. A growth rate of 25%pa is included, as it has been used historically, although some experts are now considering it to be a conservative estimate for growth over the next two decades [3]. It can been seen that the landmark achievement of a market size exceeding 1GW/Yr is expected to occur during the period 2005-2008, if not sooner [4]. Indeed, market growth is expected to be at the higher rates over at least the next few years on the basis of capacity expansions already announced [5, 6].

A major determinant of increased market growth will be reduced costs. The cost of industrial solar cell modules is presently US\$3.5-6/W_p [7], resulting in an energy cost of US\$0.4-0.6/kWh depending of the available solar insolation for a grid-connected system [8]. The ability to achieve continued cost reductions depends largely on three interrelated factors:

- Mass manufacturing of solar cells in large facilities resulting in economies of scale - The European study of Bruton *et al.* [9], based essentially on established technologies with some conservative extrapolations, has concluded that module costs could be reduced to around 1Euro/W_p (≈US\$1/W_p) for a range of technologies. Materials would be approximately two-thirds of the total cost/W_p for a large plant.
- Improved cell efficiency – A large proportion of the costs of installed PV systems are area dependent. Therefore if cell efficiency can be increased without increasing the manufacturing cost, significant reductions in energy cost can be achieved. A high efficiency approach is all the more important to make the best used of the high material cost. High efficiency approaches now

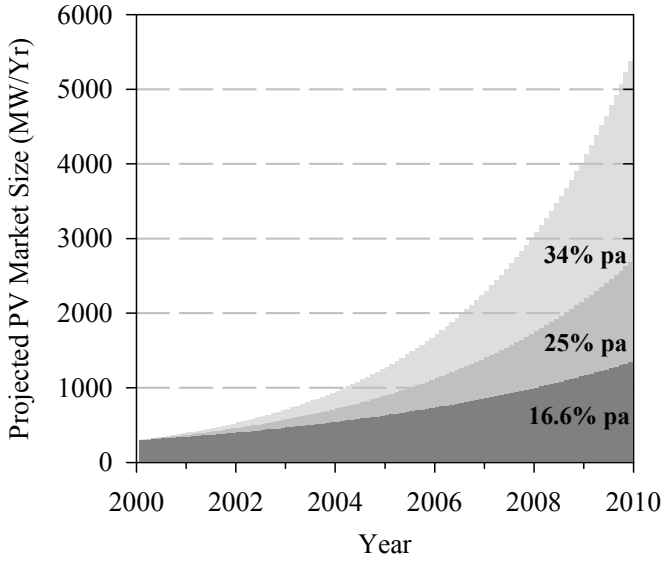


Figure 1.2: Projected market size for PV modules using a variety of growth rates for the period up to 2010.

at the industrial scale include the laser grooved buried grid (LGBG) cells produced by BPSolar under the Saturn™ name, HIT™ cells from Sanyo and OECO cells from ASE.

- Reduced material costs – Green has argued that as a cell technology matures, the constituent materials dominate the costs [10]. This is particularly true for silicon wafer based technologies where the cost of the starting wafer is currently about one half of the final module cost. Thin film and silicon based ribbon technologies (sometimes referred to as second generation technologies) avoid the cost of the silicon ingot and associated wafering and therefore offer potential savings. Indeed, the study of Bruton *et al.* [9] found that a ribbon based process would offer the lowest cost/W_p for this reason. Extrapolating, the cost assessment of Bruton *et al.* for modules based on thin ribbon substrates (<100μm) suggests that module costs close to US\$0.50/W_p are feasible.

A transition in the PV market from silicon wafer based technologies to thin film approaches has been predicted since the mid 1980's [11]. Thin film technologies currently at the pilot plant or industrial scale include cadmium telluride (CdTe), copper indium diselenide (CIS), amorphous silicon (a-Si), thin-film polycrystalline silicon (eg Pacific Power [11]), thin-film crystalline silicon (eg Astropower [12]), and silicon based ribbon technologies such as the edge-defined film-fed growth (EFG) and dendritic web. It would appear however that bulk crystalline silicon (single-crystal and multicrystalline) has actually increased its market share during the last decade. Figure 1.3 shows the market share by technology for both 1990 [13] and 2000 [2]. Over this period the total market size increased by a factor of more than six. Significantly, the market share for bulk crystalline silicon has actually increased from 67.9% to 85.4%, contrary to the perceived thin film revolution. While shipments of a-Si cells have grown

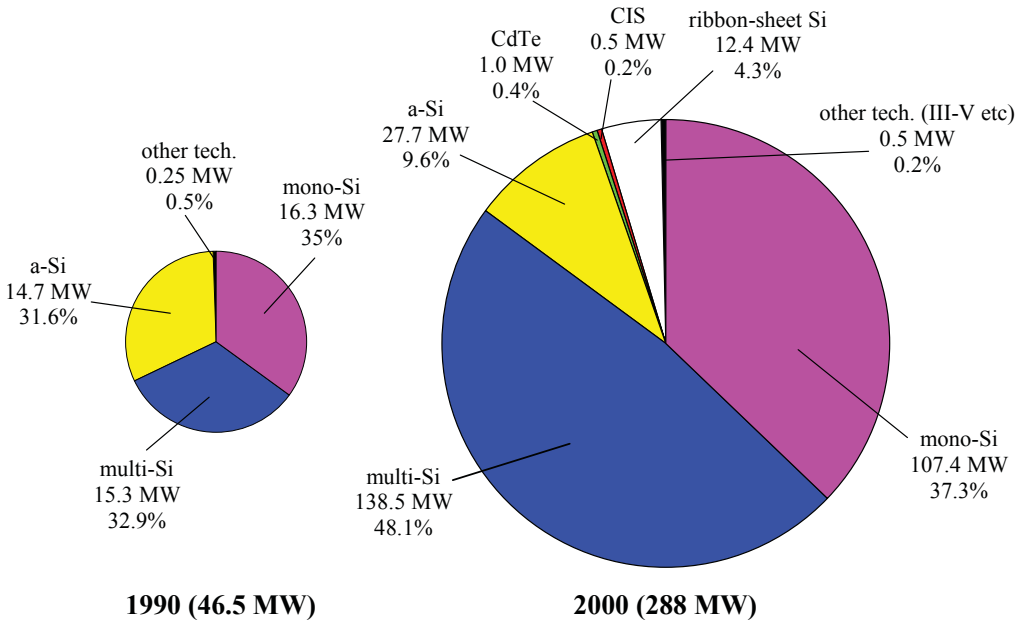


Figure 1.3: Market share of PV modules by technology type.

in absolute terms, the relative market share has reduced from 31.6% to 9.6%. The major benefactor of the reduced market share for a-Si has been multicrystalline silicon, which is now the dominant technology with a share of 48.1%. Ribbon and/or sheet silicon technologies have developed a reasonable market share of 4.3%. Thin film CdTe and CIS cells also now have a small market share (<0.5%). However, doubts are rising over the potential for these non-silicon based technologies to significantly displace silicon in large volumes due to toxicity (mainly for cadmium) and resource depletion issues (telluride and indium are relatively rare elements), problems that are not associated with silicon [14].

It appears there has been expanding diversity in cell fabrication technologies over recent years. Even for cells made from single crystal Czochralski (CZ) silicon wafers there are a number of approaches from simple screen-printed cells to more complicated LGBG and HIT cells. What does seem clear is that bulk crystalline silicon technologies are strongly placed to dominate the industry for at least the next decade and quite possible longer. Reductions in cost will require that progressively thinner wafers of higher bulk quality be used in combination with higher efficiency cell structures.

In the longer-term thin film cells are likely to dominate. Exactly what the nature of the thin film technology will be is unclear, particularly if a large scale PV industry based on silicon wafers with large amounts of invested capital becomes established, as would seem likely. There is a natural transition from thin wafer based silicon substrates to the various ribbon and sheet based technologies, or possibly other processes currently at the laboratory scale, such as the

epitaxial growth of thin crystalline silicon films [15, 16]. There are thus significant prospects for crystalline silicon to remain dominant, even in a thin film era.

A third generation of high efficiency, thin film PV technology is now being proposed [10]. This approach aims to overcome the fundamental efficiency limits associated with crystalline silicon solar cells due to thermalisation, transmission and intrinsic recombination, which account for more than 70% of the energy incident on a cell. Through band-gap engineering, it aims to achieve energy efficiencies much greater than the 15-20% currently obtained. Third generation PV is based on novel device structures such as tandem cells, hot carrier cells and multi-band cells, many of which are still at an embryonic stage of development [10].

1.2 Thesis Motivation

From the above overview, the short to medium term future for industrial solar cells appears to be based on single crystal (CZ) and multicrystalline silicon wafers. For costs reasons the substrates will have to be progressively thinner over time while simultaneously maintaining, but preferably increasing cell efficiency. Surface recombination losses thus become more significant and can indeed be the dominant mode of recombination losses for a high quality substrate, where the whole cell volume is electronically active. The minimisation of surface recombination losses, known as *surface passivation*, is a core topic of this thesis.

The current state of the art method for the surface passivation of silicon is thermal oxidation at *high temperature* (900°C-1100°C), and as such, silicon dioxide (SiO_2) passivation layers have been used for reference throughout this work. An emerging technology that offers high quality passivation layers at *low temperature* is plasma enhanced chemical vapour deposited (PECVD) silicon nitride (SiN) films, and these form the main theme investigated in this thesis. PECVD SiN films where transferred to the PV field by Hezel and co-workers in the early 1980's [17]. Due to the high hydrogen content of the films, they also offer the potential for *bulk passivation,* which is of special interest for lower quality starting material such as multicrystalline and ribbon silicon. Furthermore, their optical properties make them nearly ideal as a single layer anti-reflection coating for encapsulated solar cells. Therefore, SiN films offer great potential for increasing the efficiency of industrial crystalline silicon solar cells without increasing the fabrication cost, as they can simultaneously passivate the surfaces and the bulk as well as reduce surface reflection.

The surfaces of solar cells can be physically quite diverse. The surface may simply be the doped silicon wafer, or it may be diffused to form an emitter region. It can be planar or textured, and may or may not be contacted with metal. The degree of surface passivation provided by SiN and SiO_2 films has been investigated in this thesis for a variety of these different surface conditions. Importantly, accurate studies of surface recombination processes rely on accurate knowledge of the bulk recombination rate and on having simple, yet versatile techniques for quantifying the recombination rate. Therefore, the limits imposed on bulk recombination due to intrinsic processes (Auger recombination and radiative recombination) have also been studied, and new techniques for interpreting the recombination lifetime in terms of device characteristics have been introduced. Finally, it is important to demonstrate that the separate constituents can be put together to produce advanced solar cells. Consequently, the SiN films developed in this thesis where used to fabricate solar cells with high open-circuit voltages and high conversion efficiencies, thus demonstrating their excellent passivation properties in real devices. From a broader perspective, the data provided in this thesis for surface, emitter and bulk recombination in silicon, while useful for modeling silicon solar cells, is also of general interest for silicon semiconductor device modeling and analysis.

1.3 Thesis Outline

This thesis starts with the development of novel tools to investigate recombination losses in silicon and goes through to a detailed study of recombination in the two major regions that constitute a solar cell, the base and the emitter. Special attention is paid to their respective surfaces and an emphasis is placed on the passivation achieved using PECVD SiN technologies. Finally, the separately optimised elements are brought together to fabricate advanced solar cell devices based on the application of PECVD SiN.

Chapter 2 discusses the basic recombination mechanisms that occur within crystalline silicon. The recombination components within specific test structures of interest for this thesis are analysed and the photoconductance based methods used throughout this thesis for measuring the carrier lifetimes are described. New techniques for interpreting the effective lifetime in terms of device characteristics are introduced. Methods for determining the effective lifetime by measuring the open-circuit voltage of a device under arbitrary illumination are also described, and the equivalency of the photoconductance and voltage techniques, both quasi-static and transient, demonstrated.

Chapter 3 investigates the limits imposed on the bulk lifetime of crystalline silicon due to intrinsic recombination processes. The injection-level dependence and doping dependence is investigated for both *n*-type and *p*-type silicon of various doping densities, allowing a new general parameterisation for the intrinsic recombination rate in silicon of arbitrary injection level and dopant density to be developed. This new parameterisation is then used to re-evaluate the limiting efficiency of crystalline silicon solar cells as a function of cell thickness, dopant density and dopant type.

Chapter 4 presents a systematic study of the surface recombination properties of PECVD SiN films, fabricated using dilute silane gas, and thermal SiO_2 layers (FGA and alnealed) on *n*-type and *p*-type silicon wafers. The effects of the PECVD deposition parameters on the surface recombination velocity are investigated, and it is found that the SiN films optimised in this thesis are unique because they are *stoichiometric* in composition, where it was previously thought that well-passivating SiN films had to be silicon rich. The surface recombination velocity at the Si/SiN interface and at the Si/SiO_2 interface is reported as a function of injection level and dopant density. The limits imposed on the efficiency of SiN passivated solar cells due to surface recombination process is then determined. Finally, a characterisation of relevant non-electrical properties of the optimised stoichiometric SiN film is presented, where it is demonstrated that apart from their excellent surface passivation, they also show no absorption in the UV portion of the solar spectrum and that they can be easily patterned using photolithography and wet chemical etching

Chapter 5 investigates the recombination of n^+ and p^+ emitters passivated with optimised SiN films and thermal SiO_2 layers over a large range of sheet resistances. The role of the PECVD deposition parameters is investigated for passivating n^+ emitters, and again, the optimised SiN films are shown to be stoichiometric in composition. Device simulation is used to determine the surface recombination velocity as a function of the surface phosphorus concentration at the heavily doped n^+-Si surface when passivated with SiN or SiO_2. It is shown that the recombination properties of SiN passivated p^+ emitters is relatively poor compared to SiO_2 passivation and is worst for sheet resistances of ~150Ω/□. The efficiency potential of SiN passivated n^+p solar cells is also investigated.

Chapter 6 reports on the performance of experimental silicon solar cells passivated with stoichiometric SiN films. A variety of cell designs have been investigated, incorporating *n*-type and *p*-type float-zone silicon and *p*-type multicrystalline silicon. High open-circuit voltages are demonstrated for the different substrate types (up to 675mV for float-zone cells and up to 659mV for multicrystalline cells). The performance of large area cells, where the n^+ emitter was

formed in an industrial belt-line furnace, is also discussed. Finally, the research of this thesis is briefly summarized in **Chapter 7** and areas for future work are outlined.

CHAPTER 2

Quantifying and Measuring Recombination in Crystalline Silicon

Simply speaking, *generation* in semiconductors are the processes whereby electron-hole pairs are created [18]. The energy for the transition from the valence band to the conduction band can come from thermal processes or through the absorption of photons, as typically occurs in solar cells. *Recombination* is the opposite of generation and refers to the processes whereby electron-hole pairs are lost, with the excess energy released as either photons or phonons. Recombination therefore reduces the performance of solar cells, particularly the cell voltage and efficiency. Indeed, it has been concluded that of the avoidable losses in silicon solar cells, recombination losses are the most significant for both high efficiency laboratory cells and commercial multicrystalline cells [19, 20].

Experimentally, it is the *recombination lifetime* that is measured. The recombination lifetime, τ, of a material can be defined as the average time for an electron-hole pair to recombine following generation. It can be determined from the *recombination rate*, U, for both n-type and p-type silicon:

$$\tau \equiv \frac{\Delta n}{U} \tag{2.1}$$

where Δn (Δp) is the excess carrier density of electrons (holes) and $\Delta n = \Delta p$ in the absence of trapping effects. Schroder [21] has pointed out that the recombination lifetime is a property of the carriers within the semiconductor, rather than a property of the semiconductor itself. As such, it is a weighted average across all the carriers, whose individual behaviours may be influenced by different factors, including surfaces, bulk defects and the density of carriers, besides the fundamental properties of the semiconductor material. Interpreting the recombination lifetime can therefore be difficult, as it represents a number of specific recombination mechanisms occurring simultaneously within the bulk and at the surfaces. For this reason, the recombination lifetime is sometimes referred to as an *effective lifetime*.

A main topic of this thesis is the study of surface recombination processes. Direct measurement of the surface recombination rate is difficult and it is common to investigate surface recombination processes by measuring the recombination lifetime and then subtracting the effects of recombination processes that occur within the bulk of the silicon. Obviously minimizing the bulk recombination processes is desirable, but it is not possible to eliminate them completely, as processes such as radiative and Auger recombination are intrinsic and will still occur. Understanding and quantifying the rate of the specific bulk recombination mechanisms in crystalline silicon is thus necessary, and these are discussed in the next section. The fundamentals of surface recombination processes are then described and the recombination within specific test structures, which are applied later in this thesis, analysed. Photoconductance based methods for measuring the effective lifetime are then described and techniques for interpreting the effective lifetime in terms of device characteristics introduced. Finally, methods for determining the effective lifetime by measuring the open-circuit voltage of a device are discussed and the inter-relationship between the injection-level-dependent effective lifetime and the device characteristics emphasized.

2.1 Recombination Mechanisms

Three fundamental recombination mechanisms that occur in semiconductors are:

(i) Radiative recombination,

(ii) Auger recombination, and

(iii) Recombination through *defects* in the bandgap.

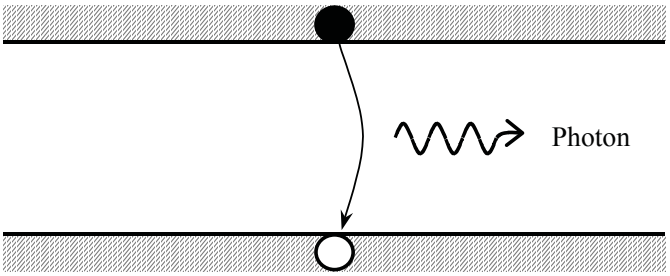


Figure 2.1. Energy band visualization of radiative recombination.

Other recombination processes within solar cells can generally be viewed as a manifestation of these three fundamental mechanisms. The surface of a semiconductor represents an abrupt discontinuity in its otherwise uniform crystal structure. The high number of dangling bonds creates a large density of defects throughout the bandgap. Therefore, surface recombination is a particular case of process (iii) above. Similarly, in the heavily doped emitter regions of a solar cell, the high doping results in Auger recombination limiting the lifetime within the emitter, in conjunction with surface recombination at the emitter surface. Emitter recombination is therefore a particular case of processes (ii) and (iii) above.

2.1.1 Radiative Recombination

Radiative recombination is simply the direct annihilation of an electron-hole pair as depicted in Figure 2.1. It is the inverse process to optical generation, the excess energy being released mainly as a photon with an energy close to that of the bandgap. It involves a conduction band electron falling from an allowed conduction band state into a vacant valence band state (a hole). The radiative recombination rate, U_{rad}, therefore depends on the concentration of free electrons, n, and free holes, p:

$$U_{rad} = Bnp \tag{2.2}$$

where B is the coefficient of radiative recombination. From detailed balance considerations, the value of B for silicon has been calculated to be $2\text{x}10^{-15}\text{cm}^3\text{s}^{-1}$ [22, 23]. Experimental determinations for the radiative recombination coefficient in silicon are significantly higher however, with B=$9.5\text{x}10^{-15}\text{cm}^3\text{s}^{-1}$ [24]. The reasons for the discrepancy are not clear, although it is believed that excitonic effects and the assumed value for the intrinsic carrier concentration in silicon are responsible [25].

From Eq. (2.1), the common relationships for the radiative lifetime in n-type and p-type material under low injection ($\tau_{rad,li}$) and high injection conditions ($\tau_{rad,hi}$) can be determined,

$$\tau_{rad,li} = \frac{1}{BN_{dop}} \quad \text{and} \quad \tau_{rad,hi} = \frac{1}{B\Delta n}, \tag{2.3}$$

where N_{dop} is the density of donor (N_D) or acceptor atoms (N_A) respectively. It can be seen that the radiative lifetime depends on the inverse of the carrier density ($\tau_{rad} \propto 1/n$). Therefore, τ_{rad} is constant at low injection, but then decreases and continues to decrease as the injection level increases.

In general, the rate of radiative recombination in silicon is considered to be small or even negligible compared to other recombination processes [26]. This is because silicon is an indirect-bandgap semiconductor and must simultaneously emit a photon and a phonon to conserve both energy and momentum. Radiative recombination is therefore a four-particle process in silicon, which inherently has a low probability of occurring. For direct-bandgap semiconductors such as GaAs, radiative recombination is typically the dominant recombination process as simultaneous phonon emission is not required. This is exploited in the operation of light emitting diodes.

Another important factor in the operation of direct-bandgap semiconductors is photon recycling [27]. This is where the photons emitted during radiative recombination are re-absorbed somewhere else in the semiconductor, resulting in new generation. The effect of photon recycling in silicon does not appear to have been extensively studied, partially because silicon is weakly absorbing at the wavelengths of interest, although light trapping schemes could make photon recycling relatively efficient even in silicon. The impact of photon recycling in silicon would be to further reduce the role of radiative recombination.

2.1.2 Auger Recombination

Traditionally, Auger recombination is viewed as a three-particle interaction where a conduction band electron and a valence band hole recombine, with the excess energy being transferred to a third free electron or hole, as depicted in Figure 2.2 [28]. The charge carriers involved are assumed to be non-interacting quasi-free particles [29]. The *eeh* process denotes when the excess energy is transferred to another electron, with the recombination rate given by $U_{eeh}=C_n n^2 p$. Similarly, the *ehh* process denotes when the excess energy is transferred to another hole, with recombination rate $U_{ehh}=C_p n p^2$, where C_n and C_p are Auger coefficients. The total Auger recombination rate, U_{Auger}, is then given by

$$U_{Auger} = C_n n^2 p + C_p n p^2 , \tag{2.4}$$

from which the common relationships for the Auger lifetime in *n*-type and *p*-type material under low injection ($\tau_{Auger,li}$) and high injection conditions ($\tau_{Auger,hi}$) can be determined. For *n*-type silicon $\tau_{Auger,li} = \dfrac{1}{C_n N_D^2}$ and $\tau_{Auger,hi} = \dfrac{1}{(C_n + C_p)\Delta p^2}$, (2.5)

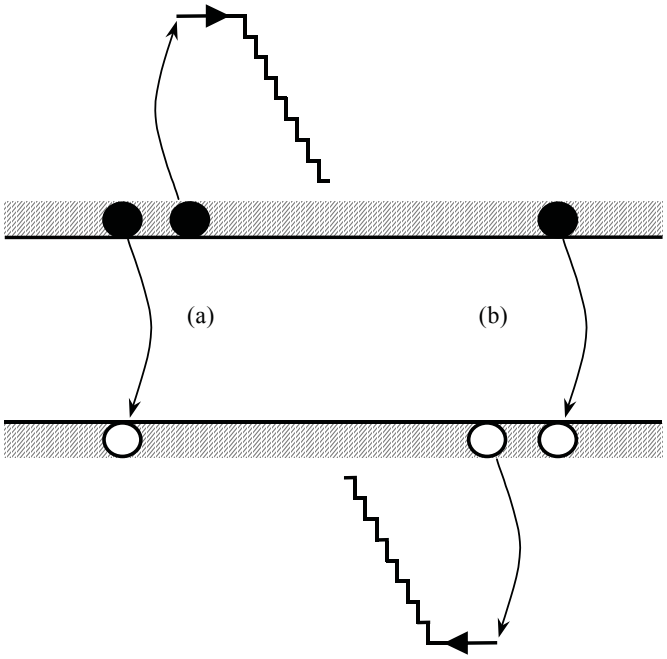


Figure 2.2. Energy band visualization of Auger recombination with the excess energy transferred to: (a) a conduction band electron; (b) a valence band hole.

and for *p*-type $\tau_{Auger,li} = \frac{1}{C_p N_A^2}$ and $\tau_{Auger,hi} = \frac{1}{(C_n + C_p)\Delta n^2}$, (2.6)

where $C_a \equiv C_n + C_p$ is the ambipolar Auger coefficient. The most commonly quoted values for the Auger coefficients appear to be those determined by Dziewior and Schmid (C_n=2.8x10^{-31}cm^{6}s^{-1} and C_p=0.99x10^{-31}cm^{6}s^{-1}) for silicon with a doping concentration greater than 5x10^{18}cm^{-3} [30]. The implied value for the ambipolar Auger coefficient is then C_a=3.79 x 10^{-31}cm^{6}s^{-1}.

From Eq. (2.5) and Eq. (2.6), it can be seen that the Auger lifetime *ideally* depends on the inverse of the carrier density squared ($\tau_{Auger} \propto 1/n^2$). It shows a stronger dependence with the injection level than τ_{rad}, and therefore, Auger recombination will become the dominant mode of recombination in silicon for high injection levels, as might occur in concentrator solar cells, or for high dopant densities, as occurs in heavily doped emitter regions.

In reality, Auger recombination is more complicated than the idealised view presented above, and significant departures from Eq. (2.5) and Eq. (2.6) have been experimentally determined [31, 32]. The reasons for these departures are more fully discussed in Chapter 3, where a new parameterisation for the enhanced Auger recombination rate will be given based on the research performed during this thesis. This new parameterisation demonstrates the required enhancement at both low injection and high injection conditions.

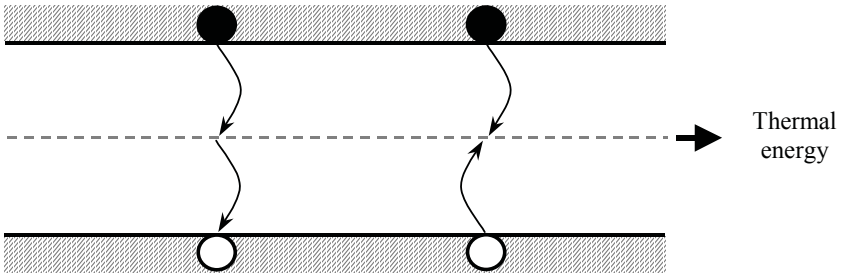


Figure 2.3. Energy band visualization of recombination through a defect state within the energy bandgap.

2.1.3 Bulk Recombination Through Defects

The presence of defects within a semiconductor crystal, be they from impurities or crystallographic imperfections such as dislocations, produces discrete energy levels within the bandgap. As shown in Figure 2.3, these defect levels, also known as *traps*, greatly facilitate recombination through a two-step process whereby a free electron from the conduction band first relaxes to the defect level and then relaxes to the valence band where it annihilates a hole [33]. The dynamics of this recombination process where first analysed by Shockley and Read [34] and Hall [35], with the recombination rate, U_{SRH}, for a single defect level given by

$$U_{SRH} = \frac{np - n_i^2}{\tau_{po}(n + n_1) + \tau_{no}(p + p_1)} \tag{2.9}$$

where τ_{po} and τ_{no} are the fundamental hole and electron lifetimes which are related to the thermal velocity of charge carriers, ν_{th}, the density of recombination defects, N_t, and the capture cross-sections, σ_p and σ_n, for the specific defect:

$$\tau_{po} \equiv \frac{1}{\sigma_p \nu_{th} N_t} \qquad \text{and} \qquad \tau_{no} \equiv \frac{1}{\sigma_n \nu_{th} N_t}\,. \tag{2.10}$$

n_1 and p_1 are statistical factors defined as:

$$n_1 \equiv N_C \exp\left(\frac{E_t - E_C}{kT}\right) \qquad \text{and} \qquad p_1 \equiv N_V \exp\left(\frac{E_C - E_G - E_t}{kT}\right). \tag{2.11}$$

where N_C and N_V are the effective density of states at the conduction and valence band edges, E_C and E_G are the conduction band and bandgap energies and E_t is the energy level of the defect.

It follows from Eq. (2.1) that the SRH lifetime, τ_{SRH}, can be expressed as

$$\tau_{SRH} = \frac{\tau_{no}(p_o + p_1 + \Delta n) + \tau_{po}(n_o + n_1 + \Delta n)}{n_o + p_o + \Delta n}, \tag{2.12}$$

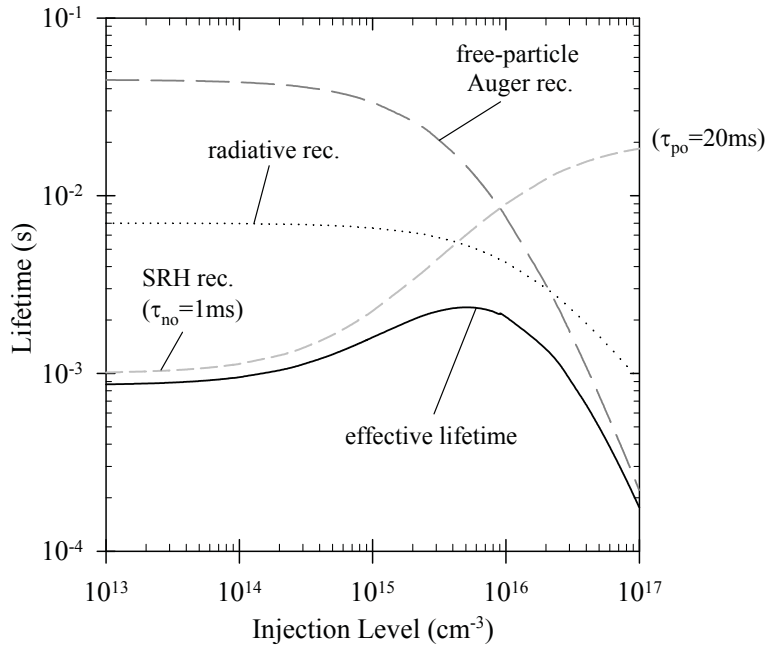


Figure 2.4. Lifetime curves for SRH recombination, radiative recombination and free-particle Auger recombination. The lifetime increases with injection level for SRH recombination through deep defects but decreases for intrinsic bulk recombination processes. The resulting effective lifetime is therefore dominated by SRH recombination at low injection and Auger recombination at high injection.

from which it can be seen that the SRH lifetime is a function of the carrier injection level and the dopant density (through n_o and p_o), as well as defect specific properties such as the concentration of traps, their energy level and their capture cross-sections. An important result that follows from Eq. (2.12) is that traps with energies close to the centre of the bandgap (deep defects) are the most effective recombination centres. Furthermore, for such deep defects, the SRH lifetime can be simplified for low injection ($\tau_{SRH,li}$) and high injection ($\tau_{SRH,hi}$) conditions

to, for *n*-type silicon $\tau_{SRH,li} = \tau_{po}$ and $\tau_{SRH,hi} = \tau_{no} + \tau_{po}$, (2.13)

and for *p*-type silicon $\tau_{SRH,li} = \tau_{no}$ and $\tau_{SRH,hi} = \tau_{no} + \tau_{po}$. (2.14)

It follows from Eq (2.13) and Eq. (2.14) that the SRH lifetime for a deep defect actually increases with injection level, and the greater the asymmetry between τ_{no} and τ_{po}, the greater the increase in the SRH lifetime.

Figure 2.4 shows lifetime curves for a 1Ωcm *p*-type silicon wafer for SRH recombination (deep defect, τ_{po}=1ms and τ_{po} = 20ms), radiative recombination and free-particle Auger recombination. It can be seen that recombination through deep defects results in a distinctly different injection level dependence than the intrinsic recombination processes (radiative and Auger), and that SRH recombination normally dominates at low injection levels, eventually

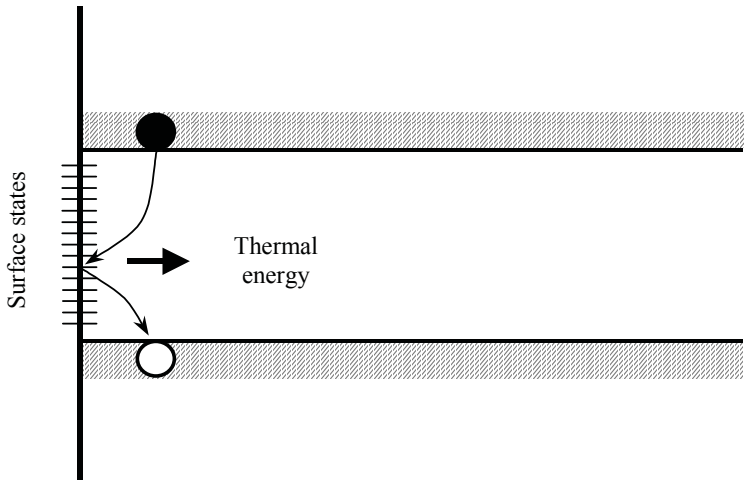


Figure 2.5. Energy band visualization of recombination at a semiconductor surface, where multiple defect states exist.

being surpassed by the rate of Auger recombination at sufficiently high injection levels. Finally, while the work in this thesis will not be directly concerned with SRH bulk recombination, the above discussion serves as a useful starting point for the analysis of defects originating at the surfaces of semiconductors, which is discussed in the next section.

2.1.4 Surface Recombination Through Defects

The surfaces or interfaces of a silicon substrate represent a severe discontinuity in its crystalline structure [25]. The large number of partially bonded silicon atoms give rise to many dangling bonds, and therefore a large density of defect levels are found within the bandgap near the semiconductor surface as illustrated in Figure 2.5. Even if the silicon surface is not bare, say due to a native oxide, the presence of silicon-oxygen bonds can stress the crystal structure at the surface, which again introduces many defect states. The SRH analysis of section 2.1.3 again applies, although it has to be reformulated in terms of recombination events per unit surface area, rather than per unit volume. For a single defect at the surface, the rate of surface recombination, U_S, is given by

$$U_S = \frac{n_s p_s - n_i^2}{\frac{n_s + n_1}{S_{po}} + \frac{p_s + p_1}{S_{no}}} \qquad (2.15)$$

where n_s and p_s are the concentrations of electrons and holes at the surface, and S_{no} and S_{po} are related to the density of surface states per unit area, N_{ts}, and the capture cross-sections, σ_p and σ_n, for the specific defect:

$$S_{no} \equiv \sigma_n \nu_{th} N_{ts} \qquad \text{and} \qquad S_{po} \equiv \sigma_p \nu_{th} N_{ts} \,. \qquad (2.16)$$

In reality, defect levels are so numerous that they can be considered to be continuously distributed throughout the bandgap, and both their density and capture cross-sections will be dependent on their energy level. Using $D_{it}(E)$ for the density of interface traps at a given energy (rather than N_{ts} for a specific energy level) and integrating over the entire bandgap, it follows that

$$U_S = \int_{E_V}^{E_C} \frac{v_{th}\left(n_s p_s - n_i^2\right)}{\frac{n_s + n_1}{\sigma_p(E)} + \frac{p_s + p_1}{\sigma_n(E)}} D_{it}(E)dE \quad . \tag{2.17}$$

Similar to the definition of the recombination lifetime (Eq. (2.1)), the *surface recombination velocity*, S, is defined as

$$U_S \equiv S\Delta n_s \,, \tag{2.18}$$

and so the surface recombination velocity can be related to the fundamental properties of the surface defects through Eq. (2.17) and Eq. (2.18). It is the surface recombination velocity, S, that is typically used for quantifying surface recombination processes, and it is used throughout this thesis, although some authors also define an effective surface lifetime, τ_S [36].

The injection level dependence of S from Eq. (2.17) has been discussed in detail by Aberle [26]. Because of the large number of energy dependent variables, it is possible for the surface recombination velocity to decrease, increase or remain constant as the injection level increases. What can be concluded from Eq. (2.17) is that there are two fundamental mechanisms for reducing the surface recombination rate at a semiconductor surface:

a) Optimise the properties of the surface states - In particular, reduce the density of the interface states and the magnitude of the capture cross-sections. By growing an appropriate dielectric layer such as silicon oxide, many of the dangling silicon bonds are passivated with oxygen or hydrogen atoms and the $D_{it}(E)$ reduced.

b) Reduce the surface concentration of electron or holes – From Eq. (2.18), the recombination rate at the surface is normally controlled by the excess concentration of minority carriers at the surface. Minimising the concentration of minority carriers therefore reduces the surface recombination rate. This can be achieved by doping the semiconductor surface to repel the minority carries such as in an emitter region or a back-surface-field (BSF). Alternatively, fixed charges in an overlying dielectric layer can be used to either repel the minority carriers (for a *p*-type wafer you would use negative charges to repel the free electrons), or in the extreme case invert the surface (large amounts of fixed positive charges would invert the surface of a *p*-type silicon wafer). This is also known as *field effect passivation*, as an electric field is essentially established near the surface.

In reality, the methods for reducing surface recombination in actual devices rely on both of these mechanisms to some extent. While a thermally grown silicon oxide layer can be very effective at reducing the density of interface states [37], the oxide layer can also contain fixed and/or mobile charge carriers [36]. It is therefore important to also consider the possibility of an electric field near the semiconductor surface, which results in a bending of the energy bands, along with a distribution of defects. Such an extension to the SRH surface recombination model has been proposed by Girish *et al.* [38]. They demonstrated that the band-bending can result in a significant change in the injection level dependence of the surface recombination velocity for a given set of defect parameters. As discussed by Aberle [26], the surface recombination rate in the presence of band-bending is minimised when the surface is accumulated or inverted, but is maximal when the surface is depleted. Additional extensions to the Girish model have also been proposed to account for [39, 40]: (i) the spatial distribution of fixed charges within a passivating dielectric layer; (ii) carrier recombination within the space-charge region for an inverted surface and (iii) the possibility of minority carriers tunnelling through the potential barrier formed by band-bending and reaching highly recombinative areas at the semiconductor surface.

It is clear that at a fundamental level, many factors affect surface recombination processes and at different injection levels different factors may dominate. It is therefore difficult to predict the injection level dependence of the surface recombination velocity. A simplifying case that can be easily analysed is when the surfaces are heavily doped, with emitter layers for example, such as in n^+pn^+ samples. This is discussed in the next section.

2.1.5 Emitter Recombination

Modelling the recombination occurring within an emitter region is relatively complicated from first principles. Doping profiles are not normally uniform and so the spatial variation in the dopant concentration needs to be considered, as does the possibility of a dead layer from the diffusion process. Heavy doping effects including the degeneracy of the semiconductor, bandgap narrowing and free-carrier absorption need to be included, along with intrinsic recombination processes and the normal SRH recombination processes related to defects, both within the emitter and at the emitter's surface. Because the emitter regions are heavily doped however, two simplifications follow. Firstly, the minority carrier concentration in the emitter region normally remains low and secondly, Auger recombination is likely to be the dominant bulk recombination mechanism. It follows that the recombination lifetime in the emitter region is constant with injection level, and the recombination current into the emitter, J_{rec}, can be expressed as [41]

$$J_{rec} = J_{oE} \frac{np}{n_i^2}, \tag{2.19}$$

where J_{oE} is defined to be the *emitter saturation current density*, and n and p refer to the electron and hole concentrations on the base side of the space-charge region. The recombination rate for the emitter, $U_{emitter}$, can be referred to the entire volume of the wafer in order to compare it with other bulk processes

$$U_{emitter} = J_{oE} \frac{np}{qWn_i^2}, \tag{2.20}$$

where q is the elementary charge of an electron, and W the width of the base region. An emitter lifetime can then be obtained for an *n*-type and *p*-type base under low injection ($\tau_{emitter,li}$) and high injection conditions ($\tau_{emitter,hi}$)

$$\tau_{emitter,li} = \frac{qWn_i^2}{J_{oE} N_{dop}} \quad \text{and} \quad \tau_{emitter,hi} = \frac{qWn_i^2}{J_{oE} \Delta n}. \tag{2.21}$$

It can be seen that the emitter lifetime will be constant at low injection and depends on the inverse of the carrier density ($\tau_{emitter} \propto 1/n$) at high injection, a similar dependence to that expected for radiative recombination. Typically however, the term J_{oE}/qWn_i^2 is much greater than B for radiative recombination.

Emitter recombination can be viewed as a special case of surface recombination. A *virtual surface* can defined just at the base side of the space-charge region and an *effective surface recombination velocity*, S_{eff}, defined for this virtual surface

$$U_S \equiv S_{eff} \Delta n \quad . \tag{2.22}$$

Combining Eq. (2.19) and Eq. (2.22) gives

$$U_S \equiv S_{eff} \Delta n \quad = \frac{J_{rec}}{q} = J_{oE} \frac{np}{qn_i^2}. \tag{2.23}$$

Which for the case of *p*-type silicon reduces to

$$S_{eff} = J_{oE} \frac{N_A + \Delta n}{qn_i^2}, \tag{2.24}$$

which is also known as the quasi-static emitter approximation [42]. It is important to differentiate such a virtual surface from the actual surface of an emitter. The S_{eff} at the virtual surface is merely another way of representing the J_{oE}. However, it is possible to used measured values for the J_{oE} and for the emitter profile, in conjunction with device modelling, to determine the surface recombination velocity at the actual emitter surface. This has been done in Chapter 5 for a variety of emitters passivated with both thermal silicon oxide and PECVD silicon nitride.

2.2 The Effective Lifetime

The five recombination mechanisms discussed in the previous section may occur simultaneously within a semiconductor. In many situations, some of the recombination processes will contribute negligibly to the overall recombination rate, particularly radiative recombination. Indeed, in many experimental situations the aim is to minimise the other recombination mechanisms to facilitate the exploration of one particular recombination process. In the study of surface recombination processes for example, high quality float-zone (FZ) silicon wafers, processed by clean-room techniques, can be used to minimise bulk recombination. In other situations, the contributions from different recombination processes will be unknown or even unavoidable. It is therefore necessary to consider how the different recombination mechanisms combine to give an overall effective recombination rate or an *effective lifetime*.

In general, the recombination processes can be considered to occur independently and the effective recombination rate, $U_{effective}$, is simply the sum of the individual rates,

$$U_{effective} = U_{rad} + U_{Auger} + U_{SRH} + U_{surface} + U_{emitter} . \tag{2.25}$$

It follows from Eq. (2.1) that the effective lifetime is given by

$$\frac{1}{\tau_{effective}} = \frac{1}{\tau_{rad}} + \frac{1}{\tau_{Auger}} + \frac{1}{\tau_{SRH}} + \frac{1}{\tau_{surface}} + \frac{1}{\tau_{emitter}} , \tag{2.26}$$

where the first three terms refer to bulk recombination processes and are often grouped into a bulk recombination lifetime

$$\frac{1}{\tau_{bulk}} = \frac{1}{\tau_{rad}} + \frac{1}{\tau_{Auger}} + \frac{1}{\tau_{SRH}} . \tag{2.27}$$

The specific test structures illustrated in Figure 2.6 are of interest in this thesis. The first test structure shows a silicon wafer which has been passivated on both sides with an identical dielectric film. The recombination rate can be expressed as

$$\begin{aligned} & U_{effective} = U_{bulk} + 2U_{surface} \\ \Rightarrow \qquad & \frac{\Delta n}{\tau_{eff}} = \frac{\Delta n}{\tau_b} + \frac{2S\Delta n_s}{W} \end{aligned} \tag{2.28}$$

For the simplifying situation where the carrier profiles are relatively uniform throughout the structure, which implies S is low, one can equate $\Delta n = \Delta n_s$ and therefore

$$\frac{1}{\tau_{eff}} = \frac{1}{\tau_b} + \frac{2S}{W} \tag{2.29}$$

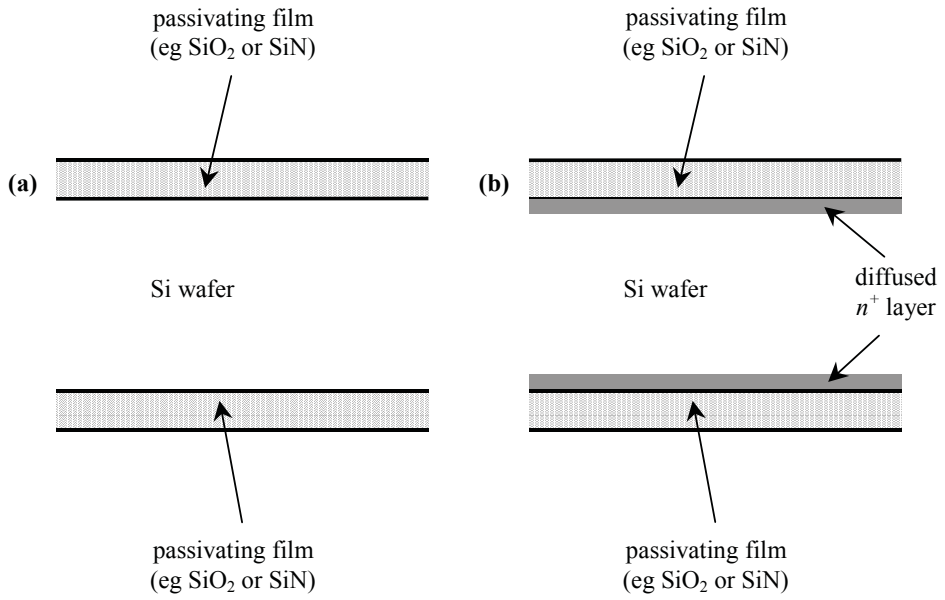


Figure 2.6. Test structures used for examining recombination at: (a) the interface of silicon and a passivating film and (b) a diffused emitter layer.

This relatively simple expression, which allows the surface recombination velocity to be determined by measuring the effective lifetime, has been used in Chapters 3 and 4. In its simplest application, an assumed value is used for the bulk lifetime. Alternatively, samples of different thickness can be measured to determine both the bulk lifetime and the surface recombination velocity. A more detailed discussion of the experimental conditions for which Eq. (2.29) is valid is given by Sproul [43].

The second test structure shown in Figure 2.6 is of a symmetrical n^+pn^+ test structure used for measuring emitter recombination. The emitter surfaces may or may not be passivated with a dielectric film. The recombination rate can be expressed as

$$\begin{aligned} U_{effective} &= U_{bulk} + 2U_{emitter} \\ \Rightarrow \qquad \frac{\Delta n}{\tau_{eff}} &= \frac{\Delta n}{\tau_b} + \frac{2J_{oE}np}{qWn_i^2} \quad , \end{aligned} \tag{2.30}$$

which reduces to

$$\frac{1}{\tau_{eff}} = \frac{1}{\tau_b} + \frac{2J_{oE}\left(\Delta n + N_{dop}\right)}{qWn_i^2} \, . \tag{2.31}$$

The injection level dependence of Eq. (2.31) forms the basis of two measurement techniques commonly used for determining J_{oE}. The first technique, developed by Kane and Swanson [41], measures the injection level dependent recombination lifetime of symmetric n^+pn^+ structures made from lightly doped silicon with the base in high injection. J_{oE} can then be

determined from the slope of $1/\tau_{eff}$ versus Δn. The second technique measures the low injection recombination lifetime of symmetric n^+pn^+ structures made from intermediately doped silicon, where $N_{dop}>>\Delta n$, and assumes a value for the low injection bulk lifetime. The first technique has the advantage that it does not require a value for the bulk lifetime and it uses data over a range of injection levels. It is therefore, potentially more accurate. Furthermore, it is relatively insensitive to variations in the recombination lifetime from bulk process, and can actually be used to evaluate the bulk lifetime [44]. This high injection technique has therefore been extensively used in Chapter 5 for measuring the J_{oE} of both phosphorus and boron diffused emitters, passivated with thermally grown silicon oxide and PECVD silicon nitride.

Having briefly discussed different forms of recombination and suitable methods for investigating surface recombination processes by measuring the effective lifetime, the methods used in this thesis for measuring the effective lifetime are covered next.

2.3 Measuring the Effective Lifetime

2.3.1 Introduction

The effective lifetime quantifies the rate of recombination occurring within a solar cell, and therefore strongly impacts its performance. Important applications of the effective lifetime include process monitoring and optimisation [45], quality control [46] and predicting the performance of finished devices from partially processed substrates [47]. Numerous techniques have been developed to measure the effective lifetime, and these are reviewed by Schroder [21]. Many of these techniques require finished devices such as the open-circuit voltage decay (OCVD) and short-circuit current decay (SCCD) methods, while others are non-contacting, such as the transient photoconductance decay (tpcd). Non-contacting techniques have the advantage that they can be applied to partially processed devices, which are free of metal contacts. This allows the devices to be designed for a specific purpose, such as examining surface recombination at a passivated surface, without having to deal with recombination at the contacts etc. Non-contacting techniques are also useful in minimising contamination if additional processing is required.

Optical methods are normally used for generating the excess carriers when measuring the effective lifetime. Sophisticated lasers and LED arrays can be applied [48, 49], although for many applications, a simple photographic flash-lamp can be used [50], as long as the sample is not significantly heated. Both the spectral content and time dependence of the illumination can

be important factors. Illumination of a silicon sample with long wavelength light (>1000nm) results in relatively uniform generation throughout the sample, while short wavelength light can be used to probe the front surface. Indeed, the possibility of doing spectrally resolved lifetime measurements has been investigated [51, 52].

Three operating regimes can be identified for the time dependence of the illumination. The first involves an abrupt cessation of the illumination and subsequent determination of the sample's excess carrier density without any illumination. This is the traditional transient technique, which can be easily applied to high lifetime samples with only simple electronics. The second regime is the steady-state illumination, which has also been historically used, although not as frequently as the transient method. In the third regime the intensity of the illumination varies monotonically with time, which is the basis of the quasi-steady-state (Qss) method first introduced by Sinton and Cuevas [50]. The interest in varying the illumination level is that a range of different operating points can be conveniently explored. Obviously the first two regimes are extreme cases of the third, which therefore represents the general case. Proper analysis of all the different possibilities requires use of the continuity equation for the excess minority carriers,

$$\frac{\partial \Delta n}{\partial t} = G_b(t,x) - U_b(t,x) + \frac{1}{q}\frac{dJ_n}{dx}, \qquad (2.32)$$

where $G_b(t,x)$ and $U_b(t,x)$ are the photogeneration rate and recombination rate in the bulk, Δn the excess minority carrier density and J_n the electron current density. For regime 1: $G_b(t,x) = 0$, while for regime 2: $\partial \Delta n/\partial t = 0$. Furthermore, the transport term reduces to surface recombination terms when Eq. (2.32) is integrated over the sample width because the sample is in open-circuit conditions. Nagel *et al.* [53] generalised the analysis procedure to define an effective lifetime regardless of the flash-lamp characteristics by combining the bulk and surface recombination rates into an effective recombination rate (U_{eff}) and not dropping any of the terms in Eq. (2.32),

$$\tau_{eff} = \frac{\Delta n_{av}(t)}{G_{av}(t) - \dfrac{\partial \Delta n_{av}(t)}{\partial t}}. \qquad (2.33)$$

To determine the effective lifetime from this generalised definition, it is therefore necessary to measure the time dependence of the excess carrier density and the generation rate within the test sample. A popular method for doing this is based on measuring the sample's excess photoconductance, which is discussed in the next section.

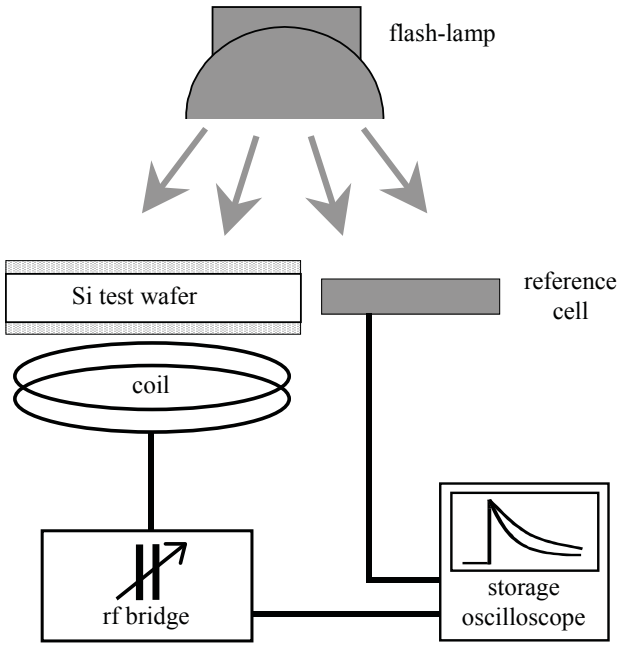


Figure 2.7. Schematic of the inductively coupled photoconductance apparatus used for measuring the effective lifetime.

2.3.2 Photoconductance Based Techniques

The experimental apparatus used in this thesis was fabricated by Sinton Consulting and a schematic is given in Figure 2.7. The sample of interest is inductively coupled by the coil to an rf-bridge circuit, which senses changes in the sample's permeability and therefore its conductance. A reference solar cell and oscilloscope are used to determine the time dependence of both the excess photoconductance of the test sample, $\Delta\sigma(t)$, and its illumination, $I(t)$, by using appropriate calibration functions. The average excess carrier density in the test sample, $\Delta n_{av} = \Delta p_{av}$, can be determined via

$$\Delta n_{av}(t) = \frac{\Delta\sigma(t)}{q\left(\mu_n + \mu_p\right)W}, \qquad (2.34)$$

where W is the sample thickness and μ_n and μ_p are the electron and hole mobilities, which are functions of the dopant density and injection level [54, 55].

The illumination intensity, I_{av}, measured from the reference solar cell is normally quoted in suns (1sun=1kW/m^2). It is a measure of the number of photons incident on the sample surface. The generation rate within the sample can therefore be determined as

$$G_{av}(t) = \frac{I_{av}(t) f_{abs} N_{ph|1sun}}{W}, \qquad (2.35)$$

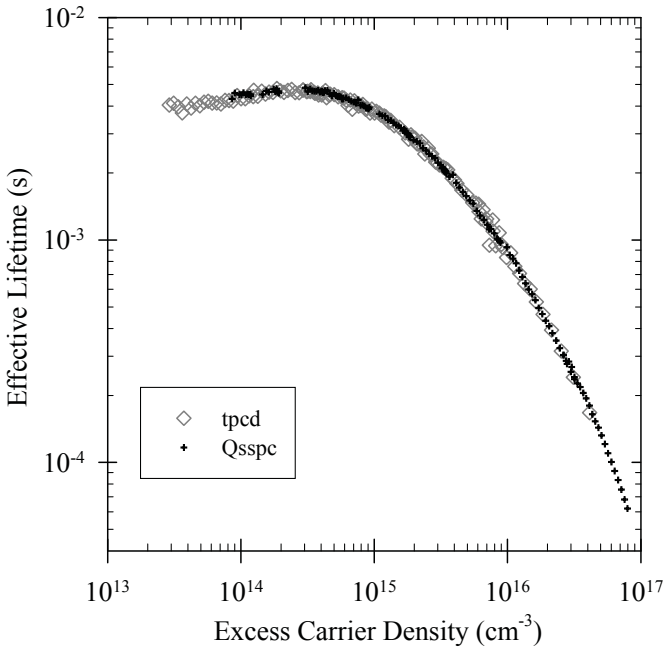


Figure 2.8. Example of an injection-level-dependent effective lifetime measurements using both the transient pcd and quasi-steady-state pc techniques. While the effective lifetime can vary over a large range with changing injection level, excellent agreement is obtained between the two techniques.

where f_{abs} is the optical absorption fraction of the sample to take into account reflection and transmission losses and $N_{ph|1sun}$ is the density of photons in solar light with an irradiance of 1sun ($1kW/m^2$), with an energy greater than the silicon bandgap. It follows that the required quantities in Eq. (2.33) can be experimentally measured and the effective lifetime determined.

An example of an injection-level-dependent effective lifetime measurement in given in Figure 2.8 for a high lifetime solar cell precursor consisting of a phosphorus diffused, high resistivity silicon substrate passivated with high quality TCA based silicon oxide on the front and rear. Measurements using both tpcd and Qss photoconductance with the generalised analysis of Eq. (2.33) are shown. It can be seen that excellent agreement is obtained between the two techniques over a large range of lifetimes and carrier injection levels.

2.3.3 Calibration Functions for Determining the Photoconductance

The oscilloscope in Figure 2.7 measures a voltage from the rf bridge which is related to the test wafer photoconductance. To obtain an accurate measurement of the photoconductance and therefore Δn and τ_{eff}, it is necessary to accurately calibrate this voltage output. A set of calibration wafers was prepared using high resistivity (150Ωcm) *p*-type silicon wafers with n^+

diffusions on both sides. The wafers where nominally etched to thicknesses of 100μm, 200μm, 300μm and 400μm, with emitter sheet resistances of approximately 5Ω/□, 10Ω/□, 20Ω/□, 35Ω/□ and 90Ω/□. The sheet resistance of each n^+ diffusion was accurately measured using a 4-point probe and a 4digit multimeter, from which the conductance of each wafer was calculated.

The calibration procedure involved placing a test wafer of known bulk resistivity on the coil and balancing the rf bridge so that the dark conductance of the test wafer is nulled. The test wafer is then replaced with each calibration wafer in turn and the excess photoconductance, which equals the conductance of the calibration wafer minus the dark conductance of the test wafer, plotted against the voltage. Figure 2.9 shows the voltage response of the rf bridge for four test wafers. It can be seen that for each test wafer, the excess conductance is a monotonically increasing function of the rf bridge voltage, which can be accurately fit with a weak quadratic function. Importantly, the calibration curves are a function of the test wafer dark conductance, or equivalently, the null point of the rf bridge. As the test wafer dark conductance increases, the excess conductance increases for given voltage. This is a significant result, as it means that to accurately measure the effective lifetime of wafers with different resistivities, or samples with differently diffused surfaces, it is necessary to use slightly different calibration constants. The data in Figure 2.9 were used to parameterise the quadratic and linear coefficients relating the excess conductance ($\Delta\sigma$) to the voltage (V), as a function of the dark conductance (σ_o) of the test wafer,

$$\begin{aligned} &\Delta\sigma = a * V + b * V^2 \\ \text{where} \quad &a = 0.0148 + 0.069\sigma_o - 0.0844{\sigma_o}^2 \\ \text{and} \quad &b = 2.45e^{-4} + 7.98e^{-4}\sigma_o - 6.67e^{-4}{\sigma_o}^2 . \end{aligned} \tag{2.36}$$

Additionally, the data for calibration wafers of different thickness have not been individually plotted in Figure 2.9, as the curve was not found to be dependent on the thickness of the calibration wafers. The calibration of Eq. (2.36) can then be used with certainty for test wafers between 100μm and 400μm (and probably thicker), which is satisfied by most samples in this thesis.

The ability to calibrate the photoconductance over a large range is a significant advantage for the inductively coupled photoconductance method compared to other methods for measuring the lifetime such as the microwave-detected photoconductance decay (MW-PCD) technique. MW-PCD is a small signal technique because the microwave reflectance is a highly non-linear function of the excess carrier density. A steady-state bias light can be used to generate a higher level of excess carriers, upon which a small signal transient pulse can be superimposed and

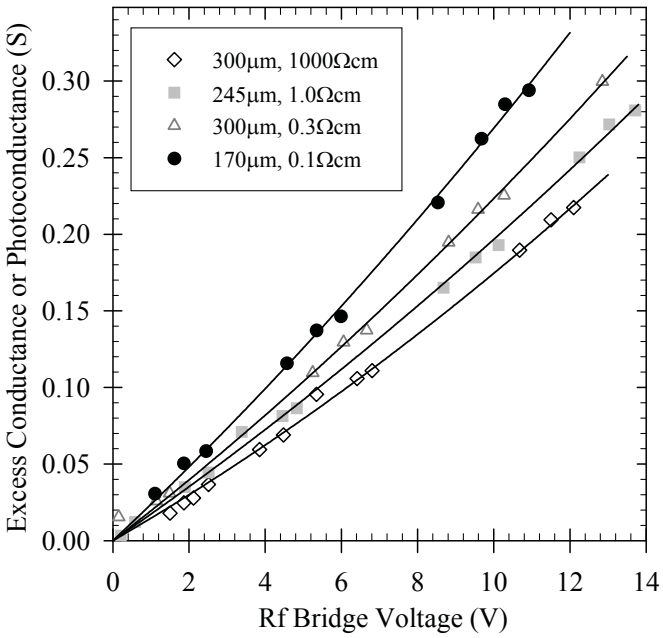


Figure 2.9. Calibration curves for converting the rf bridge voltage to a photoconductance. Curves are shown for four wafers with different dark conductance (see legend). It is necessary to include the effect of the dark conductance on the calibration curves when making accurate measurements of the effective lifetime for differently doped wafers.

detected by the microwave reflectance. MW-PCD with bias light therefore determines the *differential* effective lifetime ($\partial\tau_{eff}/\partial\Delta n$) [56]. To determine the actual effective lifetime, it is necessary to measure the differential effective lifetime over a large range of injection levels and then integrate [57]. The apparatus shown in Figure 2.7 is a large signal technique, which measures the actual effective lifetime directly. Furthermore, it also measures the carrier injection level, whereas in the MW-PCD technique, the injection level corresponding to each level of the bias light has to be determined by device simulation.

Finally, it is possible to use a high lifetime test sample, measured under transient and quasi-steady state illumination to confirm the calibration function given in Eq. (2.36). This is because the transient pcd technique is quite robust for determining the effective lifetime. When the rf-bridge voltage is less than 10V, the curves in Figure 2.9 are essentially linear and so $\Delta\sigma = a^*V$. It follows that Eq. (2.33) reduces to ($G_{av} = 0$ for the transient case)

$$\tau_{eff} = \frac{-V}{\frac{dV}{dt}}, \qquad (2.37)$$

which is independent of the calibration function. Under Qss illumination, the effective lifetime does depend on the calibration function, and so a good agreement of the effective lifetime for the tpcd and Qsspc techniques, as was observed in Figure 2.8, verifies a correct calibration

function. Indeed, the injection-level-dependent effective lifetimes reported throughout this thesis will generally be multiple Qsspc curves and multiple tpcd curves plotted on the same axis. As good agreement is generally found, the uncertainty in the effective lifetime measurement is estimated to be less than 5%, while the uncertainty in the determination of the effective carrier density is approximately 10%.

2.4 Determining Device Characteristics from the Effective Lifetime

The physical meaning underlying the generalised definition of lifetime proposed by Nagel *et al.* [53], Eq. (2.33), is that the recombination rate occurring within an illuminated sample can be affected by both the photogeneration rate at that instance, as well as the history of the sample (through the time-dependent carrier density - $\partial\Delta n/\partial t$). What is not obvious from this generalised lifetime definition is how to determine other device parameters, like the true steady-state open-circuit voltage or current-voltage characteristic of a solar cell, from Qsspc or transient decay measurements. New methods for interpreting the effective lifetime in terms of device characteristics have been developed and are discussed in this section.

2.4.1 Determination of Implied V_{oc} vs. Light Intensity Curves

Effectively, the correction of Nagel *et al.* is equivalent to defining the denominator of Eq. (2.33) as a net generation rate (G_{net}) that incorporates the actual photogeneration (G_{av}) and the carrier density history,

$$G_{net} = G_{av} - \frac{\partial \Delta n_{av}}{\partial t} . \qquad (2.38)$$

In the context of characterising the recombination parameters of solar cells and/or their precursors under real conditions (ie under true steady-state conditions), the concept of net generation can be greatly expanded. The simplest extension of the net generation concept is for obtaining implied open-circuit voltage vs. light intensity curves from photoconductance based lifetime measurements [47]. Under the quasi-steady-state assumption, the actual illumination level (I_{light} - in suns) can be plotted against an implied open-circuit voltage ($V_{oc,imp}$) using the relationship between the pn product under non-equilibrium conditions to its equilibrium value n_i^2 at the boundary of the junction space charge region (for a *p*-type wafer $n \approx \Delta n$ and $p \approx N_A + \Delta n$),

$$np \approx \Delta n(0)[N_A + \Delta n(0)] = n_i^2 \exp\frac{qV_{oc}}{\mathrm{kT}} . \qquad (2.39)$$

The actual illumination level (I_{light}), and therefore the actual photogeneration rate (G_{av}), does not necessarily account for all the recombination events occurring within the sample however. The correct analysis requires that the net generation rate (G_{net}), as defined in Eq. (2.38), should be used to determine the equivalent steady-state illumination level (I_{net}) that would need to be used to obtain the same total recombination rate, rather than I_{light}. This can be expressed in unit of *suns* (1sun=1kW/m^2) via

$$I_{net} = \frac{WG_{net}}{f_{abs} N_{ph}|_{1sun}}, \tag{2.40}$$

where the various terms are described in section 2.3. Alternatively, $f_{abs}N_{ph|1sun}$ can be replaced with an estimated or measured short-circuit current density (J_{sc}) under one sun standard illumination.

An example of an implied open-circuit voltage vs. light intensity curve both before the correction (I_{light}-$V_{oc,imp}$) and after the correction (I_{net}-$V_{oc,imp}$) is given in Figure 2.10. The flash-lamp used showed an approximately exponential reduction in light intensity over time with a decay time of ~2ms (see Figure 2.14). The effective lifetime data being analysed is from Figure 2.8. It can be seen that the uncorrected data is actually quite discontinuous, particularly at lower light levels, while the corrected data produces a smooth, continuous curve, which is physically what would be expected. Furthermore, by comparing the uncorrected and corrected quasi-steady-state data it can be seen that the correction starts to become significant at light intensities below ≈1 sun for this sample. The effect of the correction is to provide a more realistic determination of the electronic properties of the solar cell substrate. That is, the uncorrected data over-estimates the quality of the solar cell substrate by over-predicting the V_{oc}. At 0.1 sun for example, the implied V_{oc} is 662mV from the uncorrected data, which reduces to 655mV when the correct analysis is used.

An interesting, not so obvious consequence of using the net generation concept is that transient photoconductance decay measurements can be used to determine implied open-circuit voltage vs. net light intensity curves even though the actual light intensity is zero. Included in Figure 2.10 are corrected and uncorrected implied open-circuit voltage data when the lifetime is measured by the transient method. It can be seen that the two corrected curves agree very well, demonstrating the validity of the approach.

The agreement between tpcd and Qsspc data can be exploited to determine, or verify, the optical properties of the wafer, that is the factor f_{abs} in Eq. (2.40). Furthermore, the standard diode analysis and interpretation can be made on the I_{light}-$V_{oc,imp}$ curves, thus relating the injection level dependent effective lifetime of the sample to the local ideality factor at a given

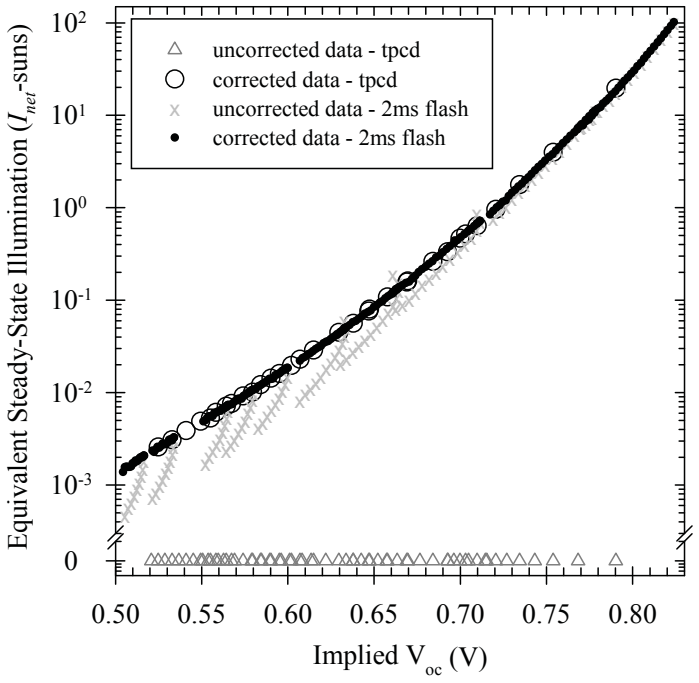


Figure 2.10. Corrected and uncorrected implied open-circuit voltage vs light intensity curves for a solar cell precursor from photoconductance measurements. A flash-lamp with a decay time of ~2ms has been used as well as in transient mode, where there is no actual illumination of the sample during the measurement. The vertical axis is determined from G_{av} for the uncorrected data and from G_{net} for the corrected data using Eq. (2.40).

open-circuit voltage. For example, the corrected I_{net}-$V_{oc,imp}$ curve in Figure 2.10 can be accurately fit at low and intermediate voltages with

$$I_{net} = \frac{J_{o1}}{J_{sc}} \exp\left(\frac{qV}{kT}\right) + \frac{J_{o2}}{J_{sc}} \exp\left(\frac{qV}{2kT}\right), \tag{2.41}$$

where J_{o1} = 25fA/cm^2 and J_{o2} = 2.6nA/cm^2 using an assumed J_{sc} = 33mA/cm^2. As is shown in Figure 2.11(a), the fit diverges from the data at very high voltages (>750mV) where Auger recombination is more dominant and thus the ideality factor is less than unity. This is better shown in Figure 2.11(b), where it can be seen that the local ideality factor for this solar cell precursor is ~0.7 at high light intensities (~100suns), which is in good agreement with the theoretical expectation of two thirds for a device dominated by Auger recombination. The local ideality factor then increases to greater than 1.6 at low light intensities (~0.004suns) due to the injection level dependence of the effective lifetime (shown in Figure 2.8).

2.4.2 Determination of Photovoltaic I-V Curves

An alternative transformation of implied open-circuit voltage vs. light intensity data is an implied photovoltaic I-V curve [58]. This transformation uses the superposition principle to

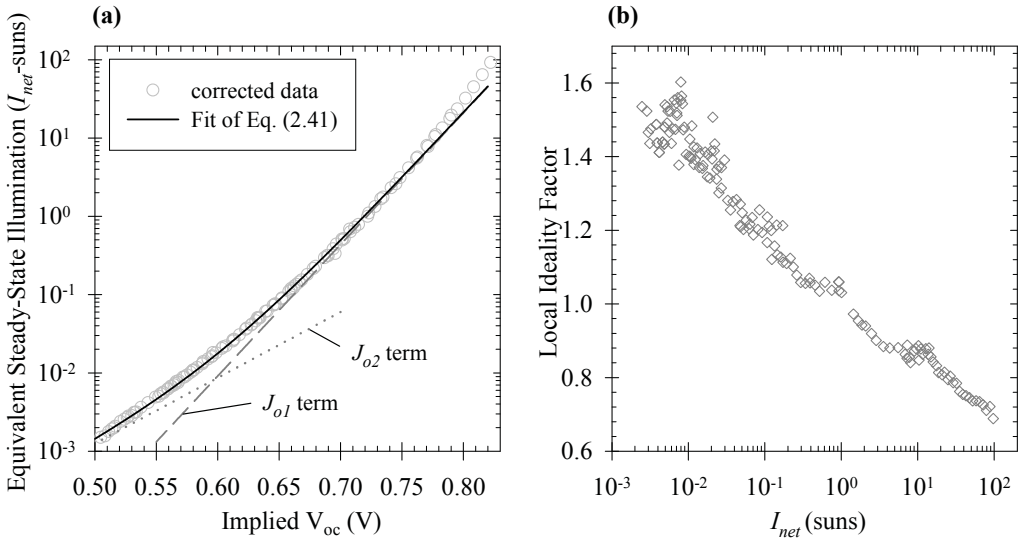


Figure 2.11. Standard diode analysis of the corrected implied open-circuit voltage vs light intensity curve from Figure 2.10. It can be seen that: (a) the data can be accurately fit with a curve that incorporates a J_{o1} and J_{o2} term, except at very high voltages where Auger recombination dominates; (b) the local ideality factor increases from ~0.7 at high light intensities to greater than 1.6.

present the data in the familiar I-V format. In this format, the customary interpretation of fill-factor, conversion efficiency (without series resistance) and shunt resistance can be easily made, even though no electric current is actually being measured. An implied terminal current (J_{imp}) is determined for each open-circuit voltage from the net illumination level (I_{net}) and an estimated short-circuit current density (J_{sc}) under one sun illumination. Indeed, an upper limit to the short-circuit current density ($J_{sc,max}$) has already been established in determining the optical absorption fraction of the sample ($J_{sc,max} = qf_{abs}N_{ph}|_{1sun}$), with the equality relationship holding when the cell has 100% internal quantum efficiency at all wavelengths,

$$J_{imp} = J_{sc}(1 - I_{net}) \leq qf_{abs}N_{ph}|_{1sun}(1 - I_{net}) \qquad (2.42)$$

An implied photovoltaic I-V curve is then obtained by plotting the implied open-circuit voltage ($V_{oc,imp}$) against the implied terminal current(J_{imp}). This is shown in Figure 2.12 for the uncorrected and corrected data (~2ms flash-lamp) from Figure 2.10, by assuming a J_{sc}=33mA/cm^2. The correction lowers the 1-sun V_{oc} from 725.0mV down to 721.6mV and the recombination limit to the fill-factor is reduced from 85.7% to 83.6%. The upper limit to the cell efficiency is reduced from 20.4% down to 19.9% and the device appears to be shunt free (note the expanded scale of the x-axis). It should be noted that these are upper limits for an actual solar cell from this substrate, as the final device would also include contact recombination, series resistance effects and shading losses. Importantly, the photovoltaic I-V

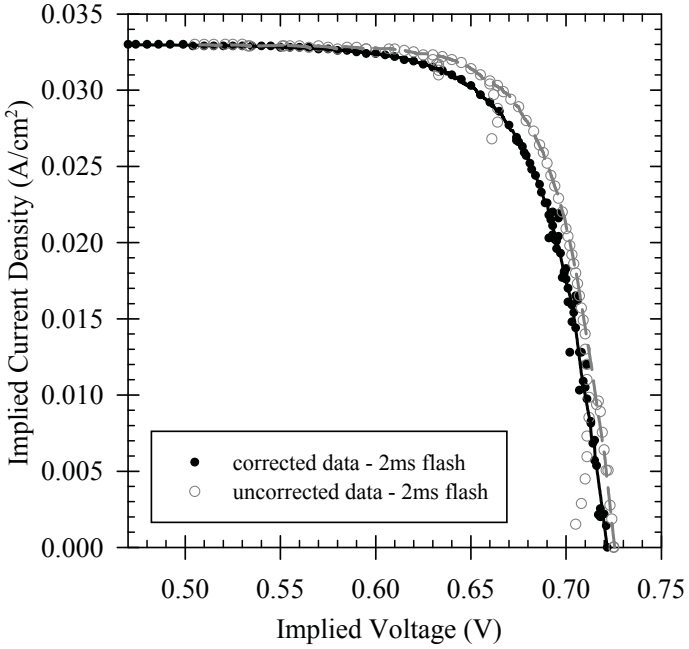


Figure 2.12. Implied photovoltaic I-V curves determined from the corrected (both Qsspc and tpcd) and uncorrected (Qsspc only) photoconductance data for the solar cell precursor of Figure 2.10. The effect of the correction is to lower the cell's open-circuit voltage and fill-factor.

curve of this sample could equally have been determined from the corrected transient data in Figure 2.10, thanks to the generalised definition of I_{net}.

2.5 Generalisation of Open-Circuit Voltage Measurements

It has been shown that the effective lifetime, determined under general illumination conditions, can be used to determine device characteristics such as the open-circuit voltage. The corollary is also true, where device characteristics such as the open-circuit voltage or short-circuit current can be measured to determine the injection level dependent effective lifetime. The measurement and analysis of open-circuit voltage data under general illumination conditions is discussed in this section. The traditional open-circuit voltage decay (OCVD) technique, where the V_{oc} is measured after the illumination has been terminated is considered, as well as the quasi-steady-state V_{oc} ($QssV_{oc}$) technique, where by analogy with the Qsspc technique, the V_{oc} is measured during illumination under a photographic flash-lamp. It will again be shown that it is necessary to use the effective net generation (Eq. (2.38)) to correctly analyse the data for the case of a time varying illumination.

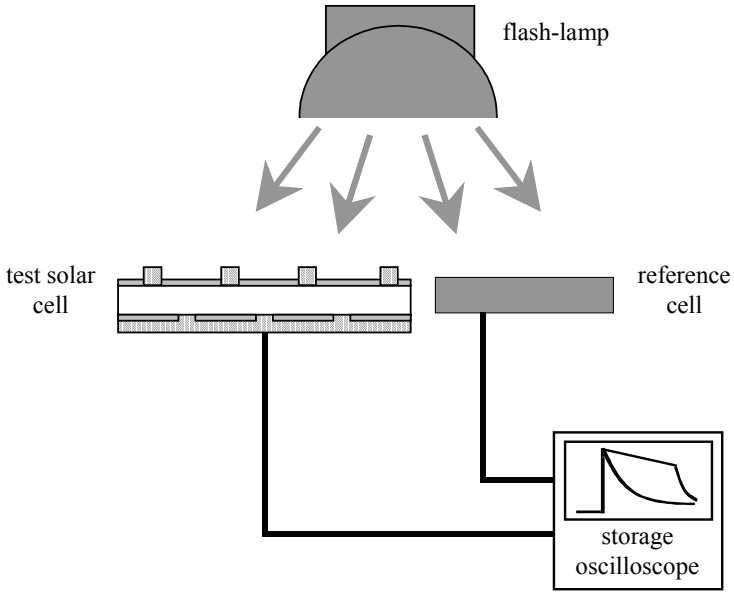


Figure 2.13. Schematic of the experimental apparatus used for measuring $QssV_{oc}$ and OCVD data.

2.5.1 Introduction

A schematic of the experimental apparatus used in this thesis for measuring $QssV_{oc}$ and OCVD data is given in Figure 2.13. It is very similar to the apparatus used for photoconductance based measurements of the effective lifetime, Figure 2.7, except that the test wafer is replaced by a test solar cell, and that the V_{oc} can be measured directly by the oscilloscope without the need for a coil or rf-bridge.

One objective of a $QssV_{oc}$ measurement is to obtain the diode characteristics (J_{o1}, J_{o2}, n) of a finished solar cell [58]. These characteristics come about by simply plotting the actual open-circuit voltage of the device as a function of the light intensity. The electric current is not actually measured, but it is replaced with the light intensity (a linear relationship between both usually holds for most solar cells). It is the **dc**, or steady-state characteristics of the device that are required, that is, the dc value of V_{oc} that corresponds to a given value of steady-state light intensity. Analogous to the discussion in section 2.4, the actual illumination level at the time (and therefore the photogeneration rate) does not necessarily account for all the carriers in the sample. In particular, it does not necessarily account for all the carriers at the boundary of the space charge region, which in-turn, determines the open-circuit voltage. Again, the photogeneration history of the sample needs to be considered by using the net generation rate of Eq. (2.38). This can be achieved by solving the quadratic expression of Eq (2.39) to determine Δn (only the positive root has a physical meaning),

$$\Delta n = \frac{\sqrt{N_A^2 + 4n_i^2 \exp\frac{qV_{oc}}{\mathrm{kT}}} - N_A}{2}. \qquad (2.43)$$

Differentiating this gives

$$\frac{\partial \Delta n}{\partial t} = \frac{qn_i^2 \exp\frac{qV_{oc}}{\mathrm{kT}}}{kT\sqrt{N_A^2 + 4n_i^2 \exp\frac{qV_{oc}}{\mathrm{kT}}}} \frac{\partial V_{oc}}{\partial t}. \qquad (2.44)$$

Which can be substituted into Eq. (2.38) and then into Eq. (2.40) to obtain the equivalent, steady-state illumination level (I_{net}) that needs to be plotted against the measured V_{oc}. This procedure outlines the generalised analysis of V_{oc} measurements as a function of the light intensity and time.

2.5.2 Experimental Illustration of the General Analysis

The open-circuit voltage as a function of light intensity was measured for a low recombination solar cell made on a 90 Ωcm phosphorus-doped silicon wafer. The cell had full area boron and phosphorus diffusions at the front and rear of the cell respectively, essentially making it a 1-dimensional device. The high open-circuit voltage at one sun, 677 mV, testifies the quality of the device (J_{sc}=32.2mA/cm^2, FF=0.781, η=17.1%). It also means that the excess carrier density is very high, which adds to the problem of maintaining steady-state conditions during a time-dependent measurement.

Figure 2.14 shows the illumination characteristics of the four different flash-lamps that were used to illustrate the method. Along with the transient mode, the decay times of the flash-lamps were ~0.35ms, ~2ms and ~4ms. The 0.35ms flash-lamp has been included to demonstrate the robustness of the correction. It would not typically be used for quasi-steady-state measurements. Neutral density filters were used to vary the intensity of light incident on the solar cell to between 100suns and 0.001suns.

Uncorrected I_{light}-V_{oc} curves for the device are plotted in Figure 2.15 along with true steady-state measurements obtained by attenuating the illumination from a solar simulator with several different neutral density filters and placing the device subsequently in open and short circuit conditions. Shifted dark I-V data are also included in Figure 2.15. Consistent with the discussion in section 2.4.1, the uncorrected curves are quite discontinuous. Most importantly, the predicted performance of the device would vary greatly depending on which flash-lamp was used and would be significantly different from the true steady-state performance. Even for the

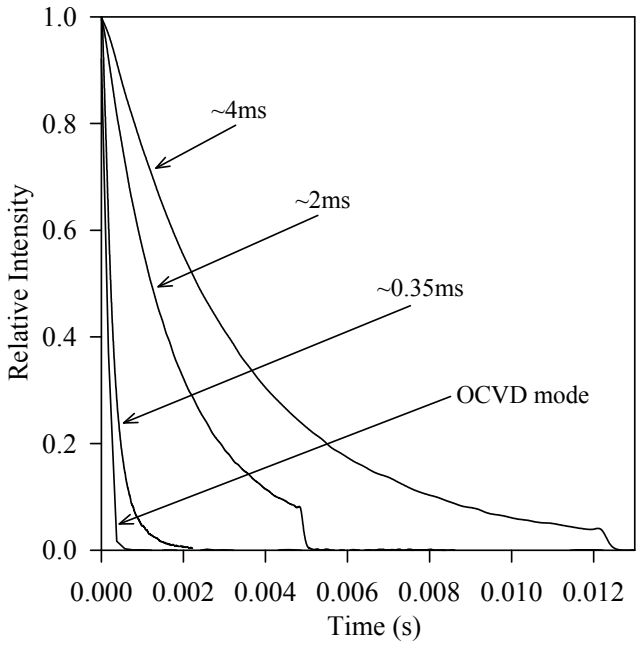


Figure 2.14. Illumination characteristics of the four flash-lamp modes used for demonstrating the correct analysis of V_{oc} data measured under a time varying illumination.

4ms flash-lamp, there is a noticeable difference between the true steady-state measurements and the uncorrected I_{light}-V_{oc} data at lower illumination levels.

The corrected I_{net}-V_{oc} curves for the device are plotted in Figure 2.16. It can be seen that applying the correction again removes the discontinuities in the curves for all the illumination modes, but most importantly, all the curves now overlap with each other and with the true steady-state measurements. Furthermore, there is also excellent agreement with the dark I-V curve measurement. One could obviously attempt to fit the I_{net}-V_{oc} curves of Figure 2.16 or determine the local ideality factor, as was done in Figure 2.11. Simplistically though, it can be seen from Figure 2.16 that as the V_{oc} decreases, the ideality factor increases from less than unity (due to Auger recombination) to ~1.6 for V_{oc} near 0.6V, and then decreases to ~1.3 for the lowest V_{oc} measured.

A second illustration of the generalised analysis of V_{oc} measurements is given in Figure 2.17 for a high performance solar cell made on a low resistivity 0.3 Ωcm *p*-type silicon substrate (V_{oc}=684mV, J_{sc}=38.6mA/cm^2, FF=0.807, η=21.3%). The effect of the correction is very small for this low resistivity substrate when a slowly decaying flash-lamp (2-4ms) is used because the recombination lifetime of the substrate is significantly less than the decay constant of the flash-lamp. Only the corrected and uncorrected I_{light}-V_{oc} data for the 0.35ms decay flash-lamp have therefore been plotted along with the true steady-state data and dark I-V data. It can

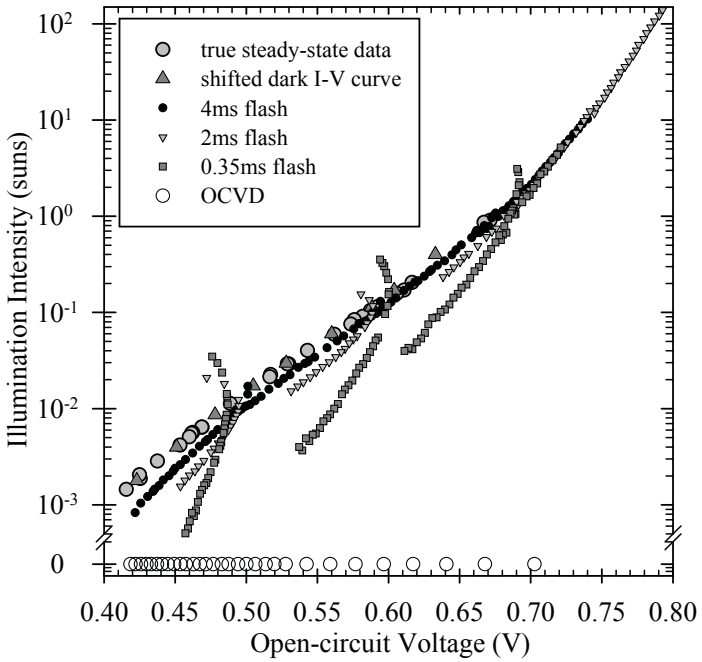


Figure 2.15. Uncorrected open-circuit voltage vs light intensity curves for a low recombination solar cell. The illumination modes for the solar cell include transient mode (OCVD) as well as flash-lamp decay times of ~0.35ms, ~2ms and ~4ms. True steady-state measurements and shifted dark I-V measurements have been included for comparison.

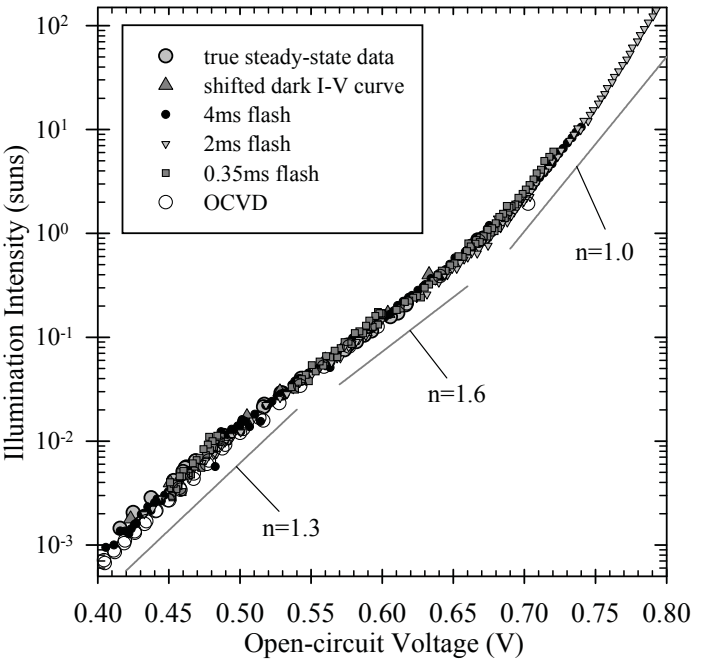


Figure 2.16. Corrected open-circuit voltage vs light intensity curves for a low recombination solar cell using four different illumination conditions. The corrected curves all essentially overlap with the true steady-state measurements. Guidelines for the change in local ideality factor have been included.

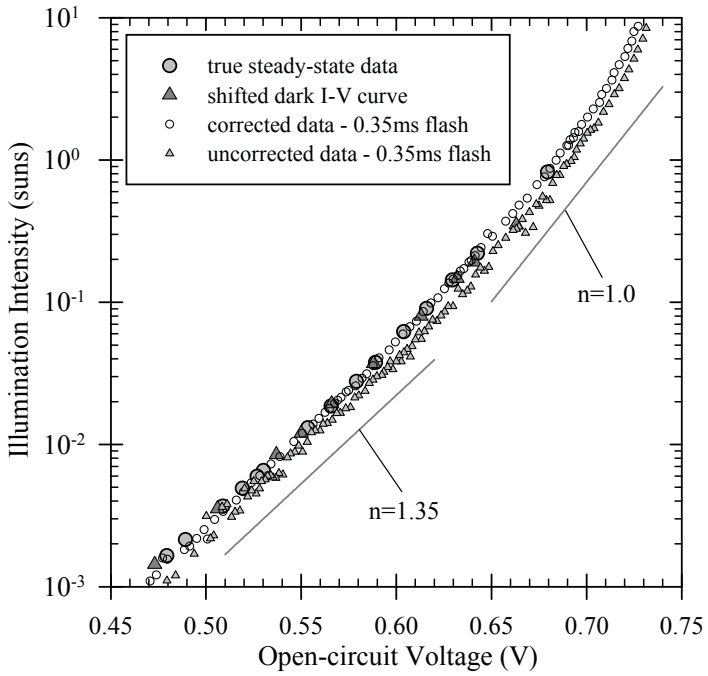


Figure 2.17. Corrected and uncorrected open-circuit voltage vs light intensity curves for a low resistivity solar cell illuminated using a flash-lamp with a ~0.35ms decay time. The corrected curve essentially overlaps with the true steady-state measurements and dark I-V measurements. Guidelines for the change in local ideality factor have been included.

again be seen that the corrected data is in excellent agreement with the true steady-state measurements and dark I-V data. Furthermore, as the V_{oc} decreases, the local ideality factor increases from less than unity to a value of ~1.35 for low V_{oc}. This is again related to the injection dependence of the τ_{eff}, which is shown in Figure 2.21.

2.5.3 Determination of the Lifetime from V_{oc}

An important application of the QssV_{oc} technique is to determine the effective lifetime in finished devices and it is a useful accompaniment to the more common OCVD technique [36]. It is again important to account for the photogeneration history of the device. The effective lifetime can be determined by substituting Eq. (2.43) and Eq. (2.44) into Eq. (2.33), giving the generalised definition of the effective lifetime from the open-circuit voltage,

$$\tau_{eff} = \frac{\sqrt{N_A^2 + 4n_i^2 \exp\frac{qV_{oc}}{\mathrm{kT}}} - N_A}{2\left(G_{av} - \frac{qn_i^2 \exp\frac{qV_{oc}}{\mathrm{kT}}}{kT\sqrt{N_A^2 + 4n_i^2 \exp\frac{qV_{oc}}{\mathrm{kT}}}} \frac{\partial V_{oc}}{\partial t}\right)}. \qquad (2.45)$$

Which, for the case of low level injection, can be simplified to a more familiar form that is easily identifiable with the OCVD lifetime when the generation rate is zero [36],

$$\tau_{eff} = \frac{\Delta n}{G_{av} - \frac{q\Delta n}{kT}\frac{\partial V_{oc}}{\partial t}}. \qquad (2.46)$$

The lifetime can thus be easily calculated from the measured voltage, its time derivative and the actual illumination level. Figure 2.18 shows the effective lifetime corresponding to a high efficiency PERL cell fabricated at Fraunhofer Institute of Solar Energy Systems on a 22 Ωcm gallium-doped silicon substrate (V_{oc}=680mV, J_{sc}=39.5mA/cm^2, FF=0.793, η=21.2%). Minority carrier lifetimes in excess of 1 ms have been independently measured for these wafers by photoconductance techniques. It can be seen that the lifetime determined using the generalised analysis of Eq. (2.45) has a maximum value of ≈1.1ms at an injection level of $3x10^{14}$ cm^{-3}.

Included in Figure 2.18 are the effective lifetime values determined for flash-lamps with decay times of 2ms and 4ms but neglecting the device's photogeneration history. The maximum lifetime depends on the decay time of the flash-lamp, with a maximum of ≈2.2ms and ≈1.6ms for a 2ms and 4ms decay constant flash-lamp respectively. Clearly, the use of the generalised analysis is required to accurately determine the effective lifetime.

2.5.4 Determination of the Photovoltaic I-V Curve from V_{oc}

Open-circuit voltage vs. light intensity data can easily be converted into a photovoltaic I-V curve as discussed in section 2.4.2. For the solar cell characterised in Figure 2.16, it is clear that the corrected data all overlap regardless of the flash-lamp characteristics. It thus follows that the photovoltaic I-V curves obtained from this data will also overlap, regardless of the flash-lamp characteristics. The extreme case of this is shown in Figure 2.19, where the photovoltaic I-V curve determined using true steady-state illumination (J_{sc}-V_{oc} data) and using transient illumination (OCVD) are compared. It can be seen that both agree very well.

Also included in Figure 2.19 is the 1-sun I-V curve (obtained by changing the voltage bias and measuring the current), which is in good agreement with the two photovoltaic I-V curves. As 1-sun I-V curves include series resistance effects but photovoltaic I-V curves do not, it is concluded that this cell has low series resistance. This is to be expected as the cell has a diffused region at the front and rear surface. Importantly, it is clear that transient mode (OCVD) can be successfully used to predict upper limits on the performance of solar cells under steady-state conditions by using the generalised I_{net}.

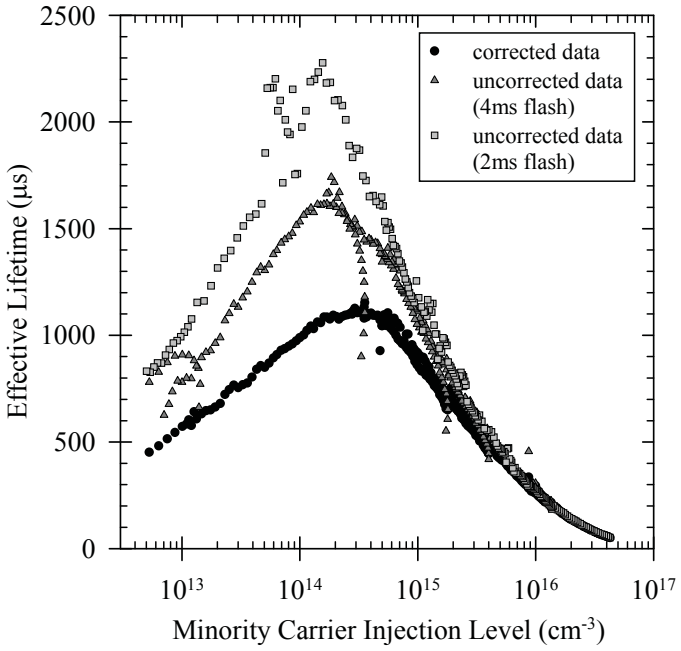


Figure 2.18. Effective lifetime data corresponding to corrected and uncorrected I_{light}-V_{oc} curves for a high efficiency PERL cell. The flash-lamps used for illuminating the cell had a decay time of ~2ms and ~4ms.

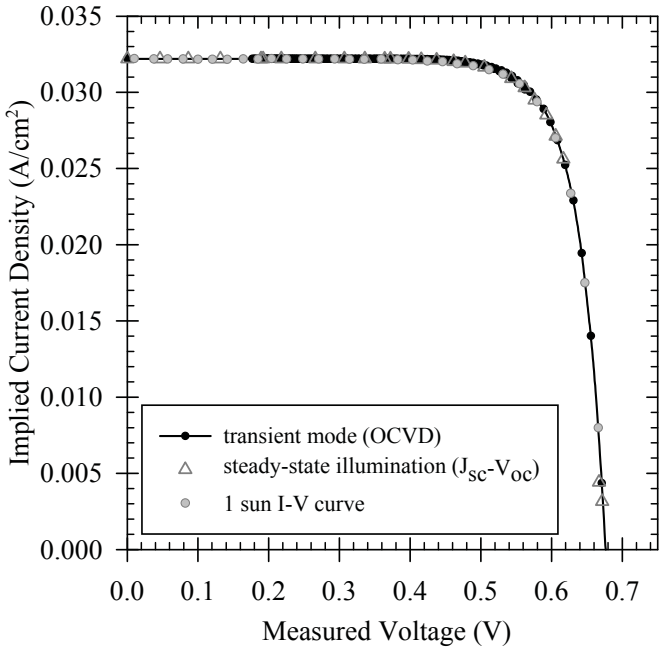


Figure 2.19. The photovoltaic I-V curve, for the solar cell characterised in Figure 2.16, using the transient mode (OCVD) and under steady-state illumination (J_{sc}-V_{oc}). The 1-sun I-V curve is included for comparison.

Another example of photovoltaic I-V curves is given in Figure 2.20 for the PERC solar cell characterised in Figure 2.17. The photovoltaic I-V curve determined from the transient mode and under Qss illumination (4ms flash-lamp) have been plotted along with the 1-sun I-V curve. Again it can be seen that the two photovoltaic I-V curves agree well. For this PERC cell the actual 1-sun I-V curve deviates from the photovoltaic I-V curves particularly near maximum power-point as is demonstrated in the inset to Figure 2.20. The photovoltaic I-V curves indicate that the fill-factor for this cell could be as high as 83.3%, which is therefore the limit imposed by recombination processes, with a resulting cell efficiency of 22.0%. This compares to a fill-factor (efficiency) of 80.7% (21.3%) from the actual I-V curve, where the losses are mainly due to series resistance effects at the rear of this cell, which are known to limit cell performance in high efficiency PERC cells.

The inset to Figure 2.20 also shows there is a slight deviation between the photovoltaic I-V curve from transient decay and from Qss illumination. This small deviation results from capacitive effects within the cell and is discussed further in section 2.6. However, it can be seen that even for a solar cell fabricated on a low resistivity substrate, the transient mode can be used to determine cell performance under steady-state conditions with good accuracy.

2.5.5 Determination of the Lifetime from the J_{sc}-V_{oc} Curve

The final relationships that can be outlined transforms J_{sc}-V_{oc} data, measured under steady-state conditions, into injection level dependent effective lifetime measurements. This is simply a limiting case of Eq. (2.45) with $\partial V_{oc}/\partial t = 0$. The minority carrier injection level is again determined from the measured V_{oc} using Eq. (2.43). The generation rate (G_{net}) in the sample can be determined by scaling the measured J_{sc} by the 1-sun J_{sc} to determine the illumination level in suns (I_{net}). Rearranging Eq. (2.42) gives

$$I_{net} = 1 - \frac{J_{sc}}{J_{sc,1sun}} . \tag{2.47}$$

Substituting Eq. (2.47) into Eq. (2.40) and rearranging gives

$$G_{net} = \frac{f_{abs} N_{ph}|_{1sun}}{W}\left(1 - \frac{J_{sc}}{J_{sc,1sun}}\right) . \tag{2.48}$$

Therefore, the effective lifetime can be determined from

$$\tau_{eff} = \frac{\Delta n}{G_{net}} = \frac{W\left(\sqrt{N_A^2 + 4n_i^2 \exp\frac{qV_{oc}}{\mathrm{kT}}} - N_A\right)}{2 f_{abs} N_{ph}|_{1sun}\left(1 - \frac{J_{sc}}{J_{sc,1sun}}\right)} . \tag{2.49}$$

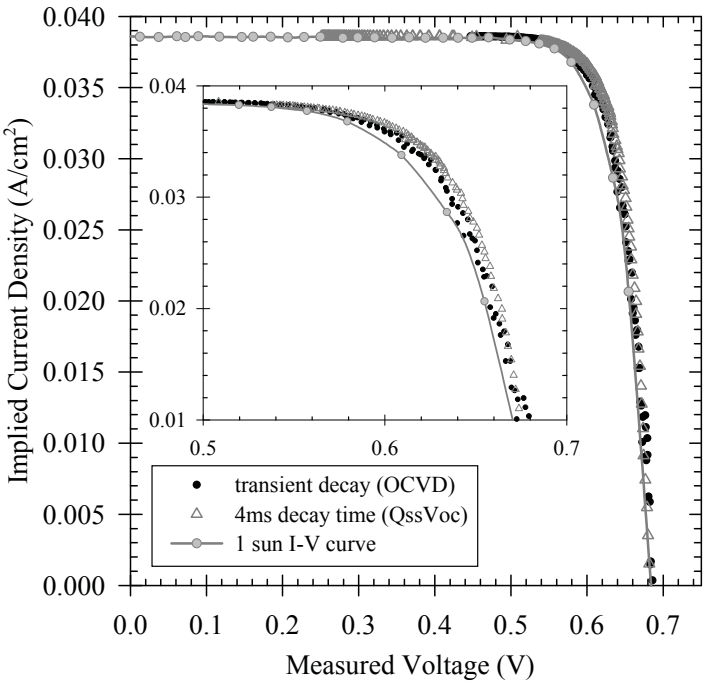


Figure 2.20. The photovoltaic I-V curve, for the solar cell characterised in Figure 2.17, using the transient mode (OCVD) and under quasi-steady-state illumination (4ms decay time). The 1-sun I-V curve is included for comparison. It can be seen from the inset that the photovoltaic I-V curve deviates from the 1-sun I-V curve near maximum power-point due to series resistance effects.

An example of determining the effective lifetime from J_{sc}-V_{oc} data is given in Figure 2.21 for the PERC cell used for Figures 2.17 and 2.20. The effective lifetime has been plotted from the steady-state J_{sc}-V_{oc} data and from a QssV_{oc} measurement (~4ms flash-lamp), with both in good agreement.

The transformation of Eq. (2.49) could be applied to 1-sun I-V data where the J_{sc} and V_{oc} are replaced by the measured terminal current (J_{term}) and voltage (V_{term}). The 1-sun I-V curve includes series resistance effects however, that are not related to recombination processes and so the obtained lifetime is not analogous to the effective lifetime. As few solar cells have negligible series resistance under one sun illumination, this transformation is not considered any further. Finally, an important advantage in determining the lifetime from V_{oc} measurements, either QssV_{oc} or J_{sc}-V_{oc} data, is that lower Δn levels can be investigated than is typically possible with non-contacting techniques such as the Qsspc method. Furthermore, the V_{oc} based techniques are practically unaffected by trapping phenomena, which is not be the case for photoconductance methods.

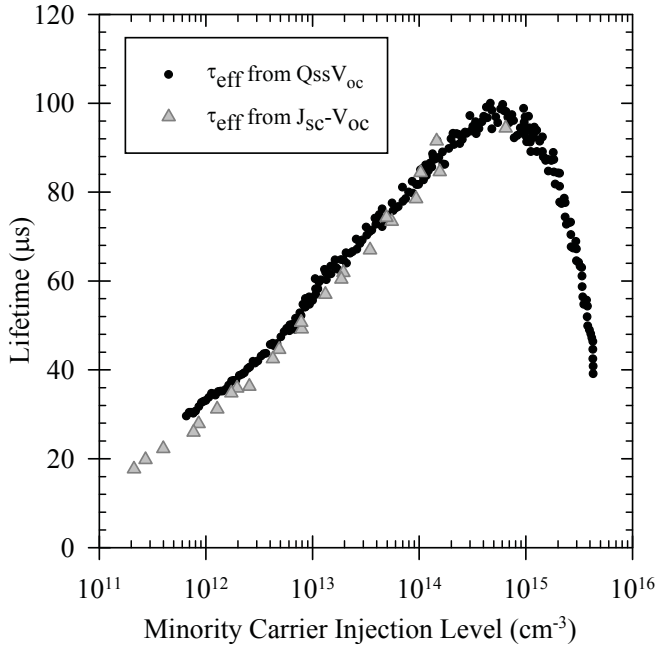


Figure 2.21. The effective lifetime, for the solar cell characterised in Figure 2.17 and 2.20, determined form J_{sc}-V_{oc} measurements and from QssV_{oc} measurements.

2.6 Discussion

Lifetime and voltage are interchangeable. A lifetime measurement of a wafer implicitly carries inside the magnitude of the voltage that the device will eventually have. Therefore, photoconductance based techniques can be used to determine the injection level dependent effective lifetime and this can be transformed into an illumination vs. implied open-circuit voltage curve and subsequently into a photovoltaic I-V curve, which clearly demonstrates the limits imposed by recombination processes and shunting on device performance parameters such as V_{oc}, fill-factor and efficiency. Conversely, a measured voltage can be translated into a photovoltaic I-V curve or the language of carrier recombination and lifetime. The extended analysis of the data presented here is important to perform such translations faithfully and has been summarised in Figure 2.22.

The extended analysis of time-dependent measurements of the excess carrier density under illumination by either conductance or voltage techniques goes beyond pure mathematical rigour. Applying it to the special case where the light excitation is abruptly terminated and the transient decay of the photoconductance or the voltage is recorded with time is very important, since the PCD and OCVD methods have historically been, and still are, widespread. As shown in this chapter, it is interesting to realise that, even if the light intensity and the electric current are zero, it is still possible to obtain the characteristic curves of the device from PCD and

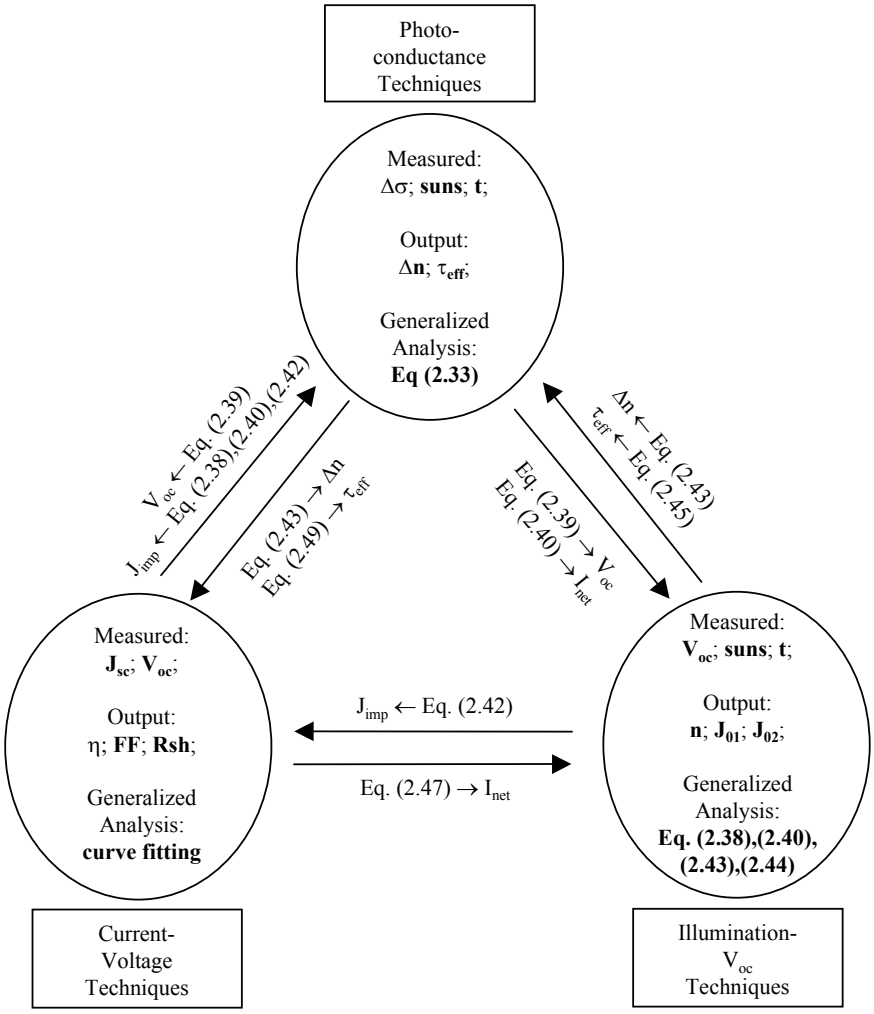


Figure 2.22. Summary of the relationships between effective lifetime measurements, illumination vs open-circuit voltage measurements and current-voltage (I-V) measurements.

OCVD measurements. The vertical axis of these plots is the rate of change of the carrier density, which represents the natural recombination rate in these situations. This generalisation of the device characteristics is conceptually important, and provides a broader understanding of the different physical mechanisms present in the semiconductor.

Extensive use has been made throughout this thesis of the transient and Qss measurement techniques. For fundamental studies of bulk, surface and emitter recombination (chapters 3, 4 and 5 respectively), the photoconductance techniques have mainly been used due to their versatility at the wafer level. Transforming the lifetime measurements into device characteristics allows upper limits for the performance (V_{oc}, fill-factor and efficiency) of silicon solar cells to be explored. When transferring the results from the fundamental studies to actual devices

(chapter 6), the $QssV_{oc}$ technique has been used to monitor the cell processing and analyse the finished devices for loss mechanisms.

From a practical perspective, it has been pointed out that using the net generation rate leads to a more realistic determination of solar cell properties (lower V_{oc} and fill-factor) from $QssV_{oc}$ measurements. The magnitude of the correction is largest when the effective lifetime of the sample is of the same order, or longer than the decay time of the flash-lamp used. In this chapter, the generalised analysis procedure has been demonstrated using high efficiency and high lifetime solar cells. For the majority of industrial solar cells the effective lifetime is quite small (10-50μs) and is much less than the decay time of the typical flash-lamps used for these measurements (decay time of ~2–4ms). Under these conditions, the effect of the generalised analysis presented here is small. Additionally, while it has been shown that both Qss and transient techniques can be accurately used to evaluate device performance, if the main objective is to determine the steady-state characteristics of the device (the steady-state recombination rate, or the dc current-voltage characteristics), then the experimental conditions should preferably approach the steady-state as much as possible. In the case of solar cells, testing under illumination is clearly closer to the intended operating conditions than testing their transient behaviour in the dark.

Plots are given in Figure 2.23 for the percentage error in determining V_{oc} and τ_{eff} from a $QssV_{oc}$ measurement, using the generalised analysis procedure from the net generation rate compared to the steady-state assumption. Plots for a flash-lamp with a 2ms decay time are given assuming the sample has a width of 300μm and a J_{sc}=35.0mA/cm^2. The error plots are made as a function of the base resistivity (a *p*-type base is assumed in these plots) and the open-circuit voltage at 0.1 suns illumination. An illumination level of 0.1 suns was chosen because it gives a voltage closer to that at maximum power-point and because the V_{oc} at 1 sun illumination may be governed by high injection recombination processes such as Auger recombination rather than bulk SRH recombination. It can be see that the errors are highest for high voltage solar cells manufactured on high resistivity substrates. Furthermore, the error in determining the effective lifetime from $QssV_{oc}$ measurements is much greater than the error in determining the V_{oc}. Finally, the percentage errors are inversely related to the flash-lamp decay time, and so the errors for a flash-lamp with a 4ms decay time would be approximately half the values shown in Figure 2.23.

Subtle differences between photoconductance based methods and illumination vs. open-circuit voltage based methods of characterising recombination effects in solar cells do exist. Firstly, the V_{oc} based methods determine the carrier density at the edge of the pn junction, while

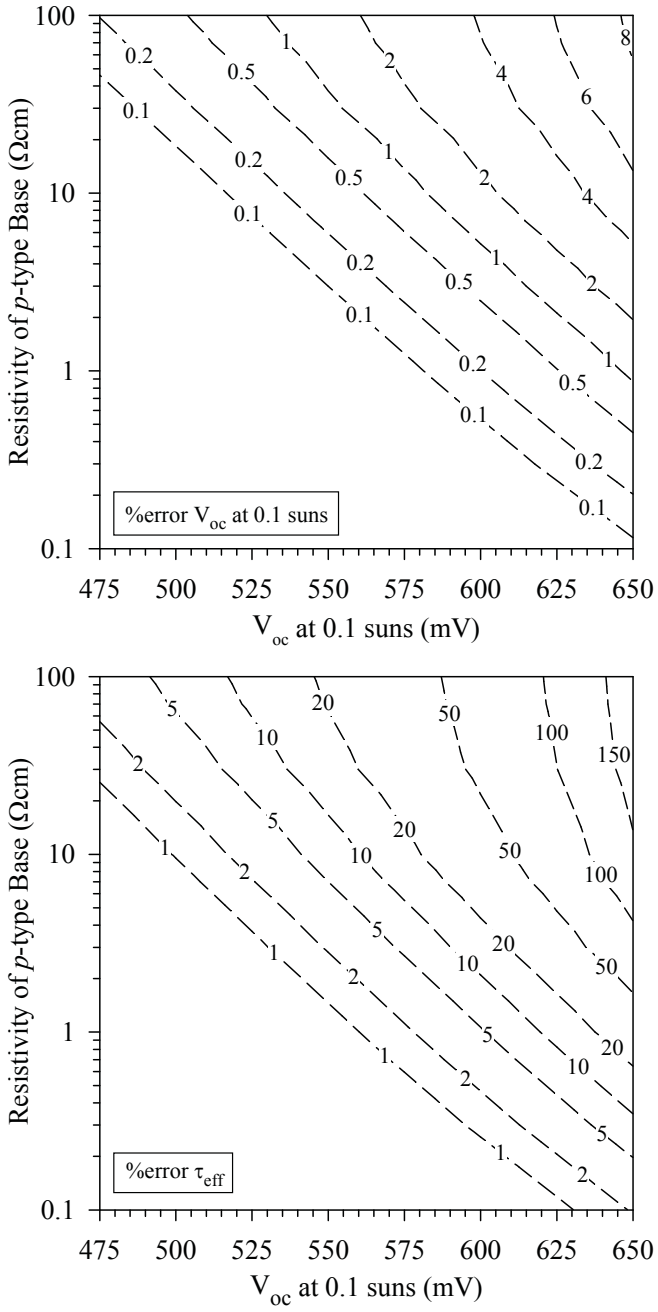


Figure 2.23. Typical errors in determining the V_{oc} at 0.1 suns and the τ_{eff} by using the steady-state assumption to analyse quasi-steady-state data.

photoconductance based methods determine an average carrier density in the sample. For devices with a sufficiently high lifetime so that the diffusion length is greater than the device thickness the two methods for determining carrier density will agree quite well. In cases where the main limitation is by bulk recombination (diffusion length is smaller than device thickness), a good agreement would only exist if infra-red illumination is used. If a white light source is used, as is most common, the carrier density at the junction will be higher than the average value. For cells dominated by surface recombination at one surface, the measurements may also

be different. In an extreme case of a cell with very high bulk lifetime, a well passivated front surface but poorly passivated rear surface the minority carrier density will decrease linearly from the front of the cell to the rear of the cell. The photoconductance based techniques will then determine a carrier density that is half the value determined from the V_{oc} based method.

Another difference is that the V_{oc} based techniques probe the entire active area of the solar cell while inductively coupled photoconductance based methods only probe the area sensed by the coil. If the solar cell is smaller than the coil, then the photoconductance technique will probe outside the active cell area. Alternatively, if the cell is large but has inhomogeneous properties, the photoconductance technique will only predict the cell performance in localised areas. These issues may make direct comparison between photoconductance and V_{oc} determinations of the lifetime non trivial for specific cases. An added complication is that V_{oc} measurements are strongly dependent on the temperature, whereas photoconductance measurements are not. In addition, the generalised analysis of V_{oc} measurements requires knowledge of the dopant density of the wafer.

Finally, although the experimental measurements plotted throughout this chapter have been focussed on the main issue of illustrating the corrected photogeneration rate, capacitive effects have been observed at very low voltages. Junction capacitance has traditionally been one of the major drawbacks of the OCVD method, since it dominates the decay of the voltage at low carrier densities [59]. The $QssV_{oc}$ technique is not totally impervious to these effects, but they only become significant at much lower voltages. The corresponding excess carrier densities are extremely low (of the order of the intrinsic carrier density), and both the recombination and generation (less than one thousand of one sun) rates are very small. In such circumstances, the capacitive effect of the pn junction becomes important. The distortion produced by this capacitance is directly related to the light source used: it is highest for the transient measurement, less severe for the 0.35 ms flash, and moderate to negligible for the 2 ms and 4 ms flashes. This indicates that the effect can be practically eliminated by using a still slower flash. Alternatively, the capacitance could be determined from the transient OCVD measurement and then its value used to correct the $QssV_{oc}$ measurement. The continuity equation would need to be modified to add a term due to junction capacitance. Additional physical mechanisms, such as a shunt resistance, could also be added to the analysis.

2.7 Chapter Summary

The principal recombination mechanisms in silicon have been discussed in this chapter. These include bulk processes such as Auger recombination and radiative recombination, and extrinsic processes involving recombination through defects both within the bulk of the silicon and at its surface. The effective lifetime incorporates all the different recombination processes, which occur simultaneously, and expressions have been derived for the effective lifetime of specific test structures used throughout this thesis. Photoconductance based methods for determining the effective lifetime are described and new techniques for interpreting the effective lifetime in terms of device characteristics have been introduced. These new techniques are based on the physical concept of a *net photogeneration rate*, which is defined as the sum of the actual photogeneration rate and the derivative of the excess carrier density with time. The net photogeneration rate permits steady-state device characteristics such as ideality factors and an implied I-V curve to be accurately determined from measurements using a time-dependent light source. Even for transient measurements of the effective lifetime, where no illumination occurs during the measurement, it is shown that steady-state device characteristics can be determined. The converse relationships for determining the effective lifetime from measurements of the V_{oc} under arbitrary illumination are also discussed, and this completes the circle formed by the photoconductance and voltage techniques, both quasi-static and transient, by allowing similar possibilities for all of them.

Ultimately, the performance of crystalline silicon solar cells is determined by the limits imposed on the lifetime by intrinsic recombination processes. This is the topic of the next chapter, where the role of the dopant type, dopant density and injection level on the intrinsic lifetime of silicon is investigated, and the efficiency limits imposed by intrinsic recombination processes re-evaluated.

CHAPTER 3

Lifetime and Efficiency Limits of Crystalline Silicon Solar Cells

3.1 Introduction

Recombination within semiconductor devices usually occurs through a number of simultaneous processes. These processes can be broadly classified as intrinsic or extrinsic in nature [60]. Intrinsic processes are unavoidable properties of the semiconductor material and include radiative recombination [24] and Coulomb-enhanced Auger recombination [28]. Extrinsic processes relate to defects (impurities, crystallographic imperfections, etc) within the material or at its surface and include Shockley-Read-Hall bulk [18] and surface recombination [61]. In principle, all defects could be eliminated and extrinsic recombination processes reduced to negligible levels. The extent to which this can be achieved in practice is strongly dependent on material quality and its subsequent processing.

The performance of many silicon devices is limited by the recombination lifetime of the charge carriers. This is particularly true of photovoltaic cells, where the entire volume of the device is active. High bulk recombination rates are known to limit the open-circuit voltage and to reduce the fill-factor in low efficiency devices [25]. Even when bulk recombination has been

practically suppressed, injection-level-dependent surface recombination rates have been shown to reduce solar cell efficiency [26]. Furthermore, most semiconductor devices undergo high temperature processes such as thermal oxidation during fabrication and achieving high carrier lifetimes within the as-grown silicon may be insufficient, since issues such as thermal degradation and possible contamination must be avoided.

Ultimately, intrinsic recombination processes will limit the achievable performance and it is important to establish what this intrinsic limit is. In this chapter, a selection of injection level dependent lifetime data are presented for silicon wafers passivated with high temperature thermal oxides. Following an aluminium anneal, or *alneal*, record effective lifetimes were measured for both *n*-type and *p*-type silicon of various doping densities. A new empirical formula to evaluate the rate of intrinsic recombination in crystalline silicon of arbitrary injection level and dopant density is then presented and validated using these record effective lifetime data. Based on this new parameterisation of the intrinsic recombination rate, the limiting efficiency of crystalline silicon solar cells is investigated as a function of cell thickness and dopant density.

3.2 Limits for the Effective Lifetime

3.2.1. Previous Work

The highest *effective lifetime* (τ_{eff}), which incorporates all the bulk and surface recombination processes, previously reported for crystalline silicon appears to be 22ms [62, 63]. Yablonovitch *et al.* [62] measured τ_{eff}=22ms for a 250μm thick <111> oriented wafer from a 150Ωcm (probably *n*-type) float-zone (FZ) boule. They passivated the surfaces by chemically oxidising the wafer in hot sulphuric acid and then submersing it in hydrofluoric acid during the lifetime measurement. The wafer, therefore, did not undergo any high temperature processing. By sequentially etching a wafer to vary its thickness (see section 2.2), the bulk and surface recombination rates were separated by Yablonovitch *et al.* and they determined a maximum τ_{bulk} of 35ms.

Very high minority carrier lifetimes have also been reported by Ciszek *et al.* [63] for specially grown FZ ingots that had been doped with gallium. The highest measured *effective* lifetime was 21.6ms, for lightly doped material (ρ=200Ωcm), with high lifetimes also measured for more heavily doped material. Surface recombination was minimised by measuring the lifetime of the ingot, rather than wafers sawn from it. The silicon material therefore did not

undergo any high temperature processing following the crystal growth phase. Lifetime measurements on large volume, low surface area FZ silicon specimens were also performed by Hacker and Hangleiter [60], who found high *effective* lifetimes of approximately 10ms for lightly doped *n*-type material at 300K, although lower lifetimes with a maximum of about 1ms were found for *p*-type material.

For silicon wafers processed at high temperatures the highest reported *bulk* lifetime appears to be approximately 11ms, as determined using the thickness variation method by Eades [37] and also by King [64]. These high resistivity 150Ωcm *n*-type FZ silicon wafers were oxidised at 1000°C in dry oxygen (no TCA) for surface passivation. The maximum *effective* lifetime actually measured by King, who only used a forming gas anneal as the final passivation step, was 1.4ms. Eades performed an *alneal* [65], and measured an *effective* lifetime of 5.6ms. He also determined a surface recombination velocity of 1.2cm/s.

Pang and Rohatgi [66] have also reported high lifetimes in oxidised silicon wafers grown by the magnetic Czochralski (MCZ) method. These MCZ wafers were 550μm thick, <100> oriented and nearly intrinsic (about 2000Ωcm, *p*-type). Surface passivation was achieved by oxidation at 1000°C in a 2% HCl/O_2 ambient for 75mins. The maximum *effective* lifetime measured was 5.2ms, while variation of the wafer thickness allowed a *bulk* lifetime of 6.65ms to be determined. Interestingly, passivating the as grown material using HF acid (similar to the experiments of Yablonovitch *et al.*) gave a higher maximum *effective* lifetime of 7.2ms and an extracted *bulk* lifetime of 8.5ms, thus indicating that some degradation of the bulk lifetime of the MCZ material occurred during the high temperature processing. A similar degradation was found for 1000Ωcm FZ silicon were they determined an as grown *bulk* lifetime of 9ms, which reduced to 4ms after oxidation.

3.2.2 Experimental Details

A wide range of substrate resistivities has been explored for both *n*-type (phosphorus) and *p*-type (boron) dopants with further details given in Table 3.1. The majority of the wafers used were FZ quality as this has historically given the best lifetimes, especially in *p*-type silicon where boron-oxygen complexes are believed to degrade the lifetime of CZ silicon [67]. The choice of CZ silicon, rather than FZ, for the 0.60Ωcm *n*-type material was purely based on wafer availability within our laboratory. All of the wafers used in these experiments were sourced from commercial stock.

Table 3.1. Details for the <100> oriented silicon wafers used in these experiments. All the wafers where grown by the FZ method except the 0.6Ωcm *n*-type substrates which where CZ. The *n*-type wafers where doped using phosphorous and the *p*-type wafers using boron. The maximum measured effective lifetimes have been included as well as the corresponding upper bound on the surface recombination velocity (SRV) at the Si/SiO_2 interface.

Dopant type	Resistivity	Dopant density	Wafer Width	Maximum τ_{eff}	Upper bound on SRV
n	90 Ωcm	$4.9x10^{13}$ cm^{-3}	265 μm	29 ms	0.46 cm/s
n	1.5 Ωcm	$3.2x10^{15}$ cm^{-3}	285 μm	6.0 ms	2.4 cm/s
n	0.6 Ωcm	$8.8x10^{15}$ cm^{-3}	590 μm	1.1 ms	26.8 cm/s
n	0.18 Ωcm	$3.5x10^{16}$ cm^{-3}	215 μm	205 μs	52.4 cm/s
p	150 Ωcm	$8.9x10^{13}$ cm^{-3}	400 μm	32 ms	0.63 cm/s
p	10 Ωcm	$1.4x10^{15}$ cm^{-3}	370 μm	13 ms	1.4 cm/s
p	1.0 Ωcm	$1.5x10^{16}$ cm^{-3}	400 μm	1.7 ms	11.8 cm/s
p	0.35 Ωcm	$4.9x10^{16}$ cm^{-3}	275 μm	300 μs	45.8 cm/s

The silicon wafers were sourced in an as-cut or lapped condition. Dilute HF/HNO_3 solution, followed by rinsing in de-ionised (DI) water, was used to remove any saw damage and to shinny etch the wafers. They where then cleaned using the standard RCA procedure [65], and immersed in dilute HF. The wafers where oxidized in a trichloroethane (TCA)-cleaned quartz furnace tube at 1050°C for 120 minutes in a TCA/O_2 ambient, which resulted in a blue coloured oxide. A post oxidation anneal in Ar was also performed at 1050°C before cooling the furnace to 800°C and unloading the wafers. These conditions were carefully optimized to maximize the effective lifetime following a high temperature oxidation. Finally, the Si/SiO_2 interfaces were *alnealed*. This involved evaporating 0.1μm of high purity (5N) aluminium onto both wafer surfaces, sintering the samples at 400°C in a forming gas ambient for 30 minutes and then subsequently etching off the aluminium layers using hot phosphoric acid (90°C).

The effective lifetime of each sample was measured at 25°C for minority carrier injection levels in the range of 10^{12} cm^{-3} to 10^{17} cm^{-3}. Both the quasi-steady-state (Qsspc) and transient photoconductance (tpcd) methods were used [50]. Excellent agreement was obtained between the two methods using the generalized analysis procedure of Nagel *et al.* [53], with relative differences less than two percent.

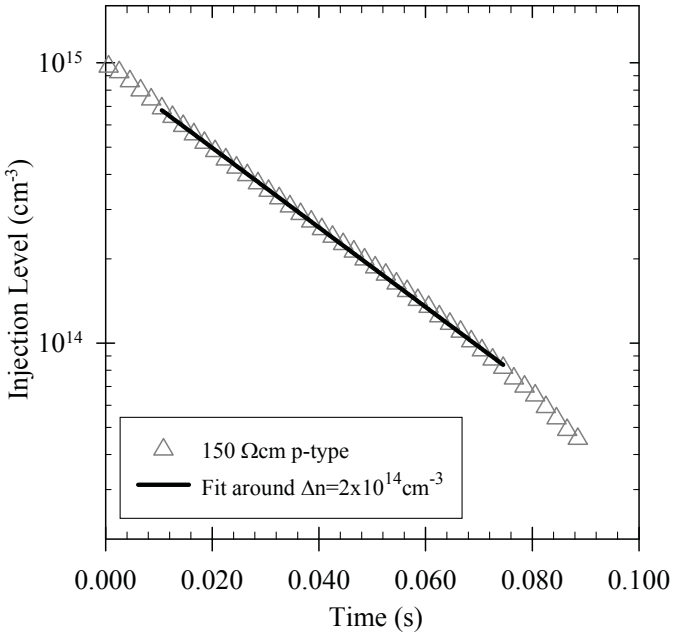


Figure 3.1. Semi-log plot of the carrier density decay of a well-passivated, 150 Ωcm *p*-type wafer from a transient photoconductance measurement. An exponential fit to the data about a carrier injection level of $2x10^{14}cm^{-3}$ gives an effective lifetime of 30.6ms. The wafer had a maximum effective lifetime of 32ms.

3.2.3 Results and Discussion

An example of a tpcd trace for a high lifetime sample (150 Ωcm *p*-type) is shown in Figure 3.1. This semi-log plot of the carrier density decay shows the expected linear slope with time. A fit of the data around an injection level of $2x10^{14}cm^{-3}$ with an exponential curve gives an effective lifetime of 30.6ms (note that the x-axis is in seconds). At the low carrier density end of the trace the slope can be observed to increase slightly, indicating a decreasing lifetime. This points out that, to fully characterize a silicon sample, the lifetime should be measured over a broad range of carrier injection levels. The injection-level-dependent effective lifetimes measured for all of the silicon wafers are plotted in Figures 3.2 and 3.3 for the *n*-type and *p*-type dopants respectively, with both figures using the same ranges for the x-scale and y-scale.

Figure 3.2 shows that a maximum effective lifetime of 29ms has been measured for lightly doped *n*-type material at an injection level of $3.5x10^{14}$ cm^{-3}. At lower injection levels the effective lifetime appears to decrease slightly and flattens out at about 15ms, indicating a relatively weak injection-level-dependent recombination rate at either the surface or in the bulk of the sample. Two additional identical samples that were oxidized in the same batch had an even weaker injection-level dependence, with effective lifetimes above 20ms for the lowest measured injection levels and a slightly lower maximum value of 24ms. At high injection levels, the effective lifetime for all the samples, both *n*-type and *p*-type doped, was observed to

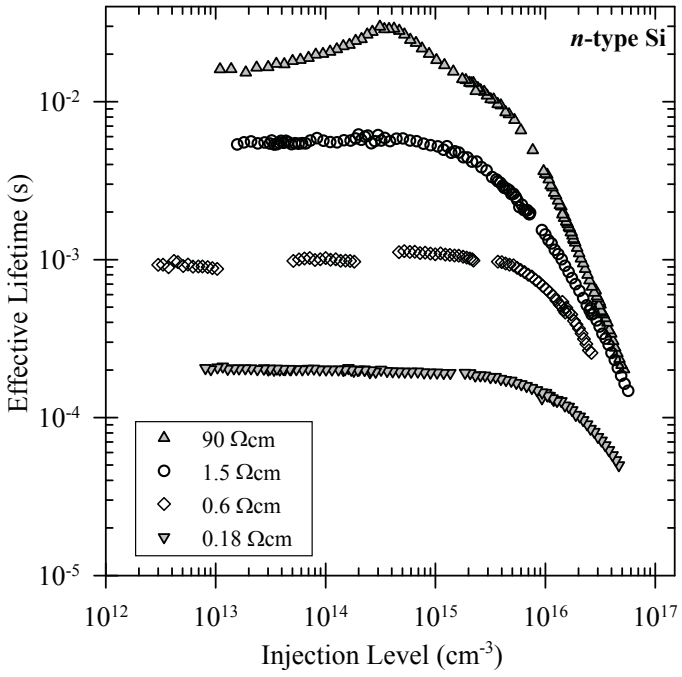


Figure 3.2. Measured effective lifetimes for oxide-passivated, alnealed *n*-type wafers. Auger recombination dominates at the higher carrier injection levels.

decrease rapidly, particularly for injection levels greater than 10^{16}cm^{-3}. This is attributed to Coulomb enhanced Auger recombination.

High effective lifetimes have also been measured for the three more heavily doped *n*-type wafers. They all show very little injection level dependence (except for Auger recombination), with maximum effective lifetimes of 6ms, 1.1ms and 0.2ms for the 1.5Ωcm, 0.6Ωcm and 0.18Ωcm wafers respectively. The high lifetime for the 0.6Ωcm wafer is particularly interesting as this material was grown by the Czochralski method.

Excellent results have also been achieved for *p*-type boron doped silicon. Figure 3.3 shows that a maximum effective lifetime of 32ms has been measured for high resistivity material at an injection level of 3x10^{14} cm^{-3}. Maximum effective lifetimes of 13ms, 1.7ms and 300μs have been measured for 10Ωcm, 1.0Ωcm and 0.35Ωcm *p*-type silicon respectively. It should be noted that these effective lifetime values should be considered as lower bounds on the actual bulk lifetime. Comparing Figures 3.2 and 3.3 shows that the injection level dependence of the effective lifetime at low carrier densities appears to be considerably more pronounced for *p*-type material than for *n*-type material. For example, the lifetime of the 150Ωcm *p*-type wafer decreases from 32 ms down to 3ms at the lowest injection level measured. It is not possible to determine if this is due to bulk or surface processes from our experiments.

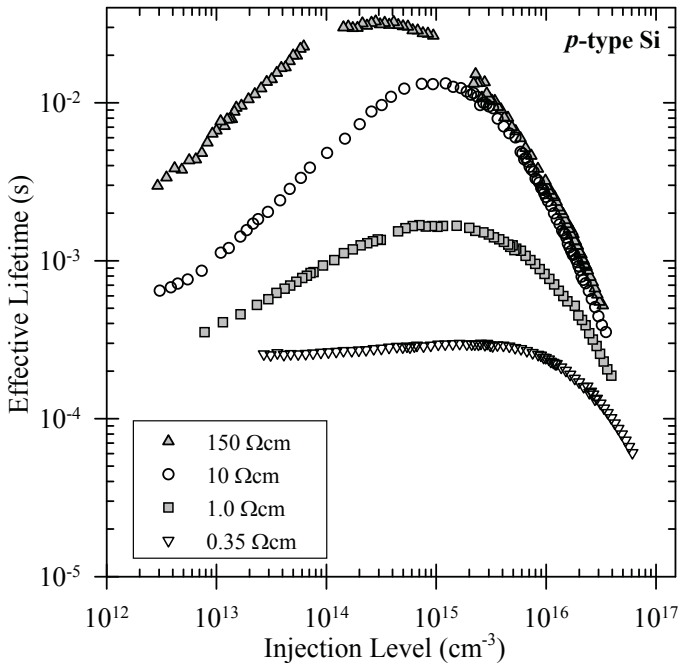


Figure 3.3. Measured effective lifetimes for oxide-passivated, alnealed *p*-type wafers. Auger recombination dominates at the higher carrier injection levels.

An upper limit for the surface recombination velocity (SRV) at the Si/SiO_2 (alnealed) interface can be determined by assuming no bulk recombination (that is, by setting $\tau_{bulk} \rightarrow \infty$ in Eq. (2.29)). Values for the SRV corresponding to the maximum effective lifetime for each wafer are given in Table 3.1. For the high resistivity *n*-type material the value for the SRV is 0.46cm/s, lower than the 1.2cm/s measured by Eades for an *alnealed* oxide. This passivation quality is equivalent to the SRV reported by Yablonovitch *et al.* [62] and Pang and Rohatgi [66] for HF passivation of high resistivity wafers. The results for the high resistivity *p*-type material are very similar, with a bound on the SRV of 0.63cm/s.

3.2.4 Conclusions

Maximum effective lifetimes of 29ms and 32ms have been measured for high resistivity *n*-type and *p*-type silicon respectively, which appear to be the highest ever reported. Similarly, the effective lifetimes determined for more heavily doped material are amongst the highest reported at those doping levels. Importantly, the silicon wafers used in this study were commercially sourced and not grown using special procedures. Furthermore, the wafers had undergone high temperature processes (over two hours at 1050°C), clearly indicating that very high effective lifetimes can be preserved by carefully optimizing the processing conditions. These effective lifetimes provide a lower bound for the bulk lifetime of the material, which may

be still higher. An upper limit for the rate of intrinsic recombination in silicon has therefore been determined. A parameterisation that fits this limit is developed in the next section

3.3 Coulomb-Enhanced Auger Recombination

3.3.1 Introduction

Auger recombination can significantly influence the performance of many silicon devices. The base region of power transistors [18] and high efficiency photovoltaic cells [25] are affected by it under high injection conditions, while the quantum efficiency and saturation current of heavily doped emitters [68] can be affected at low injection conditions. Accurate models for determining the rate of Auger recombination as a function of injection level and doping density are therefore essential, particularly for device simulation.

As discussed in Chapter 2, Auger recombination is traditionally viewed as a three-particle interaction where an electron-hole pair recombine, with the excess energy being transferred to a third free electron or hole [28]. The charge carriers involved are assumed to be non-interacting quasi-free particles [29], resulting in Eq. (2.5) and Eq. (2.6) for the Auger recombination rate. It follows that the Auger lifetime *ideally* depends on the inverse of the carrier density squared ($\tau_{Auger} \propto 1/n^2$). In reality however, Auger recombination is more complicated. Band-to-band Auger processes can occur with phonon participation (phonon-assisted Auger recombination – PAAR) and without phonon participation (direct Auger recombination – DAR) to conserve momentum. PAAR is believed to dominate in *p*-type silicon while DAR is the dominant process in *n*-type silicon [69]. For non-degenerate material, both PAAR and DAR give the same dependency for the recombination rate with doping, although they are predicted to differ in degenerately doped material [70]. Furthermore, a third Auger recombination mechanism, termed trap-assisted Auger recombination (TAAR) has been proposed by Landsberg [71], where the lifetime depends only on the inverse of the carrier density ($\tau_{TAAR} \propto 1/n$).

The assumption that the recombining electrons and holes are non-interacting, quasi-free particles has been addressed theoretically by Hangleiter and Häcker [28]. They took into account the Coulombic interaction between the mobile charge carriers and found that electrons and holes can become correlated due to the formation of excitons. The *eeh* Auger recombination rate is then strongly enhanced due to the increased electron density in the vicinity of a hole, with a similar enhancement mechanism for the *ehh* process. The strength of the Coulomb-enhancement is believed to decrease as the concentration of majority carriers increases, due to

screening of the electron-hole interaction. Coulomb enhancement of Auger recombination processes therefore introduces a departure from the ideal relationship between the Auger lifetime and doping density. This is accounted for by multiplying Auger coefficients, C_n and C_p, by the enhancement factors g_{eeh} and g_{ehh}, such that for *n*-type silicon under low injection conditions

$$\tau_{Auger,li} = \frac{1}{g_{eeh} C_n N_D^2} = \frac{1}{C_n^* N_D^2}, \tag{3.1}$$

and for *p*-type silicon

$$\tau_{Auger,li} = \frac{1}{g_{ehh} C_p N_A^2} = \frac{1}{C_p^* N_A^2}. \tag{3.2}$$

Finally, additional processes that have not yet been accounted for may impact the Auger lifetime. One such possibility is the Coulombic interactions between mobile charged carriers and fixed charges (ionized dopant atoms), which are known to be important in modeling mobilities, but do not seem to have been considered in the context of Auger recombination. It is therefore difficult to conclude what the doping and the injection level dependencies of the Auger lifetime should be from a theoretical perspective. The $1/n^2$ dependence appears to provide an upper limit on the lifetime, with the various other factors decreasing the lifetime, to a greater or lesser extent.

The alternative route of examining the available experimental data, including our own measurements, is followed in this section. A new formulation for the Auger recombination rate in silicon and is proposed and a parameterization that is consistent with the observed injection level dependent lifetime data for *n*-type and *p*-type silicon of various resistivities under high and low injection conditions is developed.

3.3.2 Existing Analytical Models

Various analytical expressions exist for estimating the Auger lifetime. Most of the models determine either the low injection Auger lifetime as a function of dopant density or the ambipolar Auger lifetime for lightly doped silicon under high injection, but not both.

3.3.2.1 Low Injection Models

The most comprehensive determination of the low injection Auger lifetime from experimental data appears to be that of Altermatt *et al.* [32]. Using the C_n and C_p values of Dziewior and Schmid [30], they performed an empirical parameterization and showed that the enhancement factors g_{eeh} and g_{ehh}, are a function of the dopant density in lowly injected silicon

$$g_{eeh}(N_D) = 1 + 44\left\{1 - \tanh\left[\left(\frac{N_D}{5x10^{16}\,cm^{-3}}\right)^{0.34}\right]\right\}, \quad (3.3)$$

$$g_{ehh}(N_A) = 1 + 44\left\{1 - \tanh\left[\left(\frac{N_A}{5x10^{16}\,cm^{-3}}\right)^{0.29}\right]\right\}. \quad (3.4)$$

Other authors have fit the minority carrier lifetime data for lowly injected, highly doped silicon (N_{dop}>1x10^{17}cm^{-3}) using an inverse quadratic expression for both *n*-type [72] and *p*-type silicon [73]. Nevertheless, Swirhun [74] noted that for *n*-type material, a better fit to the low injection Auger lifetime was

$$\tau_{Auger,li} = \frac{1}{1.9x10^{-24}\,N_D^{1.65}}. \quad (3.5)$$

A similarly simple fit was not proposed for *p*-type material.

3.3.2.2 High Injection Models

The ambipolar Auger coefficient, C_a, has been directly determined by a number of authors using a variety of techniques [75]. Typical values quoted for C_a range from 1x10^{-30}cm^{6}s^{-1} to 2x10^{-30}cm^{6}s^{-1} [76]. It has generally been found that C_a is larger than the sum of the low injection coefficients, C_n+C_p, determined for highly doped silicon. The discrepancy is also generally explained by Coulomb-enhancement [28]. This is supported by the recent analysis of Altermatt *et al.* [77] which determined that C_a decreases from 2.8x10^{-30}cm^{6}s^{-1} to 1.9x10^{-30}cm^{6}s^{-1} as the injection level in a specially designed concentrator cell (lightly doped silicon base) increased from 3x10^{15}cm^{-3} to 1x10^{17}cm^{-3}. That is, C_a and therefore the Coulomb-enhancement, is a function of the injection level.

What is not clear is if the rate of Coulomb-enhancement is the same for lowly injected, intermediate doped silicon (say N_A=10^{17}cm^{-3}) as for highly injected, lowly doped silicon. The theory of Hangletier and Hacker predicts that the Coulomb-enhancement is weaker in highly injected, lowly doped silicon. This is due to the ratio of free electrons to holes being approximately equal and so there is stronger screening of the Coulombic forces. In lowly injected, intermediate doped silicon, the concentrations of both carriers are very different, and Coulombic forces exert their full strength.

3.3.2.3 Complete Models

There are very few models that estimate the Auger lifetime as a function of both injection level and dopant density. Experimental evidence for Coulomb-enhanced Auger recombination has been found in both lowly-injected [32] and highly-injected silicon [77]. Schmidt *et al.* [78] and Altermatt *et al.* [76] have proposed a parameterization that follows both of these dependencies based on the enhancement factors given in Eq. (3.3) and Eq. (3.4). They assumed that the enhancement factors g_{eeh} and g_{ehh} depend mainly on the screening behaviour of the charge carriers, and that the screening can be described by the Debye theory. This allowed them to replace the dopant density in Eq. (3.3) and Eq. (3.4) with $n+p$. While this model has been shown to be in good agreement with experimental lifetime data for intermediately doped *p*-type silicon, it has not been tested for *n*-type silicon. Furthermore, it will shown in section 3.3.3 that this model significantly overestimates the rate of Auger recombination in highly injected, lowly doped material.

A relatively simple model that changes the rate of Auger recombination in silicon as it changes from low injection to high injection conditions is used in the device simulation package PC1D [79]. This model chooses fixed values for C_n and C_p under low injection conditions (termed $C_{n,li}$ and $C_{p,li}$), and a fixed value for C_a under high injection conditions, and then weights between them to determine effective Auger coefficients, C_n^{eff} and C_p^{eff}, that can be used in Eq. (2.5) and Eq. (2.6)

$$C_n^{eff} = C_{n,lli}\left(\frac{N_D}{N_D + p}\right) + \frac{C_a}{2}\left(\frac{p}{N_D + p}\right), \tag{3.6}$$

$$C_p^{eff} = C_{p,lli}\left(\frac{N_A}{N_A + n}\right) + \frac{C_a}{2}\left(\frac{n}{N_A + n}\right). \tag{3.7}$$

As implemented in PC1D, this model tends to underestimate the rate of Auger recombination occurring in silicon, as it does not include the effects of Coulomb-enhancement under low injection or high injection conditions. A variation to the model has been proposed by Glunz *et al.* [39] based on a slightly different weighting from low injection to high injection. The model of Glunz *et al.* incorporates the low level injection enhancement factors g_{eeh} and g_{ehh} of Eq. (3.3) and Eq. (3.4) (replacing $C_{n,li}$ at the front of equation (3.6) with $g_{eeh}C_{n,li}$ and similarly $C_{p,li}$ with $g_{ehh}C_{p,li}$), it does not however account for the injection level dependent Coulomb-enhancement effect under high injection. As a consequence, it underestimates the recombination rate for mid to high injection levels and overestimates it at very high injection levels, as will be shown in the section 3.3.3. A further weakness of this model is that there is no physical basis for the relative weighting from low injection to high injection conditions.

3.3.3 A New Auger Parameterisation

Any new parameterization of Auger recombination in silicon must correctly model the Auger lifetime of both lowly injected silicon and highly injected silicon. Furthermore, the parameterisation must demonstrate that Auger recombination is increased above the *ideal* rate, and that the increase is a function of both the doping density and the injection level. While the theory of Coulomb-enhancement can elegantly (although only qualitatively) explain the experimentally observed increase in Auger recombination from the *ideal* rate, the possibility of other physical effects cannot be discounted. Our parameterization is intended to provide the simplest functional form for the experimental observations of Auger recombination in silicon.

3.3.3.1 The Low Injection Auger Lifetime

Figure 3.4 shows the highest low injection lifetimes experimentally measured by various authors for *n*-type silicon at 300K. In general, the data by the various authors agree quite well, with the largest amount of scatter occurring for intermediate doping densities between $1x10^{17}cm^{-3}$ and $5x10^{18}cm^{-3}$. A good fit to the data for $N_D > 5x10^{15}cm^{-3}$ is the simple expression

$$\tau_{Auger,li} = \frac{1}{1.8x10^{-24} N_D^{1.65}} \qquad \text{for } n\text{-type silicon,} \tag{3.8}$$

which is consistent with the approach of Swirhun [74]. The slightly lower coefficient of $1.8x10^{-24}$ determined here is mainly due to the addition of new data points. Included in Figure 3.4 are the parameterisations of Eq. (3.8) and that of Altermatt *et al.* [32] (from Eq. (3.3)). Both parameterisations fit the data quite well with the exception of the intermediate doping densities. The fit of Altermatt *et al.* is a better match to the maximum lifetimes reported, while the fit of Eq. (3.8) is a better match to the average lifetime at each doping density. Comparing Eq. (3.1) and Eq. (3.8), our fit is equivalent to determining an enhanced Auger coefficient, C_n^*, of

$$C_n^* = g_{eeh} C_n = 1.8x10^{-24} * N_D^{-0.35} = 1.8x10^{-24} * n_o^{-0.35}, \tag{3.9}$$

which is functionally much simpler than that of Altermatt *et al.* from equation (3.3).

Similarly, Figure 3.5 shows the highest low injection lifetimes experimentally measured by various authors for *p*-type silicon at 300K. The parameterisation proposed by Altermatt *et al.* [32] (from equation (3.4)) is included, along with an alternative best fit for *p*-type silicon with $N_A > 5x10^{15}cm^{-3}$,

$$\tau_{Auger,li} = \frac{1}{6x10^{-25} N_A^{1.65}} . \tag{3.10}$$

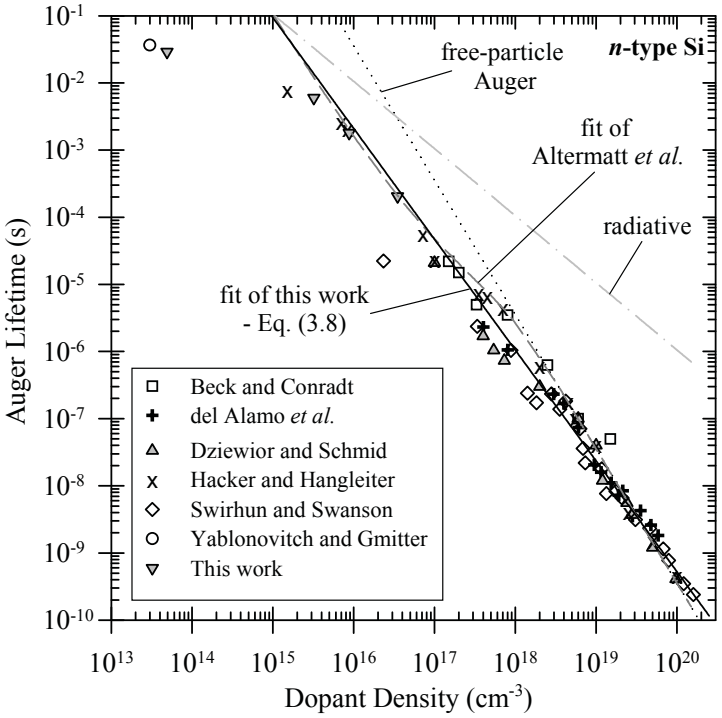


Figure 3.4. Measured values of the low-injection Auger lifetime in *n*-type silicon at 300K. The lifetime fit of this work, Eq. (3.8), and from Altermatt *et al.*, Eq. (3.3), are shown. The lifetime limit from radiative recombination and *ideal* Auger recombination are given.

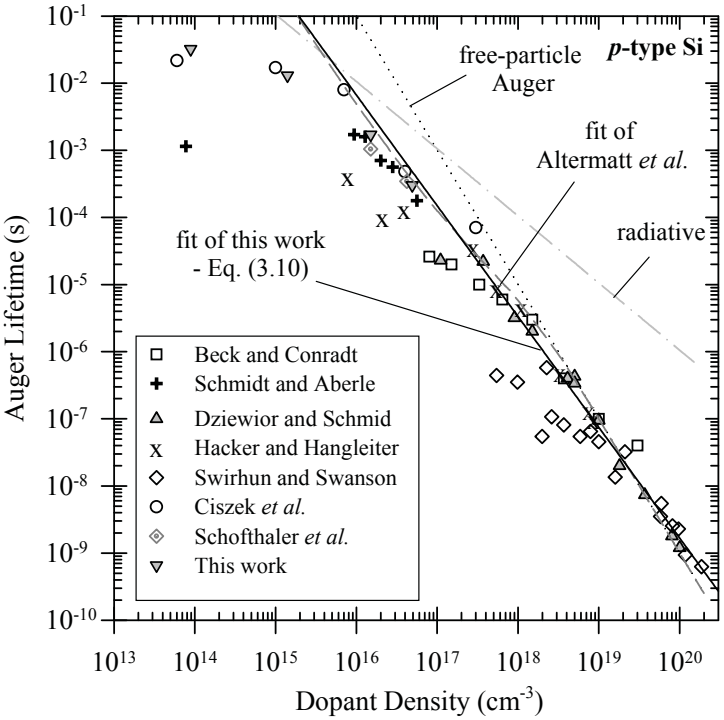


Figure 3.5. Measured values of the low-injection Auger lifetime in *p*-type silicon at 300K. The lifetime fit of this work, Eq. (3.10), and from Altermatt *et al.*, Eq. (3.4), are shown. The lifetime limit from radiative recombination and *ideal* Auger recombination are given.

Again, the data from the various authors agree reasonably well and both parameterisations fit within the experimental scatter. Indeed, it is difficult to conclude which parameter set is superior due to the scatter of the data, although both are quite acceptable. Comparison of Eq. (3.2) and Eq. (3.10) show that the parameterisation of Eq. (3.10) is equivalent to determining an enhanced Auger coefficient, C_p^*, of

$$C_p^* = g_{ehh} C_p = 6x10^{-25} * N_A^{-0.35} = 6x10^{-25} * p_o^{-0.35} . \qquad (3.11)$$

It should be noted that the new expressions of Eq. (3.9) and Eq. (3.11) retain the experimental observation that the Auger recombination rate is three times stronger in heavily doped *n*-type silicon than in *p*-type silicon.

3.3.3.2 The High Injection Auger Lifetime

The highest lifetimes reported for silicon under high injection are in the vicinity of 30ms, including the results presented in section 3.2 [62, 63]. The lifetime values reported by Yablonovitch *et al.* [62] are for the bulk lifetime of lightly doped *n*-type silicon. They include Auger recombination and radiative recombination. Many authors have considered the rate of radiative recombination to be negligible, but this is not the case for such high lifetimes. As discussed in Chapter 2, the radiative recombination rate is given by

$$U_{rad} = Bnp , \qquad (3.12)$$

where B is the coefficient for radiative recombination, equal to $9.5x10^{-15}cm^3s^{-1}$ [24]. The high injection Auger lifetime can be found by subtracting the radiative recombination rate from the bulk lifetime data of Yablonovitch *et al.*,

$$\frac{1}{\tau_{Auger}} = \frac{1}{\tau_{bulk}} - B(N_D + \Delta p) . \qquad (3.13)$$

Figure 3.6 shows the measured bulk lifetime of Yablonovitch *et al.* and the extracted Auger lifetimes. It is clear that radiative recombination is significant for injection levels from $5x10^{14}cm^{-3}$ to $3x10^{16}cm^{-3}$. Indeed, the maximum impact of radiative recombination is at carrier densities around $2x10^{15}cm^{-3}$, where the bulk lifetime was measured to be 23ms but the Auger lifetime is determined to be 49ms. Examination of the Auger lifetime data in Figure 3.6 suggests that, even for the high lifetimes measured by Yablonovitch *et al.*, there is still evidence of residual Shockley-Read-Hall (SRH) bulk recombination, which gives rise to the decreasing lifetime as the injection level decreases below $1x10^{15}cm^{-3}$. The electron lifetime, τ_{no}, of this SRH centre is ≈37ms with a comparable value for the hole lifetime.

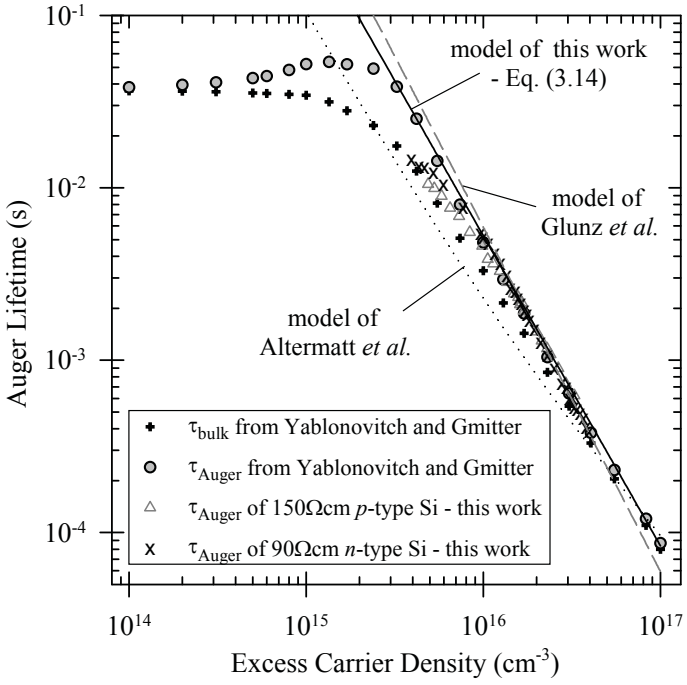


Figure 3.6. The high injection bulk lifetime and Auger lifetime from Yablonovitch and Gmitter, along with the high injection Auger lifetime measurements from section 3.2 for high resistivity *n*-type (90 Ωcm) and *p*-type silicon (150 Ωcm). The predicted lifetimes from the models of Altermatt *et al.* and Glunz *et al.* are shown, along with the fit of this work.

Included in Figure 3.6 are the lifetime measurements at high excess carrier densities, with radiative recombination subtracted, for the 90Ωcm *n*-type and 150Ωcm *p*-type silicon substrates discussed in section 3.2. It can be seen that for carrier densities above $1x10^{16}cm^{-3}$, where Auger recombination is dominant, the measurements of section 3.2 and that of Yablonovitch *et al.* are in excellent agreement. This confirms that such high lifetimes are reproducible and support that they represent the limit of Auger recombination in silicon under high injection conditions. They also show that there is no discernible difference between highly injected, lowly doped *n*-type and *p*-type silicon, as one would expect.

Also included in Figure 3.6 are the predicted high injection lifetime values from the Auger model of Altermatt *et al.* [76], as well as the modified Auger model of Glunz *et al.* [39]. It can be clearly seen that the model of Altermatt *et al.* significantly overestimates Auger recombination rates in highly injected, lightly doped silicon. For example, at an injection level of $3x10^{15}cm^{-3}$, the experimentally determined Auger lifetime is 38.5ms, while the predicted Auger lifetime is only 13.9ms. The modified Auger model of Glunz *et al.* is in better agreement with the experimental data, but it can be seen that the predicted dependence of the Auger lifetime with injection level is incorrect. This leads to the rate of Auger recombination being

overestimated for injection levels above $4x10^{16}cm^{-3}$, and underestimated at lower injection levels.

A simple parameterisation that, as shown in Figure 3.6, properly fits the injection level dependence of the available Auger data for $\Delta p > 3x10^{15}cm^{-3}$ is

$$\tau_{Auger,hi} = \frac{1}{3x10^{-27}\Delta p^{1.8}}. \quad (3.14)$$

Comparison with Eq. (2.5) shows that this is equivalent to parameterising an injection level dependent ambipolar Auger coefficient of

$$C_a^* = 3x10^{-27}\Delta p^{-0.2} = 3x10^{-27}\Delta n^{-0.2}. \quad (3.15)$$

3.3.3.3 A General Parameterisation

Experimental and theoretical considerations indicate that at least three separate parameters are required to accurately model Auger recombination. The different dominant mode for momentum conservation during Auger recombination in *n*-type silicon (DAR) compared to *p*-type silicon (PAAR) necessitates two parameters. These parameters are not constants due to the role of Coulombic forces, which depend on the density of the mobile charges. Furthermore, the strength of Coulombic forces is reduced depending on the ratio of free electrons to free holes, due to screening effects, and therefore a third parameter is required. Accordingly, it is proposed that Auger recombination is a three-particle process that depends on the equilibrium concentration of free electrons and free holes, and on the density of excess carriers such that the recombination rate is given by

$$U_{Auger} = np\left[C_1(n_o)n_o + C_2(p_o)p_o + C_3(\Delta n)\Delta n\right]. \quad (3.16)$$

From Eq. (3.9), Eq. (3.11) and Eq. (3.15) it is deduced that $C_1(n_o)=C_n^*$, $C_2(p_o)=C_p^*$ and $C_3(\Delta n)=C_a^*$. Therefore a new general parameterisation for Auger recombination in silicon is

$$U_{Auger} = np\left(1.8x10^{-24}n_o^{0.65} + 6x10^{-25}p_o^{0.65} + 3x10^{-27}\Delta n^{0.8}\right). \quad (3.17)$$

This parameterisation accounts for the enhancement of Auger recombination due to the dopant density, dopant type and the injection level. Furthermore, it does not assume any relative weighting of the recombination rate from low injection to high injection conditions.

3.3.3.4 Validation of the New Parameterisation

The proposed parameterisation for Auger recombination was constructed so that it provides a good fit to the best, low injection lifetime data available in the literature as shown in

Figures 3.4 and 3.5, and also accurately fits the best high injection lifetime data. A further test of the model is to ensure that it correctly predicts the lifetime of arbitrarily doped *n*-type and *p*-type silicon from low injection through to high injection conditions. Data of this type are relatively scarce in the literature and so the lifetime measurements presented in section 3.2 are used. Lifetime data for a 590μm thick, 0.6Ωcm *n*-type CZ wafer passivated with PECVD SiN (see Chapter 4 for a complete discussion) has been included here as it has a higher effective lifetime than the oxidised sample in Figure 3.2. The combined data set constitutes a broad characterisation of the effective lifetime of *n*-type and *p*-type silicon for excess carrier densities in the range of $10^{12} - 10^{17}$cm^{-3} and for doping densities up to $5\text{x}10^{16}$cm^{-3}.

It is important to note that what has been experimentally measured is the effective lifetime, τ_{eff}, which includes all the recombination processes occurring within the silicon wafer. These processes are mainly Auger recombination (τ_{Auger}), radiative recombination (τ_{rad}), Shockley-Read-Hall recombination (τ_{SRH}), and surface recombination ($\tau_{surface}$),

$$\frac{1}{\tau_{eff}} = \frac{1}{\tau_{Auger}} + \frac{1}{\tau_{rad}} + \frac{1}{\tau_{SRH}} + \frac{1}{\tau_{surface}} . \tag{3.18}$$

To model the effective lifetime data, the Auger recombination rate is determined from Eq. (3.17), the radiative recombination rate from Eq. (3.12) and the SRH recombination rate from the parameters determined when analysing the data of Yablonovitch *et al.* in Figure 3.6 (ie $\tau_{no}=\tau_{po}=37$ms). This SRH contribution is only significant for samples which show effective lifetimes greater than ≈5ms. Finally, surface recombination has not been included in the modelled lifetime, and therefore the modelled lifetime can be expected to be slightly higher than the measured lifetime, particularly for more heavily doped wafers where it is more difficult to passivate the surface [61].

The measured effective lifetimes and predicted lifetimes are compared in Figure 3.7 for *n*-type silicon. It can be seen that the predicted lifetimes fit the experimental data very well for all the doping densities and across the full range of excess carrier densities. It is important to note that radiative recombination and SRH recombination are only significant when fitting the lifetime data of Yablonovitch *et al.*. Auger recombination is the prevalent recombination process in the other *n*-type samples from low injection through to high injection conditions. The proposed new Auger model of Eq. (3.17) clearly works well for *n*-type silicon.

Figure 3.8 shows the measured effective lifetimes and predicted lifetimes for *p*-type silicon. The predicted lifetimes fit the data well for all doping densities at both intermediate and high injection, where Auger recombination is dominant. Again, radiative recombination and

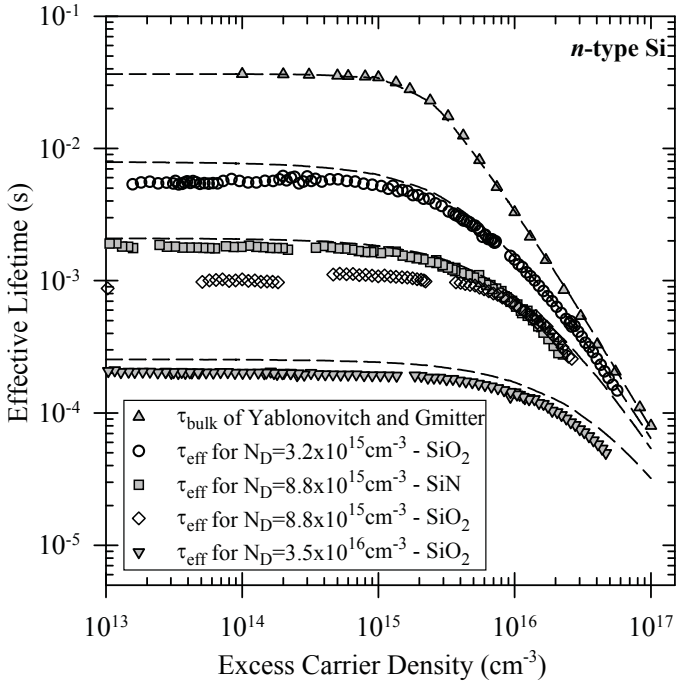


Figure 3.7. Measured values for the effective lifetime, from section 3.2, for *n*-type silicon with doping densities up to 3.5×10^{16} cm^{-3}. The predicted values for the effective lifetime from Eq. (3.18), based on the new parameterisation of the Auger recombination rate, Eq. (3.17), are included. There is excellent agreement between the experimental data and the model predictions.

SRH bulk recombination are only significant for the high resistivity (150Ωcm) lifetime data. It is well known that it is more difficult to passivate the surfaces of *p*-type silicon than *n*-type silicon [61] and so the decreasing effective lifetime of the *p*-type samples at low injection levels is attributed to an injection level dependent surface recombination velocity. Importantly, the modelled lifetime is never lower than the measured effective lifetime and therefore the Auger model of Eq. (3.17) is concluded to also work well for *p*-type silicon.

3.3.3.5 Discussion

As shown in the previous section, the new parameterisation determined for Auger recombination in silicon successfully fits the available lifetime data for arbitrarily doped and arbitrarily injected silicon. It is clear that Auger recombination is enhanced above the *ideal* inverse quadratic rate and a number of possible explanations for this have been given, the most convincing being Coulombic interactions between the charge carriers. Unfortunately, the scatter in the available data does not permit us to conclude that Coulomb-enhancement is the single reason for the enhanced rate. Indeed, there are a number of possible parameterisations that could be used to fit the available lifetime data equally well, particularly for the low injection lifetime data. One could satisfactorily use the low injection lifetime parameterisations of Altermatt *et al.*

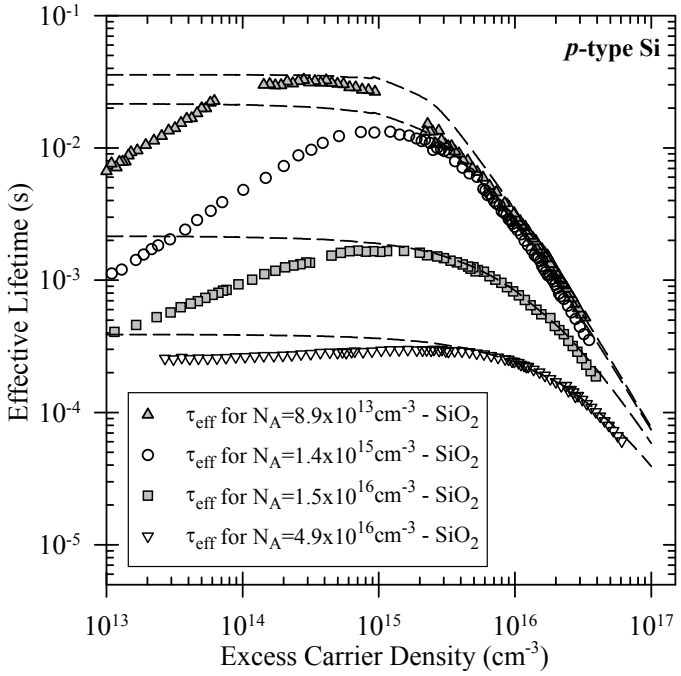


Figure 3.8. Measured values for the effective lifetime, from section 3.2, for *p*-type silicon with doping densities up to $4.9x10^{16}$ cm^{-3}. The predicted values for the effective lifetime from Eq. (3.18), based on the new parameterisation of the Auger recombination rate, Eq. (3.17), are included. There is excellent agreement between the experimental data and the model predictions for intermediate and high injection conditions.

(given in Eq. (3.3) and Eq. (3.4) here) along with the new parameterisation for the injection level dependent ambipolar Auger coefficient (Eq. (3.15)) to obtain another valid description of Auger recombination.

If Coulomb-enhancement is the dominant reason for the increased Auger recombination rate, then it is theoretically expected that once the majority carrier concentration or the injection level exceed the exitonic Mott density of approximately $1x10^{18}cm^{-3}$ at 300K [32], the formation of excitons will be greatly reduced due to screening effects. Therefore, the rate of Auger recombination should converge to the ideal rate (ie ($\tau_A \propto 1/n^2$). The low injection Auger lifetime model of Altermatt *et al.* was formulated to meet this requirement. It is also possible to parameterise the injection level dependent ambipolar coefficient to fit the Auger lifetime data of Yablonovitch *et al.* and satisfy this Mott transistion constraint, which would give

$$C_a^* = 3.79x10^{-31}\left(\frac{\Delta n + 3.8x10^{17}}{\Delta n + 6x10^{16}}\right). \tag{3.19}$$

The coefficient at the front is just the sum of C_n+C_p from Dziewor and Schmid. A comparison of the two parameterisations for C_a^* (Eq. (3.15) and Eq. (3.19)) is given in Figure 3.9. It can be seen that for excess carrier levels between $3x10^{15}cm^{-3}$ and $1x10^{17}cm^{-3}$ (the range

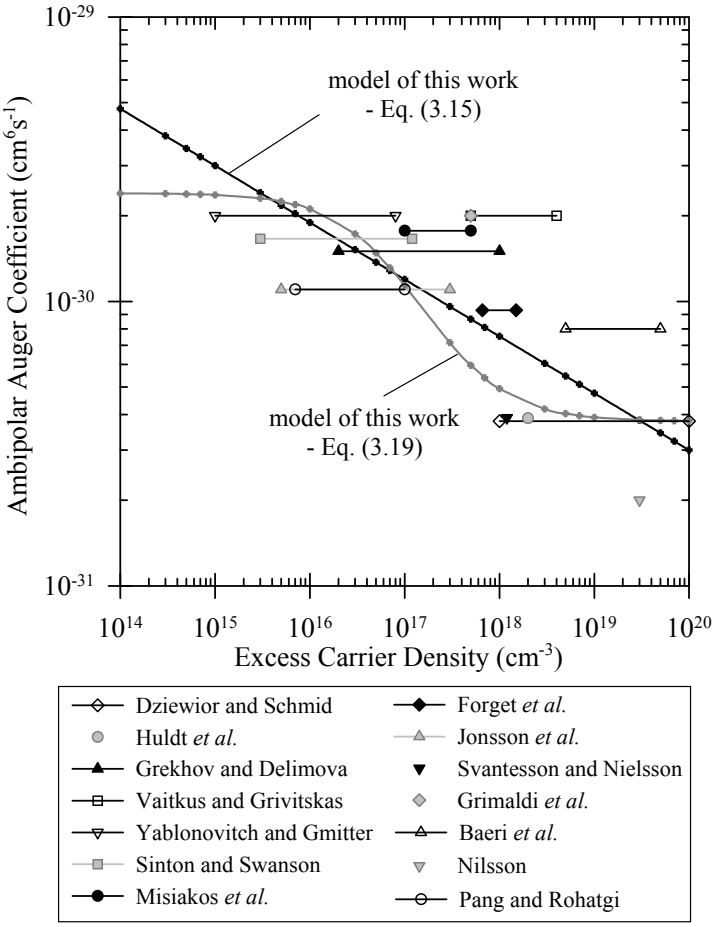


Figure 3.9. Values for the ambipolar Auger coefficient as a function of the excess carrier density from the models of this work, Eq. (3.15) and Eq. (3.19). Equation (3.15) is based on simply fitting high injection lifetime data, while Eq. (3.19) is also constrained by the Mott density (see section 3.3.3.5 for a discussion). Published values for the ambipolar Auger coefficient are included.

measured by Yablonovitch *et al.*) they agree quite well. However outside this range the two parameterisations are quite different. For lower excess carrier levels, the predicted Auger lifetimes are very high (≥100ms) and it is therefore not possible to probe this range to verify either parameterisation, as lifetimes greater than 50ms have never been measured in silicon. Included in Figure 3.9 are the values for the ambipolar Auger coefficient determined by a number of authors for excess carrier densities greater than $1x10^{15}cm^{-3}$ [30, 31, 62, 66, 75, 80-88]. There is significant scatter in the reported values and both of the parameterisations presented here for the ambipolar Auger coefficient fall within this scatter. Thus the existing experimental data is not sufficiently accurate to verify one parameterisation over the other and therefore determine if a transition at the exitonic Mott density occurs. A more accurate determination of the ambipolar Auger coefficient for excess carrier densities in the range of $1x10^{17}cm^{-3}$ to $1x10^{19}cm^{-3}$ is needed to clarify this issue.

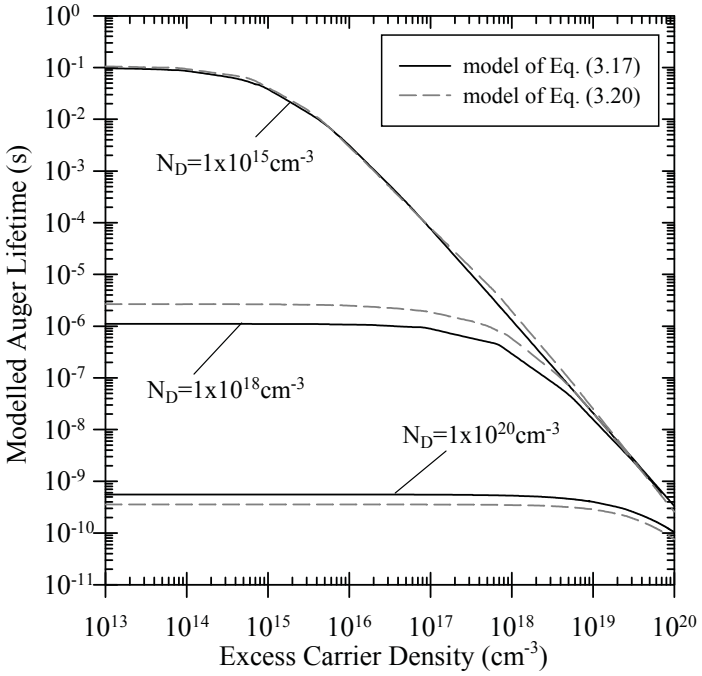


Figure 3.10. Comparison of the predicted Auger lifetimes for *n*-type silicon with various dopant densities, from the two models determined in this work. The model of Eq. (3.20) is constrained by the Mott transition.

A complete parameterisation for the Auger recombination rate using the ambipolar Auger coefficient of Eq. (3.19), such that the Mott transition occurs (based on Eq. (3.3), (3.4), (3.16) and (3.19)), would be

$$U_{Auger} = np\left(2.8x10^{-31}n_o\left\langle 1+44\left\{1-\tanh\left[\left(\frac{n_o}{2x10^{16}}\right)^{0.29}\right]\right\}\right\rangle + \right. \tag{3.20}$$

$$\left. 9.9x10^{-32}p_o\left\langle 1+44\left\{1-\tanh\left[\left(\frac{p_o}{2x10^{16}}\right)^{0.29}\right]\right\}\right\rangle + 3.79x10^{-31}\Delta n\left(\frac{\Delta n+3.8x10^{17}}{\Delta n+6x10^{16}}\right)\right).$$

Note that some of the parameters in Eq. (3.3) and Eq. (3.4) have been adjusted to be consistent with reference [76]. This is necessary or some of the predicted lifetimes would be less than the measured lifetimes in Figures 3.7 and 3.8.

Representative modelled Auger lifetimes for the parameterisations of Eq. (3.17) and Eq. (3.20) are plotted in Figure 3.10. As mentioned in section 3.3.3.1, the main deviations between the two models are expected to be in determining the low injection Auger lifetime for doping densities in the range of 1x10^{17}cm^{-3} to 5x10^{18}cm^{-3}, and to a lesser extent, for highly injected samples with excess carrier densities in the same range. This can indeed be seen in Figure 3.10. In general, however, the two models are in relatively good agreement.

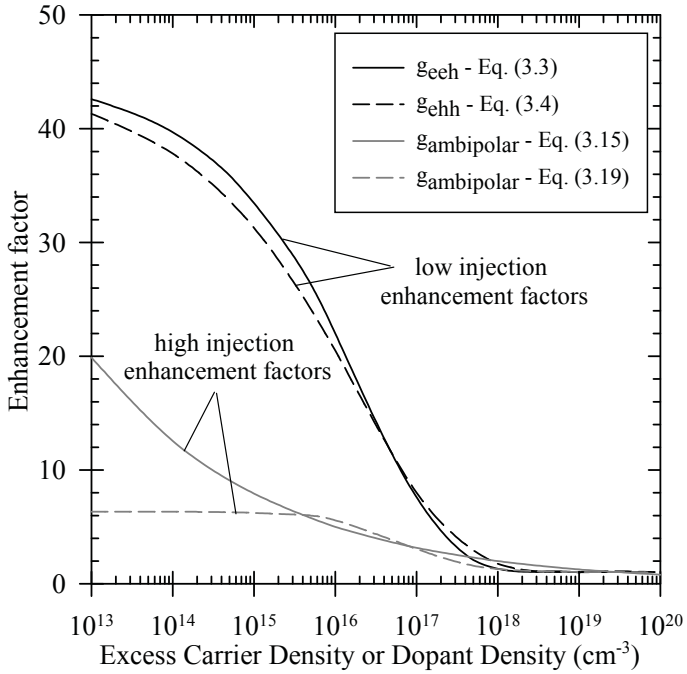


Figure 3.11. Comparison of the enhancement factor of the Auger recombination rate for highly injected, lowly doped silicon compared to lowly injected, highly doped silicon. The enhancement factor is lower for highly injected silicon, which is consistent with the Coulomb-enhanced Auger recombination theory of Hangleiter and Hacker.

A comparison of the enhancement of the Auger recombination rate, above the ideal rate, for lowly injected, intermediately doped silicon versus lowly doped but highly injected silicon can be made using the parameterisations given above. Reasonable values for the enhancement factors for lowly injected silicon as a function of doping density, g_{eeh} and g_{ehh}, are given by Eq. (3.3) and Eq. (3.4). Values for the enhancement factor for highly injected silicon as a function of injection level, $g_{ambipolar}$, are given by Eq. (3.15) and Eq. (3.19) divided by the $C_n+C_p=3.79\text{x}10^{-31}\text{cm}^6\text{s}^{-1}$ value of Dziewior and Schmid. These four curves are plotted in Figure 3.11. It is clear that the enhancement factors for highly injected silicon are lower than for low injected, highly doped silicon. This is consistent with the theory of Coulomb-enhancement by Hangleiter and Hacker. Furthermore, it appears that modelling the Auger recombination rate with a single enhancement factor as attempted in references [76, 78] is not possible.

It is important to stress that the parameterisations developed here fit the available experimental lifetime data. As such, they represent an upper limit on the Auger recombination rate or alternatively, a lower limit on the Auger lifetime. It is possible that with improved silicon growth technology and surface passivation techniques, higher lifetimes, and therefore lower rates of Auger recombination may be measured in the future.

Finally, throughout this work it has been assumed that the rate of radiative recombination can be quantified using the constant B=9.5x10^{-15}cm^{3}s^{-1}. In reality this is a simplification, as radiative recombination is also believed to be affected by Coulombic interactions [24]. The effect of this simplification is that any increase in the radiative recombination from the *ideal* rate given by Eq. (3.12), has actually been interpreted as Auger recombination. A more accurate determination of the doping and injection level dependence of radiative recombination would be required to more accurately assign the recombination events as either radiative or Auger. This may then result in a small adjustment to the new parameterisations for Auger recombination. What can be concluded is that the global rate of intrinsic recombination in silicon, $R_{intrinsic}$, can be expressed as

$$\begin{aligned} U_{intrinsic} &= U_{Auger} + U_{rad} \\ &= np\left(1.8x10^{-24} n_o^{\,0.65} + 6x10^{-25} p_o^{\,0.65} + 3x10^{-27}\Delta n^{0.8} + 9.5x10^{-15}\right), \end{aligned} \tag{3.21}$$

where the effect of the various enhancement processes for both radiative and Auger recombination are quantified by the term in brackets. Indeed, the fact that intrinsic recombination is a composite of two particle and three particle recombination processes may explain the origin of the fractional exponents in the bracketed term of Eq. (3.21). The terms can be expected to have an exponent between one and two depending on the relative proportion of two particle (radiative) and three particle (Auger) recombination events.

3.3.4 Estimate of the SRH Lifetime in Silicon

The effective lifetimes shown in Figures 3.7 and 3.8 can be used to estimate a lower bound for the SRH lifetime of the silicon substrates used in these experiments, where

$$\tau_{SRH} \geq \frac{1}{\frac{1}{\tau_{eff}} - \frac{1}{\tau_{\text{int}}}}. \tag{3.22}$$

Equation (3.21) was used to determine the intrinsic recombination rate, and therefore τ_{int}, at the injection level corresponding to the maximum τ_{eff} for each wafer in Table 3.1. The estimates for τ_{SRH} are plotted in Figure 3.12, for both *n*-type and *p*-type wafers. A simple expression that can be used to fit the τ_{SRH} data has been proposed by Kendall [89],

$$\tau_{SRH} = \frac{\tau_{\max}}{1 + \frac{C}{C_{ref}}}, \tag{3.23}$$

where C is the silicon doping concentration, τ_{max} is the low-injection SRH lifetime measured in lightly doped silicon and C_{ref} is an experimentally determined constant. As can be seen in Figure

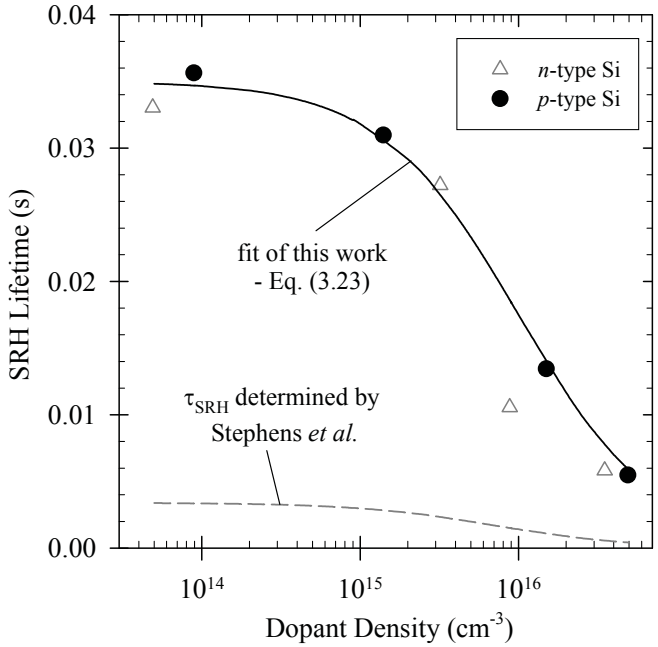


Figure 3.12. Values of the Shockley-Read-Hall lifetime for the silicon wafers in Table 3.1, based on the intrinsic recombination rate given by Eq. (3.21).

3.12, a reasonably good fit is obtained by using τ_{max} = 35ms and C_{ref} =1x10^{16}cm^{-3}. A similar parameterisation has been determined by Stephens *et al.*[89] for oxidised float-zone silicon wafers which had received only a forming gas anneal rather than an alneal. Stephens *et al.* used a much lower value for τ_{max} = 3.4ms, which as shown in Figure 3.12, results in significantly lower estimates for τ_{SRH}. The fit determined here will be used in Chapter 4 for estimating the lower limit for the surface recombination velocity of silicon substrates passivated with PECVD silicon nitride films.

3.3.5 Auger Recombination in Multicrystalline Silicon

Auger recombination is a fundamental property of the silicon material and therefore should not depend on the crystallographic orientation of the silicon etc. It should therefore be possible to observe the same Auger recombination rate in multicrystalline silicon as in float-zone silicon, as long as the surfaces can be sufficiently well passivated and the bulk lifetime kept high. While high effective lifetimes (~300μs) have been measured in specially gettered multicrystalline silicon material [90, 91], this is still considerably lower than the effective lifetimes of float-zone silicon of the same resistivity and certainly lower than the intrinsic limits estimated by Eq. (3.17). A clear determination of the Auger recombination rate in multicrystalline silicon therefore requires that the bulk and surface recombination rates be separated, by using wafers of different thickness for example (see Eq. (2.29)).

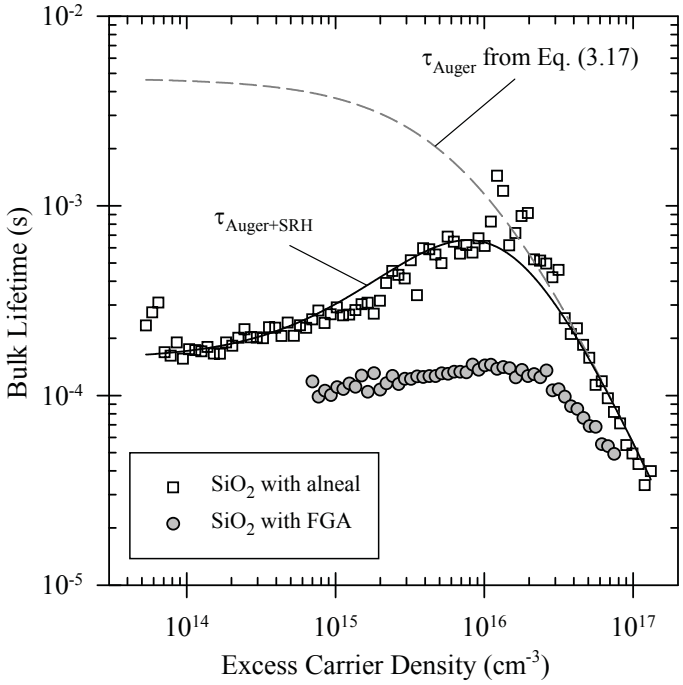


Figure 3.13. Bulk lifetime values for high quality, phosphorus gettered 1.5 Ωcm *p*-type multicrystalline silicon wafers determined from three wafers of different thickness. The lifetime limit from intrinsic recombination, based on Eq. (3.21), is included. The occurrence of Auger recombination in multicrystalline silicon is demonstrated, with the same rate as in single crystal silicon.

Three matched, high quality, 1.5Ωcm multicrystalline silicon wafers were phosphorus gettered and then etched using HF/HNO_3 solution to thicknesses of 120μm, 200μm and 430μm. The surfaces were passivated by a thermal oxidation in steam at 900°C for 2 hours, followed by an argon anneal at the same temperature and then a forming gas anneal (FGA) at 400°C for 20mins. After measuring the effective lifetime as a function of injection level, the samples were given an alneal at 400°C for 30mins and the effective lifetime re-measured. Lifetime measurements at low carrier densities were impeded for the FGA samples due to trapping effects [92]. The extracted bulk lifetimes are given in Figures 3.13, where it can be seen that the maximum effective lifetime increases from ≈150μs following a FGA, to ≈600μs at carrier densities of $10^{16}cm^{-3}$ after an alneal. At lower carrier densities, the bulk lifetime decreases to ≈200μs following a Shockley-Read-Hall dependence, while at higher carrier densities the bulk lifetime clearly decreases. The Auger lifetime predicted by Eq. (3.17) for 1.5Ωcm *p*-type silicon is included in Figure 3.13 and shows excellent agreement with the measured bulk lifetimes of these high quality multicrystalline silicon sample for carrier densities greater than $10^{16}cm^{-3}$. The occurrence of Auger recombination in multicrystalline silicon has therefore been confirmed and the rate appears to be the same as that found in single crystal silicon.

3.3.6 Conclusions

A new parameterisation for band-to-band Auger recombination in crystalline silicon at 300K has been proposed and validated with lifetime measurements. This parameterisation is a significant improvement over previous models, as it accurately fits the experimental lifetime data for arbitrary injection level and arbitrary dopant density, for both *n*-type and *p*-type dopants. It has been confirmed that Auger recombination is enhanced above the traditional free-particle rate at both low injection and high injection conditions. Furthermore, it has been shown that the rate of enhancement is less for highly injected intrinsic silicon compared to lowly injected doped silicon, which is consistent with the theory of Coulomb enhanced Auger recombination. Variations on the parameterisation, such as requiring the rate of Auger recombination to converge to the traditional free-particle rate for carrier densities above the exitonic Mott density have been discussed. Values for the rate of SRH recombination in high purity silicon samples as a function of the silicon dopant density have also been determined. The presence of Auger recombination in high quality multicrystalline silicon samples has, as expected, been confirmed to be the same in single crystal silicon and multicrystalline silicon. An application for the new parameterisation developed here for the rate of intrinsic recombination is to reassess the limiting efficiency of crystalline silicon solar cells, which is discussed in the next section.

3.4 Limiting Efficiency of Silicon Solar Cells

The limiting efficiency of crystalline silicon solar cells is of fundamental interest in photovoltaic research. It is determined by intrinsic recombination processes occurring within the semiconductor material, specifically radiative recombination and Auger recombination. Shockley and Queisser [93] used the principle of detailed balance to determine the limiting efficiency due to radiative recombination, where a maximum efficiency of 30.8% was obtained for a single junction silicon cell under one sun illumination [94]. It was subsequently shown by Green [95] and Tiedje *et al.*[22] that Auger recombination places a more severe intrinsic bound on the one sun operation. Using the traditional free-particle model for Auger recombination (see Eq. (2.4)), a peak energy conversion efficiency of 29.8% was determined for a 100μm cell with an isotropic response [22].

As discussed in the previous section, excitonic effects lead to a significant enhancement of the Auger recombination rate compared to the free-particle model. This is particularly true at the dopant densities ($<10^{17}$ cm^{-3}) [28, 32, 60] and injection levels [31] which are typical in high

efficiency silicon solar cells. Green updated his calculations to incorporate an injection level dependence for the Coulomb-enhanced Auger recombination rate for *highly injected, high resistivity* silicon (see equation 5.18 of ref [25]). This resulted in a peak efficiency of 28.8% for an 80μm thick cell with an isotropic response and a Lambertian reflector [25, 96]. The effect of dopant density or dopant type on the limiting efficiency could not be determined however, as a parameterisation for the Coulomb-enhanced Auger recombination rate at *arbitrary* injection level did not exist. The injection level dependence is important because for resistivities less than 10Ωcm, the cell will be in intermediate or even low injection conditions at maximum power-point.

In this section, new calculations are presented for the limiting efficiency of silicon solar cells based on the general parameterisation for the Coulomb-enhanced Auger recombination rate developed in the previous section (Eq. (3.17)). The effect of varying the dopant density and dopant type has been investigated as a function of cell thickness. Losses due to radiative recombination are included based on the experimentally measured value for the radiative recombination co-efficient, B=9.5x10^{-15}cm^{3}s^{-1} [24], along with a three-dimensional ray tracing model that determines the rate with which the internally emitted photons are reabsorbed or recycled.

3.4.1 Solar Cell I-V Characteristics

The current-voltage characteristics of a solar cell limited by intrinsic recombination can be expressed as

$$J = J_L - qWU_{rec} \tag{3.24}$$

where J_L is the light-generated current density, W is the cell thickness and U_{rec} is the intrinsic recombination rate. Following the approach of Green [95, 96], the "narrow base" assumption implies that the electron and hole quasi-Fermi levels are constant within the base of the device:

$$np = (n_o + \Delta n)(p_o + \Delta n) = {n_i}^2 \exp\left(\frac{qV}{kT}\right) \tag{3.25}$$

where n and p are the free electron and hole concentrations, n_o and p_o are the equilibrium concentrations of electrons and holes and Δn is the density of excess electrons, which equals the density of excess holes. Δn can therefore be determined as a function of n_o, p_o and the operating voltage by solving Eq. (3.25).

Equation (3.17) and Eq. (2.2) are used for the Coulomb-enhanced Auger recombination rate and the radiative recombination rate respectively. While the excess energy associated with Auger recombination is released as phonons, radiative recombination results in the emission of

photons that can be reabsorbed elsewhere in the silicon base. It is therefore necessary to modify Eq. (2.2) with the photon recycling rate (P_{RR}), which is the fraction of photons emitted by radiative recombination which are reabsorbed/recycled. Substituting Eq. (3.17), Eq. (2.2) and Eq. (3.25) into Eq. (3.24) and including the P_{RR} gives the current-voltage characteristic for a crystalline silicon solar cell limited by CE intrinsic recombination processes:

$$J = J_L - qWn_i^2 \exp\left(\frac{qV}{kT}\right) * \left\{1.8*10^{-24} n_o^{0.65} + 6*10^{-25} p_o^{0.65} + \right. \tag{3.26}$$

$$\left. 3*10^{-27}\left[0.5\left(\sqrt{(n_o + p_o)^2 + 4n_i^2 \exp\left(\frac{qV}{kT}\right)} - (n_o + p_o)\right)\right]^{0.8} + (1 - P_{RR}) * 9.5*10^{-15}\right\}.$$

The light-generated current density, J_L, was determined assuming a Lambertian light trapping scheme, which increases the mean path length for a light ray inside the cell to $4n^2W$, where n is the refractive index [22]. The AM1.5G spectrum at 25°C was used, normalized to an illumination intensity of $0.1W/cm^2$. Free carrier absorption has been included based on the expressions given by Green [25]. A Monte Carlo computer model was used to determine the P_{RR}, with the model development and calculations performed by Dr P. Campbell of UNSW. In this model, a Lambertian light trapping scheme was implemented using a lossless Lambertian reflector. The angular distribution about the cell surface normal of isotropic radiative emission was modeled according to sinθ; in contrast, each reflection event from the Lambertian reflector followed a sinθ*cosθ distribution to also account for incident beam energy. The effect of partial reflection at the front air/silicon interface was also included. Radiative emission was spectrally determined from the van Roosbroeck-Shockley relation, which can be used in this study at the relatively low light levels encountered. Calculated values for the P_{RR} are given in Figure 3.14. With a Lambertian reflector, it can be seen that the P_{RR} is strongly dependent on cell thickness, increasing from 0.085 for a 1μm thick silicon base to 0.995 for a 10mm thick silicon base. An equivalent interpretation is that the losses from radiative recombination are negligible for a thick cell, where most of the emitted photons are reabsorbed, while for a thin cell, the losses from radiative recombination can be significant as the recycling rate is low.

Computationally, an initial solution for the limiting efficiency was obtained from Eq. (3.26) by neglecting free carrier absorption and photon recycling, allowing Δn near the maximum power point to be estimated. This Δn was then used to evaluate the free carrier absorption coefficients and the photon recycling rate, and the solution iterated until self-consistent.

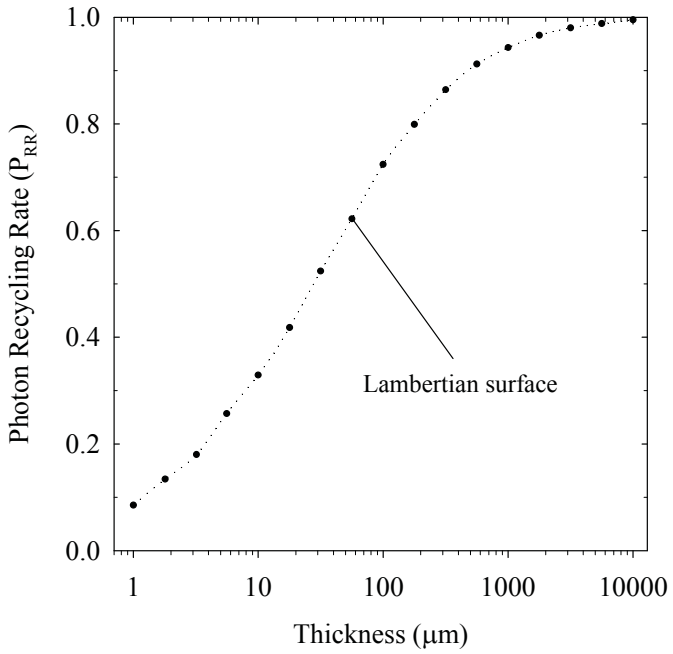


Figure 3.14. Calculated values for the photon recycling rate (P_{RR}) in silicon as a function of cell thickness. The photon recycling rate is strongly dependent on the cell thickness for a Lambertian reflector because trapped photons may be scattered into the escape cone.

3.4.2 Effect of Coulomb-Enhanced Auger Recombination

Figure 3.15 shows the limiting efficiency due to different intrinsic recombination processes for a 1Ωcm *p*-type silicon solar cell. These calculations are for a temperature of 25°C and have used an intrinsic carrier concentration in silicon of $n_i = 8.65 \times 10^9$ cm^{-3} and a thermal voltage of kT/q =25.69mV [25]. For the radiative recombination curve, the experimentally determined value for the radiative recombination coefficient [24] of $B = 9.5 \times 10^{-15}$cm^{3}s^{-1} has been used, where the curve with no photon recycling is a lower bound for the limiting efficiency due to radiative recombination alone. For the free-particle Auger recombination curve, Auger recombination coefficients [30] of $C_n = 2.8 \times 10^{-31}$cm^{6}s^{-1} and $C_p = 0.99 \times 10^{-31}$cm^{6}s^{-1} have been used.

It can clearly be seen from Figure 3.15 that, independent of cell thickness, CE Auger recombination imposes a more severe bound on the limiting solar cell efficiency than either free-particle Auger recombination or radiative recombination, even in the absence of photon recycling. The peak conversion efficiency imposed by CE Auger recombination alone (no radiative recombination) is 28.7% for a cell thickness of 55μm. This is a 1.8% lower than the limiting efficiency imposed by free-particle Auger recombination alone which would be 30.5%, and 1.1% lower than the limiting efficiency imposed by radiative recombination alone (no photon recycling) which would be 29.8%. Including photon recycling for a cell limited by

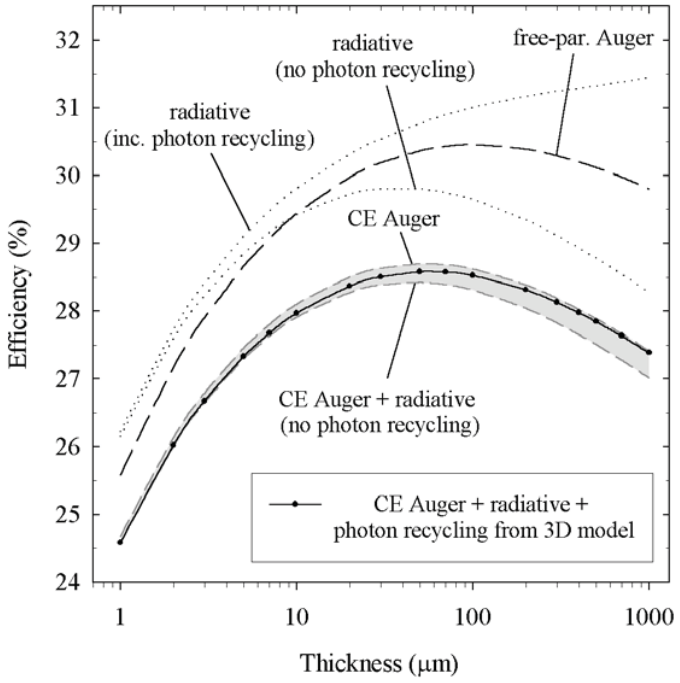


Figure 3.15. The limiting efficiency, as a function of cell thickness, for a 1Ωcm *p*-type silicon solar cell under one sun illumination at 25°C. The different curves show cells constrained by radiative recombination with (according to Fig. 3.14) and without photon recycling, free-particle Auger recombination and Coulomb-enhanced (CE) Auger recombination. Independent of cell thickness, CE Auger recombination imposes the most severe bound on the efficiency limit. The shaded region gives the upper and lower bound for the limiting efficiency including both CE Auger recombination and radiative recombination depending on the photon recycling rate, while the solid line gives the limiting efficiency including photon recycling effects.

radiative recombination alone increases the limiting efficiency, particularly for thicker cells, as shown in Figure 3.15. Indeed, the inclusion of photon recycling results in free-particle Auger recombination being more dominant than radiative recombination, as was originally noted by Green and Tiedje *et al.*. Importantly, they concluded this because they used a significantly lower value for the radiative recombination coefficient, $B=2\times10^{-15}cm^3s^{-1}$ [22, 23], which was theoretically determined from detailed balance considerations, rather than by correctly including the effects of photon recycling. Using $B=2\times10^{-15}cm^3s^{-1}$ is equivalent to assuming a photon recycling rate of $P_{RR}=0.7895$, independent of cell thickness.

A lower bound to the limiting efficiency for a 1Ωcm *p*-type cell is calculated by including both CE Auger recombination and radiative recombination with no photon recycling. An upper bound has 100% photon recycling, which is just the curve for CE Auger recombination alone. The shaded section in Figure 3.15 therefore gives the limiting efficiency as a function of cell

thickness, depending on the photon recycling rate. Including the calculations in Figure 3.14 for the photon recycling rate results in the solid black curve, which as expected, goes from the lower bound for thin cells where the photon recycling is poor to the upper bound for thick cells where the photon recycling rate is high. Consequently, the peak efficiency for a 1Ωcm p-type silicon solar cell, including CE Auger recombination, radiative recombination and photon recycling is 28.6% for a 55μm thick cell.

3.4.3 Effect of Dopant Density and Dopant Type

It was shown in section 3.3 that the rate of CE Auger recombination in crystalline silicon depends on the dopant density and dopant type. The Auger recombination rate is greater in lowly injected *n*-type silicon compared to *p*-type silicon for example. For lightly doped silicon under high injection conditions, the recombination rate is the same in *n*-type and *p*-type silicon, as the Coulombic interactions of the excess carriers dominate any effects from the equilibrium carrier densities. It is therefore expected that the limiting solar cell efficiency will also depend slightly on the dopant density and dopant type, and that the limiting efficiency should peak when the intrinsic recombination rate for electrons and holes are equal. That is, for very lightly doped silicon.

Figure 3.16 shows contour plots for the effect of the dopant density, or equivalently the base resistivity, and cell thickness on the limiting cell efficiency for both *p*-type and *n*-type silicon. As expected, the limiting efficiency decreases as the base resistivity decreases. Furthermore, solar cells with an *n*-type base show slightly lower limiting efficiency than solar cells with a *p*-type base, although the differences become negligible for high resistivity silicon. The peak conversion efficiency is for a solar cell made from high resistivity material and would be 29.05% for a cell thickness of 90μm. This is in good agreement with the results of Green [25, 96], where the slightly higher peak efficiency found here is because the parameterization of Eq. (3.17) is slightly more conservative (determines a lower recombination rate) than that used by Green for highly injected silicon. Furthermore, the difference in the peak limiting efficiency for cells with a base resistivity greater than 100Ωcm is less than 0.04%. Figure 3.16 also shows that the optimum cell thickness corresponding to the peak limiting efficiency reduces as the base resistivity decreases. For example, the peak efficiency for a high resistivity *p*-type solar cell reduces from 29.05% at 90μm to 28.6% at 55μm for 1Ωcm *p*-type silicon, then down to 27.1% at 30μm for 0.1Ωcm *p*-type silicon.

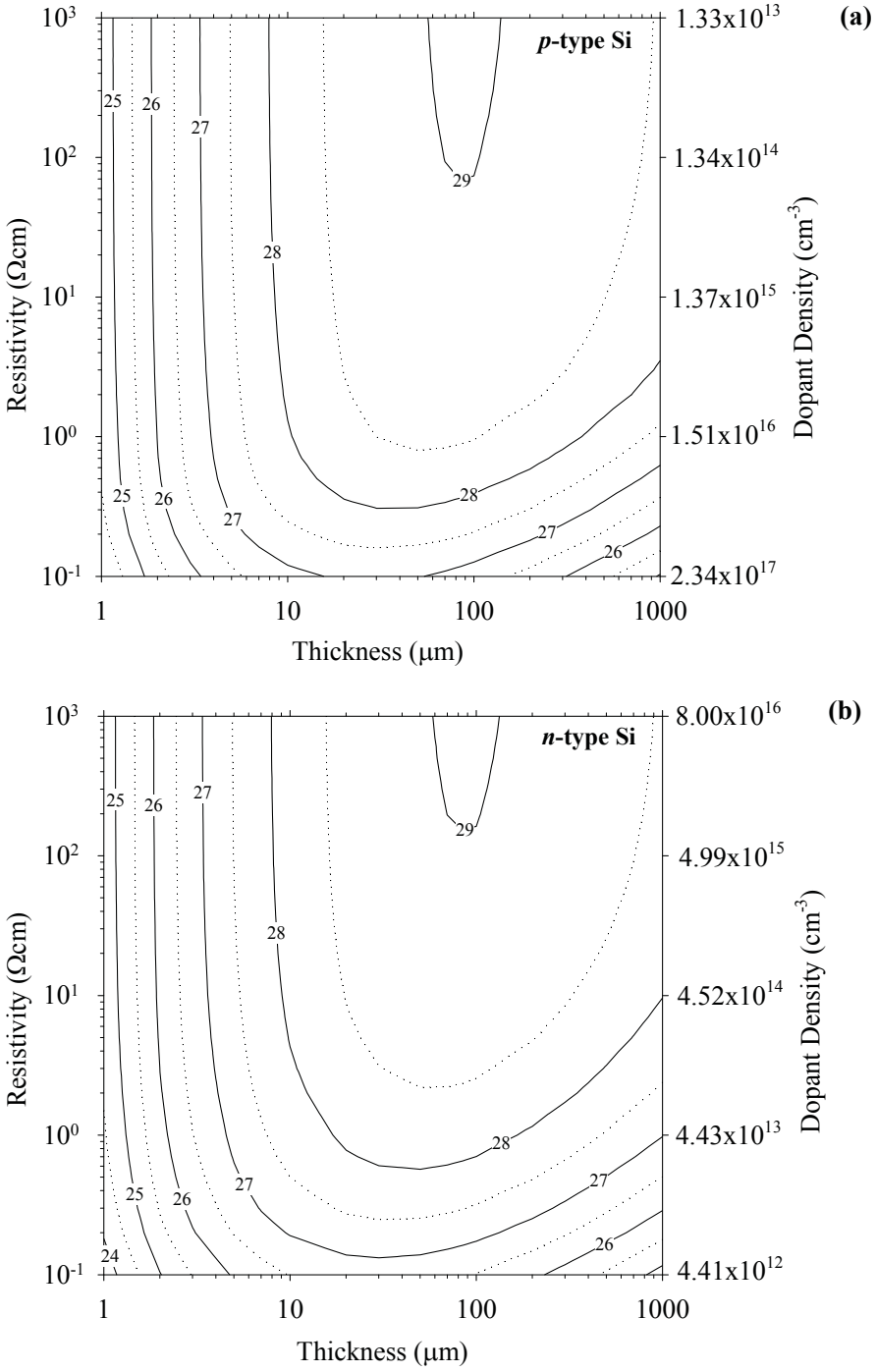


Figure 3.16. Effect of the base resistivity and cell thickness on the limiting efficiency of solar cells constrained by CE Auger recombination and radiative recombination with photon recycling for: (a) *p*-type silicon and (b) *n*-type silicon. In the absence of series resistance effects, more heavily doped cells and *n*-type cells have slightly lower limiting efficiencies. The optimum cell thickness decreases for more heavily doped silicon.

The effect of cell thickness on the short-circuit current density, open-circuit voltage and fill-factor is shown in Figure 3.17 for both *p*-type and *n*-type silicon. As the cell thickness increases, the absorption also increases resulting in higher J_{sc}. The J_{sc} is essentially independent of the resistivity, except for thick heavily doped substrates were free-carrier absorption results in a small loss of long-wavelength photons that could otherwise contribute to the current. As expected, the V_{oc} decreases with increasing cell thickness, where, for a given illumination level, a thicker cell will have a lower excess carrier density and therefore a lower V_{oc}. As the resistivity decreases, the Coulomb-enhancement of the intrinsic recombination rate increases. This results in greater recombination losses at open-circuit conditions for more heavily doped material and therefore a lower V_{oc} for more heavily doped material. The effect of free-carrier absorption on the V_{oc} is negligible and the dependency of the V_{oc} on the cell thickness and resistivity is an outcome of the doping and injection level dependence for the CE Auger recombination rate given in Eq. (3.17). Similarly, the fill-factor is strongly effected by the doping and injection level dependence of Eq. (3.17) and decreases as the cell thickness increases or the resistivity decreases. Again, free-carrier absorption has a negligible effect on the fill-factor. The limiting efficiency therefore initially increases with cell thickness due to greater absorption and therefore high J_{sc}. The losses in V_{oc} and fill-factor due to recombination also increase however, eventually outweighing the higher J_{sc} and resulting in a decreasing limiting efficiency. The reducing optimum thickness with silicon resistivity for the conversion efficiency is therefore an outcome of Eq. (3.17).

3.4.4 Effect of Emitter and Surface Recombination

Real solar cells have surfaces and need highly doped emitters to form a pn junction that facilitates the flow of current to the metal contacts. These additional recombination processes can be included in Eq. (3.24) to give a current-voltage characteristic of

$$J = J_L - qWU_{rec} - J_{oE}\exp\left(\frac{qV}{kT}\right), \tag{3.27}$$

where recombination due to the heavily doped emitter regions is characterised by a saturation current density, J_{oE}, and an exponential dependence on the voltage with an ideality factor of unity. An extrinsic surface recombination component can, following Green [96], also be included in a mathematically identical manner by replacing J_{oE} with a J_{os}.

The effect of emitter or surface recombination is included in Figure 3.18 for *p*-type silicon of three different resistivities. The J_{oE} value has been adjusted so that the open-circuit voltage of a 300μm thick, 1Ωcm *p*-type cell is 720mV and 640mV respectively. The same J_{oE} value was then used for cells of different thickness and dopant density. This approach is

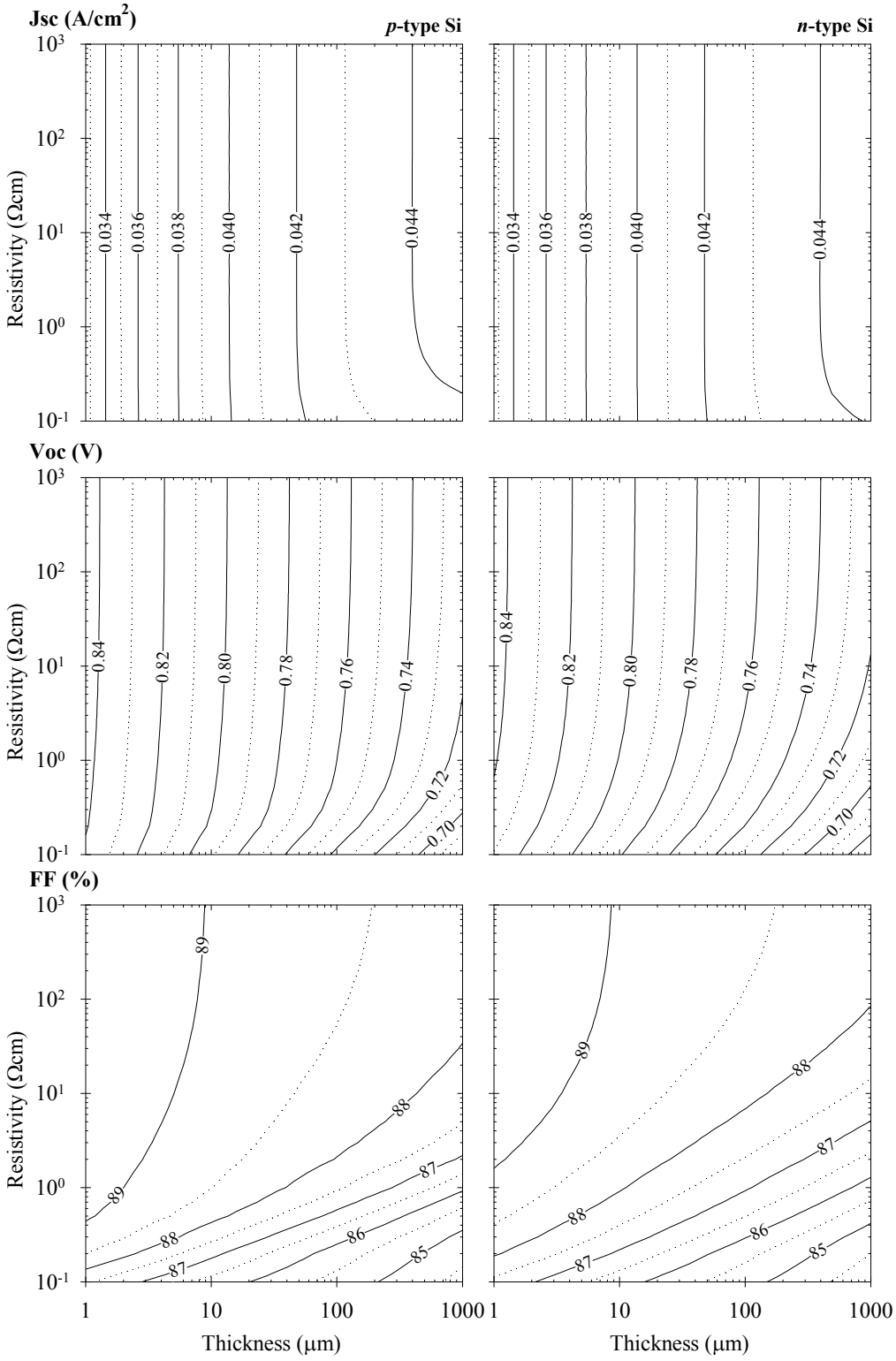


Figure 3.17. Effect of the base resistivity and cell thickness on the short-circuit current density, open-circuit voltage and fill-factor of solar cells constrained by CE Auger recombination and radiative recombination with photon recycling for: (a) *p*-type silicon and (b) *n*-type silicon.

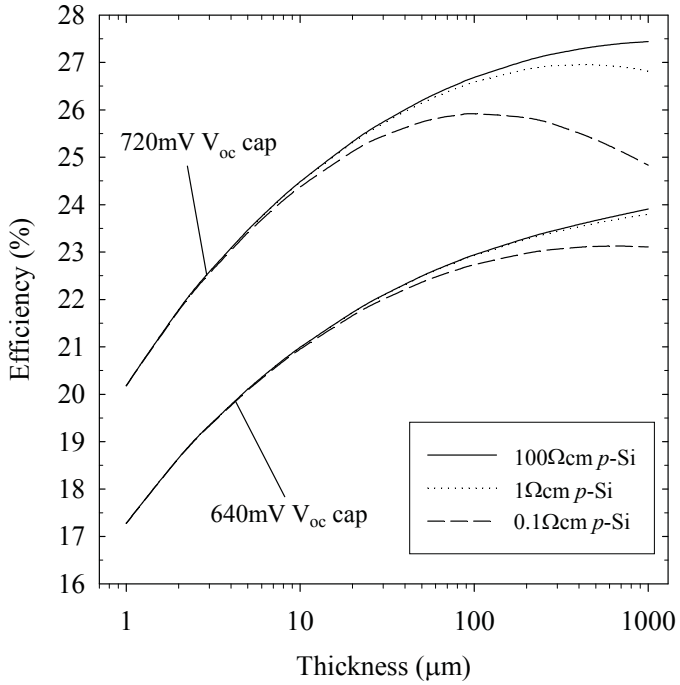


Figure 3.18. Effect of emitter or surface recombination on the limiting efficiency of *p*-type solar cells constrained by CE Auger recombination and radiative recombination with photon recycling. Emitter or surface recombination reduces the limiting efficiency and increases the optimum cell thickness. For 1Ωcm *p*-type silicon, where emitter recombination limits the open-circuit voltage to 720mV, the conversion efficiency shows a maximum of 27.0% for cells in the range of 300-500μm thick.

justified, as using a J_{oE} term for emitter recombination is not dependent on the base dopant density. Alternatively, the use of a J_{os} term for surface recombination is consistent with using a floating emitter for surface passivation. For the 720mV curve, a J_{oE} value of 17.8fA/cm^2 was used. This corresponds to a well-passivated, homogeneously doped n^+ emitter of ~110Ω/□ (see Chapter 5), and so the 720mV curves can also be interpreted as modeling the limiting efficiency of n^+p solar cells with an emitter sheet resistance of 110Ω/□.

Consistent with the results of Green [96], Figure 3.18 shows that emitter or surface recombination lowers the achievable efficiency, especially for thin cells. Comparison with Figure 3.16(a) shows that, for a given dopant density, surface recombination shifts the optimum cell thickness to a higher value. For example, from the 720mV curves (which corresponds with the highest open-circuit voltage experimentally demonstrated to date [97]), the peak in conversion efficiency for a high resistivity (100Ωcm) *p*-type cell occurs for a cell thickness in excess of 1mm, as was also concluded by Green [96]. Interestingly, for a 1Ωcm *p*-type cell, the peak efficiency of 27.0% occurs for an optimum cell thickness of 300-500μm, which is consistent with the thickness of the highest efficiency devices fabricated to date [98]. While for

more heavily doped silicon (0.1Ωcm), the optimum thickness is around 100μm. The higher rates of recombination for the 640mV curves pushes the optimum cell thickness out to even higher values.

3.4.5 Effect of Additional Bulk Recombination

In practical silicon solar cells Shockley-Read-Hall bulk recombination will also occur. Additional bulk recombination processes can be included in Eq. (3.27) to give a current-voltage characteristic of

$$J = J_L - qWU_{rec} - J_{oE}\exp\left(\frac{qV}{kT}\right) - qWU_{SRH} \tag{3.28}$$
$$= J_L - qWU_{rec} - J_{oE}\exp\left(\frac{qV}{kT}\right) - \frac{qW}{2\tau_{bulk}}\left(\sqrt{(n_o + p_o)^2 + 4{n_i}^2\exp\left(\frac{qV}{kT}\right)} - (n_o + p_o)\right)$$

where τ_{bulk} is the SRH bulk recombination lifetime.

Figure 3.19 shows the effect of addition SRH recombination on the cell efficiency for 1Ωcm *p*-type silicon with and without emitter recombination. For simplicity, a constant τ_{bulk} has been used. As expected, additional SRH recombination lowers the limiting efficiency for all cell thickness. It also lowers the optimum cell thickness, which is the opposite effect of emitter or surface recombination, which increased the optimum cell thickness. The optimum cell thickness for real solar cells, where surface, emitter and bulk SRH recombination are all significant, is therefore determined by the relative amounts of surface/emitter recombination and bulk SRH recombination. For example, Figure 3.19(b) shows that reducing the cell thickness below the industry standard of ~300μm will actually result in a reduced cell efficiency unless the surface passivation of the solar cell is very good. There is therefore a strong requirement for an effective, industrially feasible surface passivation technology.

3.4.6 Comparison with Experimental Devices

Calculated values for the limiting efficiency of silicon solar cells based on Eq. (3.28) are compared with the highest efficiency experimental cells in Table 3.2. The record 24.7% efficient PERL cell of Zhao *et al.* [98] and the 21.5% efficient thin silicon (~47μm) PERL cell of Wang *et al.* [99] are considered. Calculated values for the J_{sc}, V_{oc}, fill-factor and efficiency are given for three scenarios: (1) only intrinsic recombination occurs; (2) only intrinsic recombination occurs but with additional optical losses to lower the J_{sc} to the experimentally measured value; and (3) optical losses lower the J_{sc} and additional emitter/surface recombination lowers the V_{oc} to the experimentally measured values.

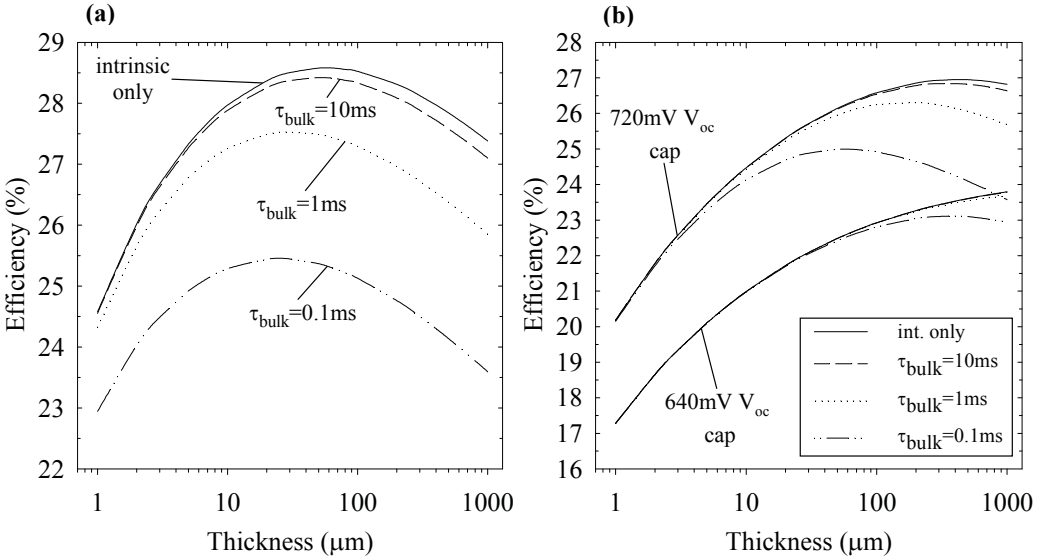


Figure 3.19. Effect of additional SRH bulk recombination on the limiting efficiency of 1Ωcm *p*-type solar cells: (a) without and (b) with surface/emitter recombination. SRH bulk recombination reduces the conversion efficiency and lowers the optimum cell thickness.

For the 24.7% PERL cell, it can be seen that the calculated limiting efficiency for this resistivity and cell thickness is 27.9% due to intrinsic recombination alone. The measured J_{sc} of 42.2mA/cm^2 is very close to the maximum calculated value of 44.0mA/cm^2, while including the J_{sc} losses reduces the peak conversion efficiency to 26.7%. Comparing the calculated and measured V_{oc} and fill-factor shows that mall improvements to the V_{oc} and in particular the fill-factor seem possible for increasing the experimental cell efficiency to above 25%. For example, a fill-factor of ~85% appears to be feasible for a 1Ωcm *p*-type cell when the J_{sc} and V_{oc} are limited to the same values as the 24.7% PERL cell (the scenario (3) calculation) in comparison to the 82.8% measured for the cell. Indeed, fill-factors greater than 84% have been reported in the literature [100]. Similarly, V_{oc}'s of ~715mV have been reported for textured silicon cells [101]. For the thin 21.5% PERL cell, improvements to the J_{sc}, V_{oc} and fill-factor all appear possible compared to the limiting case. Importantly, even when the J_{sc} and V_{oc} are limited to match the experimentally measured values (scenario (3)), the calculated efficiencies for both cells are close to, but greater than the measured efficiencies. This provides additional verification that the parameterisation developed for the intrinsic recombination rate (Eq. (3.17)) is valid, where the differences between the measured and calculated efficiencies can be attributed to resistance effects within the cell and non-ideal diode behaviour due to an injection level dependent surface recombination [102].

Table 3.2. Comparison of the best experimental silicon solar cells with calculated values for the J_{sc}, V_{oc}, fill-factor and efficiency. Scenario (1) includes only intrinsic recombination from Eq. (3.26), while scenario (2) includes additional reflectance losses to lower the J_{sc} and scenario (3) includes additional emitter/surface recombination to lower the V_{oc}.

Cell 1: 24.7% PERL cell of Zhao *et al.* [98]

Width = 450μm; Resistivity = 1.0Ωcm *p*-type $\Rightarrow N_A = 1.5 \times 10^{16} cm^{-3}$

	J_{sc} (mA/cm^2)	V_{oc} (mV)	FF (%)	η (%)
Experimentally measured	42.2	706	82.8	24.7
Calculated – scenario (1)	44.0	731	86.7	27.9
– scenario (2)	42.2	730	86.6	26.7
– scenario (3)	42.2	706	85.1	25.3

Cell 2: 21.5% PERL cell of Wang *et al.* [99]

Width = 47μm; Resistivity = 1Ωcm *p*-type $\Rightarrow N_A = 1.5 \times 10^{16} cm^{-3}$

	J_{sc} (mA/cm^2)	V_{oc} (mV)	FF (%)	η (%)
Experimentally measured	37.9	698.5	81.1	21.5
Calculated – scenario (1)	42.0	774	87.9	28.6
– scenario (2)	37.9	772	87.9	25.7
– scenario (3)	37.9	698.5	84.7	22.4

3.4.7 Conclusions

The intrinsic limiting efficiency of crystalline silicon solar cells has been determined as a function of cell thickness, including photon recycling effects. It has been shown that Coulomb enhanced Auger recombination places the most severe intrinsic bound on the limiting efficiency under one sun illumination, while losses due to radiative recombination are most significant for very thin cells (~1μm), but are almost negligible for thick cells (~1mm) due to photon recycling. A maximum conversion efficiency of 29.05% has been calculated for a cell thickness of 90μm for solar cells made from high resistivity silicon. The peak limiting efficiency decreases as the base resistivity decreases and is slightly less for *n*-type cells compared to *p*-type cells. The optimum cell thickness also decreases as the base resistivity decreases.

The effect of emitter or surface recombination is to reduce the conversion efficiency below the intrinsic limit, particularly for thin cells, and to increase the optimum cell thickness. For 1Ωcm *p*-type silicon, the maximum efficiency reduces from 28.6% for a 55μm thick cell in the absence of surface recombination, down to 27.0% for a thickness in the range 300-500μm when surface recombination limits the open-circuit voltage to 720mV. Additional SRH bulk recombination also reduces the conversion efficiency, but decreases the optimum cell thickness.

The optimum cell thickness for real solar cells is therefore a trade-off of the relative amounts of surface/emitter recombination and SRH bulk recombination. The commercial drive towards thinner substrates for cost reduction reasons will result in lower conversion efficiencies unless the surface passivation of the cells is very good.

3.5 Chapter Summary

The limits imposed by intrinsic recombination, specifically Coulomb-enhanced Auger recombination and radiative recombination, on the lifetime in silicon have been investigated in this chapter. Record values have been measured for the effective lifetime in high quality *n*-type and *p*-type silicon. Importantly, the silicon wafers used where commercially sourced and had undergone significant high temperature processing, clearly indicating that very high effective lifetimes can be preserved by carefully optimising the processing conditions. A new parameterisation for band-to-band Auger recombination in crystalline silicon at 300K has been proposed. This new parameterisation accurately fits the experimental lifetime data, from the literature and from this study, for arbitrary injection level and arbitrary dopant density, for both *n*-type and *p*-type dopants. Variations of the new parameterisation are discussed and the presence of Auger recombination in high quality multicrystalline silicon samples has been confirmed. The efficiency of crystalline silicon solar cells limited by intrinsic recombination has been re-evaluated using the newly developed parameterisation, where the effects of photon recycling have been included. The roles of dopant type, dopant density and cell thickness in determining the limiting efficiency have been investigated and compared to the best experimental devices.

Real solar cells have surfaces, which represent an additional source of recombination. A novel method for reducing the surface recombination is the low temperature deposition of PECVD SiN. This is the topic of the next chapter, where it is shown that optimised *stoichiometric* SiN films (rather than silicon rich) can be used to obtain very low surface recombination rates. In addition, they show no absorption in the UV portion of the solar spectrum and can be patterned using standard photolithographic techniques. Extensive measurements of the surface recombination rate for silicon surfaces passivated with thermally grown silicon oxide are included for comparison.

CHAPTER 4

Surface Recombination of *p*-type and *n*-type Silicon Passivated with PECVD Silicon Nitride

4.1 Introduction

Surface recombination effects are becoming progressively more important as semiconductor device dimensions are reduced. This is especially true for photovoltaic cells, where there is overriding commercial pressure towards thinner substrates to obtain lower costs, accompanied by improved wafer quality. Historically, silicon dioxide films, thermally grown into the silicon surface at high temperatures, have been the preferred means used for surface passivation. Indeed, the use of silicon oxide for passivating non-diffused surfaces resulted in the first solar cells with efficiencies >21% [100, 103].

Within the context of solar cells, surface recombination at the silicon-silicon oxide interface has been extensively studied [37, 61, 89, 104]. Very low surface recombination velocities can be obtained, particularly when the oxide is alnealed, as confirmed in section 3.2.

The high temperatures required for thermal oxidation result in a number of potential problems however, including:

- Thermal degradation of the bulk of the material, especially for lower quality substrates such as multicrystalline silicon.
- Risk of contaminating the bulk material by the diffusion of unwanted impurities.
- Restrictions to the fabrication sequence, as metallisation must occur after the oxidation steps and the drive-in of dopants.
- Potentially higher costs due to long processing times and high thermal budgets.

Various low temperature, high throughput passivation schemes using amorphous films based on hydrogenated silicon compounds have been studied as an alternative to thermal silicon oxide, particularly for solar cell applications. Significant reductions in the effective surface recombination velocity (S_{eff}) at the silicon interface have been reported when passivated with amorphous silicon [105, 106], amorphous silicon oxide [107, 108], amorphous silicon nitride [107-111] and amorphous silicon carbide [112]. The most extensively studied films are amorphous, hydrogenated silicon nitride ($Si_xN_y:H_z$), hereafter referred to as SiN films. These films are typically deposited by plasma enhanced chemical vapour deposition (PECVD) at low temperature (≤ 400°C) using silane gas and other reactant gases such as ammonia or nitrogen. Lauinger *et al.* [113, 114] have shown that the quality of the surface passivation obtained for 1.5Ωcm *p*-type silicon is strongly affected by the deposition parameters used, as well as by the mode of PECVD deposition. They concluded that films fabricated using either remote or high-frequency direct PECVD result in a lower surface recombination velocity than films prepared using low-frequency direct PECVD.

Lauinger *et al.* also showed there is a clear correlation between the refractive index of the SiN films and their ability to passivate the silicon surface. They demonstrated that the surface passivation is maximized when SiN films with a refractive index greater than 2.3 were used, that is silicon-rich SiN films. The fact that these SiN films are silicon rich brings about several issues which limits their applicability to solar cells [114]:

1. Fabricating silicon rich SiN films requires pure silane gas, which is extremely toxic, flammable and dangerous.

2. The films show a considerable absorption in the ultra-violet range of the solar spectrum, leading to a reduction of the short-circuit current by about 1mA/cm^2.

3. The etch rates of the films are extremely low, hindering the local opening of the SiN by means of patterning and chemical etching.

An alternative to using pure silane gas is to use dilute silane gas (diluted in an inert gas such as argon or nitrogen) which does not spontaneously combust when exposed to air, and can be handled more safely, particularly in an industrial environment. A systematic study of the recombination properties of PECVD SiN films fabricated using dilute silane gas is presented in this chapter. By optimizing the deposition parameters of the PECVD process, it is shown that excellent surface passivation can be achieved using *stoichiometric* SiN films rather than silicon rich SiN films. A brief characterization of these stoichiometric SiN films is also presented, where it is demonstrated that apart form their excellent passivation, they also show no absorption in the UV range of the solar spectrum and that they can be easily patterned using photolithography and wet chemical etching.

4.2 Optimisation of the PECVD Deposition Parameters

4.2.1 Process Variables and Experimental Details

Symmetrical SiN/Si/SiN lifetime test structures were fabricated to optimise the surface passivation quality of the SiN films. Double-side polished, 400μm thick, 1Ωcm *p*-type float-zone (FZ) wafers where used for the silicon substrates, as substrates of this type and resistivity are used in the highest efficiency solar cells [98]. All the silicon substrates where given an RCA clean prior to SiN deposition, including a final etch in dilute HF to remove any oxide that formed during the RCA clean. The SiN films where prepared by direct PECVD using an Oxford Plasmalab 80+ system. The process gases used were ammonia (NH_3) and a dilute silane/nitrogen mixture (4.5% SiH_4, 95.5% N_2).

Figure 4.1 shows a schematic diagram of the parallel plate PECVD reactor. The silicon substrate is placed on a heated lower electrode. The chamber is then closed and evacuated to a pressure of 10mTorr. The process gases are mixed and injected into the reactor through a 'showerhead' upper electrode at the desired flow rates. Gas is continually pumped out of the chamber so that a constant process pressure is maintained inside the reactor during the deposition. An oscillating RF field is applied between the upper and lower electrode to 'excite' the plasma, and SiN is deposited from the ionized gas species. A high excitation frequency (13.56MHz) is used to minimise the plasma damage of the silicon surface during the deposition. The process variables are therefore:

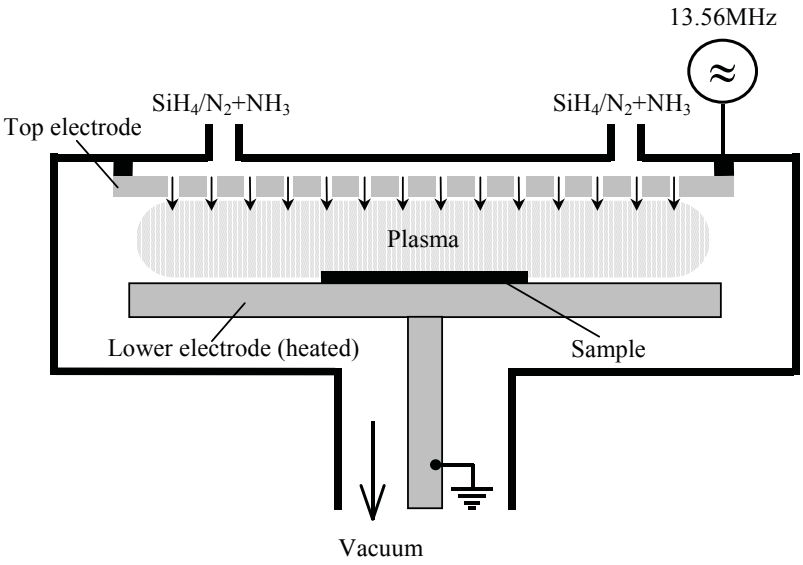


Figure 4.1. Schematic diagram of the parallel-plate PECVD reactor. The sample is placed on the lower, grounded electrode and the gases injected through the powered 'showerhead' top electrode.

- The deposition temperature – varied from 250°C to 400°C, where 400°C is the maximum possible for the system used.
- The dilute silane to ammonia gas flow ratio – varied from 4 to 20.
- The total gas flow rate – varied from 150sccm to 1100sccm.
- The process pressure – varied from 0.18 Torr to 1 Torr.
- The process power – varied from 40W to 175W.

The process variables were varied in a fractional factorial design that allows the main effects to be investigated and some, but not all, of the interactions. The use of a fractional design greatly reduces the number of samples required while still allowing all the main effects to be investigated. The remaining process variable is the deposition time, which determines the thickness of the SiN films. A time of 120 seconds was used for these optimisation experiments. This corresponds to 60-80nm of SiN depending on the values used for the other process variables, which is the approximate thickness required for a single layer anti-reflection coating [115].

The maximum effective lifetime was measured for each sample, which occurred at an injection level of approximately $10^{15}cm^{-3}$ for all the samples. As the bulk lifetime of each sample is equivalent, variations in the effective lifetime are due to variations in the surface

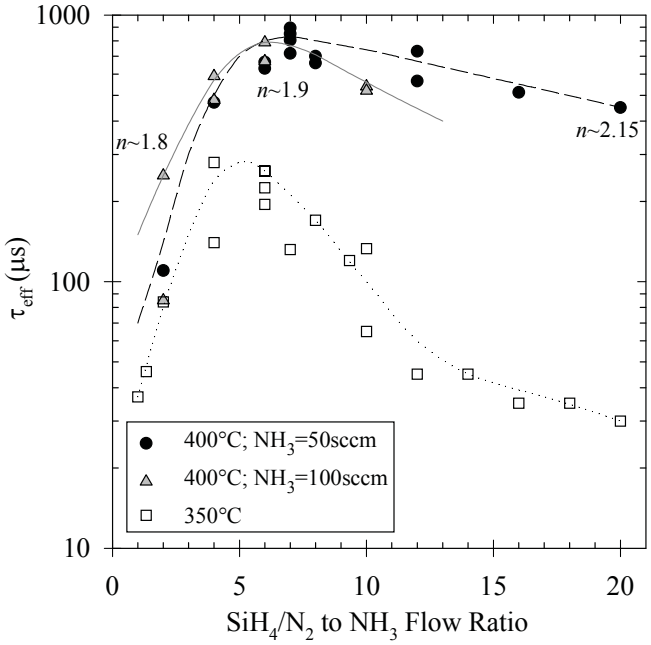


Figure 4.2. Effect of the silane/nitrogen-to-ammonia gas flow ratio on the effective lifetime of SiN/Si/SiN test structures fabricated on 1Ωcm *p*-type silicon. The refractive index (n) of some samples is indicated.

passivation. Thus, the process parameters that give the highest effective lifetime also give the lowest surface recombination velocity. The effective lifetime was therefore used as the response variable, rather than the surface recombination velocity, as the effective lifetime is directly measured.

4.2.2 Results and Discussion

4.2.2.1 Effect of Gas Flow Ratio and Rate

The effect of the dilute silane to ammonia *gas flow ratio* on the maximum effective lifetime is shown in Figure 4.2. Deposition temperatures of 350°C and 400°C are shown and the plasma power was 100W for this experiment. It is clear that the higher deposition temperature results in significantly higher τ_{eff} at each gas ratio. Furthermore, there exists an optimal gas flow ratio between 6 and 8 for the 400°C depositions. For the 350°C depositions, the optimal gas flow ratio is between 4 and 7, indicating a weak interaction between the deposition temperature and the gas flow ratio, with a slightly higher ratio being optimal for higher deposition temperature. The majority of data in Figure 4.2 are for an ammonia flow of 50sccm, but some limited data are included for 100sccm at a deposition temperature of 400°C. It again appears that the optimal gas flow ratio is ~6 or 7, even for twice the total gas flow rate, and therefore, the important SiN deposition parameter is the *ratio* of the gas flows, rather than the ammonia

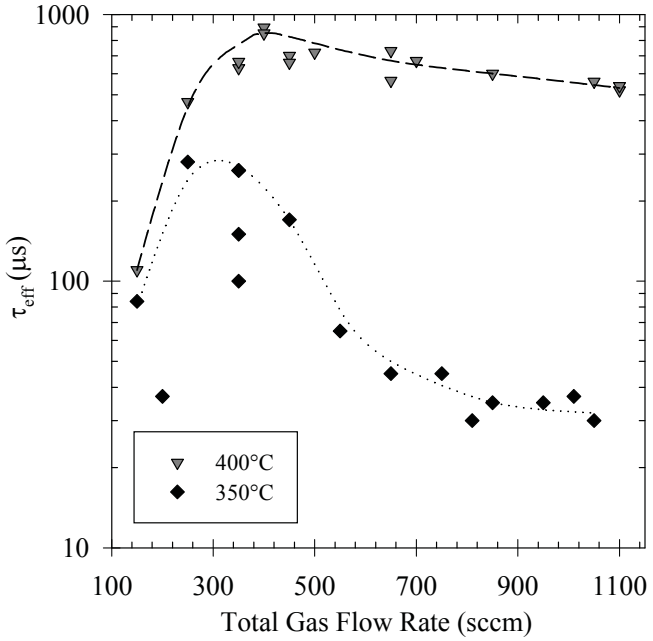


Figure 4.3. Effect of the total gas flow rate on the effective lifetime of SiN/Si/SiN test structures fabricated on 1Ωcm *p*-type silicon.

flow rate for example. Included in Figure 4.2 are the refractive index (n) for some of the SiN films. It can be seen that n increases from ~1.8 to ~2.15 as the gas flow ratio increases. Interestingly, the maximum τ_{eff} occurs for films with a refractive index of ~1.9, which indicates that the optimal SiN films are approximately stoichiometric in composition. The refractive index of the optimal films will be further discussed in section 4.2.2.3.

The effect of the total *gas flow rate* on the maximum effective lifetime is shown in Figure 4.3. Again, deposition temperatures of 350°C and 400°C are shown and the plasma power was 100W for this experiment. For the 400°C depositions, it appears that a weak maximum occurs for a total flow of 400sccm. At the lower deposition temperature, the maximum is more pronounced and the optimal flow appears to be 250-350sccm. It is therefore concluded that a total gas flow rate of 400sccm and a gas flow ratio of 6-8 are the optimal deposition parameters from the SiN films fabricated in this study. This corresponds to a dilute silane flow rate of 350sccm (gas ratio of 7) and an ammonia flow rate of 50sccm. It is also clear that higher deposition temperature is better.

4.2.2.2 Effect of Deposition Temperature, Process Pressure and Process Power

The effect of the deposition temperature on the effective lifetime is more fully demonstrated in Figure 4.4(a). The ammonia and dilute silane flow rates were set at the optimal

values for this experiment (NH_3=50sccm, SiH_4/N_2=350sccm) and a process power of 100W was used. Data for process pressures of 0.2T, 0.5T and 1T are shown. It is clear that independent of the process pressure, the deposition temperature has a very strong impact on the effective lifetime, with higher deposition temperature giving much higher τ_{eff}. Importantly, no maximum in τ_{eff} is found as the deposition temperature is increased. Temperatures above 400°C would clearly be desirable, where effective lifetimes well in excess of 1ms appear possible. Temperatures above 400°C are unfortunately not possible in the PECVD system used for these experiments, but can be achieved in similar machines, configured with a high temperature electrode assembly.

A maximum in τ_{eff} can neither be found as the process pressure is varied, as shown in Figure 4.4(b). A deposition temperature of 400°C, optimal gas flow rates and a process power of 100W were used for this experiment. The τ_{eff} continues to increase as the process pressure is decreased. The lowest pressure possible in this experiment was 0.17T. At pressures lower than this, the plasma could not be sustained during the attempted deposition. It is therefore concluded that the maximum obtainable deposition temperature (400°C) and the minimum sustainable process pressure (0.17T) are the optimal parameters for depositing the SiN films fabricated in this study. Significantly, these optimised parameter values do not represent their global maxima, which are outside the ranges obtainable with the PECVD reactor.

The effect of process power on the effective lifetime is shown in Figure 4.4(c). Optimal values for the gas flow rates and deposition temperature were used in these depositions, although a non-optimal process pressure of 0.5T was used. There is a weak maximum to the τ_{eff} for process powers between 100W and 150W and therefore it is concluded that the optimal value for the process power is 125W. It is assumed that the same process power is also optimal for lower process pressures, that is, the main effects dominate.

It can be seen from these experiments that effective lifetimes upto 900μs have been achieved. It will be shown in section 4.3 that using the optimal values for all five process variables results in effective lifetimes of 1ms for 1Ωcm *p*-type silicon. Thus, the surface passivation achieved with these optimised SiN films prepared using dilute silane is comparable with the best surface passivation achieved with PECVD SiN films fabricated using pure silane [109, 116].

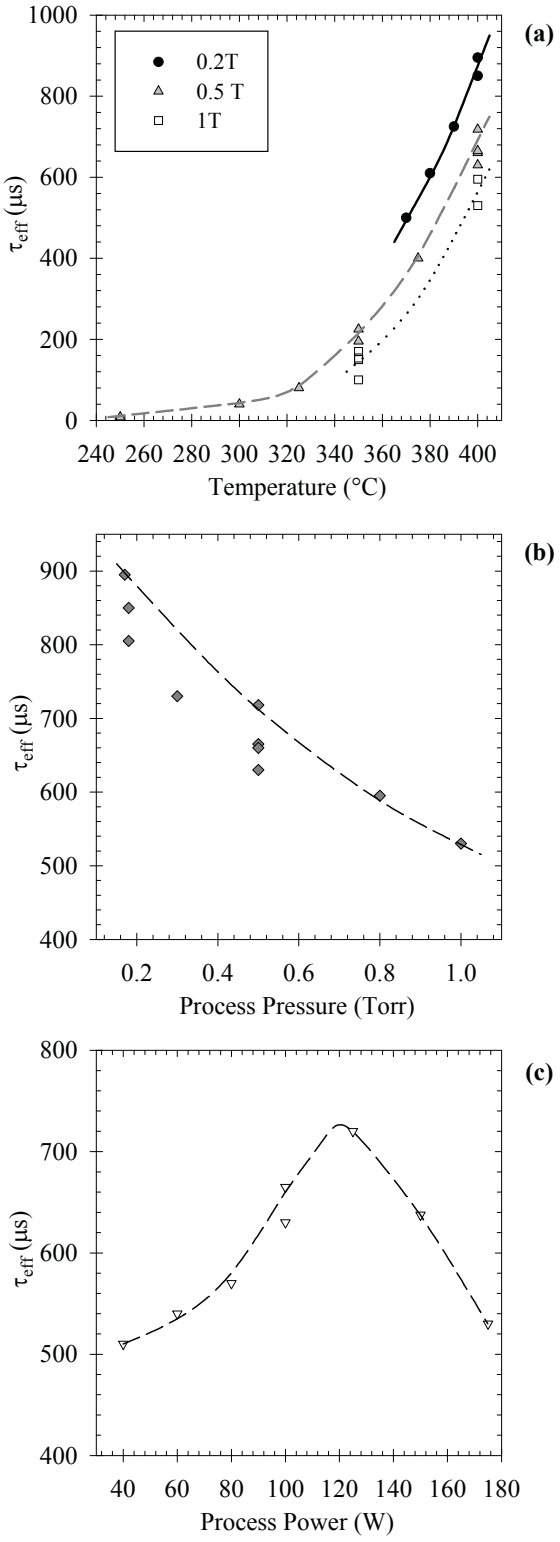


Figure 4.4. Effect of: (a) the deposition temperature, (b) the process pressure and (c) the process power on the effective lifetime of SiN/Si/SiN test structures fabricated on 1Ωcm *p*-type silicon.

4.2.2.3 Effect of Deposition Time

The final process variable to consider is the deposition time, which as mentioned before, determines the SiN film thickness. Using optimised values for the other process variables except for a pressure of 0.5T, the deposition time was varied up to 250s. Figure 4.5(a) shows the effect of the deposition time on the effective lifetime. It can be seen that as the deposition time is increased from zero, the effective lifetime increases to a constant value for deposition times greater than ≈60s, which was satisfied in the experiments for optimising the other process variable where a deposition time of 120s was used. An alternative interpretation is that as the SiN film thickness increases, the effective lifetime increases, reaching a constant value for films above a critical thickness.

The thickness and wavelength dependent refractive index, n(λ), of the SiN films were determined from the reflectance data recorded with a Filmetrics F20 spectrometer. In addition, some films were also investigated by spectral ellipsometry, with good agreement found between the two techniques. Figures 4.5(b) and 4.5(c) shows the variation of the film thickness and refractive index, for λ=630nm, with the deposition time. In can be seen from Figure 4.5(b) that the film thickness is linear with deposition time, corresponding to a deposition rate of 32nm/min. The critical SiN film thickness required to achieve the maximum surface passivation is therefore ≈30nm. For SiN films greater than this critical thickness, it can be seen from Figure 4.5(c) that the refractive index is constant and has a value of 1.95. It is therefore concluded that the optimal SiN films determined in this work are actually nearly stoichiometric in composition. Furthermore, for SiN films thinner than this critical thickness of 30nm, the refractive index appears to be less than 1.95, and reduces as the film thickness decreases. Extrapolating the refractive index values to very thin SiN films suggests that the limiting value for the refractive index is ≈1.5.

Finally, from the perspective of antireflection properties, the optimal SiN film thickness for use in a solar cell is in the range of 56-78nm depending on the SiN refractive index, the absorption coefficient and whether a single or double layer antireflection coating is used [115, 117]. Given that the critical SiN thickness determined for the SiN films optimised here is ≈30nm, it follows that it is possible to simultaneously minimize the reflection losses and maximise the surface passivation properties of these optimal stoichiometric SiN films.

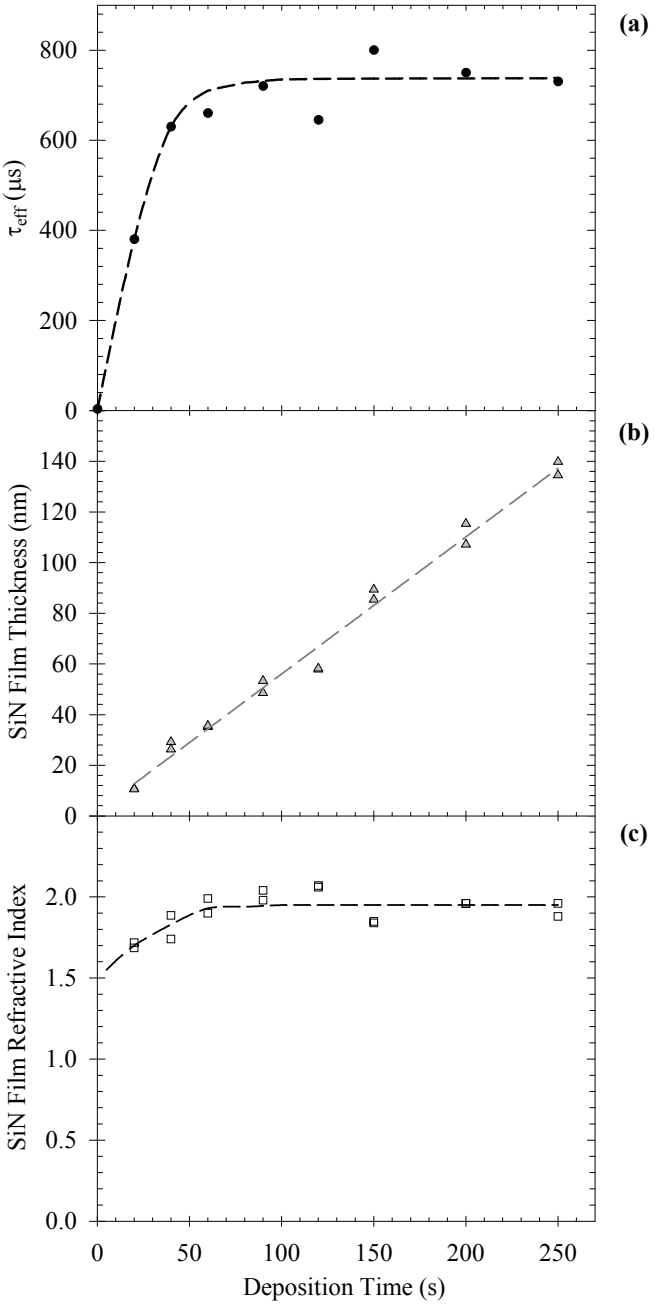


Figure 4.5. Effect of the deposition time on: (a) the effective lifetime of SiN/Si/SiN test structures fabricated on 1Ωcm *p*-type silicon, (b) the SiN film thickness and (c) the SiN film refractive index.

4.2.2.4 Optimal Parameters for 0.3Ωcm p-type Silicon

The above results show that the most important process parameters for determining the effective lifetime of 1Ωcm *p*-type silicon passivated with SiN films were the dilute silane to ammonia gas flow ratio, the deposition temperature and the process pressure. Optimal values for these process parameters were also investigated for passivating the surfaces of more heavily

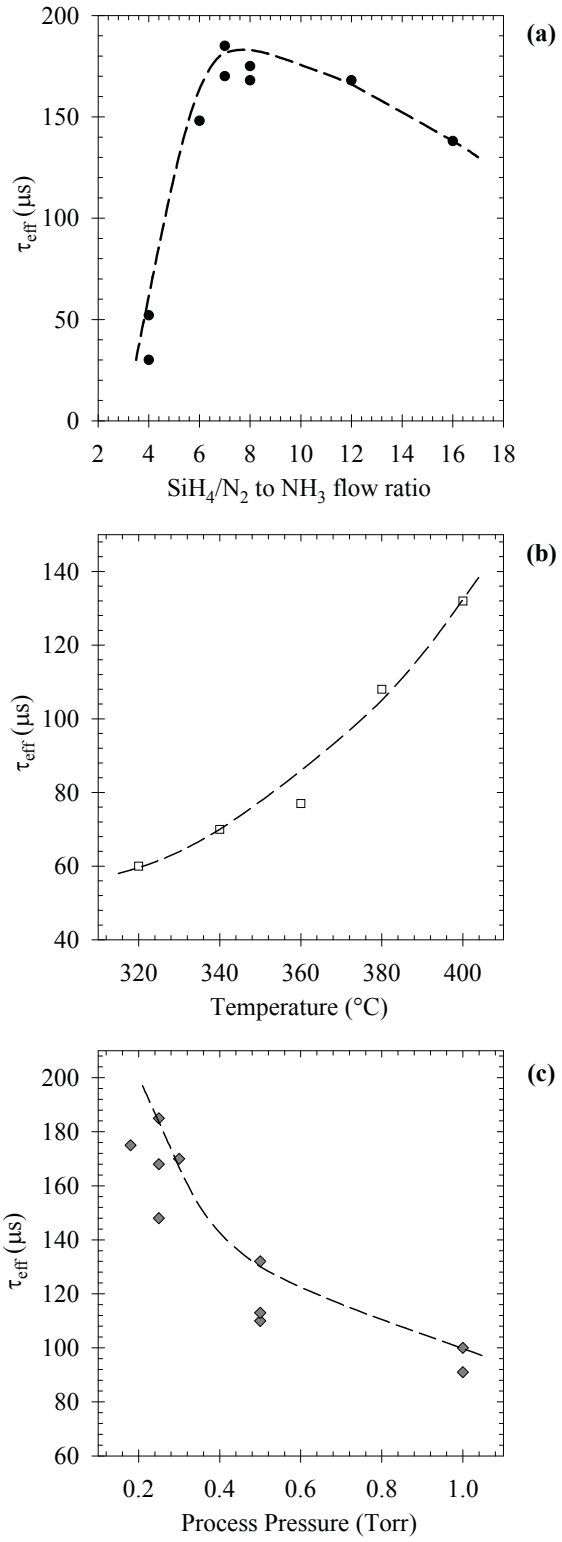


Figure 4.6. Effect of: (a) the silane/nitrogen-to-ammonia gas flow ratio, (b) the deposition temperature and (c) the process pressure on the effective lifetime of SiN/Si/SiN test structures fabricated on 0.3Ωcm *p*-type silicon.

doped 0.3Ωcm *p*-type silicon, which might typically be used in high efficiency PERC cells for example. As shown in Figure 4.6, it is again found that the optimal gas flow ratio is in the range of 6 to 8. For the deposition temperature, the τ_{eff} increases with increasing temperature, with the maximum occurring for a temperature greater than 400°C. For the process pressure, the τ_{eff} increases with decreasing pressure, with the maximum occurring for the lowest sustainable process pressure of 0.17Torr. Therefore, the optimal values for the process variables appear to be the same for both 1Ωcm *p*-type silicon and 0.3Ωcm *p*-type silicon.

4.2.3 Comparison with Previous Work

4.2.3.1 Effect of Deposition Temperature

The importance of optimising the process variables for obtaining excellent surface passivation of 1-2Ωcm *p*-type silicon surfaces using PECVD SiN has been discussed by Lauinger *et al.* [113, 114]. They observed a strong impact for the deposition temperature on τ_{eff} for both direct (high and low frequency) and remote PECVD systems when using pure silane and ammonia as the process gases. They also showed that the optimum range for the deposition temperature was relatively broad for each system. The data of Lauinger *et al.* for a high frequency direct PECVD system, like the one used in this thesis, are plotted in Figure 4.7. It can be seen that the optimum temperature range was 350°C-375°C. Reasonably good lifetimes of ≈500μs could still be obtained at temperatures as low as 300°C and the τ_{eff} actually decreased as the temperature increased above 375°C.

The results of Lauinger *et al.* are distinctly different to those in section 4.2.2.2, which are included in Figure 4.7 for comparison. The optimal SiN films from both Lauinger *et al.* and this study result in maximum effective lifetimes close to 1ms for 1-2Ωcm *p*-type silicon . It appears however, that by using dilute silane has caused the optimum temperature range to shift to higher values, and the dependence of τ_{eff} on the deposition temperature to become more pronounced.

4.2.3.2 Effect of Other Process Variables and Correlation with the Refractive Index

For the other process parameters, Lauinger *et al.* found the surprising result that the effect of the deposition parameters on the effective lifetime is correlated with their effect on the refractive index of the SiN films. They found that as the refractive index (measured at 633nm) is increased from 1.8, the τ_{eff} increases monotonically, reaching a constant value for SiN films with a refractive index ≥ 2.3 . [114]. For example, increasing the pure silane to ammonia gas

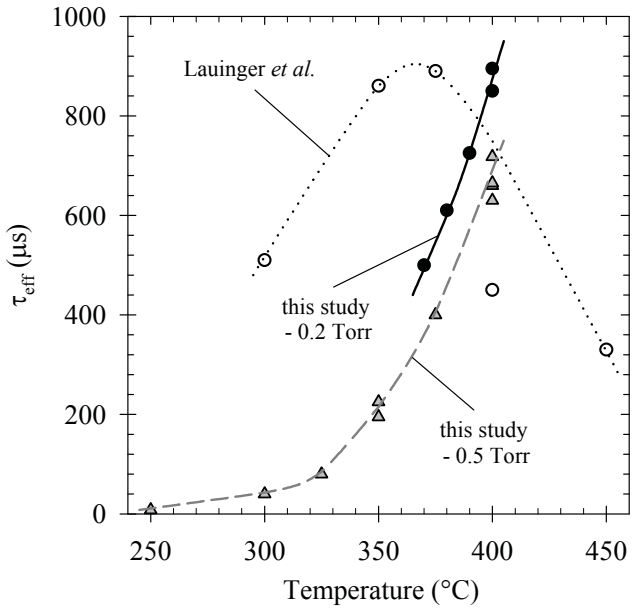


Figure 4.7. Effect of deposition temperature on the τ_{eff} of 1-2Ωcm *p*-type silicon passivated with SiN films. The SiN films of Lauinger *et al.* were deposited using pure silane gas onto 1.5Ωcm wafers, while the SiN films in this study were deposited using 4.5% silane in nitrogen onto 1.0Ωcm wafers.

flow ratio results in SiN films that are more silicon rich and have a higher refractive index, and therefore results in a higher τ_{eff}. This lead Lauinger *et al.* to conclude that silicon-rich silicon nitride films are required for an excellent surface passivation.

It has already been shown in this section that by using dilute silane, the same excellent degree of surface passivation can be achieved as with pure silane, but the refractive index of the optimal films is ≈1.95, ie *stoichiometric* rather than silicon rich. Figure 4.2 showed that as the dilute silane to ammonia gas flow ratio was increased above the optimum value of 7, the refractive index of the films increased to as high as 2.15 for a ratio of 20. The effective lifetime decreases down to 450µs however, which while still being a respectable lifetime, demonstrates a very different dependence for τ_{eff} with the refractive index than was observed by Lauinger *et al.*. It therefore appears that the use of dilute silane also causes the dependence of τ_{eff} on the other process variables to be markedly different than the case where pure silane is used. Importantly, it is concluded that it is essential to optimise the process parameters for a PECVD system depending on the concentration of the silane gas used, rather than assume that silicon rich SiN films are the optimal films.

Finally, the above results suggest it is possible to vary the silane carrier gas composition to achieve the highest τ_{eff} at any desired refractive index between n~1.95 (4.5% silane in

nitrogen) to n≥2.3 (pure silane) by varying the concentration of the silane in the carrier gas. This ability to independently optimise the passivation quality and the optical properties of SiN films is important to the commercial application of PECVD SiN films to solar cells. Clearly, an optimisation study of the surface passivation as a function of the silane carrier gas composition is warranted.

4.2.3.3 Effect of SiN Film Thickness

Both Elmiger and Kunst [118] and Lauinger *et al.* [114] have also observed that the effective lifetime of SiN passivated silicon wafers increases until a SiN film thickness of 25-30nm is deposited, after which the τ_{eff} remains constant. Indeed, for very thin SiN films (<5nm), Elmiger and Kunst have observed a decrease in the τ_{eff} as the SiN film thickness increases from 0nm to ≈5nm, and then an increasing τ_{eff} from ≈5nm to ≈30nm. They attribute the initial decrease in τ_{eff} to plasma induced damage of the silicon surface, although they do not explain the source of the damage and even point out that it is not created by ion bombardment for their high frequency PECVD system. The increase in τ_{eff} as the SiN film thickness increases from 5nm to 30nm was attributed to two reasons. The first reason is an increase in the density of fixed charges, Q_f, within the SiN films, which they have shown increases with the SiN film thickness reaching a constant value for films ≥30nm [119]. The second reason is a change in the film structure with thickness, which they deduced from measurements showing that the refractive index of the films increases from <1.6 to ≈1.9 as the film thickness was increased to 20nm. Using Rutherford backscattering, Elmiger and Kunst showed the increase in refractive index of the films is because the films change from being silicon oxynitride films to silicon nitride films as the film thickness increases. The measurements presented in section 4.2.2.3 for the refractive index as a function of SiN film thickness for the optimal SiN films in this study are in good agreement with those of Elmiger and Kunst. It is therefore concluded that the same explanations for the increase in τ_{eff} with SiN film thickness apply.

An increasing τ_{eff} with SiN film thickness has implications for understanding recombination at the SiN/silicon interface. The high fixed charge density ($Q_f \geq 10^{12}cm^{-2}$) of PECVD SiN films is well known from C-V measurements [17] (which are normally performed in the dark). However, Schmidt and Aberle [120] have proposed that in order to explain the injection level dependence of the surface recombination velocity, the majority of the fixed charge must be neutralised by free electrons when under illumination. This occurs because the energy position of the K^+ centre, which is normally considered responsible for most of the fixed charge, is within the silicon bandgap. Thus under illumination, the electron quasi-fermi level can rise to fill the K^+ centres, even to a depth of 30nm into the films [26]. The energy position

of the K^+ centre is unknown, other than it is believed to be in the upper half of the bandgap and that very low illumination levels of less than 1/1000 suns ($0.1mW/cm^2$) are sufficient for the electron quasi-fermi level to neutralize the K^+ centres [26]. Importantly, Aberle concludes that even when the K^+ centres are neutralized, PECVD SiN films will still have some fixed charge density due to specific silicon dangling bond configurations, which are also found in oxide passivated interfaces. The energy position of the fixed charges from the dangling bonds is outside the band gap and cannot be neutralized. Furthermore, the fixed charge density of PECVD SiN films, when illuminated, is therefore expected to be similar to that of thermally grown silicon oxide films (Q_f~10^{11}cm-2) [26].

Effective lifetimes are measured under illumination however, certainly illumination levels greater than 1/1000 of a sun. By proposing a model whereby the K^+ centres are filled under illumination, Aberle [26] is essentially concluding that the increase in τ_{eff} with SiN film thickness is not due to fixed charges, but only due to changes in film composition. The clear correlation shown by Elmiger and Kunst [118] of an increasing τ_{eff} and Q_f with the SiN film thickness (up to 30nm) suggests that the fixed charges do play an important role in the surface recombination processes under illumination however.

4.2.4 Conclusions

The PECVD deposition parameters have been optimised for passivating silicon wafers with SiN films when using dilute silane (4.5% silane in nitrogen) and ammonia as the process gases. The gas flow ratio, the deposition temperature and the process pressure were found to be the most significant deposition parameters. Effective lifetimes approaching 1ms have been achieved for 1Ωcm *p*-type wafers passivated with the optimised SiN films, which is comparable to the best surface passivation reported in the literature for SiN films fabricated using pure silane. Interestingly, the optimised SiN films of this study are nearly stoichiometric in composition rather than being silicon rich. A detailed study of the injection-level-dependent surface recombination velocity obtainable using these optimised *stoichiometric* SiN films on a variety of *p*-type and *n*-type silicon substrates is presented in the next section.

4.3 Surface Recombination Properties

4.3.1 Review of Previous Work

Literature values for the effective surface recombination velocity (S_{eff}) at the Si/SiN interface have mainly been determined by measuring the effective lifetime (τ_{eff}) of symmetrical SiN/Si/SiN test structures and using Eq. (2.29). The main error in determining S_{eff} arises from the uncertainty in τ_{bulk}, which is often assumed.

4.3.1.1 Low-Frequency Direct PECVD SiN Films

Aberle, Schmidt and co-workers have extensively studied the injection level dependence of S_{eff} at the Si/SiN interface for SiN films fabricated using low-frequency direct PECVD. The first reported data appears to be that of Aberle *et al.* [121] for boron doped *p*-type float-zone (FZ) wafers with resistivities in the range 1.5Ωcm-3000Ωcm. The wafers were passivated with near stoichiometric SiN films. They found that S_{eff} decreases as the wafer resistivity increases and shows an injection level dependence similar to that of thermally oxidized (SiO_2) *p*-type silicon. That is, S_{eff} actually decreases for *p*-type wafers as the injection level increases from low to intermediate injection, except for very high resistivity wafers. The minimum value determined for S_{eff} was ≈9cm/s for the 3000Ωcm wafer assuming τ_{bulk}≈4ms. Assuming a higher value for τ_{bulk} gives S_{eff} ≤15cm/s.

Schmidt and Aberle[120] extended this study to include *n*-type doped wafers with resistivities of 10Ωcm and 1000Ωcm, passivated with the same near stoichiometric, low-frequency direct PECVD SiN films. They showed the injection level dependence of S_{eff} to be flat at low injection levels, and then increases for higher injection levels ($\Delta n > 10^{14} cm^{-3}$), again, similar to the Si/SiO_2 system. The lowest S_{eff} reported was ≈5.5cm/s for the 1000Ωcm wafer. The uncertainty in this determination is quite high however [122], and S_{eff} could have been as high as 10cm/s depending on the value used for the bulk lifetime.

Schmidt and Aberle [120] also determined the fundamental properties for the interface between low-frequency direct SiN and silicon, such as the density of interface states (D_{it}) and the capture cross-sections (σ_n, σ_p). Using the extended Shockley-Read-Hall model for surface recombination [38, 61] they showed it was possible to obtain good agreement between the measured and calculated $S_{eff}(\Delta n)$ dependencies, as long as various scaling factors where applied to the measured interface parameters. This included reducing the Q_f, D_{it} and σ_p by one order of magnitude and σ_n by two orders of magnitude. Even using these scaling factors, an area of

discrepancy was for high resistivity wafers, both *n*-type and *p*-type, where the model predicted that S_{eff} values ≤1cm/s should be possible. Such low S_{eff} values were not verified experimentally, particularly if a large value was assumed for the bulk lifetime of the lightly doped silicon (τ_{bulk}≥10ms). For large τ_{bulk}, the lowest S_{eff} determined from their measurements would be ≈10cm/s. Given the reciprocal relationship between effective lifetime and S_{eff} (see Eq. (2.29)), this discrepancy in S_{eff} equates to a large discrepancy in the effective lifetime.

4.3.1.2 Remote and High-Frequency Direct PECVD SiN Films

Lauinger *et al.* measured the injection level dependence of S_{eff} for 0.7Ωcm and 1.5Ωcm *p*-type FZ wafers passivated with Si-rich SiN films prepared by remote PECVD [109]. A record low S_{eff} of 4cm/s (20cm/s) was determined for the 1.5Ωcm (0.7Ωcm) material by assuming a τ_{bulk}=1.7ms (τ_{bulk}=1.0ms). By assuming a higher bulk lifetime, Lauinger *et al.* showed that the S_{eff} was at most 15cm/s (35cm/s) for the planar 1.5Ωcm (0.7Ωcm) material. Indeed, in subsequent measurements by the same group on similar 1.5Ωcm wafers, a τ_{bulk}=3.3ms was assumed resulting in a re-evaluation of the minimum S_{eff} to be ≈13cm/s [123].

Schmidt and Aberle have shown that the $S_{eff}(\Delta n)$ dependence for remote and high-frequency direct SiN films is similar, and much stronger than for low-frequency direct SiN films [120]. They showed that remote and high-frequency direct SiN films give an S_{eff} around 10cm/s for 1.5Ωcm *p*-type silicon for $\Delta n \approx 1x10^{15}cm^{-3}$, but as shown in the simplified plot of Figure 4.8, this increases to over 400cm/s, a factor of forty greater, for $\Delta n < 1x10^{12}cm^{-3}$. Low-frequency direct SiN films give an S_{eff} of ≈95cm/s at $\Delta n = 1x10^{15}cm^{-3}$, but this increases to only 260cm/s, a factor of three greater, for $\Delta n < 1x10^{12}cm^{-3}$. They concluded that the stronger $S_{eff}(\Delta n)$ dependence of the remote and high-frequency direct SiN films was due to a different ratio for the capture cross sections for the defects dominating the surface recombination.

Lauinger *et al.* [109] have shown that for remote SiN passivated wafers, the $S_{eff}(\Delta n)$ dependence is much weaker for 0.7Ωcm substrates than for 1.5Ωcm substrates, which is also shown in Figure 4.8 (Schmidt and Aberle [48] show a similar result for 0.7Ωcm and 1.1Ωcm substrates). A surprising result from their work is that more heavily doped 0.7Ωcm wafers actually show a lower S_{eff} than for 1.5Ωcm wafers at injection levels below $2x10^{13}cm^{-3}$, an outcome not observed for substrates passivated with thermally grown silicon oxide.

While *p*-type wafers with dopant densities around 1Ωcm are very important for solar cell applications, there does not appear to be any data in the literature for the $S_{eff}(\Delta n)$ dependence of these Si-rich SiN films for other resistivities, or indeed for any *n*-type doped substrates. Schmidt

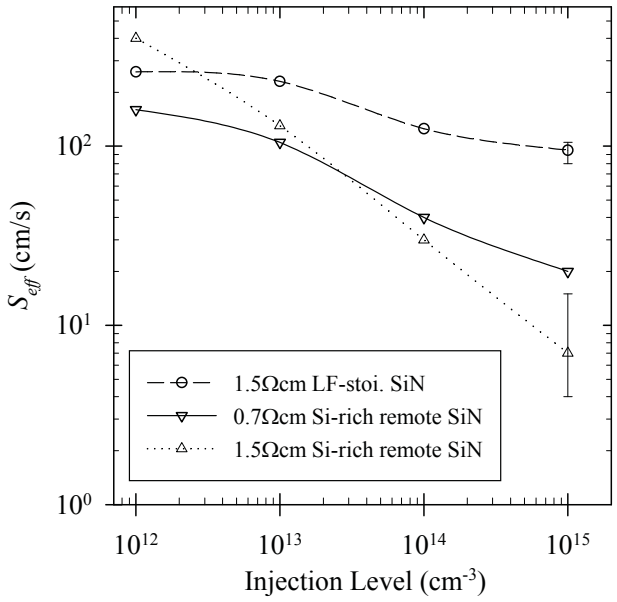


Figure 4.8. Comparison of literature data for the injection level dependent S_{eff} for intermediately doped (~1Ωcm) *p*-type silicon passivated with PECVD SiN films.

and Aberle [48] have reported some single τ_{eff} values measured for a number of wafers with different resistivities, mainly *p*-type, passivated with the same Si-rich SiN films. A maximum effective lifetime of <1.6ms was determined, even for high resistivity *n*-type and *p*-type material. This is in disagreement with lifetime measurements using other passivation techniques such as thermal SiO_2 and HF passivation where, as shown in section 3.2, much higher effective lifetimes have been measured, particularly for high resistivity material [62, 66]. Furthermore, reliable studies of the fundamental properties of the interface between these well passivating Si-rich SiN films and silicon are not possible using standard techniques such as capacitance-voltage (C-V) measurements or deep level transient spectroscopy (DLTS). This is because the MIS capacitors required for these techniques exhibit large leakage currents when fabricated using Si-rich SiN films.

Elmiger *et al.* have reported values for the *differential* S_{eff} ($\equiv \partial S_{eff}/\partial \Delta n$) for a variety of *n*-type and *p*-type substrates passivated with stoichiometric SiN films prepared by high frequency direct PECVD [124]. While the *differential* S_{eff} values could be quite low (around 10cm/s), the recombination rate at the surface is determined by the actual S_{eff}. This is obtained by integrating the *differential* S_{eff} values over the injection level, Δn. Reported values by Elmiger *et al.* for the actual S_{eff}, for both high resistivity *n*-type and *p*-type silicon (50Ωcm), were approximately 100cm/s [118]. This is approximately one to two orders of magnitude greater than can be achieved with such films.

4.3.2 Experimental Details

Symmetrical SiN/Si/SiN lifetime test structures were fabricated on mainly float-zone (FZ) silicon wafers with a <100> orientation. A wide range of substrate resistivities has been explored for both *n*-type (phosphorous) and *p*-type (boron) dopants with further details given in Table 4.1. The choice of Czochralski (CZ) silicon, rather than FZ, for the 0.6Ωcm *n*-type material was purely based on wafer availability within our laboratory. All of the wafers used in these experiments were sourced from standard commercial stock.

The silicon substrates were sourced in a variety of surface conditions (polished, lapped and as-cut). All substrates were etched in dilute HF/HNO_3 and rinsed in de-ionised water to remove any saw damage and to shiny etch the wafers. The wafers where then cleaned using the standard RCA procedure [65] and immersed in dilute HF. Silicon nitride films with a thickness of ≈70nm were deposited on both sides of the wafers in a high frequency (13.56MHz) direct PECVD reactor using the optimised deposition parameters described in the previous section.

The effective lifetime of each sample was measured for minority carrier injection levels in the range of $10^{12}cm^{-3}$ to $10^{17}cm^{-3}$. Both the quasi-steady-state (Qsspc) and transient photoconductance (tpcd) methods were used, with good agreement between them [50]. The carrier injection level was determined from the excess photoconductance using the carrier mobility data of Krausse [54] and Dannhauser [55]. The Qsspc and tpcd methods are large signal techniques that determine the actual effective lifetime rather than a differential quantity.

Values for S_{eff} at the Si/SiN interface were determined using Eq. (2.29) and the measured widths given in Table 4.1. It is assumed that bulk recombination is determined solely by intrinsic recombination, that is radiative recombination [24] and Coulomb-enhanced Auger recombination [28, 32]. The parameterisation developed in section 3.3, specifically Eq. (3.21), is used to quantify the bulk recombination rate as a function of dopant density, dopant type and injection level. The results presented here appear to be the first time that effective surface recombination velocities have been determined using an intrinsic recombination rate that depends on both the doping density and injection level. Previous determinations have assumed a constant bulk lifetime that does not depend on the injection level. This is appropriate if the substrate always stays in low injections conditions but is a simplification if the sample reaches intermediate or high injection conditions.

The uncertainty in the evaluation of S_{eff} can be estimated by determining an upper limit for S_{eff}, $S_{eff\text{-}max}$, by assuming no bulk recombination (that is, by setting $\tau_{bulk} \to \infty$). While such an assumption is physically unrealistic, it represents the extreme case. It is important to stress that

Table 4.1. Details for the <100> oriented silicon wafers used in these experiments. All the wafers where grown by the FZ method except the 0.6Ωcm *n*-type substrates which where CZ. The *n*-type wafers where doped using phosphorous and the *p*-type wafers using boron. The maximum measured effective lifetimes have been included as well as the low injection τ_{bulk} values used for determining S_{eff} and $S_{eff\text{-}min}$ at the Si/SiN interface. $S_{eff\text{-}max}$ was determined by setting $\tau_{bulk} \rightarrow \infty$. The minimum S_{eff} values determined for each substrate are included, as are the upper and lower bounds on that S_{eff}. Note that the maximum τ_{eff} and the minimum S_{eff} do not necessarily occur at the same Δn as the rate of intrinsic recombination in injection level dependent.

Resis. (Ωcm)	Dopant type	Dopant density (cm^{-3})	Wafer Width (μm)	Low inj. τ_{bulk} for S_{eff} (ms)	Low inj. τ_{bulk} for $S_{eff\text{-}min}$ (ms)	Max. measured τ_{eff} (ms)	S_{eff} (cm/s)	$S_{eff\text{-}min}$ (cm/s)	$S_{eff\text{-}max}$ (cm/s)
90	*n*	$4.9x10^{13}$	275	1600	34.1	10.0	1.37	0.97	1.38
20	*n*	$2.0x10^{14}$	185	370	31.4	3.4	2.7	2.4	2.7
1.5	*n*	$3.2x10^{15}$	305	9.9	7.2	2.15	5.5	4.8	7.2
0.6	*n*	$8.8x10^{15}$	350	2.22	1.98	0.96	9.8	8.5	18.3
150	*p*	$8.9x10^{13}$	440	1080	33.6	9.6	2.2	1.5	2.3
10	*p*	$1.4x10^{15}$	390	52	19.3	4.6	3.4	2.7	4.6
4.5	*p*	$3.1x10^{15}$	290	19.5	11.3	2.25	5.3	4.8	7.0
1.5	*p*	$9.8x10^{15}$	310	4.18	3.38	1.39	6.6	5.7	13.2
1.0	*p*	$1.5x10^{16}$	400	2.29	1.97	1.05	7.8	6.4	21.8
0.4	*p*	$4.0x10^{16}$	300	0.536	0.498	0.270	17.2	15.1	71.3
0.3	*p*	$5.4x10^{16}$	285	0.338	0.317	0.176	33.7	30.9	81.0

it is well known that for more heavily doped samples or for samples that are in high injection conditions, that the bulk lifetime is limited by intrinsic recombination processes [32]. As such, the upper error bars determined using this assumption of no bulk recombination will be greater for heavily doped and highly injected samples, where the assumption is physically less realistic.

A lower limit for S_{eff}, $S_{eff\text{-}min}$, is determined by considering that a low level of Shockley-Read-Hall (SRH) recombination may be occurring within the bulk of the sample along with the intrinsic recombination processes. An expression for the bulk SRH lifetime (τ_{SRH}) in high quality FZ silicon was determined in section 3.3.4. The lower limit for the bulk lifetime is then determined from τ_{SRH} and the intrinsic recombination lifetime ($\tau_{intrinsic}$)

$$\frac{1}{\tau_{bulk}} = \frac{1}{\tau_{intrinsic}} + \frac{1}{\tau_{SRH}} \qquad (4.1)$$

It should be noted that the value used here for τ_{SRH} is significantly larger than is typically used in previous works, which was ≤4ms [89, 109, 120]. The effect is that the values

determined for the lower limit of S_{eff} are more conservative than would be determined by assuming $\tau_{SRH} \leq 4$ms. In fact, as will be shown in the next section, it is not physically realistic for τ_{SRH} value of 4ms to be used, as effective lifetimes greater than this have been measured for a number of substrates. Included in Table 4.1 are the low-injection bulk lifetimes that have been used for the determination of S_{eff}, $S_{eff\text{-}max}$ and $S_{eff\text{-}min}$ for each substrate type. Note that, particularly for the high resistivity wafers, the assumed values for the bulk lifetimes are very high.

4.3.3 Results

Figure 4.9 shows the injection-level dependent effective lifetime for *n*-type silicon wafers passivated with optimised stoichiometric SiN films. It can be seen that high effective lifetimes ≥ 1ms have been obtained for all the wafers. The maximum τ_{eff} measured for each of the different resistivities is included in Table 4.1, with the highest τ_{eff} being 10.0ms for the lightly doped material (90Ωcm). This is by far the highest effective lifetime ever measured for a SiN passivated silicon substrate, regardless of the silicon content or deposition method for the SiN films. It can also be seen that $\tau_{eff}(\Delta n)$ is nearly constant at low injection conditions for all the wafers. Furthermore, as the injection level increases, the effective lifetime decreases, as Auger recombination becomes a more dominant process. As expected, the τ_{eff} decreases as the wafer doping increases for any given Δn. The $\tau_{eff}(\Delta n)$ dependence of the 90Ωcm *n*-type substrate shows an unexpected "bump" near $\Delta n \approx 10^{15}cm^{-3}$. The origin of this "bump" is unclear at this time, however it is also observed in SiO_2 passivated samples and appears to be due to bulk SRH recombination through a defect with an energy level close to the band edge.

Figure 4.10 shows the $\tau_{eff}(\Delta n)$ dependence of *p*-type silicon wafers passivated with stoichiometric SiN films. Again, very high effective lifetimes have been measured for all the substrate resistivities and these are included in Table 4.1. The highest measured τ_{eff} was 9.6ms for the 150Ωcm *p*-type material, in excellent agreement with the highest τ_{eff} measured on high resistivity *n*-type silicon. The $\tau_{eff}(\Delta n)$ dependence for the *p*-type substrates is quite different to that of the *n*-type substrates. As Δn increases from low injection to intermediate injection the τ_{eff} increases significantly rather than remain constant. As Δn increases further, the τ_{eff} then decreases due to Auger recombination in the bulk. It is clear that the $\tau_{eff}(\Delta n)$ dependence from low to intermediate injection is actually stronger as the doping density decreases. Indeed, for the most heavily doped *p*-type material investigated (0.3Ωcm), the $\tau_{eff}(\Delta n)$ dependence is almost flat. Again, the τ_{eff} decreases as the wafer doping increases for any given Δn, that is, the $\tau_{eff}(\Delta n)$ curves for different resistivity wafers do not cross over. Interestingly, it appears that for very

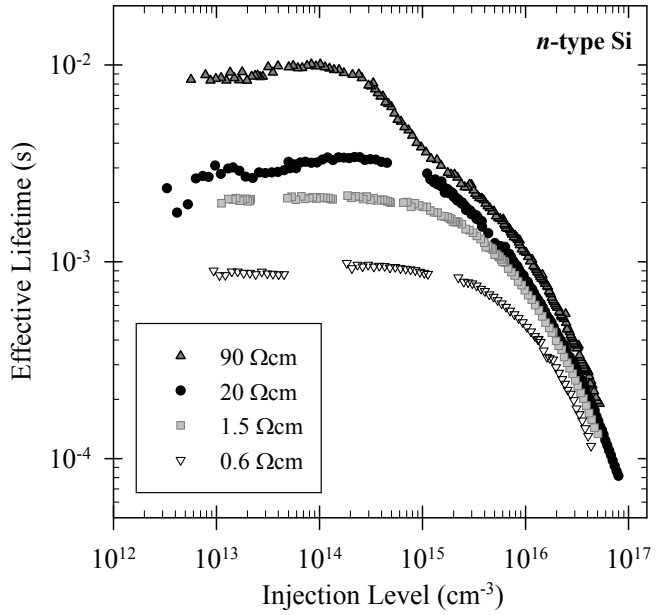


Figure 4.9. Measured effective lifetimes for *n*-type silicon passivated with optimised stoichiometric SiN films. The effective lifetime is nearly constant at low injection conditions, where lifetimes greater than 1ms have been measured for all the resistivities investigated. A maximum effective lifetime of 10.0ms has been measured.

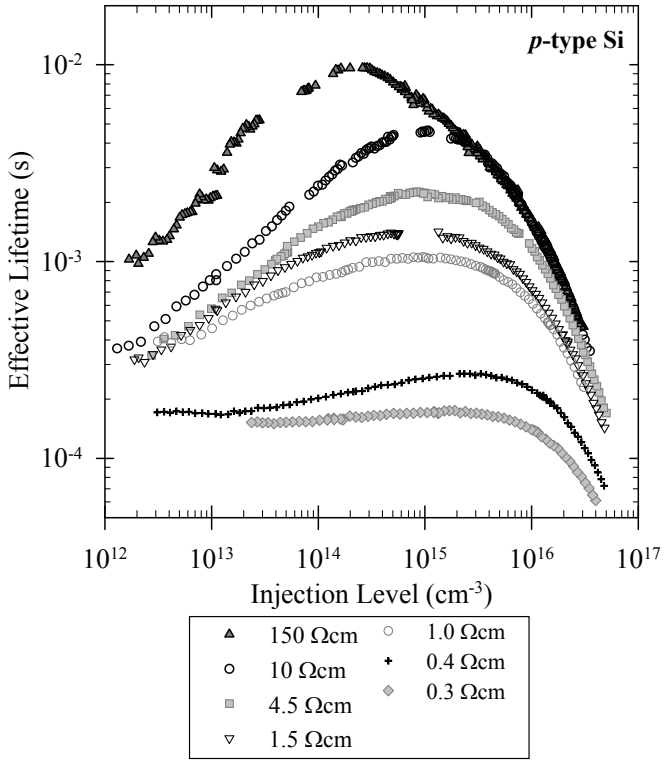


Figure 4.10. Measured effective lifetimes for *n*-type silicon passivated with optimised stoichiometric SiN films. The effective lifetime is nearly constant at low injection conditions, where lifetimes greater than 1ms have been measured for all the resistivities investigated. A maximum effective lifetime of 10.0ms has been measured.

low injection levels ($\Delta n<10^{12}cm^{-3}$), the $\tau_{eff}(\Delta n)$ values for different resistivity wafers are converging towards an effective lifetime of approximately 160μs.

Figure 4.11 shows the $S_{eff}(\Delta n)$ dependence for SiN passivated *n*-type silicon. For low injection conditions, the $S_{eff}(\Delta n)$ values determined are very low and are constant with injection level for each wafer. The S_{eff} values are given in Table 4.1. As Δn goes into high injection, S_{eff} increases. Using the intrinsic lifetime for the bulk lifetime, a very low S_{eff} of 1.37cm/s is determined for the 90Ωcm wafer. Assuming no bulk recombination puts an upper limit on S_{eff} of 1.38cm/s. Assuming a bulk SRH lifetime of 35ms reduces this to 0.97cm/s. Clearly S_{eff} values of the order of 1cm/s can unambiguously be achieved using SiN passivation for lightly doped silicon. For the other resistivity *n*-type wafers, low S_{eff} values have also been achieved with the low-injection S_{eff} being 9.8cm/s for the 0.6Ωcm material. The "bump" observed in the $\tau_{eff}(\Delta n)$ dependence for the 90Ωcm wafers translates to a similar "bump" in the $S_{eff}(\Delta n)$ dependence, although as mentioned above, it is believed that this is actually due to bulk SRH recombination.

Figure 4.12 shows the $S_{eff}(\Delta n)$ dependence for SiN passivated *p*-type silicon. For each resistivity there is a distinct minimum found for S_{eff}, normally at an injection level close to the wafer doping density (ie intermediate injection). The values for the minimum S_{eff} are included in Table 4.1. A low S_{eff} of 2.2cm/s has been determined for the 150Ωcm wafer, which reduces to 1.5cm/s when a bulk SRH lifetime of 35ms is assumed. Again, S_{eff} values of ≈1cm/s can clearly be achieved using SiN passivation on high resistivity substrates. Very low S_{eff} values have been determined even for more heavily doped *p*-type silicon. For example, a minimum S_{eff} of 3.4cm/s, 7.8cm/s and 33.7cm/s have been demonstrated for 10Ωcm, 1.0Ωcm and 0.3Ωcm material respectively. For lower Δn, the S_{eff} for each wafer increases from this minimum, with the injection level dependence of S_{eff} actually being stronger for the higher resistivity wafers. Indeed, the $S_{eff}(\Delta n)$ dependence for the most heavily doped *p*-type material is quite flat, increasing by a factor of only two as Δn decreases from $10^{16}cm^{-3}$ to $10^{13}cm^{-3}$. For the high resistivity *p*-type substrates, S_{eff} increases by a factor of 20-30 for the same decrease in Δn.

Interestingly, at very low injection levels ($\Delta n<10^{12}cm^{-3}$), it appears that S_{eff} for all the resistivities are converging to a common value of ≈ 70cm/s. A final observation is that the $S_{eff}(\Delta n)$ curves do not cross over for most of the *p*-type substrates. The exception is for the high resistivity 150Ωcm material, which gives very low S_{eff} values for $\Delta n<3x10^{14}cm^{-3}$, but for higher Δn actually intersects with the curve of the 10Ωcm and 4.5Ωcm material (although S_{eff} remains low at <10cm/s for Δn up to $3x10^{16}cm^{-3}$). It is not clear if this is a fundamental property of the

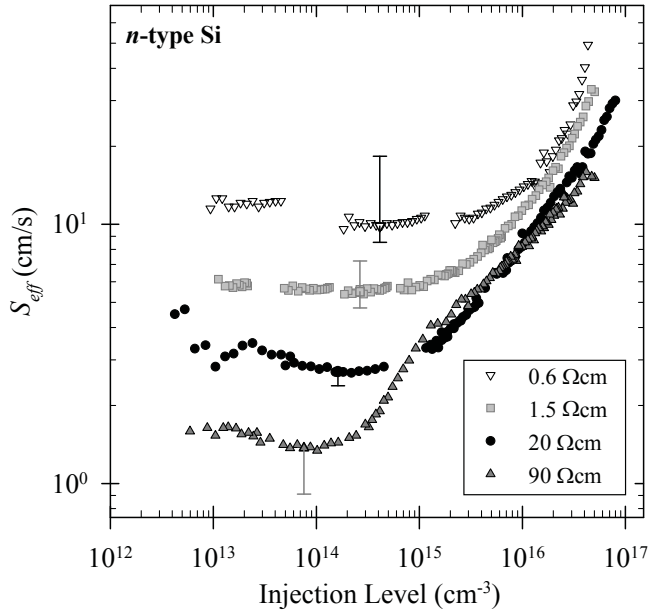


Figure 4.11. Measured $S_{eff}(\Delta n)$ dependence for *n*-type silicon passivated with optimised stoichiometric SiN films. S_{eff} values as low as 1cm/s are clearly obtainable at the surfaces of high resistivity *n*-type silicon. Low S_{eff} values (~10cm/s) have also been achieved for resistivities as low as 0.6Ωcm.

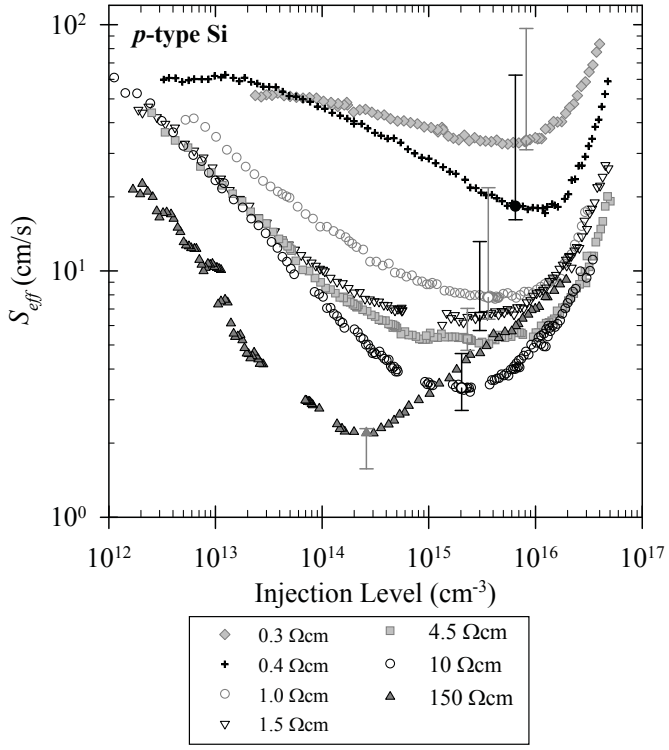


Figure 4.12. Measured $S_{eff}(\Delta n)$ dependence for *p*-type silicon passivated with optimised stoichiometric SiN films. A minimum in the $S_{eff}(\Delta n)$ curve exists for each substrate at intermediate injection. S_{eff} values as low as 2cm/s are clearly obtainable at the surfaces of high resistivity *p*-type silicon.

stoichiometric SiN films, or if it is due to some residual bulk recombination within the substrate that has not been accounted for in the analysis.

4.3.4 Discussion

4.3.4.1 Comparison with Literature Data for $S_{eff}(\Delta n)$

A direct comparison can be made between literature data and the results of Figure 4.12 for the S_{eff} of 1.5Ωcm *p*-type silicon passivated with different types of PECVD SiN. The comparison is compromised somewhat by the fact that the S_{eff} is measured in different ways by different authors, the wafers are sourced from different suppliers and that different assumptions are made for the bulk lifetime of the wafers. Nevertheless, Figure 4.13 shows such a comparison, where it can be seen that distinctly different values have been determined for the S_{eff}. The results of this study for stoichiometric high-frequency (HF) direct PECVD SiN films show some similarity in shape with those for low-frequency (LF) direct SiN films by Schmidt and Aberle [120, 121], albeit at significantly lower levels. The magnitude of the S_{eff} values from this study tend to be about one order of magnitude lower when the same assumptions are made for the bulk lifetime, but the dependency of S_{eff} on Δn appears to be quite similar. Furthermore, both studies find that for *n*-type substrates, S_{eff} is constant for low Δn and then increases as the substrate goes into high injection. For *p*-type substrates, a minimum S_{eff} is observed at intermediate injection and S_{eff} increases for lower or higher Δn. This possibly suggest that similar defects are dominating the surface recombination processes at the interface for both LF and HF direct SiN films, but the density of the defects are lower in the HF direct SiN films, where ion bombardment of the silicon surface can be avoided during plasma deposition.

A comparison of the measurements here with the results of Lauinger *et al.* [109] for their well passivating Si-rich SiN films prepared by remote or high-frequency direct PECVD is also shown in Figure 4.13. It can be seen that at intermediate injection densities around $10^{15}cm^{-3}$, both SiN films provide excellent passivation of ~7-10cm/s. For lower injection densities however, the stoichiometric SiN films of this study appear to have a weaker dependence on injection level, which can be particularly important for solar cell operation at maximum power-point. Furthermore, the results presented in Figure 4.12 for the $S_{eff}(\Delta n)$ of more heavily doped *p*-type wafers do not show the cross-over for S_{eff} that was observed by Lauinger *et al.* as the resistivity is decreased from 1.5Ωcm to 0.7Ωcm. It is therefore concluded that the fundamental properties of the dominant defects at the Si/SiN interfaces in this study are different to those of Lauinger *et al.*.

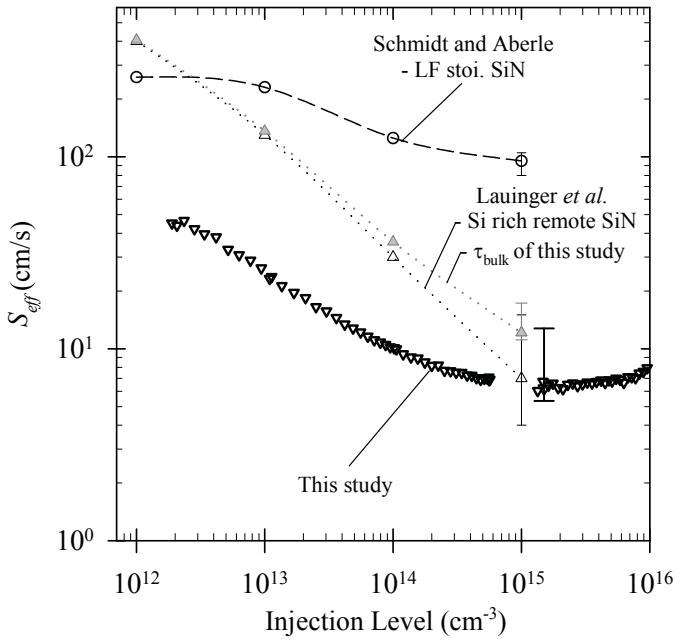


Figure 4.13. Comparison of $S_{eff}(\Delta n)$ from this study with literature data for 1.5Ωcm *p*-type silicon passivated with different type of PECVD SiN films. The data of Lauinger *et al.* has been re-analysed using the τ_{bulk} values determined in Chapter 3, which results in a small increase in the S_{eff}.

It should be pointed out that the τ_{bulk} values assumed by Lauinger *et al.* were quite different to those of this study (they used a constant τ_{bulk} of 1.7ms). The $S_{eff}(\Delta n)$ data of Lauinger *et al.* [109] are re-plotted in Figure 4.13 using the same assumptions for τ_{bulk} that are described in section 4.3.2. It can be seen that this increases the S_{eff} determined by Lauinger *et al.* by a small amount, although the shape of the injection level dependence does not significantly change. Importantly, the use of τ_{bulk}=1.7ms does not appear to be appropriate for 1.5Ωcm *p*-type wafers, as it has been reported in Table 3.1 that *effective lifetimes* of 1.7ms have been measured for 1.0Ωcm *p*-type wafers passivated with alnealed silicon oxide. The bulk lifetime of less heavily doped 1.5Ωcm *p*-type wafers should therefore be greater than this.

4.3.4.2 Physical Mechanisms for Recombination at the Si/SiN Interface

To gain some insight into the possible mechanisms responsible for surface recombination at the Si/SiN interface using the stoichiometric SiN films of this study, the local ideality factor, n_{loc}, was determined for some of the $\tau_{eff}(\Delta n)$ curves in Figure 4.9 and Figure 4.10. For the general case of arbitrary injection level and dopant density,

$$n_{loc} = \frac{(n+p)\Delta n}{np\left(1 - \frac{\Delta n}{\tau_{eff}}\frac{d\tau_{eff}}{d\Delta n}\right)}. \qquad (4.2)$$

As can be seen in Figure 4.14(a), n_{loc} for *n*-type wafers has a constant value of unity, except at the highest injection levels where it decreases below unity presumably due to Auger recombination. Such behaviour for n_{loc} is consistent with very low injection conditions prevailing at the silicon surface. If the SiN films have a high positive fixed charge density (under illumination), then an accumulation of electrons will occur near the silicon surface. This automatically produces a very low injection level for minority holes at the surface. An ideality factor of unity at low injection may also be explained by a constant, injection independent recombination mechanism even in the absence of an accumulation layer, but the previous explanation is more likely.

For *p*-type wafers, the n_{loc} data is much nosier, as shown in Figure 4.14(b). It does appear however, that for the higher resistivity wafers, n_{loc} increases from below unity at high injection towards a value of two at low injection. In general, a variable n_{loc}, with a value greater than 1, is indicative of a carrier injection dependent recombination mechanism. Specifically, an ideality factor of two is normally associated with recombination within a space-charge region. Such behaviour for n_{loc} could therefore be interpreted as a high positive fixed charge density in the SiN films causing the silicon surface to be inverted, even under illumination. An emitter like region would form near the silicon surface and a space-charge region would form between the induced n^+ emitter and the *p*-type quasi-neutral base region. At low injection levels, recombination within the space-charge region would dominate giving n_{loc}~2. As the injection level increases, recombination at the surface proper and within the inversion layer itself would become more prominent and n_{loc} would therefore reduce towards unity. At even higher injection levels, Auger recombination would result in sub-unity ideality factors. Importantly, for the heavily doped 0.4Ωcm *p*-type wafer shown in Figure 4.14(b), the ideality factor does not converge towards two as the injection level decreases. Instead, it seems to peak at a value of ≈1.4 and then decreases towards one as the injection level decreases. This suggests that space-charge recombination is not prevalent at this doping density for the injection levels investigated. Indeed, the extent of an induced space charge region is expected to be co-related to the dopant density.

It is therefore possible to hypothesize that surface recombination for the stoichiometric SiN films studied here is consistent with the films having a high positive fixed charge density, even under illumination. If the fundamental properties of the defects at the Si/SiN interface where known, it would in principle be possible to model the $S_{eff}(\Delta n)$ dependence using the extended SRH formulism, including band-bending [38] and space-charge recombination [40]. The fundamental properties are not known however, but for the case where Q_f is sufficiently

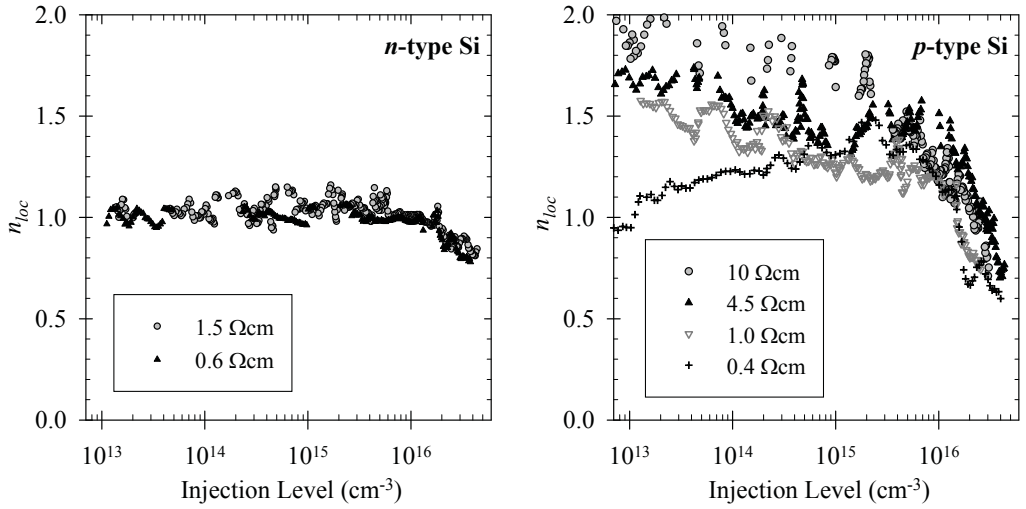


Figure 4.14. The local ideality factor determined from the effective lifetime data of Figures 4.9 and 4.10. It can be seen that: (a) n_{loc} has a constant value of one for *n*-type silicon except at high injection where it is less than one and (b) n_{loc} increases from less than one at high injection towards two at low injection for most of the *p*-type wafers investigated.

high, the band-bending behaviour results in the surface behaving like an emitter region. The surface recombination current can then be written as

$$J_{rec} = qWU_{rec} = 2qS_{eff}\Delta n = 2J_{o1}\left(\exp\frac{qV}{kT} - 1\right) + 2J_{o2}\left(\exp\frac{qV}{2kT} - 1\right)$$

$$\Rightarrow S_{eff} = \frac{J_{o1}}{q\Delta n}\left(\frac{np}{n_i^2} - 1\right) + \frac{J_{o2}}{q\Delta n}\left(\frac{\sqrt{np}}{n_i} - 1\right). \qquad (4.3)$$

As mentioned above, the simple model of Eq. (4.3) is not appropriate for modeling the 0.4Ωcm sample and would result in a poor fit to the experimentally measured S_{eff} data. Furthermore, as mentioned previously, a constant can be added to the right-hand side of Eq. (4.3) and still be consistent with the n_{loc} values determined above.

Figure 4.15 and 4.16 show the measured $S_{eff}(\Delta n)$ data along with fits based on Eq. (4.3) for *n*-type and *p*-type wafers respectively. For *n*-type wafers, J_{o2} was always set to zero and J_{o1} was varied to obtain the best fit for each dopant density, while for *p*-type wafers, both J_{o1} and J_{o2} were varied to obtain the best fit. It was found that a constant value had to be included in Eq. (4.3) to obtain a reasonable fit for the *n*-type wafers but not for the *p*-type wafers. The physical origin of including a constant could be additional bulk recombination that had not been considered when determining S_{eff} from τ_{eff}. It can be seen that a good fit can be made at all injection levels for the 1.5Ωcm and 0.6Ωcm *n*-type wafers. The fit is fair for the 20Ωcm wafer, but poor for the 90Ωcm wafer due to the bump previously discussed. For the *p*-type wafers, a very good fit can be achieved for wafers between 1Ωcm and 10Ωcm, although the fit is poor for

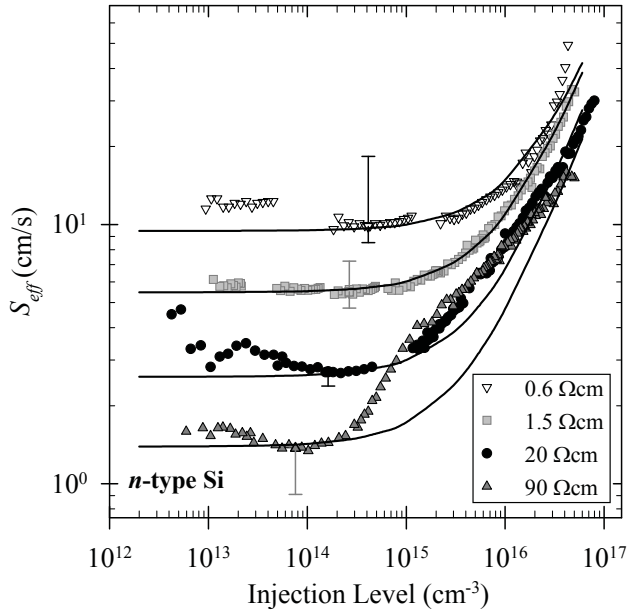


Figure 4.15. Measured $S_{eff}(\Delta n)$ dependence for *n*-type silicon passivated with optimised stoichiometric SiN films. The fits are based on Eq. (4.3), where it has been assumed that a high positive fixed charge density results in accumulation of the *n*-type surface, even under illumination.

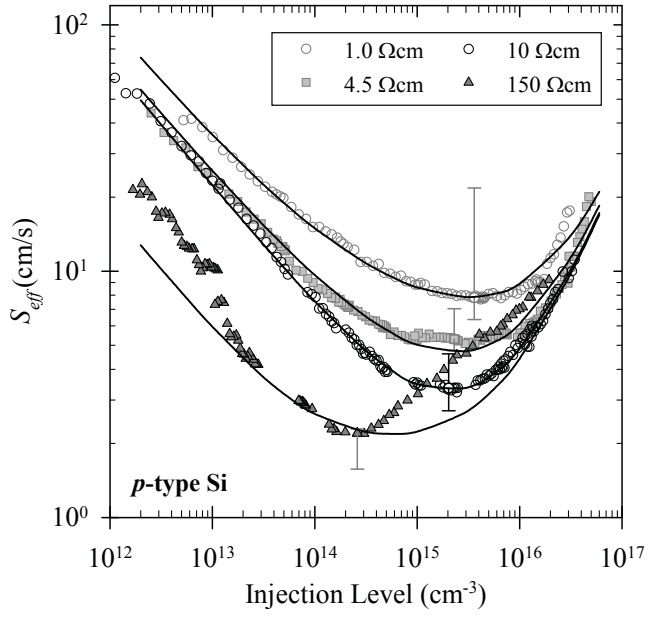


Figure 4.16. Measured $S_{eff}(\Delta n)$ dependence for *p*-type silicon passivated with optimised stoichiometric SiN films. The fits are based on Eq. (4.3), where it has been assumed that a high positive fixed charge density results in inversion of the *p*-type surface. Recombination within the space-charge region causes the $S_{eff}(\Delta n)$ to increase at low injection levels.

the 150Ωcm wafer, mainly for injections levels above $3x10^{14}cm^{-3}$. As mentioned, a sensible fit cannot be made to the S_{eff} data for the 0.4Ωcm wafer.

It seems that the simple approach of Eq. (4.3) can, to a reasonable extent, fit the injection level dependent S_{eff} data for most of the wafers investigated. The unsatisfactory fits for the very high resistivity wafers may be due to the fact that these wafers are the most sensitive to bulk recombination processes, which may not have been fully accounted for in the analysis described in section 4.3.2. The good fits for the other resistivities do indicate however, that the experimental data is consistent with the hypothesis that a high fixed charge density plays a significant role in the surface recombination processes of the SiN films investigated here, even under illumination. This is consistent with the work of Elmiger and Kunst [118], but as discussed in section 4.2.3.3, is in contrast to that of Schmidt and Aberle [120]. A defining test of whether a high fixed charge density is responsible for the surface passivation obtained with SiN films will be the ability, or not, of the SiN films to passivated heavily doped *p*-type surfaces, where the doping is sufficiently high that the *p*-type surface can not be inverted by the charges. This is investigated in Chapter 5.

4.3.5 Comparison of Stoichiometric SiN and Thermal SiO_2

The most common method for obtaining a high quality surface passivation of silicon surfaces is to grow a thermal silicon dioxide layer (SiO_2) at high temperature [37, 89, 125, 126]. A systematic comparison of the S_{eff} obtained using both the stoichiometric SiN films of this study and thermal SiO_2 is given in Figures 4.17 and 4.18 for *p*-type and *n*-type silicon respectively. The SiO_2 films were grown at 1050°C for 2 hours in a TCA ambient resulting in a blue coloured oxide. A post-oxidation anneal in Ar was performed at 1050°C before cooling the furnace to 800°C and unloading the wafers. The samples were then given a forming gas anneal (FGA - 5% hydrogen in argon) at 400°C for 30mins and the effective lifetime measured. The same samples were then alnealed, the aluminium layers removed and the effective lifetime re-measured. The injection level dependent S_{eff} and associated error bars were determined in the same way described in section 4.3.2 (ie upper error bars assume an infinite bulk lifetime etc).

It can be seen that the S_{eff} can vary from less than 1cm/s to over 1000cm/s and that the S_{eff} depends strongly on the surface passivation method, injection level, dopant density and dopant type of the silicon wafer. Some broad observations can be made however:

- The best surface passivation is generally obtained using an *alnealed* SiO_2 film for both *n*-type and *p*-type silicon independent of the dopant density and injection level.

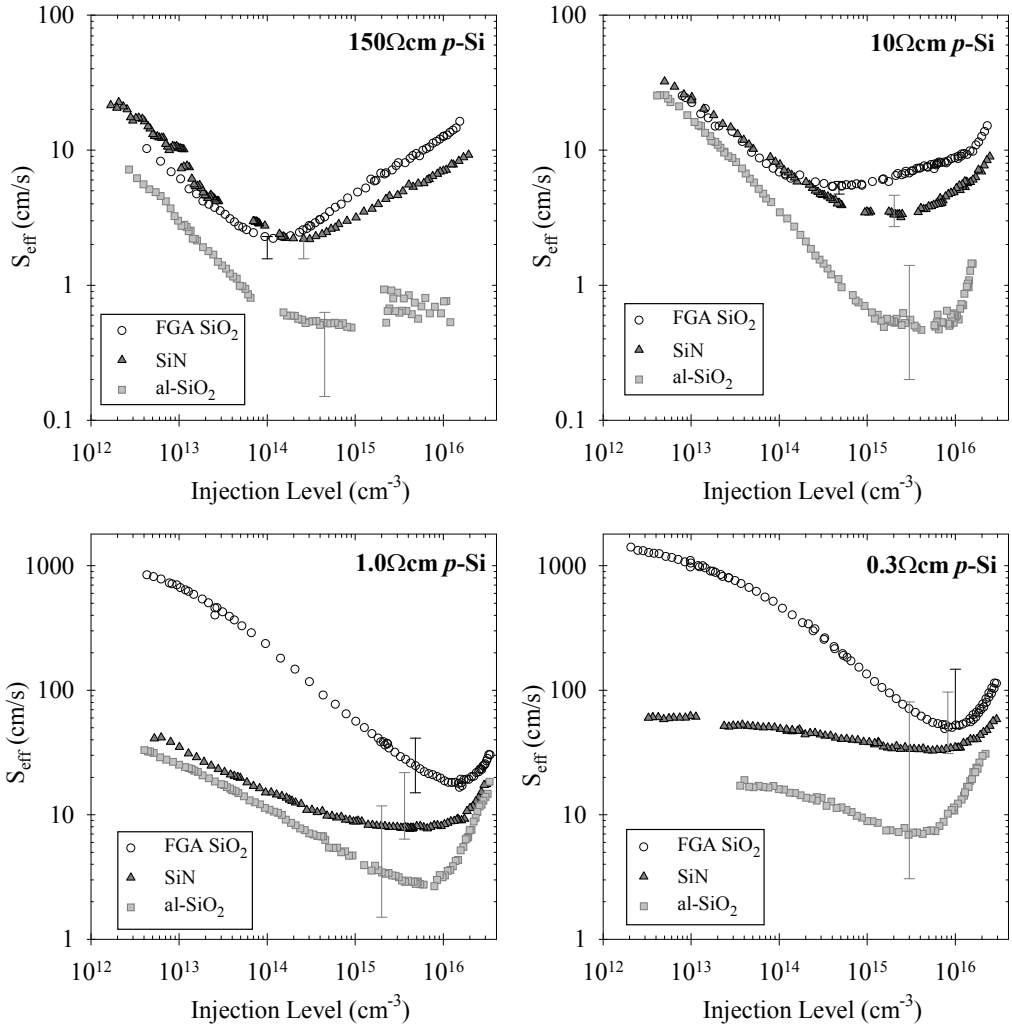


Figure 4.17. Comparison of the $S_{eff}(\Delta n)$ dependence for *p*-type silicon of different dopant densities passivated with forming gas annealed (FGA) SiO_2, optimised stoichiometric SiN films and *alnealed* SiO_2. The alnealed SiO_2 films give the best surface passivation, while the SiN films give significantly better surface passivation than FGA SiO_2 for $N_{dop}>10^{15}cm^{-3}$.

- Excellent surface passivation (~1-2cm/s) can be achieved for high resistivity silicon passivated with a FGA SiO_2 film. As the dopant density increases, the S_{eff} increases quite strongly, particularly at low injection levels. It appears that FGA SiO_2 is more effective at passivating *n*-type silicon than *p*-type of the same dopant density. This is normally explained by differences in the capture cross-sections for electrons and holes for the defects at the Si-SiO_2 interface [26].
- For high resistivity silicon, the S_{eff} values obtained with SiN passivation and FGA SiO_2 passivation are reasonably similar. It appears that stoichiometric SiN films offer slightly better passivation at higher injection levels.

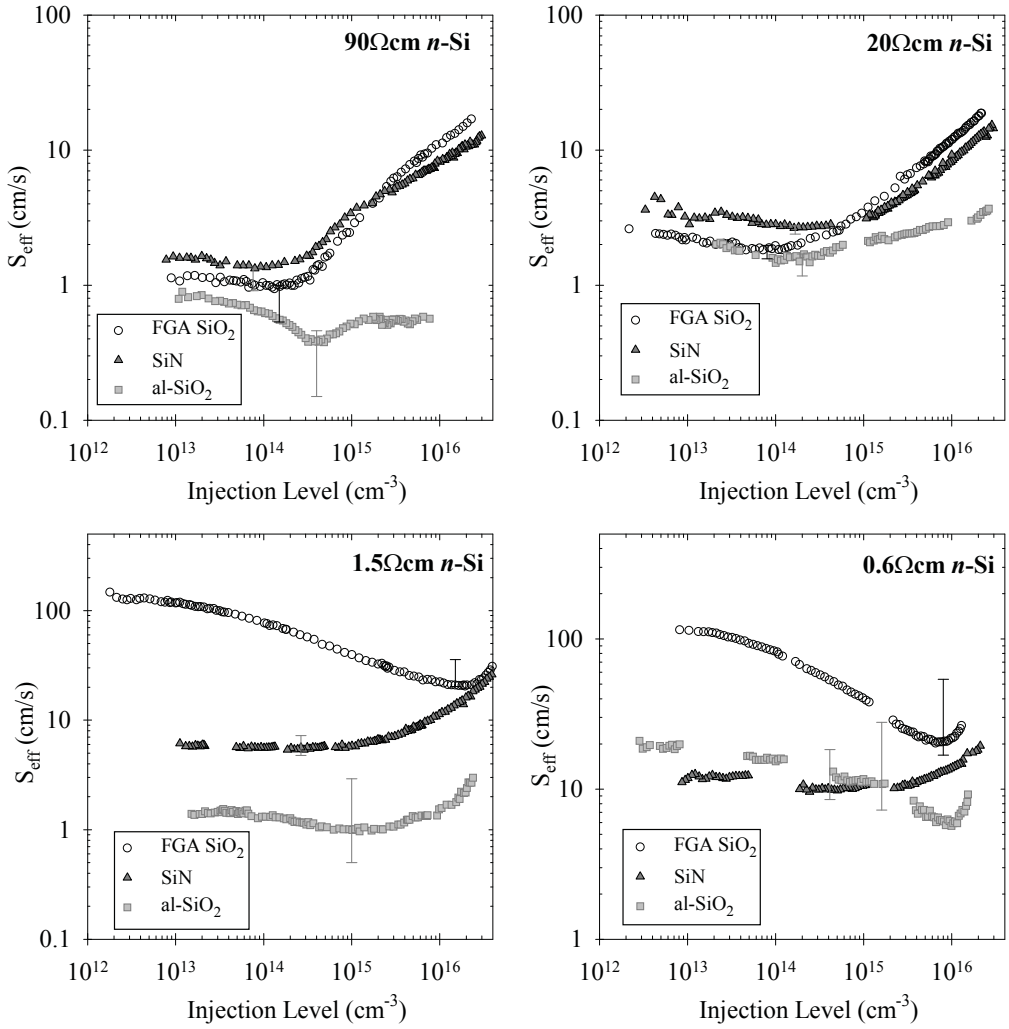


Figure 4.18. Comparison of the $S_{eff}(\Delta n)$ dependence for *n*-type silicon of different dopant densities passivated with forming gas annealed (FGA) SiO_2, optimised stoichiometric SiN films and *alnealed* SiO_2. The alnealed SiO_2 films give the best surface passivation, while the SiN films give significantly better surface passivation than FGA SiO_2 for $N_{dop}>10^{15}cm^{-3}$.

- For more heavily doped silicon ($N_{dop}>10^{15}cm^{-3}$), SiN films offer significantly better surface passivation at all injection levels than FGA SiO_2. In terms of solar cells, where moderately doped silicon is normally used, SiN films therefore offer significant benefits compared to FGA SiO_2 for passivating the non-diffused surfaces.
- For the 0.6Ωcm *n*-type wafers, SiN films appear to result in lower S_{eff} than even the alnealed SiO_2 films. It is possible however that there was some degradation of the bulk lifetime in these CZ wafers during the high temperature oxidation, which did not occur for wafers of different dopant densities which where FZ. The SiN passivated wafers had not undergone any high temperature processing and so did not suffer from the bulk degradation.

It is interesting to note that the $S_{eff}(\Delta n)$ curves for alnealed SiO_2 passivated *p*-type silicon also show a minimum value for S_{eff}. At lower injection levels, the S_{eff} increases as the injection level decreases. In the context of SiN passivation, recombination within a space-charge region has been used to justify the shape of the $S_{eff}(\Delta n)$ curves. For alnealed SiO_2 passivation, the energy dependency of the D_{it} and the asymmetry of the capture cross-sections are typically used to explain this curve shape, as the quantity of fixed charge at the Si/SiO_2 interface is generally considered low [26, 61]. It remains unclear if additional bulk recombination, occurring at a low level and with a weak-injection level-dependence, is actually responsible for some or all of the $S_{eff}(\Delta n)$ dependence shown in Figure 4.17 for the alnealed SiO_2 case. Indeed, there does not appear to be data in the literature showing an injection independent lifetime for a well-passivated (say τ_{eff}>1ms) intermediately doped *p*-type silicon wafer passivated by other means. Furthermore, there may be effects of boron depletion near the silicon surface during oxidation and possible interactions between the boron atoms near the surface and atomic hydrogen, either from the alnealing or from the SiN, which need to be considered.

4.3.6 Limiting Efficiency of SiN Passivated Solar Cells

It has been shown in section 3.4 that surface recombination process can significantly reduce the achievable solar cell efficiency, particularly for thin cells. The injection level dependent S_{eff} values reported above for both SiN and SiO_2 passivated surfaces can be used to calculate the limiting efficiency as a function of cell thickness in the presence of surface recombination. For the case where bulk recombination is given by the intrinsic recombination rate and the entire front and rear surface are passivated by the SiN or SiO_2 films, the current-voltage characteristic is given by

$$J = J_L - qWU_{\text{int}} - 2qS_{eff}\Delta n \,, \tag{4.4}$$

which represents the extreme case of a point contact cell with the diffused areas covering a negligibly small area.

Plots of the limiting efficiency as a function of cell thickness are given in Figure 4.19 for the important case of 1Ωcm *p*-type silicon. The calculations are for 25°C, where the various assumptions for determining the J_L, the photon recycling rate etc have been described in section 3.4. It can be seen that passivating the surfaces with an alnealed SiO_2 layer results in the highest cell efficiencies, with a peak of 27.4% for a 200μm thick cell. SiN passivated 1Ωcm *p*-type cells also offer a high efficiency potential of upto 27.0% for a 300μm thick cell. Cells passivated with FGA SiO_2 show much lower limiting efficiencies due to the higher S_{eff} values.

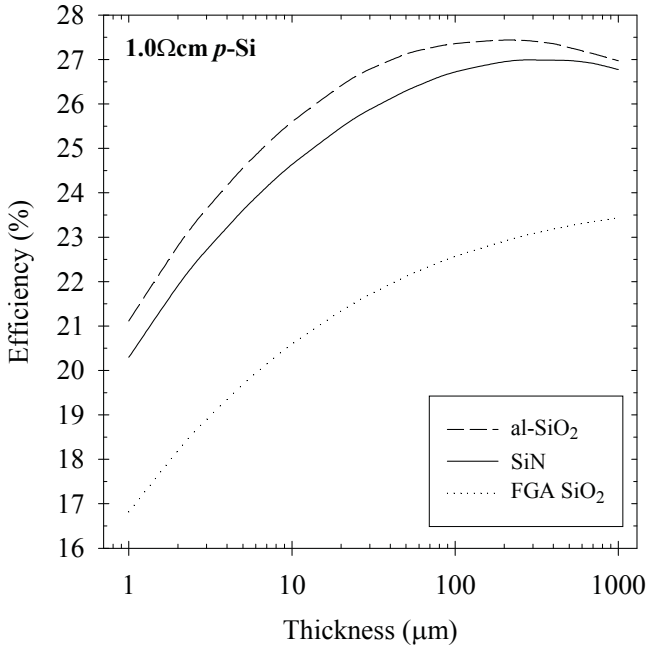


Figure 4.19. Calculated values for the limiting efficiency of a 1Ωcm *p*-type silicon solar cell at 25°C due to surface recombination processes. The $S_{eff}(\Delta n)$ data of Figure 4.17 are used for surfaces passivated with alnealed SiO_2, stoichiometric SiN and FGA SiO_2.

The effect of the dopant density and dopant type on the limiting efficiency of SiN passivated solar cells is shown in Figure 4.20. It can be seen that the maximum efficiency potential is ~27% for relatively thick cells (~300μm) made from 1Ωcm-5Ωcm *p*-type material. Furthermore, *p*-type cells offer slightly higher limiting efficiencies than *n*-type cells. Comparison with Figure 3.16, where there is no surface recombination, shows that surface recombination at the Si/SiN interface significantly lowers the conversion efficiencies and alters the optimum cell thickness and base resistivity for obtaining maximum efficiency.

Practical solar cells will not be able to obtain the very high short circuit current densities calculated in Figure 4.20, where a Lambertian light trapping scheme was assumed. More realistic performance limits for SiN passivated cells can be calculated by assuming a lower J_{sc} of 35mA/cm^2 and 40mA/cm^2, which, based on the experimental measurements presented in Chapter 6, are representative of what can be achieved with a planar surface and pyramidally textured surface respectively. Table 4.2 shows calculated values for the performance limits of a 400μm thick cell for different resistivity wafers. It can be seen that the SiN films studied in this work are suitable for the fabrication of high-efficiency solar cells. Open-circuit voltages >700mV appear to be possible for all the substrate resistivities investigated and both dopant types. Interestingly, the obtainable V_{oc} appears to decrease slightly with increasing doping density for *n*-type silicon, while for *p*-type silicon there is a weak maximum for resistivities of ≈5Ωcm. The effect of the $S_{eff}(\Delta n)$ dependence on the fill-factor is relatively small with fill-

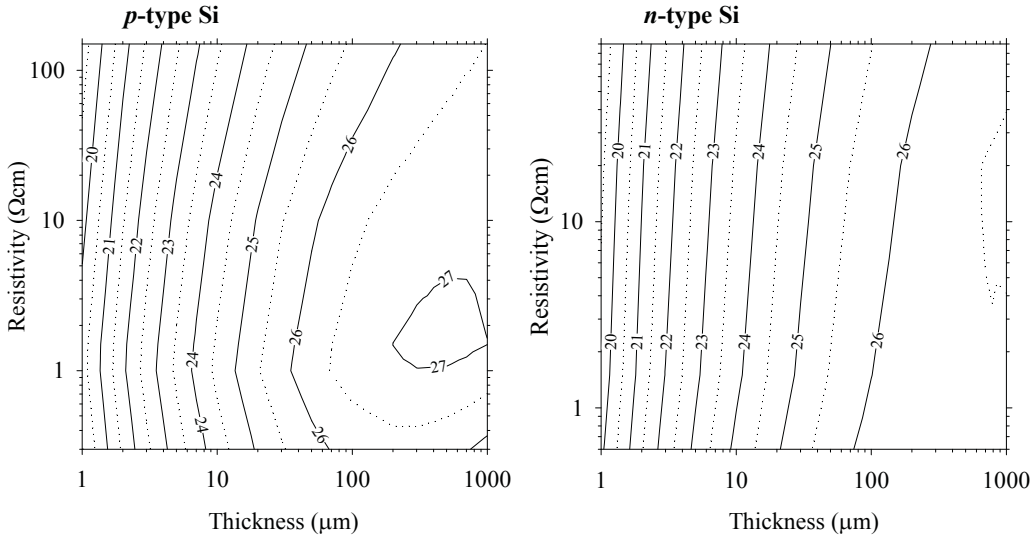


Figure 4.20. Effect of base resistivity and cell thickness on the limiting efficiency of SiN passivated solar cells for *p*-type and *n*-type silicon. Recombination at the Si/SiN interface significantly lowers the limiting efficiency compared to the case of no surface recombination, and also alters the optimum cell thickness and resistivity for obtaining the maximum efficiency.

factors in the range of 82-84% obtainable. The general trend is for a slight increase in implied fill-factor as the doping density increases, an outcome of the $S_{eff}(\Delta n)$ dependence being flatter as the doping density increases. The surface recombination limit to the efficiency potential of SiN passivated cells is approximately constant at around 21% for planar cells and 24% for textured cells. There appears to be a slight increase with doping density, mainly due to the fill-factor, but given that the increased short-circuit current that would be possible from higher resistivity material has not been considered, this trend is not considered to be significant. Importantly, the above analysis does not consider additional losses that would occur in the cell emitter, at the metal contacts or at the cell periphery, nor series resistance effects, which would lower the V_{oc} and cell efficiency below the values calculated above.

4.3.7 Conclusions

Record high effective lifetimes of 10ms have been measured for silicon nitride passivated, high resistivity *n*-type and *p*-type silicon substrates, resulting in S_{eff} values as low as 1 cm/s being unambiguously determined. Low S_{eff} values have also been determined for more heavily doped silicon using stoichiometric, high-frequency direct PECVD SiN films, comparable with the S_{eff} values for other Si-rich silicon nitride passivation schemes. The $S_{eff}(\Delta n)$ dependence of these stoichiometric SiN films has been shown to be nearly constant for *n*-type silicon under low injection conditions. For *p*-type silicon, there is a clear minimum to S_{eff}

Table 4.2. Performance limits imposed by surface recombination for 400μm thick high-efficiency SiN passivated solar cells illuminated under one sun conditions. Short circuit current densities of 35mA/cm^2 and 40mA/cm^2 have been assumed to be representative of planar and textured solar cells.

Resis. (Ωcm)	Dopant type	J_{sc} Limit of 35mA/cm^2			J_{sc} Limit of 40mA/cm^2		
		V_{oc} (mV)	Fill-factor (%)	Efficiency (%)	V_{oc} (mV)	Fill-factor (%)	Efficiency (%)
90	*n*	713	82.0	20.5	717	82.4	23.6
20	*n*	712	83.1	20.7	716	83.3	23.8
1.5	*n*	706	84.4	20.8	709	84.5	24.0
0.6	*n*	703	84.7	20.8	706	84.7	23.9
150	*p*	716	82.2	20.6	721	82.3	23.7
10	*p*	721	83.4	21.1	725	83.8	24.3
4.5	*p*	720	83.4	21.0	724	83.4	24.2
1.5	*p*	719	84.9	21.4	722	85.0	24.6
1.0	*p*	719	84.6	21.3	722	84.7	24.5
0.4	*p*	710	83.7	20.8	714	83.7	23.9
0.3	*p*	706	84.4	20.9	710	84.4	24.0

for injection levels close to the doping density, while the $S_{eff}(\Delta n)$ dependence appears to weaker than that of high quality, silicon rich SiN films prepared by remote PECVD. A simple physical model, whereby recombination at the Si/SiN interface is determined by a large fixed positive charge density within the SiN film, can be used to fit the injection level dependent S_{eff} reasonably well for most of the wafers investigated. Although this simple model breaks down for the most heavily doped *p*-type wafers (N_A~$5x10^{16}cm^{-3}$) in this study.

A comparison of the surface passivation obtained with optimised SiN films and thermal SiO_2 (FGA and alnealed), shows that the alnealed SiO_2 films give the best surface passivation, while the SiN films give significantly better surface passivation than FGA SiO_2 for $N_{dop}>10^{15}cm^{-3}$. Based on measured surface recombination velocities for the Si/SiN interface, open-circuit voltages in excess of 700mV appear possible for SiN passivated solar cells fabricated on *n*-type or *p*-type substrates with a wide range of doping densities. The surface recombination limit to the efficiency potential of SiN passivated solar cells is ~21% for planar cells and 24% for textured cells when short circuit current densities of 35mA/cm^2 and 40mA/cm^2 respectively are assumed.

4.4 Characterisation and Thermal Stability of the Optimal SiN Films

The excellent surface passivation properties reported in the previous section for stoichiometric SiN films makes them highly promising for use in high efficiency solar cells. The fabrication of high efficiency solar cells, such as PERC or PERL cells, requires that the SiN films have additional properties however including: (a) low absorption from the solar spectrum allowing a high current density to be obtained; (b) the ability to locally open the SiN films so that point contacts can be formed at either the front or rear surface and (c) stability of the surface passivation at the temperatures required to form and sinter the metal contacts (~400°C).

4.4.1 Absorption Coefficient

The wavelength dependent extinction coefficient, k(λ), of some of the SiN films was also determined from reflectance data and by spectral ellipsometry (see section 4.2.2.3). From this, the absorption coefficient, α(λ), was calculated from $\alpha=4\pi k/\lambda$. Figure 4.21 shows the wavelength dependence of the absorption coefficient for an optimised stoichiometric SiN film and a silicon-rich SiN film with refractive indices of 1.95 and 2.15 at λ=630nm, respectively. It can be seen that the silicon-rich SiN film shows a pronounced absorption in the ultraviolet range of the solar spectrum, whereas the optimised stoichiometric SiN film does not absorb any UV photons with wavelengths above 320nm. The reduced absorption of the well passivating stoichiometric SiN films improves the solar cell short-circuit current density by 0.5-1mA/cm^2 at 1 sun (AM1.5G spectrum) in comparison to the silicon-rich SiN films investigate by Lauinger *et al.* [114, 116].

Stoichiometric SiN films have the optimum refractive index for a single layer antireflection coating (SLARC) on silicon, such as for laboratory solar cells. For the important case of a glass encapsulated solar cells which are used in industry, the optimum refractive index for a non-absorbing SLARC on silicon is ~2.3. Increasing the refractive index of the SiN films above 1.95 for glass encapsulated solar cells therefore results in lower reflection losses, but also results in increased absorption losses. It is calculated that the refractive index of the stoichiometric SiN films of this study would result in a short-circuit current loss of 1mA/cm^2 for a glass encapsulated solar cell. This is equivalent to the loss that would be incurred by absorption in a silicon-rich SiN film with n=2.3 [114]. Indeed, Duerinckx and Szlufcik have very recently concluded from experiments, that the refractive index of SiN films used for front surface passivation of glass encapsulated solar cells should be limited to a value of 2.0, or the

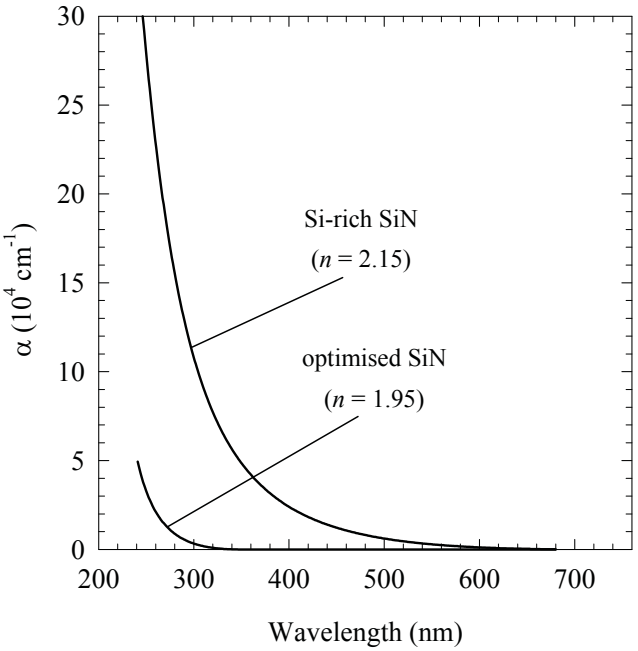


Figure 4.21. Measured absorption coefficient, α, of a stoichiometric and a silicon-rich SiN film prepared using dilute silane. The refractive index of the SiN films at λ=630nm are indicated.

benefits from reduced reflection are overcompensated by the increased absorption losses [127]. The stoichiometric SiN films developed in this thesis using dilute silane gas, therefore appear to offer both excellent surface passivation and near ideal optical properties even for glass encapsulated solar cells. Importantly, when using pure silane gas, literature data indicates that the surface passivation is degraded when the refractive index is limited to 2.0. Lauinger *et al.* for example, found a maximum τ_{eff} of ~700μs for n=2.0, which increased to ~1ms for $n \geq 2.3$ [113].

4.4.2 Etch Rates

The etch rates of different SiN films in buffered HF were determined and are compared in Figure 4.22. The etch rate of the well passivating stoichiometric SiN films is ~35nm/min. Given that the required SiN film thickness for good antireflection properties is ~70nm, the required etching time is therefore approximately two minutes. By comparison, the etch rate for a thermally grown SiO_2 film was determined to be 62nm/min and is included in Figure 4.22. A greater thickness of SiO_2 is required for good antireflection properties however (~110nm), and therefore the etching time is also ~2mins. It follows that the optimised stoichiometric SiN films can be easily patterned by means of photolithography and chemical etching, using the same procedures developed for thermal SiO_2.

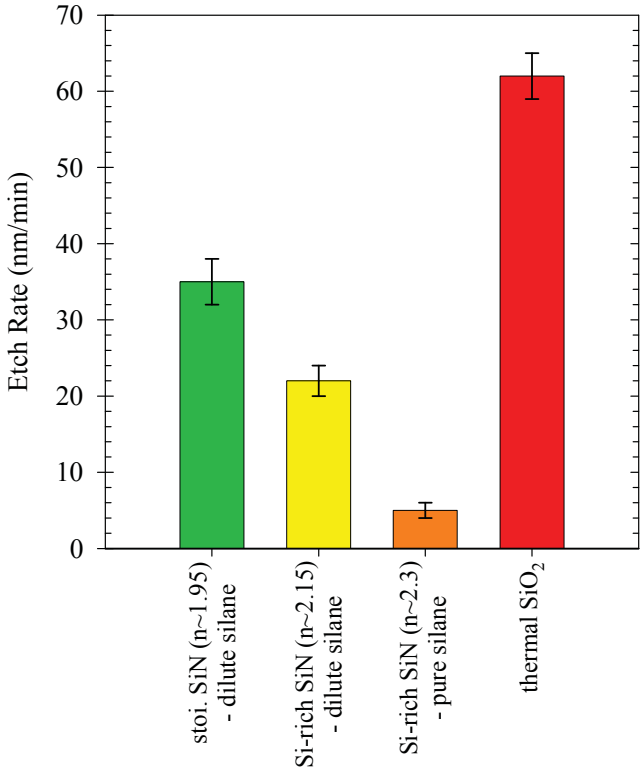


Figure 4.22. Measured etch rates for the various dielectric films in buffered HF. The stoichiometric SiN films of this study can easily be etched and patterned using standard photolithographic techniques.

Lower etch rates were determined for the silicon-rich SiN films, as would be expected [65]. For an n=2.15 silicon-rich SiN film, prepared using dilute silane, the etch rate was determined to be 20-25nm/min. This would require an etching time of ~3mins, and could therefore still be easily patterned. For an n=2.3 silicon-rich SiN film as used by Lauinger *et al.* (pure silane), the etch rate was determined to be ~5nm/min. The required etching time for such a film would be ~12-14mins, which is too long for standard photoresists to withstand the buffered HF and so more sophisticated techniques would be required to pattern these films. Interestingly, Lauinger *et al.* found little difference for the etch rate in buffered HF of their silicon-rich SiN films with refractive indices between 2.1 and 2.4. This suggests that n=2.1 silicon-rich SiN films prepared in these experiments using dilute silane, show a much higher etch rate than similar films prepared using pure silane. As the etch rates of PECVD SiN films are normally attributed to the bonding of the hydrogen atoms [65], this suggests that the hydrogen atoms in SiN films prepared using dilute silane/nitrogen mixture are bonded differently than in SiN films prepared using pure silane.

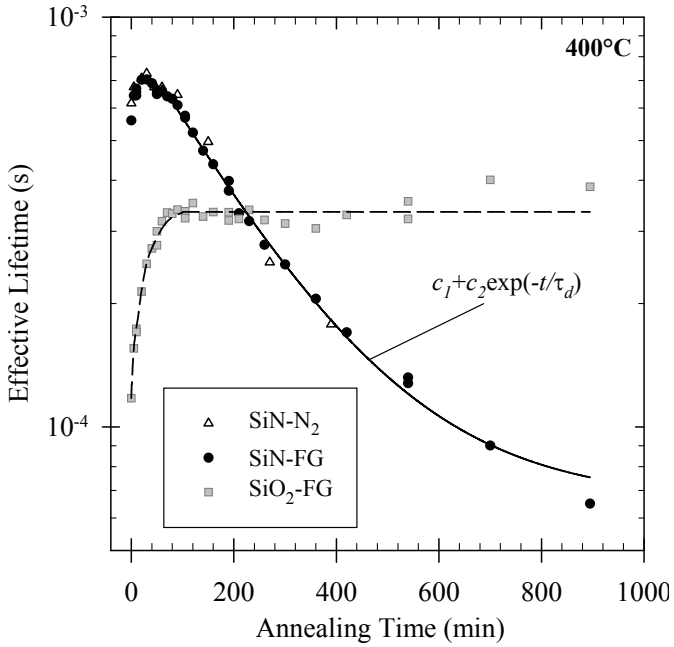


Figure 4.23. Annealing behaviour of the effective lifetime at 400°C for 1Ωcm *p*-type silicon wafers passivated by stoichiometric SiN films and thermally grown SiO_2.

4.4.3 Thermal Stability

A general problem with the surface passivation of PECVD SiN films is the poor stability of the passivation quality during annealing treatments [114]. As the annealing behaviour of the surface passivation can be of considerable importance for a potential solar cell fabrication process, the thermal stability of our optimised stoichiometric SiN films has been investigated. Figure 4.23 shows the annealing behaviour of the optimised SiN passivation in both forming gas (5% H_2, 95% Ar) and nitrogen at 400°C, an annealing treatment routinely used in solar cell processing for sintering the metal contacts. The annealing behaviour for a thermally oxidised silicon wafer at 400°C in forming gas is included for comparison. It can be seen that the behaviours of the plasma SiN and the thermal SiO_2 passivation are very different. The effective lifetime of the oxidised silicon wafer increases during the first 50mins of the anneal and then saturates to a constant lifetime value. The increase in τ_{eff} is attributed to the hydrogenation of the silicon dangling bonds at the Si/SiO_2 interface. For the SiN passivated wafer, the lifetime increases during the first 30mins of the anneal and then decreases with time following an exponential law. The same behaviour was observed for SiN passivated silicon wafers annealed in a nitrogen ambient instead of forming gas. From this comparison, it is concluded that, in contrast to the thermally oxidised silicon surface, the forming gas is not actively involved in the annealing process. Hence, the large reserviour of hydrogen in the silicon nitride (~15-20 at.%) seems to be responsible for the initial increase of τ_{eff} with the annealing time. Within the bulk of

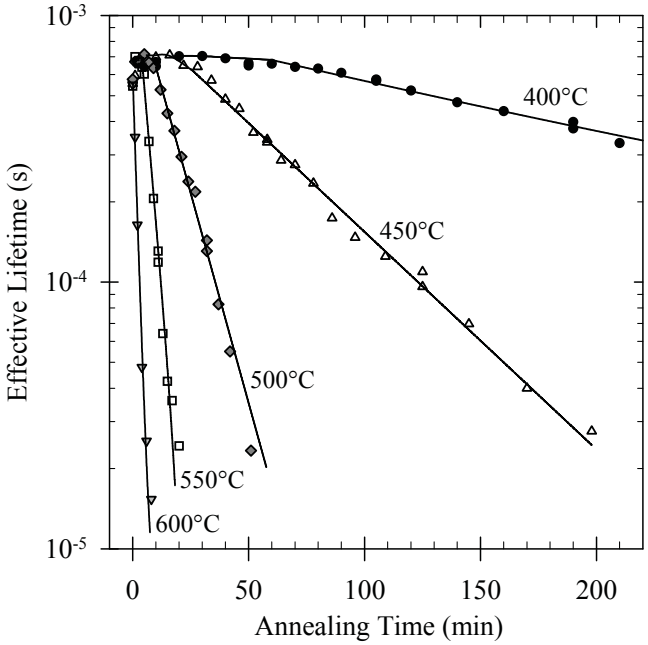


Figure 4.24. Thermal degradation of the effective lifetime of SiN passivated 1Ωcm *p*-type silicon wafers at different temperatures.

the SiN film the hydrogen is present in the form of Si-H and N-H bonds, where the weaker N-H bonds break up more easily than the stable Si-H bonds during annealing. The hydrogen set free from the N-H bonds appears to passivate the silicon dangling bonds at the Si/SiN interface and within the bulk of the SiN, thereby decreasing the surface recombination rate at the Si/SiN interface and, consequently, increasing τ_{eff}. As two kinds of N-H bonds with very different bonding energies exist in SiN [128], mainly the weak type of N-H bonds are expected to break up and the density of the strong N-H bonds remain unchanged. As soon as all the weak N-H bonds are dissociated, the dominant dissociation process becomes the breaking up of Si-H bonds. During this process, new silicon dangling bonds are created at the Si/SiN interface and τ_{eff} degrades.

In order to improve the understanding of the physical mechanism behind the thermal degradation, annealing experiments were performed at different temperatures and are shown in Figure 4.24. The time constant, τ_d, of the degradation process was determined as a function of the annealing temperature, T, by fitting a single-exponential function $c_1+c_2exp(-t/\tau_d)$ to the measurements. It can be seen that τ_d is strongly temperature dependent, reducing from 190mins at 400°C to only 2mins at 600°C. Figure 4.25 shows an Arrhenius plot of the degradation time constant. From this plot, the activation energy of the degradation process is determined to be $E_a \approx 1.2$eV. This value is in good agreement with the activation energy reported by Lauinger *et al.* [114]. However, it is about twice as large as the activation energy reported for the dissociation

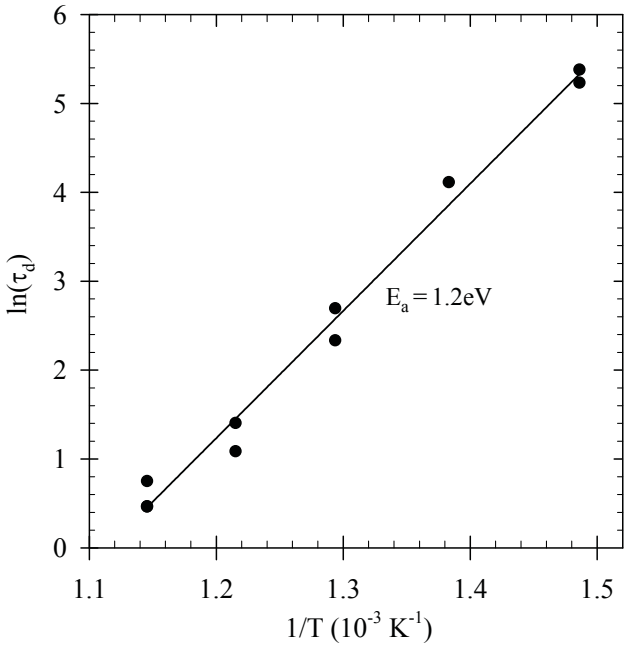


Figure 4.25. Arrhenius plot of the degradation time constant τ_d.

of the Si-H bond [128], which indicates that the mechanism responsible for the thermal degradation of the SiN passivation quality is probably more complicated than previously assumed. Further experimental investigations seem to be necessary to reveal the detailed mechanism of the thermal degradation process.

4.5 Chapter Summary

The surface recombination properties of well passivating SiN films on *p*-type and *n*-type silicon wafers have been investigated in this chapter. The PECVD deposition parameters were optimised for passivating silicon surfaces, with the deposition temperature, gas flow ratio and process pressure identified as the most significant parameters. The optimised SiN films are unique in the fact that they are stoichiometric in composition, rather than being silicon-rich, which was previously thought to be required to obtain good passivation from SiN films. The injection-level dependence of the effective lifetime and the S_{eff} has been investigated for a range of *n*-type and *p*-type wafers passivated with the optimised stoichiometric SiN films. Record high effective lifetimes of 10ms have been measured for SiN passivated, high resistivity *n*-type and *p*-type substrates, resulting in S_{eff} values as low as 1cm/s being unambiguously determined. The $S_{eff}(\Delta n)$ dependence was shown to be nearly constant for *n*-type silicon under low injection conditions, while for *p*-type silicon, there is a clear minimum to S_{eff} for injection levels close to the wafer dopant density. A simple physical model has been proposed, whereby the

recombination at the Si/SiN interface is determined by a large fixed charge density within the SiN film (even under illumination), and has been used to fit the injection level dependent S_{eff} reasonably well for most of the wafers investigated.

The surface passivation obtained with the optimised SiN films and with thermally grown SiO_2 (FGA and alnealed) has been compared for both *n*-type and *p*-type silicon. It has been shown that alnealed SiO_2 gives the best surface passivation for all dopant densities, while the SiN films give significantly better surface passivation than FGA SiO_2 for $N_{dop}>10^{15}cm^{-3}$. The efficiency limits imposed by surface recombination for SiN passivated solar cells has been determined as a function of cell thickness, dopant density and dopant type. Open-circuit voltages in excess of 700mV appear possible, along with an efficiency potential of ~21% and ~24% for planar and textured cells respectively, based on reasonable estimates for the short-circuit density.

Additional properties of the optimised stoichiometric SiN films have been investigated. It has been demonstrated that they show little absorption of UV photons from the solar spectrum and that they can be easily patterned by means of photolithography and chemical etching. Studies of the thermal stability showed that the surface passivation provided by the SiN films is stable during the standard contact sinter used for laboratory cells (<30mins at 400°C), but degrades at higher temperatures.

These stoichiometric SiN films therefore have useful properties for fabricating high V_{oc} and high efficiency solar cells. Importantly, most solar cells also have large areas of n^+ and p^+ diffused emitter regions, and passivating diffused regions is the topic of the next chapter. Although the emphasis is on n^+ emitters, which are prevalent in today's cells, p^+ emitters are also investigated for completeness and to better understand the overall electronic behaviour of SiN films.

CHAPTER 5

Passivating Diffused Emitters

5.1 Introduction

Diffused regions are used in silicon solar cells for many purposes. Their main use is to form an emitter or p-n junction to collect and separate the photogenerated carriers. A voltage can then be established within the device due to the separation of the quasi-Fermi levels, and an electric current extracted. Other important uses of diffused regions in solar cells depend on the cell design and include:

- Contact facilitation – Metal contacts are normally used to extract the electric current from a solar cell. The formation of good quality, ohmic contacts is aided when the work function difference between the metal and the silicon is low, as tunneling is facilitated. This occurs when the silicon is heavily doped.

- Contact passivation – Metal contacts are areas of high surface recombination. The recombination rate can be reduced by minimising the concentration of minority carriers in the vicinity of the contact. This can be achieved by using a relatively thick and heavily doped area at the metal contact [25].

- Surface passivation – Reducing the concentration of minority carriers at the surface of non-contacted areas can also reduce surface recombination losses. Heavily diffused regions can be used to repel the minority carriers. The diffused atoms can be the same type (donor or acceptor) as the dopant atoms in the base wafer such as in a back-surface-field or front-surface-field [129]. Alternatively, the diffused atoms can be the opposite type and a *floating junction* can be formed [130].

- Reducing series resistance – The lateral flow of carriers within a solar cell can strongly contribute to the distributed series resistance, particularly if the base dopant density is low, resulting in poor fill-factors. Large area diffused regions, reduce the spreading resistance and therefore the series resistance and are commonly used on the front surface of most solar cells but also at the rear in designs such as for PERT cells [98].

An important factor in the design of the diffused regions for solar cells is the recombination losses occurring within the diffused region and at their surface, which is the topic of this chapter. Emitter passivation is an important aspect of high efficiency silicon solar cells [131, 132] and resulted in the first solar cells with efficiencies greater than 20% [133]. As the majority of solar cells have the emitter on the front surface, not only must the passivating layer reduce the surface recombination to acceptably low levels, it must also be compatible with antireflection coatings to maximize the photogenerated current within the silicon substrate. In the highest efficiency laboratory cells, this is achieved by appropriately annealing a thin, high temperature thermal oxide, and subsequently depositing ZnS/MgF_2 antireflection coatings [134]. For commercial solar cells, a promising technology to simultaneously provide surface passivation and an effective antireflection coating is the PECVD of SiN [135]. PECVD SiN films have the additional benefits that they are deposited at low temperature (≤400°C) and are thus compatible with many other commercial fabrication processes like screenprinted metal contacts [26].

In this chapter, the results from a systematic study of phosphorus-diffused and boron-diffused emitter passivation are presented. Thin (~15nm) high temperature thermal oxides and PECVD SiN films have been investigated for phosphorus emitters, while conventional thermal oxides (~105nm) and SiN films are investigated for boron emitters. Values of the emitter saturation current (J_{oE}) are reported for both planar and textured emitters suitable for laboratory and commercial solar cells (sheet resistivities ranging from ≈30-430Ω/□). For the phosphorus emitters, the doping profiles of the planar samples were measured by means of the Stripping Hall technique and device simulation was used to determine the surface recombination velocity

(S_p) at the highly doped *n*-type silicon interface. Some brief results are also presented for *n*-type industrial emitters formed in a simple belt-line furnace.

5.2 n^+ Emitters

5.2.1 Previous Work

Comprehensive experimental studies for oxide passivated n^+-diffused emitters have been carried out by King *et al.* [131], Cuevas *et al.* [136] and Glunz *et al.* [137]. In general, all three studies show increasing J_{oE} and S_p as the surface phosphorus concentration increases. The effect of post-oxidation anneals using either forming gas (FGA) or aluminium (alneal) is to lower the S_p for a given surface phosphorous concentration (N_s), the lowest surface recombination velocities being obtained for the alnealed condition. Typical values for the S_p of planar emitters are about 800cm/s for N_s=1x10^{19}cm^{-3} following a forming gas anneal and about 400cm/s following an alneal [136]. Textured emitters have typically shown an increase in J_{oE} by a factor of two to three. The increase in J_{oE} being attributed to the increase in surface area of the emitter and the possibility of increased surface recombination on the <111> oriented silicon planes.

Experimental data for PECVD SiN passivated n^+-emitters are less available in the literature. Ruby *et al.* [135] and Chen *et al.* [108] deposited high frequency direct PECVD SiN films onto ≈100Ω/☐ emitters and obtained J_{oE} values of 80 and 220fA/cm^2 respectively. Cai *et al.* [138] reported a J_{oE} of 55fA/cm^2 for a 90Ω/☐ emitter using the same PECVD system as Chen *et al.* as long as the sample was given a post-deposition anneal at 350°C. Lenkeit *et al.* [139] have published J_{oE} data for 40Ω/☐ and 100Ω/☐ emitters for different PECVD methods concluding that remote and high frequency direct PECVD give the best results. Moschner *et al.* [140] also published J_{oE} data for PECVD SiN passivated emitters with sheet resistances of 40Ω/☐ and 90Ω/☐, investigating both planar and textured emitters. Consistent with the studies of oxide passivated emitters, the PECVD SiN studies showed increasing J_{oE} for increased emitter doping, and increased J_{oE} on textured surfaces. There does not appear to be J_{oE} data for SiN passivated emitters at other sheet resistances, particularly for lightly doped emitters (>100Ω/☐). Furthermore, there appears to be no data on the extracted S_p for the highly doped *n*-type silicon/PECVD SiN interface.

Data comparing conventional furnace oxide passivation and PECVD SiN passivation for n^+-emitters have been published by Aberle [26] and Moschner *et al.* [140] for 40Ω/☐ and

90Ω/□ emitters respectively. Both concluded that the passivation achieved by the best PECVD SiN films is comparable to that of a thermal oxide.

5.2.2 Experimental Details

The n^+pn^+ test structures used to investigate the emitter passivation were prepared using shiny etched 50Ωcm *p*-type FZ wafers. Texturing was performed in a mixture of KOH and isopropanol to produce random pyramids, which were ≈10μm in size. All diffusions were performed in a quartz tube at temperatures between 840°C and 925°C using liquid $POCl_3$ as the dopant source. After stripping the phosphorus glass, the samples were oxidised at 900°C for 30mins. This produced a thin oxide layer (≈13nm) and simultaneously drove-in the diffusion. The samples were then divided into four batches:

- Batch 1 – The J_{oE} was measured for the as-oxidized samples, forming gas annealed (FGA) samples and alnealed samples (planar and textured surfaces). The thin oxide layers were stripped using dilute hydrofluoric acid (HF), optimized SiN layers deposited on both sides, and the J_{oE} remeasured (planar and textured surfaces). The low temperature used for the PECVD depositions (400°C) should not result in a significant redistribution in the phosphorous doping profile and so direct comparison of the data for oxide passivated and SiN passivated emitters is valid.

- Batch 2 – Optimised SiN layers were deposited on top of the thin oxide layers (both sides) and the J_{oE} measured (planar and textured surfaces).

- Batch 3 – Si-rich SiN layers were deposited on top of the thin oxide layers (both sides) and the J_{oE} measured (planar surfaces only).

- Batch 4 – The thin oxide layers were stripped using dilute hydrofluoric acid (HF) and the J_{oE} of the unpassivated samples measured (planar surfaces only). A thin transparent layer of aluminium (≈30Å) was then evaporated onto the rear side of the samples only and the J_{oe} re-measured. From these measurements, the J_{oE} of the unpassivated and metallized diffusion can be determined.

The SiN films were fabricated in the same high frequency (13.56MHz), direct PECVD reactor described in the previous chapter. Ammonia (NH_3) and 4.5% silane (SiH_4:N_2) in nitrogen were used as the process gases. Optimised deposition parameters were determined using planar samples with a sheet resistance of 120Ω/□. The J_{oE} was determined using the quasi-steady-state photoconductance method [41, 44] with the samples in high injection

($\Delta n > 1x10^{15}cm^{-3}$), as discussed in section 2.2. The J_{oE} measurements where made at a temperature of 25°C using an intrinsic carrier concentration of $8.65x10^{9}cm^{-3}$. Following J_{oE} measurements on the passivated samples, the passivating layers were etched in dilute HF and the emitter sheet resistance determined using a four-point probe (the sheet resistance for the textured samples was measured on the actual sample). The electrically active phosphorus doping profile for the planar samples was determined using the stripping Hall technique. The semiconductor device simulation program PC1D (ver 5.3) was then used to extract the S_p at the passivated, heavily doped *n*-type silicon surface by adjusting the S_p values in the model so that the measured and calculated J_{oE} coincide.

5.2.3 PECVD SiN Deposition Parameters

Similar to the optimisation study for doped wafers (see section 4.2), the deposition parameters optimised were the substrate temperature, the gas flows, the silane to ammonia gas flow ratio $[SiH_4:N_2]/[NH_3]$, the total gas pressure and the plasma power. Only main effects were studied with interactions assumed to be small.

5.2.3.1 Effect of Deposition Temperature and Gas Flow Ratio

Substrate temperature and gas flow ratio were again found to be the most important deposition parameters with their effects shown in Figure 5.1. A minimum in J_{oE} occurs for a high ammonia flow (50sccm), with a gas flow ratio between 6 and 9. Also, higher substrate temperature leads to lower J_{oE}. The global minimum for J_{oE} occurs for temperatures above 400°C, which could not be attained in these experiments. The optimal deposition temperature and gas flows for minimising recombination at the surface of a phosphorus diffused emitter are therefore the same as was found for passivating *p*-type wafers in the previous chapter. The refractive index (n) of some of the SiN films are included in Figure 5.1(a) and again show that stoichiometric SiN films (n~1.95) provide the best passivation for the gas system used here (4.5% SiH_4 in N_2 and 100% NH_3). As mentioned previously, these stoichiometric SiN films are suitable as a single layer anti-reflection coating (SLARC) for non-encapsulated solar cells and their high hydrogen content allows them to be patterned using standard photolithography and wet chemical etching.

5.2.3.2 Effect of Process Power and Process Pressure

The effect of process power and pressure are minimal as can be seen in Figure 5.2. A higher process power results in a higher deposition rate and therefore process powers in the range of 125-150W are preferred. For the process pressure, higher process pressures improve

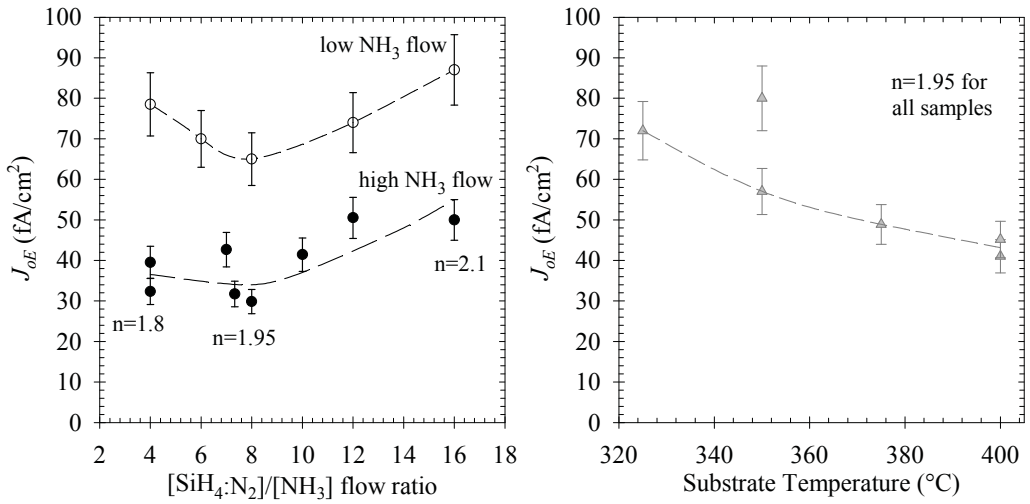


Figure 5.1. Effect of the: (a) silane/nitrogen-to-ammonia gas flow ratio and (b) deposition temperature on the J_{oE} of SiN passivated emitters. The refractive index (n) of some samples is indicated.

the film homogeneity and also give a higher deposition rate. Therefore pressures in the range of 0.6-1.0Torr appear optimal. Plasma instabilities were sometimes observed for pressures at the upper end of this range and so a process pressure of 0.6Torr was preferred. Furthermore, there appears to be a slight increase in the J_{oE} for pressures above 0.6Torr when non-optimal gas flows are used.

Comparing with the results in Chapter 4 for doped wafers, the effect of process power was also minimal with a weak maximum for 125W. The effect of process pressure is distinctly different for doped wafers and diffused emitters however. For the doped wafer (see Figure 4.4), superior passivation was clearly found at lower process pressures. The fundamental reason for this different behaviour is not known, although it is clear that the surface defects are being effected in such a way that the heavily doped emitter surface is not sensitive too.

It is important to note that the optimal films have been considered to be those with the lowest J_{oE}. These are not necessarily the best films for solar cell applications. While the high refractive index films do not offer quite as good a J_{oE}, they are suitable for the first layer of a DLARC or as a SLARC for glass encapsulated solar cells. High refractive index SiN films may therefore result in a nett increase in cell efficiency due to increased photogeneration when compared to the lowest J_{oE} films.

5.2.3.3 Comparison with Previous Work

Optimisation studies of the PECVD deposition parameters for SiN passivation of solar cell emitters have been presented by a number or authors [135, 138, 139]. Different PECVD

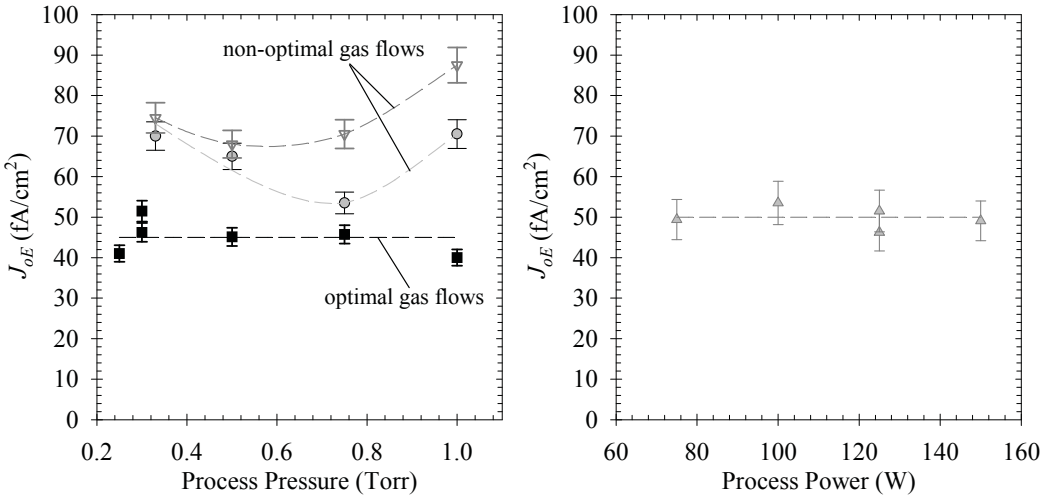


Figure 5.2. Effect of the: (a) process pressure and (b) process power on the J_{oE} of SiN passivated emitters.

systems and different concentrations for silane gas were used. A consistent conclusion from the various studies was that higher temperature results in the lowest J_{oE}, an outcome also observed here. Cai *et al.* [138] have reported that lower process power and higher process pressure result in a lower J_{oE}, which they attribute to surface damage. The same trends were not observed here with both pressure and power having a minimal effect on J_{oE} for our films. Both Ruby *et al.* [135] and Lenkeit *et al.* [139] observed a strong correlation between the J_{oE} and the refractive index of the SiN films, with a higher refractive index ($n \geq 2.4$) resulting in better surface passivation. Such a correlation is not observed here, where stoichiometric SiN films give a lower J_{oE}. Interestingly, Lenkeit *et al.* found that for stoichiometric SiN films, the optimal deposition temperature was 300-350°C with higher temperatures reducing the surface passivation. The difference in the results is attributed to the fact that we used 4.5% silane in nitrogen while Lenkeit *et al.* used pure silane. As with the passivation of *p*-type surfaces, this again suggests that it is possible to vary the silane carrier gas composition to achieve the lowest J_{oE} at any desired refractive index between $n \approx 1.9$ (dilute silane in nitrogen) to $n \geq 2.4$ (pure silane). This ability to independently optimise the passivation quality and the optical properties of the SiN films is important to the commercial application of PECVD SiN films for solar cells, particularly for the emitter surface which is usually exposed to the light.

5.2.4 Passivation Results and Discussion

5.2.4.1 J_{oE} measurements for planar SiN passivated samples

The effect of sheet resistance on the J_{oE} of SiN passivated, phosphorus diffused emitters is shown in Figure 5.3. The range of sheet resistances covered is from 30-430Ω/□. This

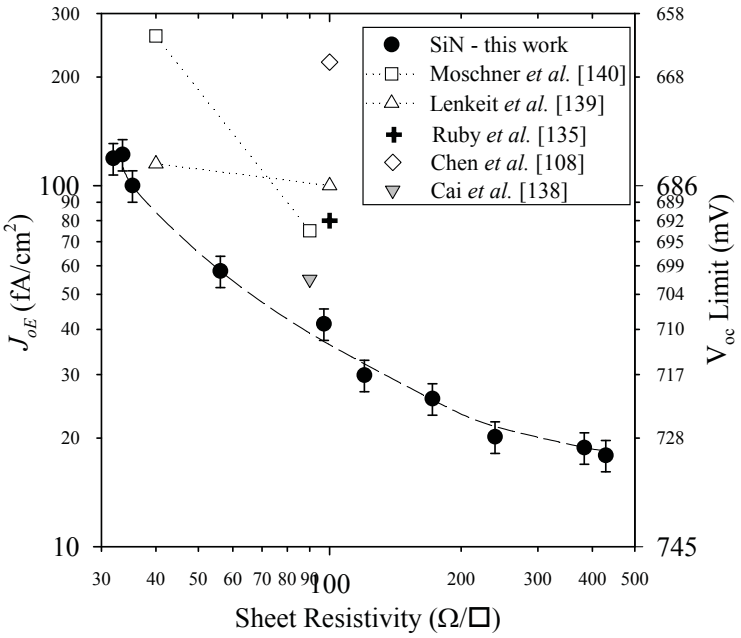


Figure 5.3. Effect of sheet resistance on the J_{oE} of SiN passivated phosphorus diffused emitters with a planar surface.

covers: i) emitters which can accommodate screen-printed contacts (≈40Ω/□); ii) high efficiency homogenous emitters suitable for evaporated contacts (≈100Ω/□); and iii) transparent, lightly doped emitters as would occur at un-contacted sections of a selective emitter structure (>150Ω/□). The error bars in the figure represent an estimated error of ±10% in the J_{oE} value. The dashed line is included as a visual guide.

As expected, the J_{oE} increases as the sheet resistance decreases. J_{oE} values as low as ≈20fA/cm^2 have been measured for lightly doped emitters and ≈100fA/cm^2 for industrial like emitters. Assuming a short circuit current density of 40mA/cm^2, these J_{oE} values limit the open circuit voltage of a solar cell to 727mV and 686mV respectively (not including recombination in the bulk or at the contacts). The surface passivation of these PECVD SiN films is clearly very good. It is worthwhile mentioning that emitter passivation provided by the PECVD SiN films was not altered by either a forming gas anneal for 30 minutes at 400°C nor by an anneal in nitrogen gas for 30mins at 400°C.

Included in Figure 5.3 are data for other PECVD SiN passivated solar cell emitters obtained from the literature. While the diffusion profiles, PECVD deposition parameters, mode of plasma excitation and method for measuring J_{oE} are different for some of these data, the J_{oE} values using the optimised SiN films of this study compare favourably with other SiN films.

5.2.4.2 J_{oE} measurements for planar thin oxide passivated samples

The effect of sheet resistance on the J_{oE} of planar, thin oxide samples is shown in Figure 5.4. The data for the SiN passivated samples are included for comparison. Again, the J_{oE} increases as the sheet resistance decreases as expected. Furthermore, while the SiN films offer good passivation, it can be seen that a thin oxide offers superior passivation, particularly when the oxide is FGA or alnealed. Indeed, for the alnealed oxides, J_{oE} as low as 5-10fA/cm^2 have been measured for sheet resistances above 200Ω/□. The very low J_{oE} values measured for lightly doped emitters with an alnealed thin oxide are comparable with the values published by King *et al.* [131] and Cuevas *et al.* [136]. At lower sheet resistances, where the emitters are more opaque, there is minimal difference in the passivation quality of the SiN films compared to any of the oxide films. This is a significant result, as it indicates that on industrial like emitters, PECVD SiN films are capable of passivating the surface as well as the best solid film passivation schemes available.

Another highly effective passivation scheme is the thin oxide/SiN stack as used by Moschner *et al.* [140]. Figure 5.5 compares the J_{oE} of alnealed thin oxides with oxide/SiN stacks. Data for both optimal SiN (n≈1.95) and Si-rich SiN (n≥2.1) have been included. It can be seen that the three passivation schemes are all outstandingly good and essentially equivalent. This suggests that the effect of the SiN layer on the thin oxide is similar to that of an annealed aluminium layer and it is therefore likely that atomic hydrogen in the SiN layer is diffusing to the silicon/SiO_2 interface and passivating dangling bonds. Furthermore, for these oxide/SiN stacks, the Si-rich SiN stack would be superior due to the potentially better antireflection properties if used in a DLARC or after encapsulation under glass.

5.2.4.3 J_{oE} measurements for textured samples

The measured J_{oE} values for random pyramid textured samples passivated with SiN layers and thin thermal oxides are shown in Figure 5.6. For the SiN passivated emitters, the J_{oE} values range from 47-105fA/cm^2 as the sheet resistance decreases from 380-50Ω/□. Again, this emitter passivation is very acceptable, with the open circuit voltage limited to between 685-705mV depending on the emitter sheet resistance. Comparison of the data in Figure 5.4 and Figure 5.6 for SiN passivated emitters indicates that the J_{oE} increases by a factor of 1.5-2.5 when going from a planar to a textured surface. This is similar to the increase measured by Moschner *et al.* [140] and is consistent with the increase in surface area by a factor of 1.73 compared to a planar surface, and the possibility of an increased surface recombination rate for <111> silicon planes.

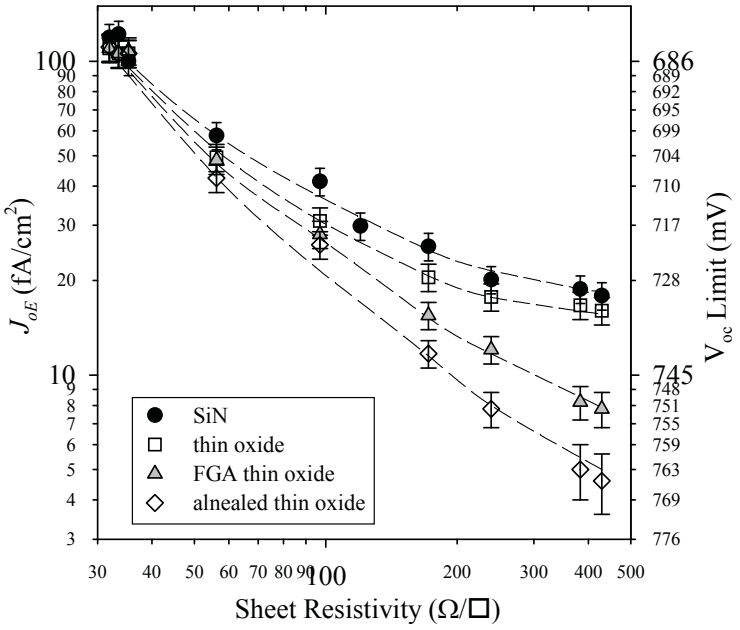


Figure 5.4. Comparison of the J_{oE} of phosphorus diffused, planar emitters passivated with PECVD SiN and thin thermal oxides.

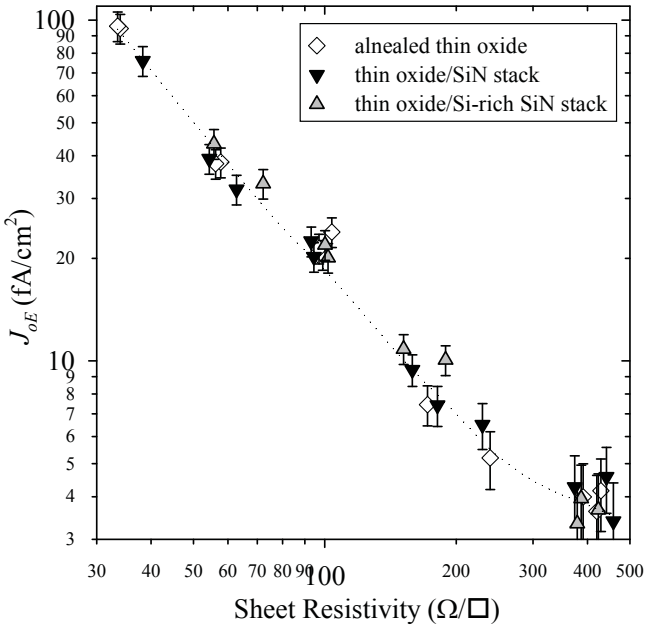


Figure 5.5. Comparison of the J_{oE} of phosphorus diffused, planar emitters passivated with alnealed thin thermal oxides and oxide/SiN stacks.

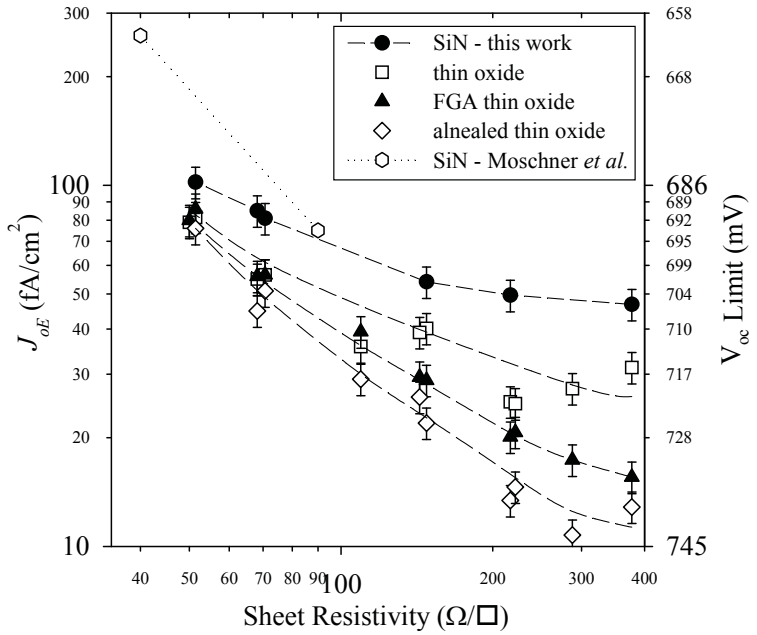


Figure 5.6. Comparison of the J_{oE} of phosphorus diffused, textured emitters passivated with PECVD SiN and thin thermal oxides.

The data in Figure 5.6 for oxide passivated emitters again shows that thin oxide passivation is superior to SiN passivation. Similarly, an alnealed oxide is superior to a FGA oxide, which is superior to the as-oxidised samples. Also, the thin oxide/SiN stack gave comparable passivation to the alnealed oxide samples. The lowest J_{oE} measured for textured samples (the alnealed oxide) was ≈12fA/cm^2 for sheet resistances above 300Ω/□. The increase in J_{oE} when comparing textured and planar oxide passivated samples was a factor of 1.5-2.5, the same as for the SiN samples. It appears that the ratio of J_{oE} for a textured emitter to the J_{oE} for a planar emitter of the same sheet resistance increases as the sheet resistance increases.

5.2.4.4 J_{oE} measurements for planar unpassivated samples

The effect of sheet resistance on the J_{oE} of unpassivated and metal coated, phosphorus-diffused emitters with a planar surface is shown in Figure 5.7. It can be seen that without a passivating layer, increased sheet resistance results in increased J_{oE}. This is the opposite behaviour to that of passivated emitters, and is consistent with the results of other studies [136]. The increase in J_{oE} with sheet resistance for un-passivated emitters results from the fact that only the electric field associated with the gradient of the dopant profile is acting. The more heavily doped emitters provide a greater barrier to the diffusion of holes to the n^+-doped surface and therefore show lower J_{oE}.

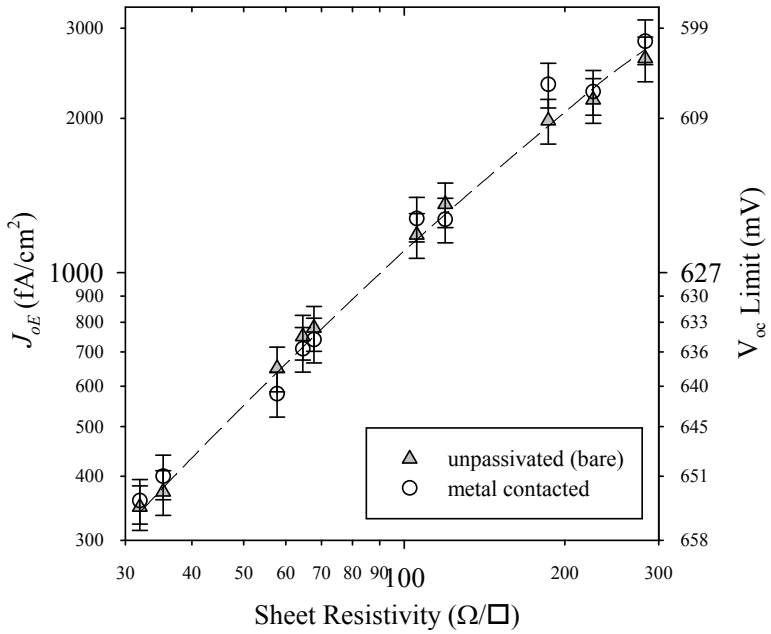


Figure 5.7. Effect of sheet resistance on the J_{oE} of unpassivated and metal coated, phosphorus diffused emitters with a planar surface.

It can also be seen from Figure 5.7 that there is little difference in the recombination properties of the un-passivated and metal contacted emitters. Furthermore, comparing Figures 5.4 and 5.7 show that even for the more heavily doped emitters (N_{surf} ~ $2x10^{20}cm^{-3}$), a SiN or thin oxide passivating layer still results in a significant reduction of the J_{oE} ($J_{oE,pass}$≈120fA/cm^2 c.f. $J_{oE,unpass}$≈400fA/cm^2). If the SiN films relied solely on fixed positive charges near the Si/SiN interface for surface passivation, then it is unlikely that SiN films would be able to passivate heavily diffused samples well. As the SiN films do passivate heavily doped emitters quite well, this suggests that the SiN films derive some proportion of their surface passivation from reducing the density of interface traps (chemical passivation), particularly for heavily doped surfaces.

5.2.4.5 Electrically active phosphorus profiles

The electrically active phosphorous profile of nine planar samples was determined using the Stripping Hall technique. The profiles for some of the samples are shown in Figure 5.8. The phosphorus surface doping concentration of the profiles ranged from $N_s=7.5x10^{18}cm^{-3}$ to $N_s=1.8x10^{20}cm^{-3}$, with the junction depths ranging from ≈0.25μm to ≈0.8μm respectively. In general, the emitter sheet resistance's determined by integrating the electrically active phosphorus profiles agree well with the values determined using the 4-point probe. The largest discrepancies between the two measurements of emitter sheet resistance are found for the lightly doped emitters, where the 4-point probe measures a heavier sheet resistance (for the

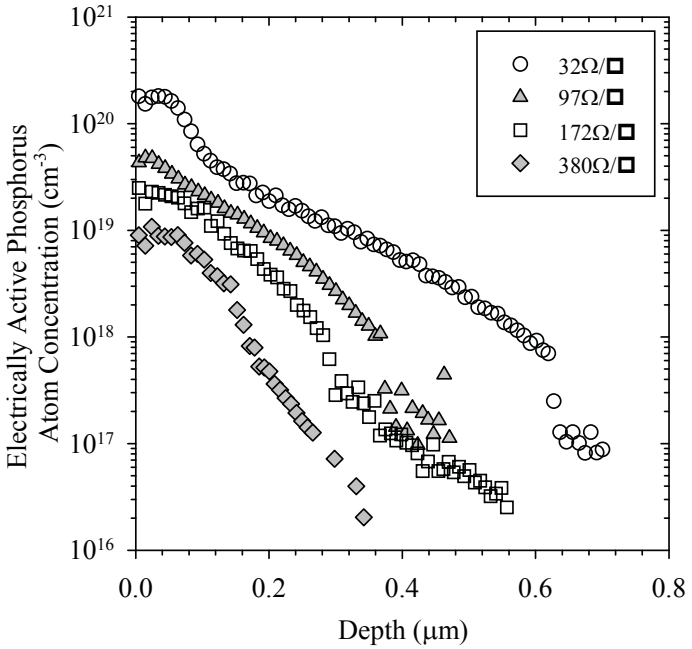


Figure 5.8. Electrically active phosphorus profiles of some of the planar emitter samples used in this study.

lightest doped emitter, the 4-point probe gives 430Ω/□ while the integrated dopant profile gives ≈470Ω/□).

5.2.4.6 Band gap narrowing (BGN) parameters for PC1D

The S_p determined from the measured J_{oE} data is dependent on the model used for the BGN, as the model determines how the recombination losses in the emitter are divided between the bulk of the emitter and at the surface. The semiconductor device simulation tool PC1D uses a simplified band gap narrowing model, while more sophisticated models are possible in three dimensional modelling programs such as used by Altermatt *et al.* [141]. An important aspect to using the model in PC1D is to obtain a self-consistent data set for the BGN parameters and the extracted S_p. To achieve a self-consistent data set, the BGN parameters in PC1D were adjusted so that the measured J_{oE} of the unpassivated, metallized emitters resulted in a S_p of 1×10^7cm/s, which is the thermal velocity limit for silicon [141].

Figure 5.9 shows the apparent band gap narrowing used in this work as a function of doping concentration. The straight line in Figure 5.9 is the default BGN model in PC1D and is taken from Cuevas *et al.* [132]. It can be seen that for the lightly doped emitters, the default BGN model and the model used in this work agree. However, for the more heavily doped emitters, the model used in this work diverges from the default. The effect of this divergence is to reduce the amount of recombination occurring within the bulk of the emitter and therefore the

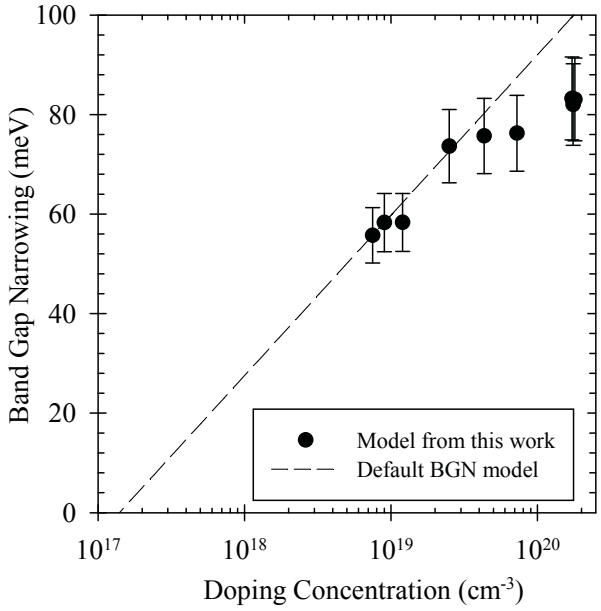


Figure 5.9. Apparent band gap narrowing model determined for the emitters of this work and the default BGN model of PC1D.

S_p extracted using this modified BGN model will be higher than if the default model had been used.

5.2.4.7 Extracted S_p for passivated emitters

Figure 5.10 shows the S_p determined for each of the planar emitter samples for the different passivation schemes. The dashed lines are fits and are described by the expression

$$S_p = aN_s^{\,b} + cN_s^{\,d} \qquad \text{for } 7\text{x}10^{18} < N_s < 2\text{x}10^{20} \qquad (5.1)$$

where the coefficients (a, b, c, d) are given in Table 5.1. Consistent with other studies, S_p increases as the surface doping concentration increases. For SiN passivated emitters, S_p increases from about 1400cm/s to 25000cm/s as N_s increases from $7.5\text{x}10^{18}\text{cm}^{-3}$ to $1.8\text{x}10^{20}\text{cm}^{-3}$. As expected from the J_{oE} data, the S_p at the Si/SiN interface is higher than for the Si/SiO_2 interface for a given surface doping. The lowest S_p values were obtained for an alnealed thin oxide passivation with S_p ranging from 250cm/s to 21000cm/s.

The values determined in this study for the oxide passivated emitters (FGA and alnealed) are in reasonable agreement with the data reported by Cuevas *et al.* [136] and King *et al.* [131] (the results of King have to be revised to account for the new value of n_i), as is shown in Figure 5.11. The small differences in the data sets can be attributed to different processing conditions such as the oxidation temperature (varied from 900°C to 1000°C) and the oxide thickness (from 13nm to 105nm) used in the different studies. Also included in Figure 5.11 are the low injection

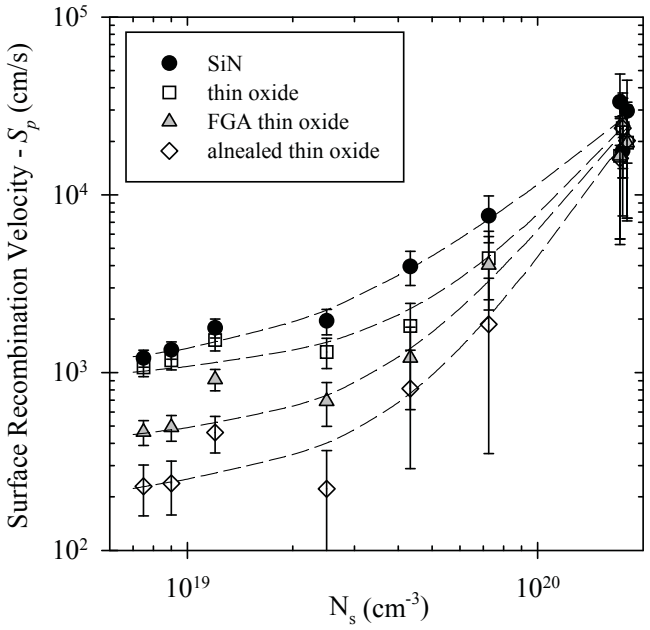


Figure 5.10. Extracted S_p values for the different passivation schemes as a function of the phosphorus surface concentration (N_s) for <100> oriented planar silicon surfaces.

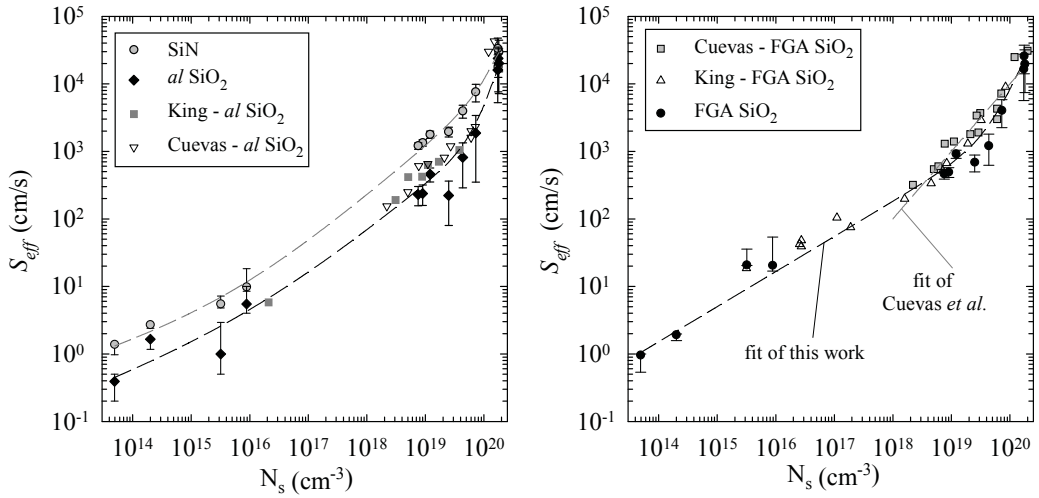


Figure 5.11. Measured values for the low injection S_{eff} for phosphorus doped surfaces passivated with SiN and SiO_2. The data of King *et al.* and Cuevas *et al.* are included for comparison. The dashed lines are parameterised by Eq. (5.1) and the coefficients given in Table 5.1

S_{eff} data from Chapters 3 and 4 for *n*-type doped wafers. The dashed lines are fits to the combined data set using an expression similar to Eq. 5.1 (a third term, gN_s^f, was required to accurately fit the SiN and alnealed SiO_2 data set) for phosphorus surface concentrations covering nearly seven orders of magnitude ($4.9\text{x}10^{13} < N_s < 2\text{x}10^{20}$). The coefficients for the fits to the combined data sets are given in Table 5.1. The most noticeable feature of the fits is that

Table 5.1. Parameterisations for the S_p, or equivalently the low injection S_{eff}, of phosphorus doped <100> silicon surfaces passivated with SiN and SiO_2.

$$S_p = aN_s^b + cN_s^d + eN_s^f$$

	Diffused n^+ emitters of this study (Figure 5.10) for $7*10^{18} < N_s < 2*10^{20}$				Combined data sets (Figure 5.11) for $4.9*10^{13} < N_s < 2*10^{20}$		
	SiN	SiO_2	FGA SiO_2	*al*-SiO_2	SiN	FGA SiO_2	*al*-SiO_2
a	$10^{1.14}$	$10^{-0.02}$	$10^{-0.75}$	$10^{-3.31}$	$10^{-3.9}$	$10^{-7.1}$	$10^{-5.05}$
b	0.101	0.16	0.18	0.3	0.29	0.52	0.34
c	10^{-29}	$10^{-41.2}$	$10^{-44.25}$	$10^{-52.4}$	10^{-11}	$10^{-36.2}$	$10^{-11.2}$
d	1.65	2.25	2.4	2.8	0.74	2.0	0.72
e	-	-	-	-	$10^{-40.28}$	-	$10^{-50.5}$
f	-	-	-	-	2.2	-	2.7

there appears to be two or three distinct regions of different slope, where the S_p values increase more rapidly at higher N_s (the same feature can also be seen in Figure 5.10). This is consistent with the fits proposed by King [64], although the reason for the changing slope remains unclear. King has conjectured that for a heavily doped surface ($N_s \geq 10^{19}cm^{-3}$), the high surface concentration of dopant atoms may result in additional interface traps above those due to dangling bonds alone. The S_p would therefore increase due to the additional interface traps. Indeed, Snell has reported an increasing interface trap density for surface dopant concentrations above $2x10^{17}cm^{-3}$ [142], although the energy dependent capture cross sections are unknown.

Cuevas *et al.* [132] have proposed a much simpler fit of $S_p = N_s*10^{-16}$, where $N_s > 10^{18}cm^{-3}$, for surfaces passivated with a forming gas annealed SiO_2. This fit has been included in Figure 5.11 for comparison. It can be seen that this fit lies within the scatter of the combined data set, but does not show the change in slope which seems evident for $N_s > 10^{19}cm^{-3}$.

5.2.5 Industrial Phosphorus Emitters

The phosphorus emitters studied in the above sections where prepared in a tube furnace using liquid $POCl_3$ as the dopant source. While the surface concentration for phosphorus atoms reached relatively high levels (an electrically active concentration of $\sim 2x10^{20}cm^{-3}$), this is lower than would normally be found for n^+ emitters formed by simple industrial methods. For a commercial belt-line process for example, the surface phosphorus concentration typically reaches the solid solubility of phosphorus in silicon ($\sim 10^{21}cm^{-3}$). Experiments to measure the J_{oE} of emitters formed in an industrial belt-line furnace are described below.

5.2.5.1 Experimental Details

BP Solar fabricates single and multicrystalline silicon solar cells in Sydney. The emitter is formed in a belt-line furnace using vaporized phosphoric acid as the dopant source. The emitter is essentially unpassivated, with a titanium oxide anti-reflection coating. By varying the belt speed and the quantity of phosphoric acid used, a total of six different emitters ranging from relatively heavily doped emitters to more lightly doped emitters were investigated. The belt speeds used where 10ipm (inches per minute), 20ipm and 30ipm, and the dopants weights used where $\approx 56 \mu g/cm^2$ and $\approx 170 \mu g/cm^2$.

High resistivity (50Ωcm), *p*-type float-zone silicon samples where used for the experiments. Initial sample processing was performed at ANU and consisted of shinny etching the wafer to remove any saw damage and passivating the rear surface of the samples with a light phosphorus diffusion (>200Ω/□, tube based using $POCl_3$) and a thick TCA thermal oxide (150nm thick grown at 1050°C). The front surface was etched to be free of any diffusion or oxide, while reference 50Ωcm wafers passivated on both sides with this light n^+ diffusion and thick thermal oxide where also prepared to determine the J_{oE} of the rear surface. The front surface of duplicate sets of samples was diffused in the BP Solar belt-line furnace at a temperature of 870°C. The front phosphorus glass was then removed using dilute HF. Half of the samples received an APCVD TiO_2 coating on the front surface and the other half where passivated with stoichiometric SiN. The sheet resistance of the diffusions where measured by four-point probe after the phosphorus glass had been removed and the J_{oE} of the diffusions where measured after the phosphorus glass had been removed, after the TiO_2 coating and after the stoichiometric SiN deposition. The J_{oE} of the rear passivation was subsequently subtracted to give the J_{oE} of the belt-line diffused emitter.

5.2.5.2 Results and Discussion

Figure 5.12(a) shows the measured sheet resistance for the different diffusion parameters. It can be seen that the emitter sheet resistance can be varied from approximately 50Ω/□ to 90Ω/□. As expected, the sheet resistance decreases as the belt speed is reduced due to the extra time for each wafer in the furnace hot-zone. Surprisingly, increasing the doping weight actually increases the sheet resistance for a given belt speed. This suggests a complex interaction between the formation of the phosphorus glass, the oxide content of the glass and the diffusion of phosphorus from the glass into the silicon substrate. The phosphorus doping profile for one particular 70Ω/□ emitter measured by SIMS is shown in Figure 5.12(b). It indicates that the

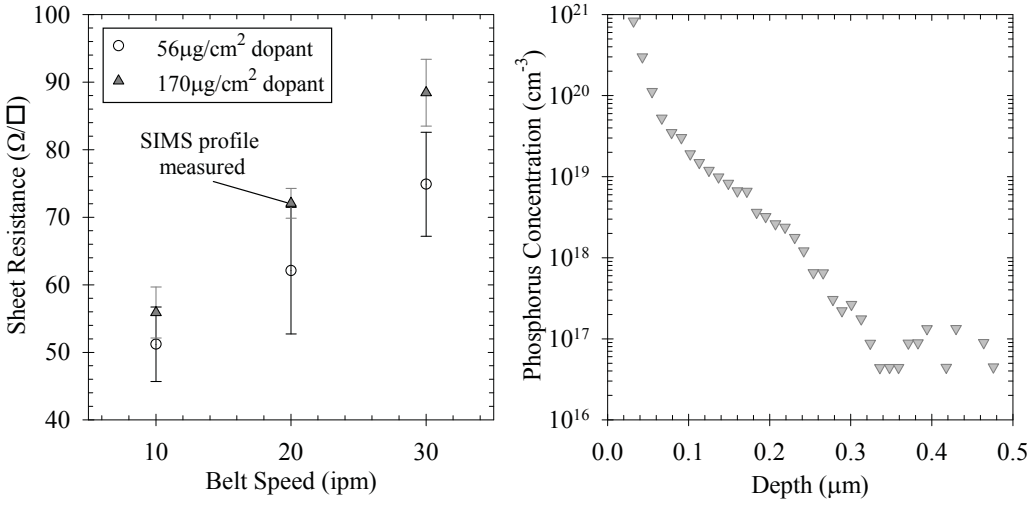


Figure 5.12. Measured sheet resistances of industrial n^+ emitters formed in a beltline furnace. The phosphorus dopant profile, measured by SIMS, is shown for one 70Ω/□ emitter is shown. It can be seen that the surface doping reaches the solid solubility of phosphorus in silicon (~10^{21}cm^{-3}).

surface doping does indeed reach the solid solubility of phosphorus in silicon and that the junction is relatively shallow with a depth of approximately 0.35μm.

The J_{oE} data for the different emitters are shown in Figure 5.13, along with data from section 5.2.4 for SiN passivated and unpassivated n^+ emitters from tube diffusions. It can be seen that even for a silicon surface saturated with phosphorus atoms, the SiN films are still passivating these industrial emitters to a reasonable degree, with a lower J_{oE} than that determined for the bare or TiO_2 coated surface. Interestingly, the TiO_2 films do appear to offer a small degree of passivation compared to the bare surface, although the J_{oE} for the TiO_2 coated surface increases slightly as the sheet resistance increases, which is indicative of a poorly passivated surface. In comparison, the J_{oE} for the SiN passivated industrial emitters decreases as the sheet resistance increases, down to values less than 200fA/cm^2. In terms of a limit to the open-circuit voltage of an industrial solar cell, the standard 55Ω/□ emitter passivated with SiN would be limited to 650mV compared to 639mV for a TiO_2 coating (assuming a J_{sc} of 31mA/cm^2 which is typical for an industrial multicrystalline silicon solar cell). For the lighter 90Ω/□ emitter passivated with SiN, the V_{oc} limit would be 662mV compared to 636mV for TiO_2.

Comparing the J_{oE} data for the SiN passivated industrial and tube based emitters in Figure 5.13 clearly shows that the tube based emitters have better recombination properties. This is because the tube based emitters are deeper and less heavily doped for a given sheet resistance. As shown in section 5.2.4.7., the surface recombination velocity increases with the surface

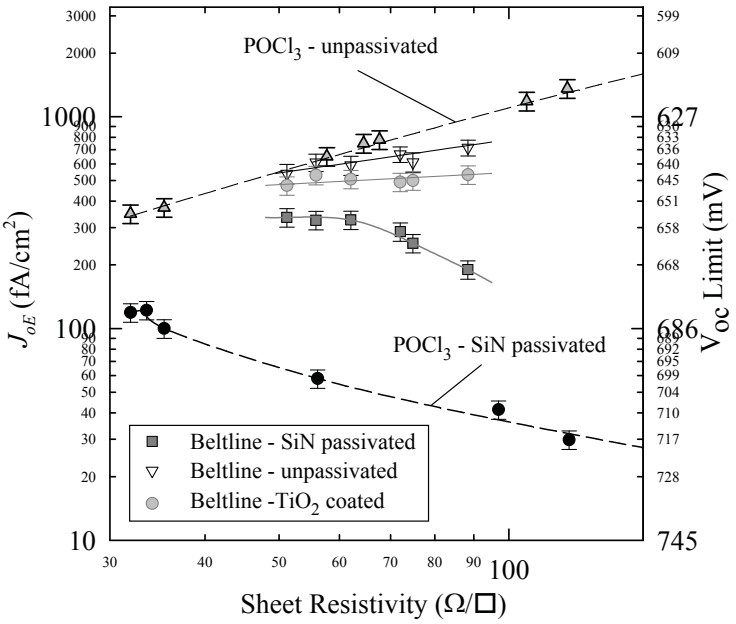


Figure 5.13. Effect of sheet resistance on the J_{oE} of industrial n^+ diffusions with no surface passivation, an APCVD TiO_2 coating and passivated with stoichiometric PECVD SiN. J_{oE} data for unpassivated and SiN passivated n^+ diffusions prepared using $POCl_3$ in a tube furnace are included for comparison.

phosphorus concentration, and so the rate of surface recombination will be greater at the surface of the industrial emitters. Furthermore, as discussed in Chapter 3, the Auger recombination rate in the bulk of the industrial emitters will also be higher as they are more heavily doped. Finally, comparing the J_{oE} data for the unpassivated industrial and tube based emitters in Figure 5.13 shows there is reasonable agreement between the two data sets for the heavily doped emitters. For the unpassivated lightly doped emitters, those formed in a belt furnace have a lower J_{oE}, presumably because the higher N_s more effectively screens the surface.

5.2.6 Conclusions

A systematic comparison of phosphorus diffused emitter passivation achieved with thin, high temperature thermal oxides and PECVD SiN has been made. Optimised deposition parameters for the PECVD SiN layers have been identified, resulting in J_{oE} values as low as 20fA/cm^2 for a lightly doped, 400Ω/□ emitter on a planar surface. For more heavily doped SiN passivated emitters, the J_{oE} increased to 120fA/cm^2 for a sheet resistance of 30Ω/□. These J_{oE} values correspond to a S_p value at the heavily doped n^+-Si/SiN interface of between 1400 and 25000cm/s as the N_s increases from $7.5\text{x}10^{18}\text{cm}^{-3}$ to $1.8\text{x}10^{20}\text{cm}^{-3}$. The optimised SiN films were also shown to provide a reasonable degree of passivation on industrial n^+ emitters formed

in a belt line furnace, where the surface doping concentration reaches the solid solubility of phosphorus in silicon.

The J_{oE} and S_p values determined for thin oxide passivated emitters were consistent with other studies and were found to be superior to those obtained with SiN passivation. The best passivation was provided by an alnealed thin oxide or a thin SiO_2/SiN stack, with J_{oE} values between 5 and 100fA/cm^2 for a planar surface as the sheet resistance decreased from 400-30Ω/□. Parameterisations for the S_p as a function of dopant density are given for phosphorus doped planar silicon surfaces. For textured surfaces, the J_{oE} values were a factor of 1.5-2.5 greater.

5.3 p^+ emitters

5.3.1 Introduction

The majority of silicon solar cells, at both the laboratory and the commercial scale, are fabricated using *p*-type silicon substrates. The reasons for this are partly historical and partly technological and include greater resistance to radiation damage in space environments for *p*-type substrates, higher minority carrier mobility in *p*-type substrates and better engineering control for producing high quality *n*-type emitters using phosphorus as the doping source. A number of potential advantages exist for silicon solar cells fabricated using *n*-type substrates however, including:

1. The effective minority carrier lifetime is higher in *n*-type substrates compared to *p*-type substrates of the same resistivity.

2. The surfaces of *n*-type substrates can be easier to passivate due to the lower capture cross-section for holes than electrons at a Si/SiO_2 interface.

3. Lower cost *n*-type CZ substrates do not exhibit the light-induced performance degradation found in boron doped *p*-type CZ substrates and appear to have comparable electrical characteristics to *n*-type FZ substrates.

4. Self-doping aluminium screen-printed contacts could be used to easily form a selective emitter structure.

5. The formation of a heavily doped, phosphorus back-surface field (Ph-BSF) could be easily achieved in a commercial environment using standard techniques.

The fabrication of silicon solar cells on *n*-type substrates using large area boron emitters has typically been avoided however because they are generally perceived to have poorer recombination properties than phosphorus-diffused emitters of the same sheet resistivity and may also be detrimental to the bulk lifetime of the silicon substrate. The issue of bulk-lifetime degradation has generally resulted in boron diffusions being limited to small, heavily diffused areas of the silicon surface to provide contact passivation such as in point-contact cells [125] and PERL cells [143].

A brief study of the recombination properties of boron-diffused emitters passivated with high temperature thermal oxides and PECVD SiN layers is presented in this section. Values of the boron emitter saturation current (J_{op+}) are reported for planar emitters as a function of the emitter sheet resistance. Data for the effective and bulk lifetime of the samples following boron diffusion are also presented to investigate possible degradation of the bulk.

5.3.2 Previous Work

While comprehensive experimental studies have been carried out by a number of authors for oxide passivated n^+-diffused emitters [131, 132, 137], there appears to be little information available for p^+-diffused emitters. *King et al.* has reported data for oxide passivated, boron-diffused, planar emitters on high resistivity (>390Ωcm), *n*-type FZ substrates where a boron-doped SiO_2 layer formed by APCVD was used as the boron source [144]. Importantly, King *et al.* avoided the use of TCA when growing the passivating oxide layer as they found this resulted in degradation of the Si/SiO_2 interface. The conclusions from this study were that the J_{op+} decreases as the sheet resistance of the boron emitter increases, consistent with the phosphorus emitter studies. Surprisingly however, the extracted surface recombination velocity was found to be independent of the surface doping level with an average value of 1640cm/s. King *et al.* did not directly report data for the bulk lifetime but it appears to have been around 4-5ms for samples with a light boron diffusion on both sides [64]. For unpassivated, boron diffused silicon, King *et al.* reported a constant surface recombination velocity of 1.65×10^5cm/s.

Cuevas *et al.* performed a similar study on planar, high resistivity (1000-5000Ωcm), *p*-type substrates but used liquid BBr_3 as the dopant source [145]. This had the advantage that an in-situ oxidation could be performed in the same furnace to passivate the surface. While unable to obtain the low J_{op+} and surface recombination velocities reported by King *et al*., they also found that J_{op+} tends to decrease as the sheet resistance increases. Furthermore, the surface

recombination velocity at the p^+-Si/SiO_2 interface was found to increase from 4000cm/s to 20000cm/s with increasing surface boron concentration, instead of being constant. This implied that the surface recombination velocity at the p^+-Si/SiO_2 interface is higher than for the n^+-Si/SiO_2 interface, although the dependence with surface concentration is weaker for p^+ emitters. Finally, Cuevas *et al.* measured the average bulk lifetime of their SiO_2 passivated samples to be ~860μs, suggesting little degradation of the bulk quality, and for unpassivated, boron diffused silicon, reported a near constant surface recombination velocity of 2 x 10^5cm/s in good agreement with King *et al.*.

A limited amount of data has been published or can be determined from research at UNSW. Slade *et al.* has reported J_{op+} values of 300fA/cm^2 for planar, 100Ωcm *p*-type substrates with an oxide passivated 7.5Ω/□ BBr_3 diffusion on each side [146]. Effective lifetimes of >1ms where achieved for a variety of diffusion conditions with sheet resistivities in the range of 7.5 to 18Ω/□. Zhao *et al.* has fabricated PERT type solar cells on *p*-type and *n*-type substrates using a light boron-diffused emitter from a liquid BBr_3 source on the rear and front surface respectively [147]. While neither the sheet resistance nor the J_{op+} of these emitters are published, the total J_o of the solar cells (assuming ideality 1 behaviour) was approximately 50fA/cm^2 for cells with either the boron emitter on the planar rear surface or on the textured (inverted pyramids) front surface. This represents an upper limit on what should be expected for the boron emitter alone. Interestingly, the UNSW uses BBr_3 for the doping source as they find it compatible with TCA based processing, contrary to King *et al.* who observed a degradation of the interface.

A limited amount of information is available on suitable processing conditions to obtain boron diffused emitters with low J_{op+} without degradation of the bulk lifetime. The two groups that produce the highest efficiency 1-sun solar cells (UNSW and Frauhhofer ISE) both appear to do their boron depositions at 900°C and then vary the drive in conditions to achieve the desired sheet resistivity and junction depth [148, 149]. Slade *et al.* states that a pre-deposition oxidation is crucial to maintaining lifetime and lowering the saturation current through minimising surface damage [150]. This approach is somewhat analogous to that of the Stanford group (eg King *et al*.) where the boron is effectively diffusing into the silicon from a doped oxide.

There does not appear to be any published data for boron-diffused silicon solar cell emitters passivated in other ways such as by PECVD silicon nitride. Nor does there appear to be data available for textured, boron-diffused emitters.

5.3.3 Experimental Details

The p^+np^+ test structures used to investigate the passivation of boron emitters were prepared using shiny etched, high resistivity (90Ωcm and 20Ωcm) *n*-type, <100> oriented, FZ wafers. All diffusions were performed in a quartz tube at temperatures between 895°C and 1015°C using liquid BBr_3 as the dopant source. After stripping the boron glass, the samples were oxidised at 1050°C for 38 minutes, with TCA included for some of the samples. This produced a thick oxide layer (≈100nm) to act as a rudimentry anti-reflection coating and simultaneously drove-in the diffusion. An anneal in Ar was included at the end of the oxidation to further drive-in the diffusion and to re-distribute some of the boron back towards the silicon surface. The J_{op+} of the samples was then measured for the as-oxidised condition and again following a forming gas anneal (FGA). The oxide layers were then stripped in dilute hydrofluoric acid (HF), SiN layers deposited on both sides and the J_{op+} re-measured. The low temperature used for the PECVD depositions (400°C) should not result in a significant redistribution in the boron doping profile and so direct comparison of the data for oxide passivated and SiN passivated emitters is valid. The SiN deposition parameters used where those optimised in chapter 4 for passivating *p*-type silicon with resistivities from 0.3-1.0 Ωcm (ie Temp = 400°C; SiH_4/N_2 flow = 350 sccm; NH_3 flow = 50 sccm; Pressure = 0.2 Torr; Power = 125W). The same parameter set also gives excellent passivation for n^+ emitters where the process pressure was not found to be significant (see Figure 5.2)

5.3.4 Results and Discussion

5.3.4.1 J_{op+} measurements for planar oxide passivated samples

The effect of sheet resistance on the J_{op+} of oxide passivated (with and without TCA), boron diffused emitters is shown in Figure 5.14. Consistent with previous studies, the J_{op+} decreases as the sheet resistance of the emitter increases, with J_{op+} values as low as 20fA/cm^2 being measured. The use of TCA during the oxidation appears to make little difference to the passivation achievable. Assuming a short circuit current density of 40mA/cm^2, these J_{op+} values limit the open circuit voltage of a solar cell to between 690mV and 730mV depending on the sheet resistance of the emitter (for sheet resistances ≥ 30Ω/□).

The J_{op+} values of this study are in reasonable agreement with those reported by King *et al.* (when adjusted for the new n_i) [144], which is also shown in Figure 5.14. It appears that King *et al.* achieved slightly lower J_{op+} values for heavily doped emitters (<40Ω/□), which is possibly an outcome of the higher drive-in temperatures and times used by King *et al.* (130mins

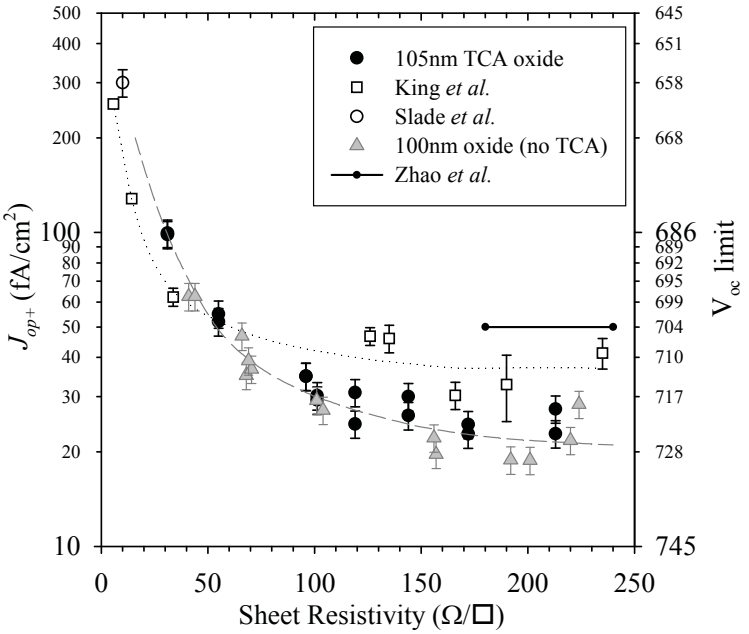


Figure 5.14. Effect of sheet resistance on the J_{op+} of oxide passivated boron diffused emitters with a planar surface.

at 1120°C) and therefore a lower surface concentration of boron atoms. For lightly doped emitters, slightly lower J_{op+} values were obtained in this study. This seems feasible as the finished PERT cells of Zhao *et al.* [147] have J_o values almost as low as the J_{op+} values reported by King *et al.* for lightly doped emitters (~35fA/cm^2 reported by King *et al.* compared to ~50fA/cm^2 for finished PERT cells).

A comparison of Figure 5.4 and 5.14 shows that lower emitter recombination has been achieved for oxide passivated n^+ emitters compared to p^+ emitters, particularly for lightly doped emitters. Importantly, it was found that annealing the p^+np^+ samples in forming gas made no difference to the J_{op+} values obtained, nor did subsequent alnealing of a few of the samples. This is quite different to the behaviour of the n^+pn^+ samples in Figure 5.4, which gave lower emitter recombination when FGA or alnealed. Indeed, the J_{oE} and the J_{op+} are quite similar when passivated with a non-FGA oxide, the main difference with the p^+ emitters appears to be the lack of response to a FGA or alneal.

5.3.4.2 J_{op+} measurements for planar SiN passivated samples

Attempts to measure the J_{op+} of SiN passivated p^+np^+ samples proved difficult due to the strange injection level dependence of the effective lifetime for these samples. This is shown in Figure 5.15 for a 20Ωcm *n*-type sample with 150Ω/□ p^+ diffusions, where the inverse effective lifetime (minus the Auger component) is plotted against the excess carrier density. The J_{op+} is

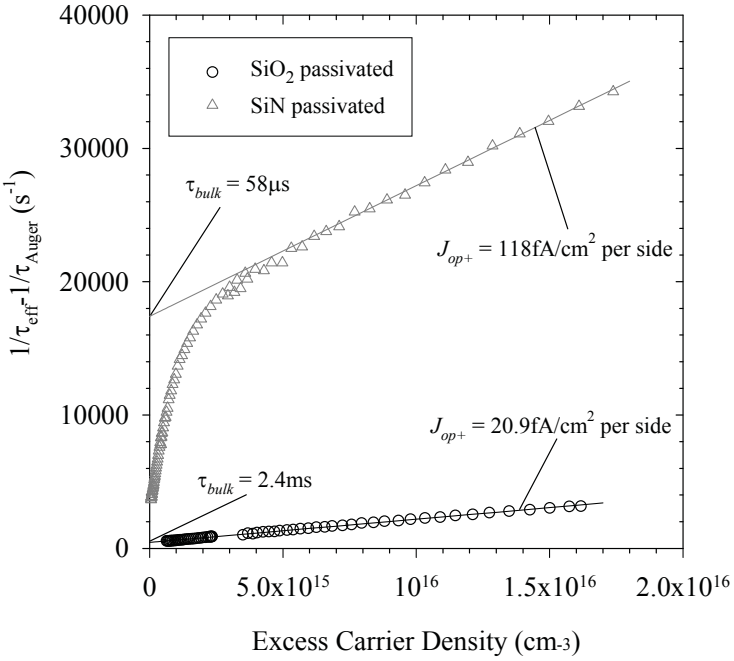


Figure 5.15. Injection level dependence of the inverse lifetime for a passivated p^+np^+ sample with 150Ω/□ diffusions. The J_{op+} and bulk lifetime can be determined for the oxide passivated sample, but the standard interpretation of J_{op+} is not valid for the SiN passivated sample.

normally determined from the slope of the high injection portion of the curve and the bulk lifetime from the intercept [41]. It can be seen that for the oxide passivated case, a straight line can be fitted to the data over a very large range of injection levels, resulting in a low J_{op+} of 20.9fA/cm^2 per side and a bulk lifetime of 2.4ms. This is perfectly consistent with the low injection effective lifetime, which was measured to be 2.05ms.

When the oxide layers where removed and replaced with SiN films, it was only possible to fit the inverse lifetime with a straight line for $\Delta n > 5x10^{15}cm^{-3}$. This suggests a J_{op+} of 118fA/cm^2 and a bulk lifetime of 58µs. The measured effective lifetime clearly exceeds 58µs however, which when combined with the restricted Δn range that a straight line can be fitted to the SiN passivated data, indicates that the standard interpretation of J_{op+} cannot be used for these samples [41]. Importantly, when the silicon wafer was etched to remove the SiN films and also the p^+ emitters, and the surfaces subsequently passivated with new SiN films, effective lifetimes greater than 2ms were achieved with the same injection level dependence shown in Figure 4.9. That is, the bulk lifetime of the sample does not appear to have been adversely affected by the processing and the strange injection level dependence for the effective lifetime shown in Figure 5.15 must be due recombination either at the surface or within the emitter.

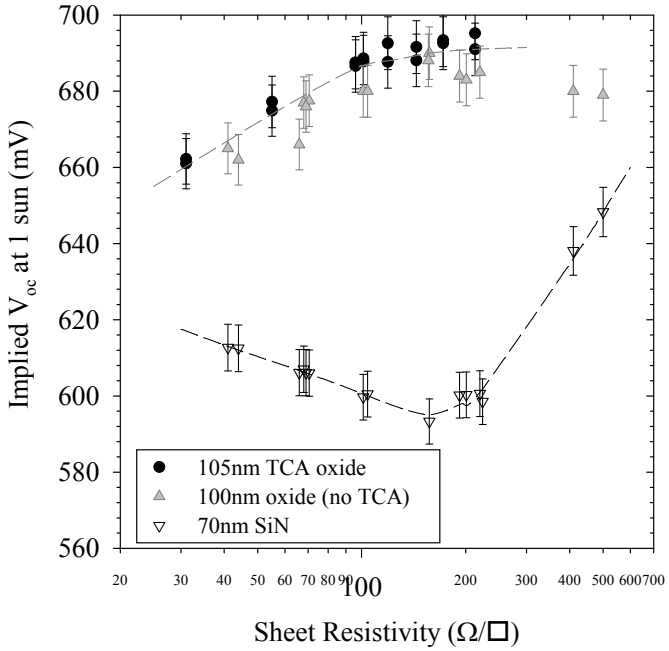


Figure 5.16. The implied V_{oc} at 1-sun of passivated p^+np^+ samples. SiN passivation clearly results in higher recombination emitters for all sheet resistances. The minimum in the implied V_{oc} of the SiN passivated samples is consistent with a high fixed positive charge density in the SiN films, resulting in a silicon surface which is in deep depletion for a sheet resistance of ~150Ω/□. This results in very high surface recombination as the concentration of electron and holes are similar. A higher (lower) sheet resistances the silicon surface is in weak inversion (depletion), where there is some screening of the minority carrier concentration and therefore a higher implied V_{oc}.

Due to the uncertainty in the determination of J_{op+}, an alternative measure of recombination in the SiN passivated p^+np^+ samples is required. One such measure is the implied open-circuit voltage at 1-sun, which, as described in section 2.4, can be obtained from the injection level dependent effective lifetime. Figure 5.16 shows the 1-sun implied V_{oc} for the oxide and SiN passivated p^+np^+ samples. It should be noted that the 1-sun implied V_{oc} is only indicative of what might be achieved with an actual solar, as for the case of Figure 5.16, it incorporates two large area boron diffusions (where a cell would only have one) and is also dependent on the sample thickness. Nevertheless, it can be seen that the SiN films provide significantly worse passivation than the oxide films at all the sheet resistances measured. For the oxide passivated samples, V_{oc}'s of the order of 690mV are feasible and the V_{oc} drops off at low sheet resistances, where emitter recombination is strongest. The behaviour for the SiN passivated samples is distinctly different however, with a clear minimum in the implied V_{oc} of ~590mV at a sheet resistance of 150Ω/□.

It was hypothesized in Chapter 4 that the SiN films optimised in this study show a high fixed positive charge density even under illumination. This hypothesis can be used to qualitatively explain the minimum observed in Figure 5.16 for the SiN passivated samples. In essence, the p^+ emitter dopant profile and the high fixed positive charge density within the SiN films compete to determine the electron and hole concentrations near the silicon surface. While the p^+ boron doping will reduce the electron concentration, the fixed positive charges will increase the electron concentration. For lightly doped p^+ emitters, the fixed positive charge density is sufficient to overcome the field effects due to the p^+ emitters and the silicon surface may be inverted. This would result in a reasonable degree of surface passivation and hence relatively high implied V_{oc}'s can be obtained (the right hand side of Figure 5.16). As the p^+ emitter doping is increased, the competing action of the fixed positive charges results in progressively weaker inversion of the silicon sample and therefore a decreasing implied V_{oc}. Eventually, the silicon surface will no longer be inverted but will actually be in deep depletion, where surface recombination is maximised due to the similar concentrations of electrons and holes. The implied V_{oc} will then be at a minimum. As the p^+ emitter doping is increased even further, the action of the fixed positive charge in determining the electron and hole surface concentrations becomes progressively less important, with the silicon surface being only weakly depleted. The implied V_{oc} then increases compared to the case of deep depletion. In the limit of a very heavily doped p^+ emitter, the SiN films result in little change to the electron and hole concentrations, and the surface recombination rate will be similar to that of an unpassivated (bare) p^+ surface. In addition, the J_{op+} becomes less sensitive to the surface.

The hypothesis of a high fixed positive charge density in the SiN films is also consistent with the inability to determine a J_{op+} for the SiN passivated samples. For the case of Figure 5.15 (R_{sheet} =150Ω/□), it is inferred from Figure 5.16 that the surface is in deep depletion. It follows that the surface region is not in low injection conditions and therefore the J_{op+} cannot be defined nor determined in the standard way. As the injection level in the bulk of the wafer changes (x-axis of Figure 5.15), so does the internal bias voltage across the p^+n junction and hence the number of carriers injected towards the emitter. The carrier injection level at the surface will hence change and, as is typical of a SRH process, the recombination rate (y-axis of Figure 5.15) will also change. This makes an unambiguous determination of J_{op+} impossible and essentially, Figure 5.15 is an example of an injection-dependent J_{op+}.

Finally, it is important to stress that the poor recombination properties of the SiN passivated p^+ emitters studied here is strongly dependent on the properties of the SiN films used, specifically their fixed positive charge density. A re-optimisation of the PECVD

deposition parameters could quite possibly result in SiN passivated p^+ emitters with lower recombination rates.

5.3.4.3 Degradation of the bulk lifetime during boron diffusion

The injection level dependent effective lifetime for four planar p^+np^+ samples is shown in Figure 5.17. The samples were all fabricated using shinny etched 90Ωcm *n*-type silicon and the emitter surfaces where passivated with a TCA processed oxide. It can be seen that for low injection conditions, the measured effective lifetimes are very high, ranging from 4ms to 10ms depending on the sheet resistance of the p^+ emitters. The dashed lines in Figure 5.17 are fits to the effective lifetime data using the expression (see chapter 2 for more discussion)

$$\frac{1}{\tau_{effective}} = \frac{1}{\tau_{Auger}} + \frac{1}{\tau_{bulk}} + 2 * J_{op+} * \frac{N_{dop} + \Delta n}{qWn_i^2} . \qquad (5.2)$$

Where the J_{op+} (taken from the slope of the high injection portion of the curve) and the τ_{bulk} (varied to best fit the data) are given in the table of Figure 5.17. The increasing J_{op+} with decreasing sheet resistance is expected as the more heavily doped emitters will be deeper and have a greater surface concentration of boron atoms. The decreasing τ_{bulk} with decreasing sheet resistance indicates that there is some degradation of the bulk lifetime of the *n*-type base during the high temperature processing. Importantly however, the degradation appears to be small with a bulk lifetime of ~6ms maintained for the heaviest p^+ diffusions investigated. The potential for degradation of the p^+-Si/SiO_2 interface during storage, as noted by King *et al.* [144], has not yet been investigated.

5.3.5 Conclusions

The recombination properties of oxide (with and without TCA) and SiN passivated p^+ emitters has been investigated as a function of the emitter sheet resistance. For oxide passivated emitters, the emitter saturation current density (J_{op+}) was found to decrease with increasing sheet resistance. J_{op+} values as low as ~20fA/cm^2 where obtained for lightly doped emitters (>200Ω/□). The use of TCA during the oxidation step resulted in little difference to the passivation obtained compared to samples oxidised without TCA. Furthermore, a post-oxidation forming gas anneal or alneal was not found to alter the J_{op+}. The bulk lifetime of the *n*-type base was observed to degrade slightly during the high temperature processing, although bulk lifetimes ≥ 5.8ms were maintained for all the p^+ emitters investigated here.

The recombination properties of SiN passivated p^+ emitters was found to be significantly poorer than oxide passivated emitters and also showed a different dependence with the emitter

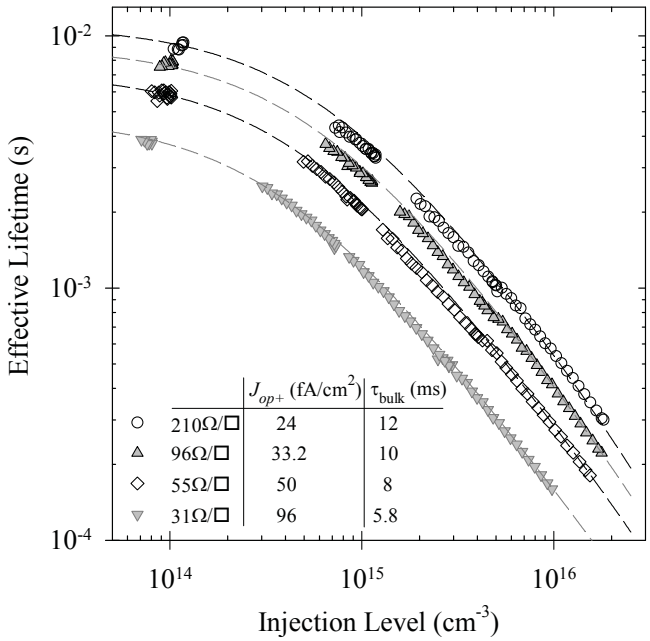


Figure 5.17. Measured effective lifetimes for oxide passivated p^+np^+ samples with different sheet resistivities. The bulk lifetime within the *n*-type base appears to have degraded slightly during the high temperature processing, although it remains very high at ≥ 5.8ms.

sheet resistance. It was not possible to determine the J_{op+} of the SiN passivated p^+np^+ samples due to the strange injection level dependence of their effective lifetime and so the implied open-circuit voltage at 1-sun was used as alternative measure of emitter recombination. It has been shown that the recombination properties of SiN passivated p^+ emitters is worst for sheet resistances of ~150Ω/□, where an implied V_{oc} of only ~590mV was obtained. The hypothesis that the SiN films optimised in this study show a high fixed positive charge density under illumination has been used to explain inability to define a J_{op+} for the SiN passivated samples and also their recombination properties as a function of sheet resistance. For an emitter sheet resistance of ~150Ω/□, the silicon surface appears to be in deep depletion, which maximises the surface recombination rate (and therefore minimises the V_{oc}) as the concentration of electrons and holes are similar. At higher sheet resistances, the surface is weakly inverted, while at lower sheet resistances the surface is weakly depleted and so a higher implied V_{oc} is obtained.

5.4 Efficiency Potential of SiN Passivated n^+p Cells

The recombination properties reported in this chapter for passivated and unpassivated emitters, along with the data in Chapter 4 for recombination at the surface of undiffused silicon, can be used to model the recombination limits to the efficiency of a variety of solar cell

structures. The discussion in this section is limited to n^+p solar cells passivated with SiN films on both the front and rear surface, as cells of this type are the principal topic of the next chapter. The methods used to model the cell efficiency have been described in Chapters 3 and 4 and result in a current-voltage characteristic of

$$J = J_L - qWU_{\text{int}} - J_{oE}\exp\left(\frac{qV}{kT}\right) - qS_{eff}\Delta n\,, \tag{5.3}$$

where bulk recombination is given by the intrinsic recombination rate, U_{int} (see Chapter 3), recombination in the n^+ emitter is determined by the J_{oE} (see section 5.2) and recombination at the p-type rear surface is determined by S_{eff} (see section 4.3).

The effect of the n^+ emitter sheet resistance and the p-type base resistivity on the efficiency potential of n^+p cells are shown in Figure 5.18 for the case where contact recombination has been assumed to be negligible. The cell width has been fixed at 400μm and both planar cells (assumed J_{sc} of 35mA/cm^2) and cells with random pyramid texturing (assumed J_{sc} of 40mA/cm^2) have been considered. Series resistance effects within the base have not been considered nor has additional recombination mechanisms such as bulk SRH or periphery recombination. While the experimental scatter in the data results in some sharp edges in the contour lines, it can be seen that peak cell efficiency is for a base resistivity of ~1.5Ωcm and for a very light emitter (~400Ω/□) when lateral series resistance within the n^+ emitter is not included. The optimum base resistivity of ~1.5Ωcm is determined by the injection level dependence of the S_{eff} at the rear surface, which was previously discussed in section 4.3. As expected, a higher efficiency is obtained by using a more lightly doped emitter, where lower recombination is achieved when the surface is passivated. The bottom two plots of Figure 5.18 include the effects of lateral series resistance within the n^+ emitter by assuming a finger spacing of 800μm (the solar cells fabricated for the next chapter used this finger spacing) [33]. It can be seen that the peak cell efficiency now occurs at a lower sheet resistance of ~250Ω/□ (~200Ω/□) for a planar (RP textured) front surface. This shift towards lower sheet resistance is expected because the power losses due to lateral resistance are greater for lighter emitters.

The data in Figure 5.7 for metalised n^+ emitters can be used to include the effects of recombination at the front contacts for a homogeneously doped n^+ emitter. The equivalent J_{oE} of the entire emitter, including both the passivated and contacted parts, can be determined by assuming two separate diodes [151]

$$J_{oE} = F_m J_{oE,metal} + (1 - F_m) J_{oE,passivated}\,, \tag{5.4}$$

where F_m is the metalisation fraction. Figure 5.19 shows the equivalent J_{oE} for planar and RP textured n^+ emitters with SiN passivation and metal contact fractions up to 3%. It can be seen

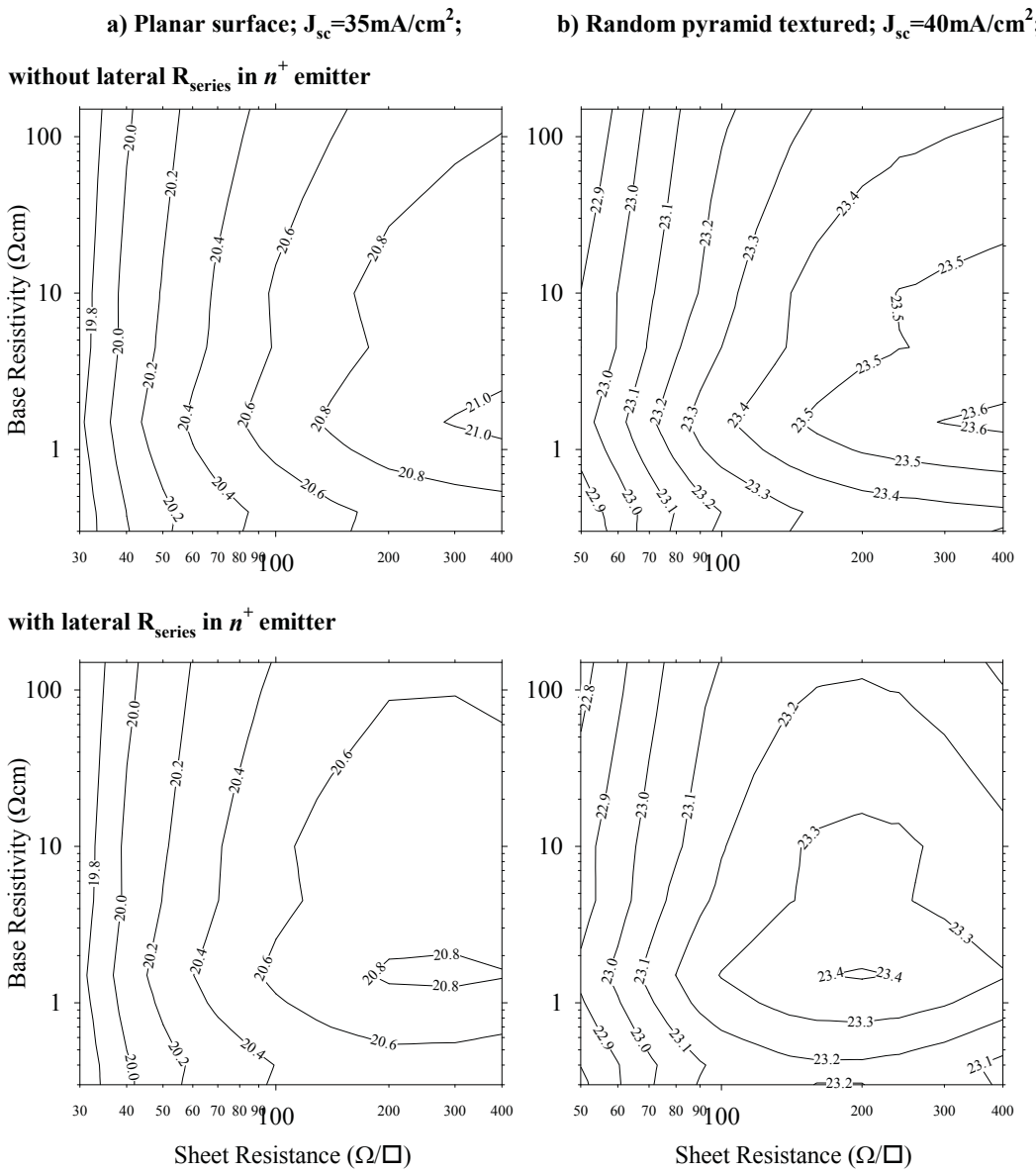


Figure 5.18. The efficiency limit due to recombination processes for an n^+p cell passivated with SiN films at the front and rear surface, both with and without lateral series resistance within the n^+ emitter. The cell width is fixed at 400μm and series resistance effects in the base are not included. It is assumed that there is negligible recombination at the metal contacts. It can be seen that recombination within the emitter gives a higher cell efficiency for a lighter emitter, but including the lateral R_{series} reduces the optimum sheet resistance to ~200-300Ω/□.

that the inclusion of recombination under the metal contacts increases the J_{oE}, particularly for the higher sheet resistances. The outcome is that the optimum emitter sheet resistance, for a homogeneously doped n^+ emitter, reduces from ~400Ω/□ with no contact recombination to ~160Ω/□, and finally ~100Ω/□ as the contact fraction increases from 1% to 3%.

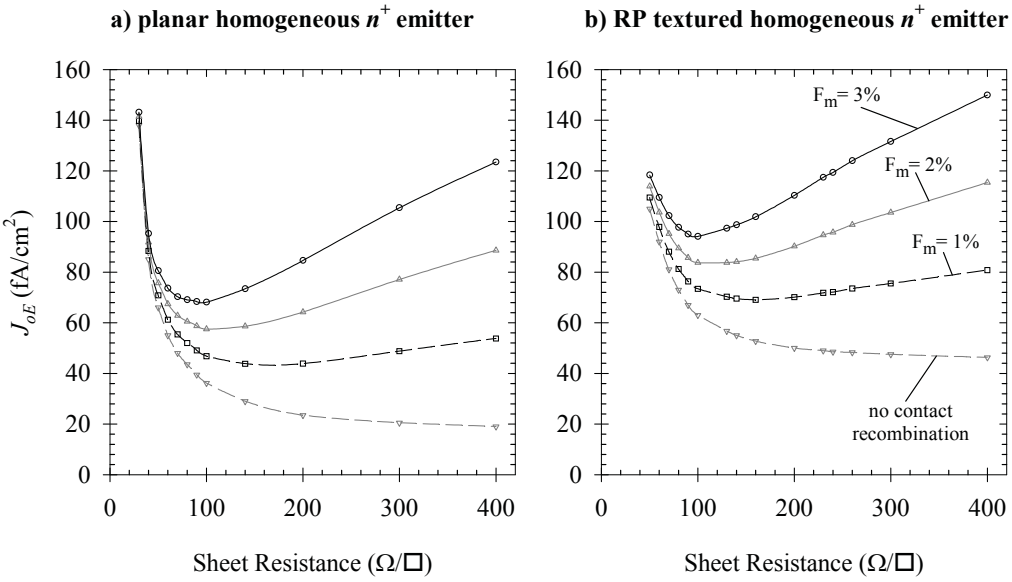


Figure 5.19. Equivalent J_{oE} as a function of sheet resistance for a homogenous SiN passivated n^+ emitter including recombination under the metal contacts. Metal contact fractions between 0% and 3% are shown.

Figure 5.20 shows the effect of the n^+ emitter sheet resistance and the *p*-type base resistivity on the efficiency potential of n^+p cells including recombination at the front contacts (F_m=3%). The cell width has again been fixed at 400μm and lateral series resistance within the n^+ emitter included. It can be clearly seen that the optimum sheet resistance has shifted to ~80-90Ω/□ for both a planar and RP textured front surface. Again, the optimum base resistivity is ~1.5Ωcm due to the S_{eff} at the rear surface. Contour plots for the cell V_{oc} and fill-factor have also been included in Figure 5.20. It can be seen that the V_{oc} is largely determined by the n^+ emitter sheet resistance with maximum V_{oc}'s of 686mV (682mv) obtainable for a planar (RP textured) front surface. The cell fill-factor can be seen to be a maximum in the lower left-hand corner of the contour plots and reduces as either the base resistivity or sheet resistance increases.

The effect of including series resistance within the *p*-type base would be to shift the optimum towards the bottom of the plots (lower base resistivity) and lower the efficiency potential. Likewise, recombination at the rear contacts would lower the efficiency potential and V_{oc} in particular, where the amount would depend on the type of rear contact (PERC or PERL type rear contact for example). Essentially though, recombination appears to limit the efficiency potential of planar and RP textured n^+p cells, passivated with SiN on the front and rear surfaces, to less than ~20% and ~23% respectively.

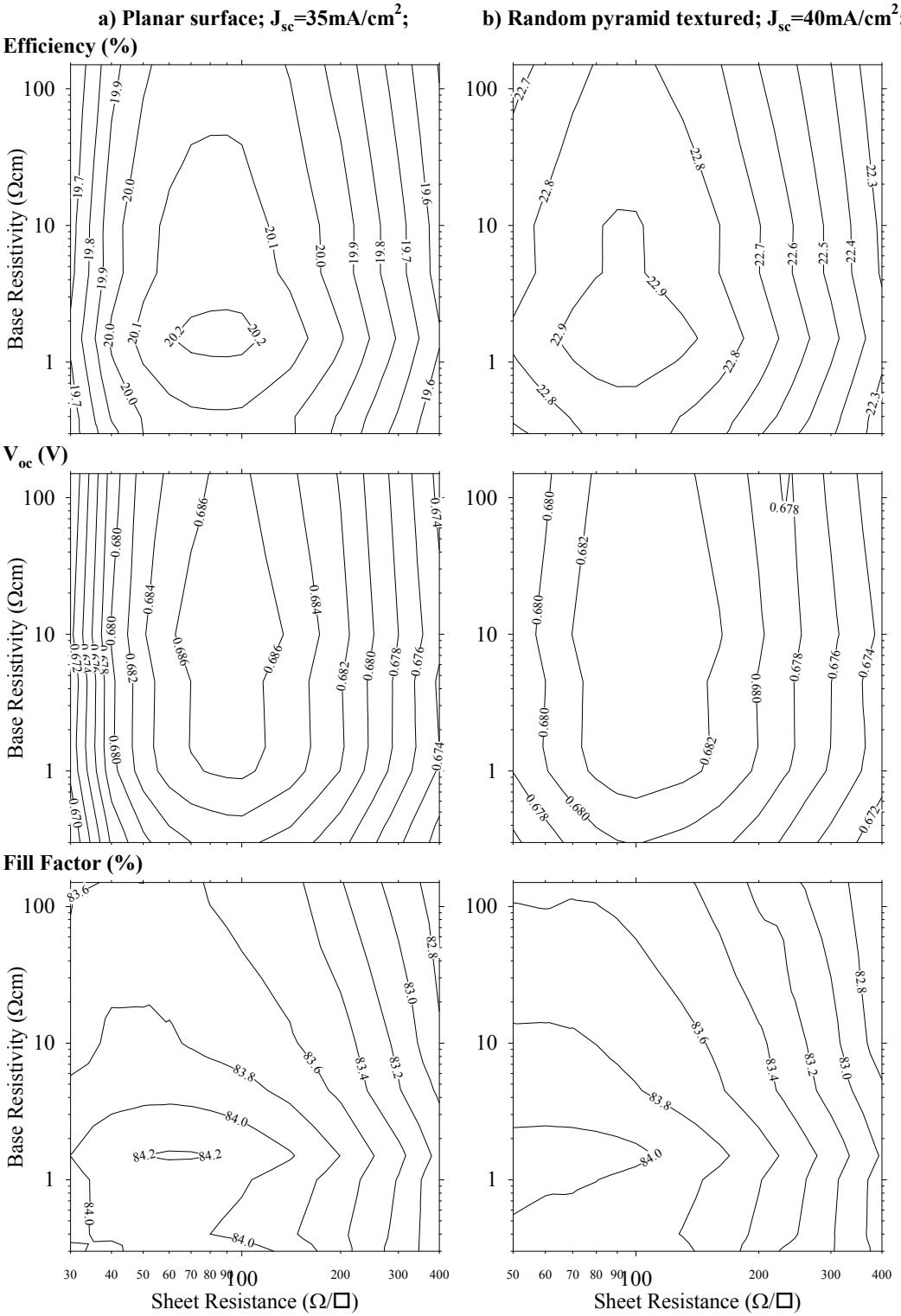


Figure 5.20. The efficiency limit due to recombination processes for an n^+p cell passivated with SiN films at the front and rear surface including recombination under the front metal contacts. The cell width is fixed at 400μm and series resistance effects within the n^+ emitter but not the base are included. It is assumed that there is negligible recombination at the rear metal contacts. It can be seen that the optimum sheet resistance for peak cell efficiency is reduced to ~80-90Ω/□.

5.5 Chapter Summary

The recombination properties of n^+ and p^+ emitters passivated with optimised SiN films and thermal SiO_2 have been investigated in this chapter. The PECVD deposition parameters were optimised for passivating n^+ emitters, with the deposition temperature and gas flow ratio identified as the most significant parameters. The optimised SiN films were again stoichiometric in composition. The J_{oE} value of SiN passivated n^+ emitters has been investigated as a function of sheet resistance for both planar and textured surfaces. Surface recombination velocities of between 1400 and 25000cm/s were determined using device simulation for the heavily doped n^+-Si/SiN interface, where the S_p increases with the surface concentration of phosphorus atoms. The optimised SiN films were also shown to provide reasonable passivation on industrial n^+ emitters formed in a belt line furnace, where the surface doping concentration reaches the solid solubility of phosphorus in silicon.

It was found that the surface recombination properties of SiN passivated p^+ emitters was relatively poor and could not be quantified in terms of an emitter saturation current density as is normally done for emitter recombination. Using the implied V_{oc} at 1-sun for passivated p^+np^+ test structures, it was shown that the recombination properties of SiN passivated p^+ emitters is worst for sheet resistances of ~150Ω/□, and improves at both higher and lower sheet resistances. It is hypothesised that fixed positive charges within the SiN films result in the silicon surface being in deep depletion for a p^+ emitter sheet resistance of ~150Ω/□, which maximises the surface recombination rate and therefore minimises the V_{oc}. At higher sheet resistances the surface is weakly inverted, while at lower sheet resistances the surface is weakly depleted and so a higher implied V_{oc} is obtained. The importance of positive charges in determining the surface recombination properties of the *p*-type Si/SiN interface is consistent with the findings in Chapter 4.

The J_o and S_p values determined for SiO_2 passivated emitters (both n^+ and p^+) were consistent with other studies and found to be superior to those obtained with SiN passivation. For n^+ emitters, the best passivation was provided by an alnealed SiO_2 film or a thin SiO_2/SiN stack, while for p^+ emitters, a post-oxidation forming gas anneal or alneal was not found to improve the J_{op+}. Furthermore, the use of TCA during the oxidation was not found to improve the recombination properties of SiO_2 passivated p^+ emitters.

The efficiency potential of SiN passivated n^+p cells with either a planar or random pyramid textured front surface has been calculated. A sheet resistance of 80-100Ω/□ and a base resistivity of 1-2Ωcm are optimal, assuming no resistive losses in the bulk or at the rear contact.

Open-circuit voltages of 670-680mV and efficiencies up to ~20% and ~23% appear possible for SiN passivated planar and textured cells respectively. The demonstration of SiN passivated solar cells with high V_{oc}'s and high efficiencies is the topic of the next chapter.

CHAPTER 6

Solar Cell Structures Passivated with Stoichiometric PECVD Silicon Nitride

6.1 Introduction

High quality surface passivation schemes are required to fabricate solar cells with a high open circuit voltage (V_{oc}). It has been demonstrated in the previous two chapters that optimised stoichiometric PECVD SiN films can be used to obtain low surface recombination velocities for both doped wafers (Chapter 4) and diffused n^+ surfaces (Chapter 5). The purpose of this chapter is to use these well-passivating SiN films to fabricate solar cells with high V_{oc} and therefore demonstrate that the good surface passivation qualities provided by the SiN films can be maintained in real devices. Furthermore, in addition to their electronic qualities, stoichiometric SiN films have properties that are useful for fabricating high V_{oc} and high efficiency solar cells, including:

(i) An optimum refractive index for a single layer anti-reflection coating for non-encapsulated solar cells.

(ii) No absorption in the UV range of the solar spectrum.

(iii) Easily patterned using photolithography and wet chemical etching.

(iv) Good insulating properties and thus compatible with aluminium layers for a back surface reflector.

(v) Fabricated using a low temperature process.

Properties (iii) and (iv) are salient features because they allow solar cells with local rear contacts to be fabricated.

The majority of both laboratory and commercial solar cells are fabricated using *p*-type silicon. Following this trend, most of the solar cells described in this chapter have been made using *p*-type float-zone (FZ) silicon. A variety of rear device structures have been investigated including cells with a full rear metal contact, a localised PERC type contact and a full or local aluminium back-surface field. Some brief experiments have also been performed to demonstrate the excellent surface passivation of the SiN films in solar cells made from *p*-type multicrystalline silicon and *n*-type FZ silicon. Emphasis has primarily been placed on demonstrating high open circuit voltages as this is the best indicator of the overall recombination rate within the cell, and secondly in developing high cell efficiencies.

6.2 Previous Work

The implementation of PECVD SiN films into cell designs that can produce a high V_{oc} has recently been demonstrated by a number of researchers [123, 152-156]. It appears that virtually all the work has been performed using *p*-type substrates of varying resistivity, with little relevant data published for *n*-type solar cells.

6.2.1 p-type Float-Zone Silicon Solar Cells

6.2.1.1 Front and Rear SiN Passivated Cells

The highest V_{oc} reported by other researchers for a solar cell passivated with SiN at the front and rear surface (all-SiN cells) appears to be 649mV as achieved by Hubner *et al.* [152]. They applied Si-rich remote PECVD SiN films to the front and rear of bifacial solar cells fabricated on 1.5Ωcm *p*-type FZ material. The front surface of their cells was textured using random pyramids and had a double layer anti-reflection coating of PECVD SiN and PECVD silicon oxide. The rear contacts were passivated with a local aluminium back surface field (Al-

BSF). Importantly, the front and rear contact metals were evaporated through shadow masks before SiN deposition, as it is not possible to use photolithographic techniques to locally open the silicon-rich SiN films. This resulted in relatively large metal contact fractions of 4% at the front and 6% at the rear, which can reduce V_{oc}. Under front illumination, these cells had an efficiency of 20.1%, which is the highest efficiency reported in the literature for an all-SiN passivated solar cell.

Muramatsu *et al.* [153] have also achieved relatively high V_{oc} for all-SiN passivated cells. They fabricated PERL type cells with inverted pyramids on 10Ωcm *p*-type CZ wafers using a microwave excited afterglow plasma to fabricate the PECVD SiN films. They reported open circuit voltages up to 640mV, but not the cell efficiency, stating only that it was less than 20%. Interestingly, they found that replacing the rear SiN layer with a high quality thermal oxide increased the V_{oc} by 20mV.

6.2.1.2 Rear SiN Passivated Cells

Solar cells with higher open circuit voltages and efficiencies have been reported when only the rear surface is passivated with SiN. Glunz *et al.* [155, 157] have fabricated a number of excellent RP-PERC devices using a photolithographically patterned, high temperature thermal oxide for the front surface and a very silicon-rich PECVD SiN at the rear surface (refractive index ~2.8). The very high silicon content of the rear SiN film requires it to be patterned by means other than photolithography and techniques such as laser ablation [154], plasma etching [158] and laser fired contacts [156] have been developed. Excellent performance has been achieved for each of their techniques, with the results for their best cells given in Table 6.1. It can be seen that open-circuit voltages between 660mV and 674mV and efficiencies greater than 19% have been obtained. It is interesting to note that the plasma etched cell shows a superior short-circuit current of $\geq$2mA/cm^2 and significantly higher fill-factor than the other cells, resulting in an efficiency of 21.5%, which is the highest efficiency reported for a solar cell with a rear SiN passivation. Reference cells using an alnealed silicon oxide at the rear were also manufactured by Glunz *et al.* and showed that the plasma etched rear SiN cells were performing comparably with the reference cells, but that both the laser ablated and laser fired contact cells had 2-3mA/cm^2 lower short-circuit current. This indicates that the rear SiN film is responsible for the reduced short-circuit current of some of the cells rather than the use of a laser in the contact formation.

Table 6.1. Literature data for the performance of silicon solar cells passivated with SiN at the rear surface.

Rear contact patterning	Plasma Etching [148]	Laser Ablation [144]	Laser Fired Contacts [146]	Mechanically Scribed [114]
V_{oc} (mV)	674	660	667	654
J_{sc} (mA/cm^2)	39.4	37.4	36.7	37.1
Fill Factor (%)	81.1	79.7	79.0	80.2
η (%)	21.5	19.7	19.4	19.5

Also included in Table 6.1 are the results of Dauwe *et al.* for rear SiN passivated MIS n^+p solar cells [123]. Using a silicon-rich silicon nitride for the rear passivation (refractive index ~2.3), which was mechanically scribed to open local contacts, they also achieved excellent results. A high V_{oc} of 654mV and an efficiency of 19.5% was obtained. Again however, the short-circuit current was 2.1mA/cm^2 less than that obtained with a reference cell fabricated using an annealed thermal oxide at the rear. Dauwe *et al.* has very recently explained this short circuit current loss to be from a shunt formed between an *n*-type inversion layer underneath the rear SiN films and the rear contacts [159]. The formation of an *n*-type inversion layer at the SiN passivated rear surface has also been independently proposed in this thesis due to a high fixed charge density within the SiN films even under illumination. This hypothesis is based on the injection level dependence of the S_{eff} in Chapter 4 and the poor passivation provided by SiN films for p^+ emitters discussed in Chapter 5.

6.2.1.3 Cells Incorporating SiN at the Front Surface

Solar cells with high V_{oc} and efficiencies have also been fabricated by incorporating a SiN film at the front surface only. Hubner *et al.* [152] have reported a monofacial PERC type cell with a V_{oc} of 657mV and an efficiency of 20.9%. This cell was similar to their bifacial cell described in section 6.2.1.1, except that 0.6Ωcm FZ material was used and the rear surface passivation was achieved with a photolithographically defined, alnealed thermal oxide. Very high open-circuit voltages of 666mV and 693mV have also been reported by Metz *et al.* [160] and Hampe *et al.* [161] for MINP and PN-IL (inversion layer) solar cells respectively. These cells used a thin thermal oxide at the front between the silicon surface and the SiN layer, and an alnealed thermal oxide at the rear.

6.2.2 p-type Multicrystalline Silicon Solar Cells

The use of PECVD SiN for multicrystalline silicon solar cells has been widely studied, particularly for large area, industrial like processes [162-171]. Fukui *et al.* have reported a V_{oc} of 621mV and a very impressive efficiency of 17.1% for a 15cm by 15cm cell fabricated from 1.2Ωcm Sumitomo multicrystalline silicon [162]. The front surface incorporated an RIE texturing and was passivated with SiN. The rear surface had a full area Al-BSF. Duerinckx *et al.* has recently reported very similar results for a variety of multicrystalline substrates with resistivities in the range 0.5-1Ωcm and a cell area of 12.5cm by 12.5cm [165]. These cells were given an isotropic acidic texturing and a double layer anti-reflection coating of PECVD SiN and MgF_2. Using a selective emitter structure, along with special tabbing of the busbars, high open-circuit voltages of 635mV were achieved.

Higher efficiencies have very recently been reported for small area multicrystalline cells (2cm by 2cm) passivated by remote PECVD SiN films on both the front and rear surface [171]. The front surface was alkaline textured with a double layer anti-reflection coating of PECVD SiN and PECVD silicon oxide. A local Al-BSF was used on the rear surface (5% contact fraction). An independently confirmed V_{oc} of 641mV and an excellent efficiency of 18.1% were achieved. Identically processed planar devices gave a V_{oc} of 635mV and an efficiency of 16%.

6.2.3 n-type Silicon Solar Cells

Very little information is available for *n*-type silicon solar cells passivated with PECVD SiN films, presumably because of the difficulty in forming a high quality p^+ junction without degrading the lifetime in the bulk of the material, as is frequently experienced with boron diffusions. Using a simple process based on screen-printing, Ebong *et al.* have fabricated n^+np^+ solar cells where the collecting junction is formed at the rear of the cell by alloying aluminium [172]. SiN films were used to passivate the front surface and for anti-reflection control. Using 200μm thick, <111> oriented, 2 Ωcm *n*-type FZ silicon, a V_{oc} of 619mV and an efficiency of 14.9% was achieved. On 100μm thick, 20 Ωcm *n*-type dendritic web silicon, the V_{oc} was 606mV and the efficiency was 14.2%. These are respectable results for such a simple process, although the V_{oc}'s were relatively low, which may be mainly due to the rear Al p^+ layer. From the point of view of passivating *n*-type wafers, these devices do not provide any new information however, as the SiN films are passivating an n^+ phosphorus diffusion.

6.3 Development of Simplified PERC Cells with SiN Passivation

6.3.1 Cell Design

The PERC cell structure was originally introduced by Blakers *et al.* in 1989 [103]. Various simplified versions of the PERC structure with reduced processing requirements have since been investigated [126, 173, 174]. Despite the reduced processing, these simplified PERC structures have demonstrated high open circuit voltages (>670mV) and excellent conversion efficiencies (up to 22%). Simplified PERC structures were initially chosen in this study because:

i) They are suitable for demonstrating the high V_{oc} potential of stoichiometric PECVD SiN films with reduced cell processing.

ii) The requirements on the rear passivating layer of PERC, PERL and PERT cells are similar.

iii) The results on single crystal silicon are readily transferable to multicrystalline silicon.

A schematic of the cell structures used in this work is shown in Figure 6.1. The cell structure differs from the original PERC cell structure in three main ways:

i) The front surface is not textured with inverted pyramids.

ii) A single step emitter is used rather than a two-step selective emitter.

iii) Low temperature (400°C) PECVD SiN is used as a surface passivating, anti-reflection coating on the front and for surface passivation on the rear, rather than high temperature thermal oxides.

Both planar cells and cells textured with random pyramids have been investigated. Planar cells were of interest as they are the simplest to make and are indicative of the maximum potential for this cell structure on multicrystalline silicon, while textured cells were expected to give a higher conversion efficiency.

6.3.2 Cell Fabrication

Cells were fabricated using the sequence shown in Figure 6.2 on 300μm thick, <100> oriented, 0.7 Ωcm and 0.3 Ωcm *p*-type float zone silicon wafers, and on gettered 200μm thick,

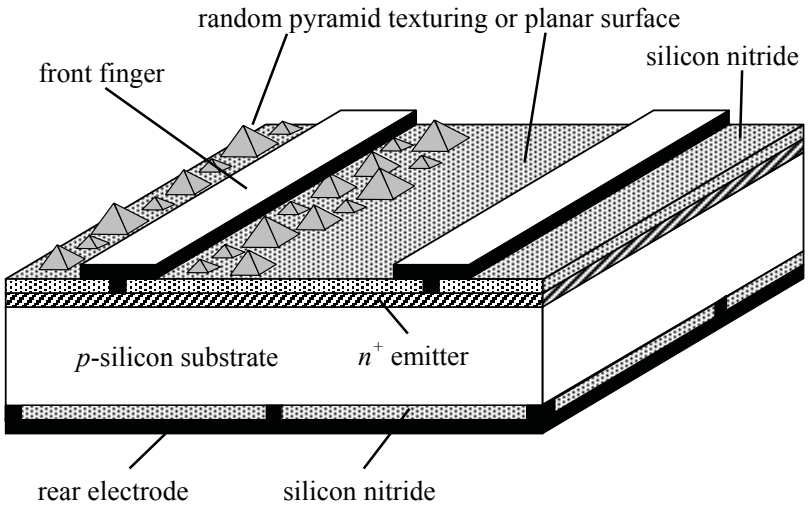


Figure 6.1. Schematic of the simplified PERC cell structure used in this work.

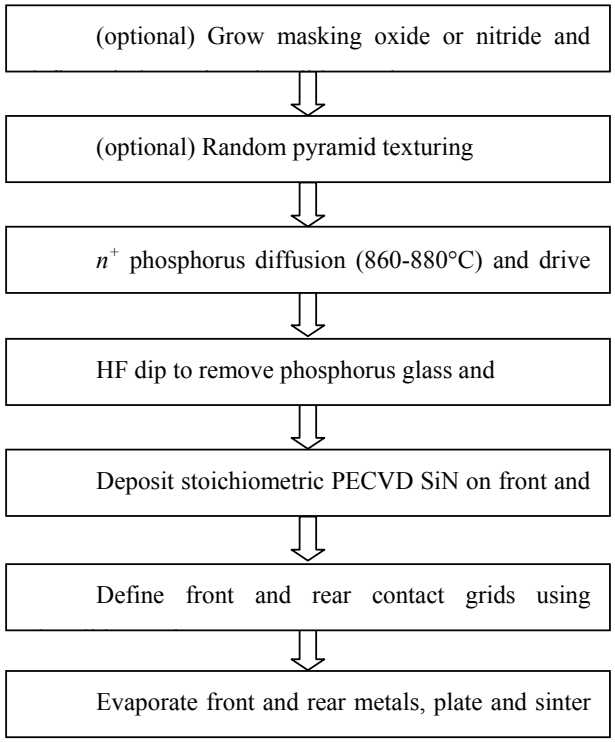


Figure 6.2. Processing sequence used for fabricating simplified PERC cells passivated with stoichiometric SiN.

0.2 Ωcm *p*-type multicrystalline substrates from Eurosolare. The wafers were given a standard RCA clean before processing. The texturing was performed into either oxide or nitride masked windows using a mixture of KOH and isopropanol. The n^+ diffusion was performed in a quartz tube at temperatures between 860°C and 880°C using liquid $POCl_3$ as the dopant source. After removing the phosphorus glass, the diffusion was driven-in for 30mins at 900°C for the planar

cells and for 35mins at 1050°C for the textured cells. Following drive-in, the sheet resistance was measured to be in the range of 100-130Ω/□ for the planar cells and 60-70 Ω/□ for the textured cells. The SiN films were prepared using the optimised deposition parameters described in Chapters 4 and 5. The front SiN was patterned to form a metal grid by the lift-off technique. The front metallization scheme involved evaporating Ti/Pd/Ag and subsequent Ag plating. The rear SiN was patterned and aluminium evaporated onto it. The aluminium layer has the dual role of making local ohmic contact to the *p*-type base and forming an efficient back surface reflector in conjunction with the SiN film. The rear contact area is approximately 4%. The cells were sintered in forming gas at 400°C to ensure a good ohmic contact and the nominal cell area is 4cm^2. Reference cells using a rear thermal oxide were also fabricated with FZ substrates, where the masking oxide was kept on the rear surface.

6.3.3 Cell Results and Discussion

6.3.3.1 Planar Float-Zone Silicon Solar Cells

Results for the best planar cells are summarized in Table 6.2. The data for cell p1 was independently determined at Sandia National Laboratories and so cell p1 was used as a reference for the other cell measurements. The all-SiN passivated cells p1 through p3 have a very high V_{oc} between 667mV and 671mV, confirming the excellent front and rear surface passivation provided by the stoichiometric SiN films. This V_{oc} is a significant improvement over the previous record for all-SiN passivated solar cells of 649mV [152], and is comparable with the best V_{oc} values determined for cells incorporating SiN at either the front or rear surface only.

Spectral response and reflectivity measurements are given in Figure 6.3 for cell p1. This cell had a J_{sc} of 33.1mA/cm^2, which is reasonable for a single layer anti-reflection coating on a planar surface. The short and long wavelength EQE are relatively low however, and clearly this cell would benefit from reduced reflection at these wavelengths. The IQE for cell p1, between the wavelengths of 350-650nm, is approximately 100%, which gives additional proof of the excellent front surface passivation. The long wavelength IQE is relatively low however, and so the inclusion of light trapping features would be advantageous.

The illumination-V_{oc} characteristic of cell p1, measured by the QssV_{oc} technique, is given in Figure 6.4(a). The resulting photovoltaic I-V curve is compared with the actual I-V curve in Figure 6.4(b), where the differences between the two I-V curves are mainly attributable to series resistance effects (see Chapter 2). The fill factor from the actual I-V curve is 80.7%, which is reasonable for this cell design, and results in a cell efficiency of 17.8%. The fill factor from the

Table 6.2. Calibrated measurements of planar all-SiN passivated PERC cells fabricated in this study using FZ silicon.

Cell	p1*	p2	p3	p4	p5
Base Resistivity (Ωcm)	0.3	0.3	0.7	0.3	0.3
Front passivation	SiN	SiN	SiN	SiN	SiO_2/SiN
Rear passivation	SiN	SiN	SiN	*al*-SiO_2	*al*-SiO_2
n^+ emitter definition	oxide mask	mesa-etched	mesa-etched	oxide mask	oxide mask
V_{oc} (mV)	667.3	671	668	661	673
J_{sc} (mA/cm^2)	33.1	32.5	32.6	33.5	33.6
Fill Factor (%)	80.7	81.5	77.8	80.0	81.0
η (%)	17.8	17.8	17.5	17.7	18.3

* Independently confirmed at Sandia National Laboratories

photovoltaic I-V curve is 83.5%. This represents the fill factor limitation for this cell due to recombination processes and possible shunting. Series resistance has therefore reduced the fill factor by 2.8% in absolute terms, which is partially attributable to the large spacing between the rear dot contacts (2mm).

The standard diode analysis of the illumination-V_{oc} characteristic of Figure 6.4(a) can be performed. The injection level dependent S_{eff} data reported in Chapter 4 for the SiN passivated rear surface implies that terms for both an n=1 ideality factor and an n=2 ideality factor (see Eq. 2.41 and Eq. 4.3) are required. It can be seen in Figure 6.4(a) that a fit of this type is good for voltages >0.45V, but is poor for lower voltages. It is necessary to include an additional term for a shunt resistance to obtain a good fit over the entire range of voltage data. The resulting fit parameters being J_{o1} = 178fA/cm^2, J_{o2} = 5.7nA/cm^2 and R_{shunt} = 23000Ω. The physical origin of this shunt will be more fully discussed later in the chapter.

Cells p2 and p3 in Table 6.2 were fabricated without a masking oxide during the phosphorus diffusion, but by subsequently defining the emitter area by mesa etching. Such a process is desirable for multicrystalline substrates, as it only requires a single high temperature step. It can be seen that the results for the mesa-etched cells are comparable to those fabricated using a masking oxide. Furthermore, there appears to be little difference between all-SiN cells fabricated on 0.3Ωcm and 0.7Ωcm substrates, except for the possibility of a slightly higher J_{sc} for the 0.7Ωcm substrates.

For comparison, similar cells with different passivation schemes including thermally grown TCA oxides on the rear and thin SiO_2/SiN double layers on the front surface are included in Table 6.2. A similar V_{oc} was found for all-SiN passivated cells (cells p1 to p3) and for

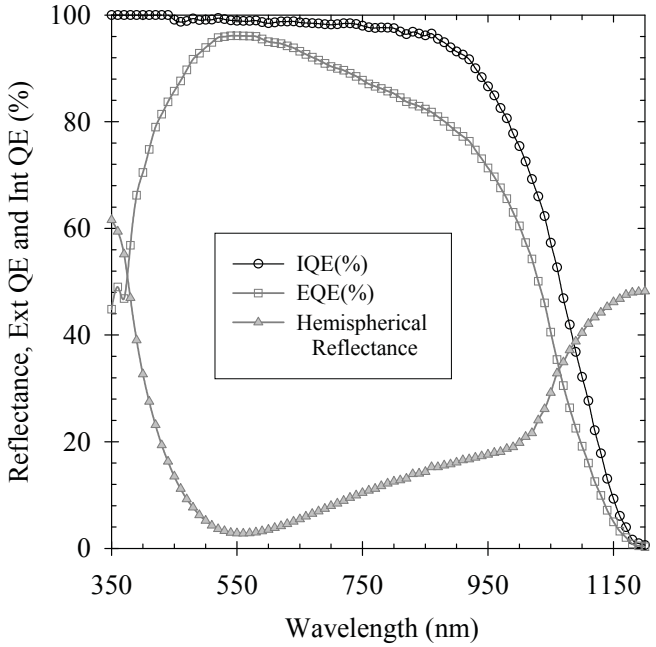


Figure 6.3. Spectral response and hemispherical reflectance for a planar, all-SiN passivated simplified PERC cell (cell p1 in Table 6.2).

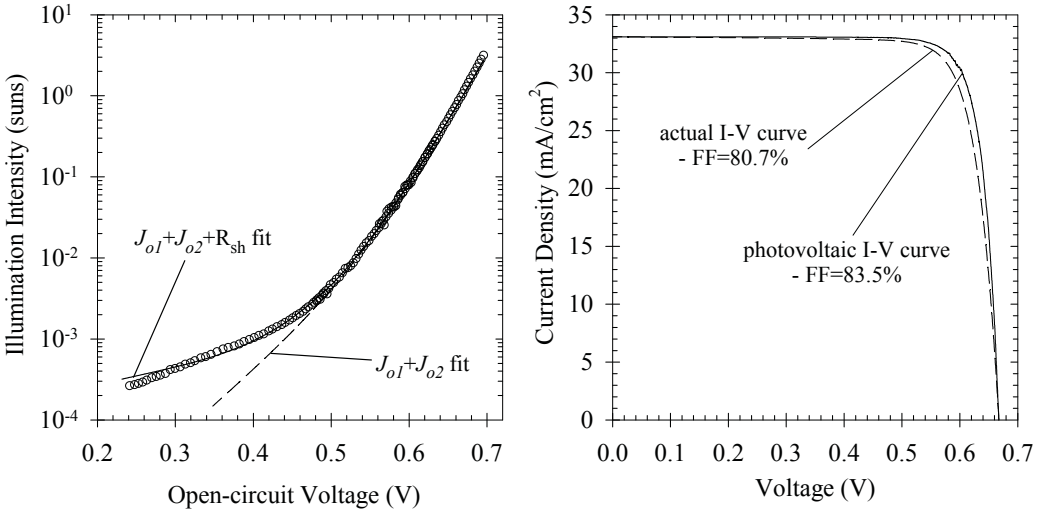


Figure 6.4. Illumination-Voltage characteristic and I-V curves for a planar, all-SiN passivated simplified PERC cell (cell p1 in Table 6.2).

devices with SiN at the front and an alnealed SiO_2 at the rear (cell p4). This is in contrast to the results of Muramatsu *et al.* [153], where replacing the rear SiN with an alnealed thermal oxide gave a 20mV increase in V_{oc}. The highest V_{oc} shown in Table 6.2 was 673mV for cell p5, which had an efficiency of 18.3%. The improved performance of cell p5 is partly due to the slightly better surface passivation of the SiO_2/SiN double layer on the n^+ diffused emitter compared to a single SiN layer (see Chapter 5) and partly due to the lower S_{eff} at the rear surface from the alnealed SiO_2 layer. A final but important observation is that for the 0.3Ωcm cells in Table 6.2,

it appears that those with a rear SiO_2 passivation have a slightly higher J_{sc} (by ~0.5-1mA/cm^2) than those with a rear SiN film. Otherwise, on the basis of these planar cells, it appears that the efficiency potential of the different passivation schemes is similar.

The results in Table 6.2 can be compared with the values determined in section 5.4 for the limits imposed by recombination on the performance of planar all-SiN passivated cells (see Figure 5.20 in particular). The modeled performance for 0.3Ωcm *p*-type base with a 130Ω/□ emitter and the appropriate front finger design, assuming a J_{sc} of 35mA/cm^2, was V_{oc}=681mV, FF=83.9% and η=20.0%. Reducing the J_{sc} to the measured value of 33.1mA/cm^2 changes the other parameters to V_{oc}=679mV, FF=83.9% and η=19.0%. Given that recombination and resistive losses at the rear contacts were not included in the modeled results, there is quite good agreement with the actual cell data, where the modeled fill-factor is best compared with the fill-factor determined from the photovoltaic I-V curve (83.5%).

6.3.3.2 Planar SiN Passivated Multicrystalline Silicon Solar Cells

The mesa-etched cells described in the above section were fabricated with only one high temperature step (the phosphorus diffusion). Such a process is ideal for fabricating high V_{oc} multicrystalline solar cells, as it would minimise any degradation of the minority carrier lifetime from thermal processing. Results for the best all-SiN multicrystalline PERC cells fabricated in this study are given in Table 6.3. The data for cell m1 was independently determined at Sandia National Laboratories and was therefore used as a reference for the other cell measurements. Very high V_{oc} between 655mV and 659mV have been measured, which are the highest ever reported for a SiN passivated multicrystalline cell and equal to the highest ever recorded for multicrystalline silicon (obtained using alnealed SiO_2 passivation) [49, 175]. Remarkably, the V_{oc} achieved for these multicrystalline PERC cells is even slightly higher than the previous record for all-SiN passivated cells made using float-zone silicon. The high V_{oc} results not only from the excellent surface passivation but also from the ability of the cell fabrication process to maintain a relatively high bulk lifetime (>20μs). A strong degradation of the same 0.2Ωcm mc-Si material was observed during standard high-temperature oxidation (τ_{eff}<2μs after oxidation). Furthermore, the potential for bulk defect passivation by atomic hydrogen in the PECVD SiN films could also contribute to the high V_{oc}. The highest efficiency obtained was 17.3%, which is respectable for a relatively thin cell (~180-200μm) with a planar front surface and only a single layer antireflection coating. This cell exhibited a fill-factor of 81.3%, which is very high for a multicrystalline solar cell.

Table 6.3. Calibrated measurements of planar all-SiN passivated PERC cells fabricated in this study using gettered 0.2Ωcm multicrystalline silicon. The n^+ emitter was defined by mesa etching.

Cell	m1*	m2	m3
Front passivation	SiN	SiN	SiN
Rear passivation	SiN	SiN	SiN
V_{oc} (mV)	655.4	656	659
J_{sc} (mA/cm^2)	31.0	32.2	32.6
Fill Factor (%)	78.9	81.3	70.1
η (%)	16.1	17.3	15.1

* Independently confirmed at Sandia National Laboratories

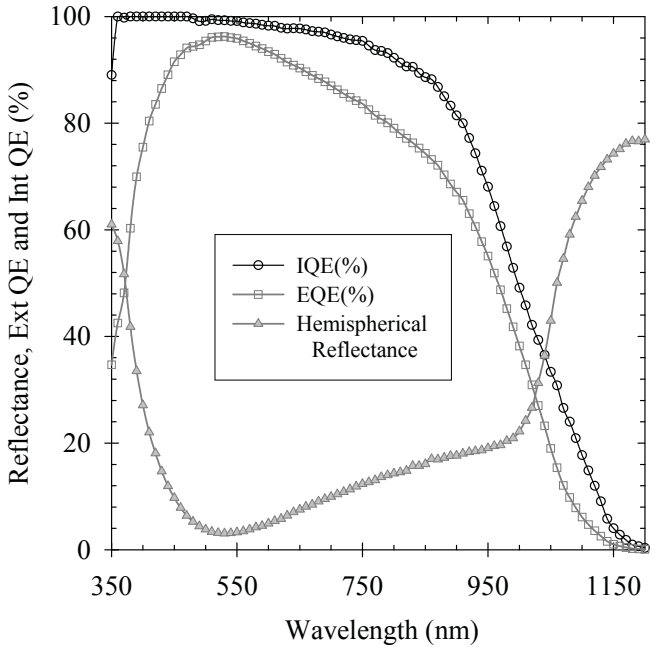


Figure 6.5. Spectral response and hemispherical reflectance for a planar, all-SiN passivated multicrystalline PERC cell (cell m1 in Table 6.3).

Spectral response and reflectivity measurements for the multicrystalline cell m1 are given in Figure 6.5. As with the planar float-zone cells, the IQE between the wavelengths of 350nm to 650nm is approximately 100%, an outcome of the excellent front surface passivation. The near-bandgap wavelength reflectance data for the cell are quite high compared to the data for the float-zone cell of Figure 6.3. This is partly due to the multicrystalline substrate being thinner, but it demonstrates that a significant amount (>80%) of the long wavelength light is being reflected from the rear surface of the cell. Thus, the rear aluminium reflector is operating

effectively. Clearly however, the cell is poor at trapping light and has a relatively low J_{sc}. A front surface texture would be highly desirable to reduce the cell reflectance and to obliquely couple the light into the substrate. Isotropic "tubs" texturing [175, 176] using PECVD SiN as the etching mask, rather than a thermal oxide, could be used for texturing these multicrystalline substrates or even random pyramids [171]. With the inclusion of texturing and possibly a double layer anti-reflection coating, the efficiency potential of these all-SiN multicrystalline PERC cells is clearly greater than 18%.

6.3.3.3 Random-Pyramid Textured Float-Zone Silicon Solar Cells

The cell results in section 6.3.3.1 suggest that high efficiency solar cells (η>20%) could be produced by incorporating a front surface texture into the float-zone cells. This should boost the J_{sc} by reducing the front surface reflection and improving the light trapping features. Table 6.4 shows results for cells textured with random pyramids. For the all-SiN passivated cell, the measured V_{oc} of 655mV again demonstrates that a high V_{oc} can be achieved using stoichiometric PECVD SiN films, even when the front surface is textured. Comparison of the V_{oc} for the two cells in Table 6.5 shows that there is no difference in the V_{oc} for textured cells passivated with a rear SiN or thermal SiO_2, which is consistent with the results for planar cells. Comparison of the V_{oc} for all-SiN passivated planar PERC cells with textured PERC cells shows there has been a reduction of ~12mV in V_{oc}. Some of the V_{oc} loss can be attributed to the higher J_{oE} for a textured n^+ emitter compared to a planar emitter (see section 5.2). Also, the sheet resistance of the emitter for the textured cells (60-70Ω/□) was lower than that of the planar cells (100-130Ω/□), which results in additional recombination in the emitter. Nevertheless, these initial results for textured cells were disappointing in terms of V_{oc}. After continued development, V_{oc}'s of 666mV have been achieved for all-SiN passivated PERC cells with random pyramid texturing by using a modified fabrication sequence, as will be shown in section 6.3.3.4.

The J_{sc} measured for the all-SiN passivated cell was 36.8mA/cm^2. A comparison of the J_{sc} for the two cells in Table 6.4 shows that the J_{sc} of the rear SiN passivated cell is significantly lower (1.5mA/cm^2) than that for the rear oxide passivated cell, even though they have an identical front surface. This is consistent with the results for planar cells, although the J_{sc} difference is now even larger. As mentioned previously, a J_{sc} loss for rear SiN passivated cells compared to oxide reference cells has also been found by Dauwe *et al.* [123], Preu *et al.* [154] and Schneiderlochner *et al.* [156], but not by Glunz *et al.* [155] for plasma etched RP-PERC cells.

Table 6.4. Calibrated measurements of RP textured all-SiN passivated PERC cells fabricated using 0.3Ωcm FZ substrates. The n^+ emitter was defined using a masking oxide.

Cell	T1*	T2*
Front passivation	SiN	SiN
Rear passivation	SiN	SiO_2
V_{oc} (mV)	655.6	654.0
J_{sc} (mA/cm^2)	36.8	38.3
Fill Factor (%)	76.9	77.9
η (%)	18.5	19.5

* Independently confirmed at NREL

The fact that the two cells in Table 6.4 have an identical front surface suggests that the loss in J_{sc} is related to an effect at the rear surface. Figure 6.6(a) shows the measured EQE of these two cells, from which it can clearly be seen that the oxide passivated cell has a superior long wavelength EQE (λ>800nm). As longer wavelength light is absorbed closer to the rear of the cell, it therefore seems that the rear surface is indeed the cause for the reduced J_{sc}. A number of possible explanations for the J_{sc} loss can be hypothesized, including:

- A difference in the reflectance from the rear surface due to the higher refractive index of the SiN at the rear surface (1.95 for SiN compared to 1.54 for SiO_2).
- A strongly injection level dependent surface recombination velocity for the *p*-type Si/SiN interface.
- Shunting of an induced junction formed at the rear of the cell due to the fixed positive charges within the SiN film.

Figure 6.6(b) shows measurements of the reflectance for RP textured cells with SiN on the front and either SiN or thermal SiO_2 on the rear. It can be seen that there is little difference in the reflectance from the two different rear structures, at least for stoichiometric SiN (the same result may not hold true for silicon-rich SiN). Therefore the loss in J_{sc} can not be attributed to optical effects.

The cells in Table 6.4 have the same V_{oc} and so the global effective lifetime and the surface recombination velocity at an injection level corresponding to 1-sun illumination must be very similar. At the lower injection levels corresponding to short-circuit conditions, it is possible that a very different surface recombination velocity would result in a different J_{sc}. The results presented in Chapter 4 for effective lifetime measurements on test structures do indeed show that an alnealed thermal oxide results in better surface passivation than stoichiometric SiN

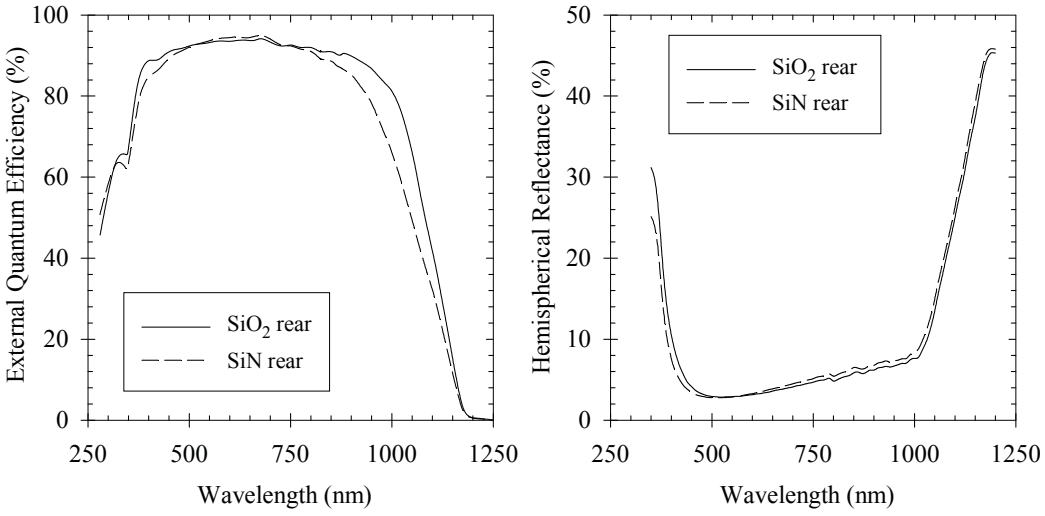


Figure 6.6. External quantum efficiency and hemispherical reflectance for RP-PERC cells passivated with SiN and SiO_2 at the rear surface. Both cells were passivated with SiN at the front surface.

films. However, the SiN films still result in an injection level dependence that is relatively weak, especially on the 0.3Ωcm wafers used for these solar cells. Thus while a small difference in the J_{sc} could be explained by this mechanism, it cannot account for the majority of the J_{sc} loss.

A significant amount of experimental evidence has been presented in Chapters 4 and 5 that indicates that the SiN films of this study have a high fixed charge density, even under illumination. For SiN passivated *p*-type wafers, it follows that electrons are accumulated at the surface. If the *p*-type dopant density is not too high, a shallow n^+ inversion layer will form (that is, an induced junction) and a low S_{eff} is obtained. In the context of PERC type solar cells, an induced rear junction would directly touch the rear metal contacts, and could result in a parasitic shunt of the solar cell and a subsequent loss in J_{sc}. Carriers generated closer to the rear surface would tend to be collected by the induced junction and subsequently lost through shunting, and so this mechanism is consistent with the EQE results of Figure 6.6(b). Furthermore, such a parasitic shunt would be more detrimental for textured cells, where a greater proportion of long wavelength light is captured. This is consistent with the results of this chapter, where the J_{sc} difference between SiN rear passivated PERC cells and oxide rear passivated reference cells was much greater for textured cells compared to planar cells.

Dauwe *et al.* have also found that an induced junction forms at the rear surface of *p*-type solar cells passivated with silicon-rich SiN films and independently proposed that parasitic shunting causes a loss in J_{sc} [159]. They concluded this by fabricating cells with a novel rear passivation scheme, which consisted of a small area of alnealed SiO_2 around the rear metal contacts and silicon-rich SiN elsewhere. They showed cells with this novel rear structure had

very similar J_{sc} to reference cells that only had alnealed SiO_2 on the rear. Their results therefore provide additional verification to the hypothesis that well-passivating PECVD SiN films contain a high fixed charge density, even under illumination.

Reducing the parasitic shunt at the rear surface could be achieved by a number of methods. Solar cells could be fabricated using *n*-type silicon, where the positive charges would not result in an induced junction, and indeed, the accumulation layer formed by the positive charges might actually have benefits for the cell fill-factor. A second method would be to diffuse a local p^{++} back-surface field between the *p*-type contact and the induced junction, resulting in a rear structure similar to that of a PERF cell [177]. Indeed, the bifacial cells of Hubner *et al.* [152] inadvertently had such a rear structure and this helps explain why these cells had J_{sc} as high as 38.9mA/cm^2. A third, much simpler method investigated here, might be to etch the silicon within the vicinity of the rear contact dot. As the induced junction is very shallow, etching away something like 1μm of silicon at the rear dots might result in the rear metal contacting the silicon away from the induced junction. The shunt conductance would then be decreased and subsequently the loss in J_{sc} reduced. Incidently, this may be the reason why the rear SiN passivated, plasma etched RP-PERC cells of Glunz *et al.* [155], show equivalent J_{sc} to the rear oxide cells, because the plasma also etches some of the silicon away. Work on this approach is described in the next section.

6.3.3.4 Alternative Rear Contact Schemes

A variety of random pyramid textured solar cells with alternative rear cell designs were fabricated to further investigate the loss in J_{sc} for rear SiN passivated solar cells. A full area rear contact (no SiN passivation) consisting of either non-alloyed aluminium or alloyed aluminium (Al-BSF) was investigated. High purity (5N) aluminium was evaporated on to the rear of the cells, and the alloying was done for 15mins at 900°C in a nitrogen ambient. More RP-PERC cells with SiN passivation were fabricated, but with the approximately 1μm of silicon removed from the rear contact dots before the rear aluminium contact was evaporated. The silicon was removed using registration etch, with baked photoresist protecting the SiN film. Finally, to determine an upper limit for the cell processing, RP-PERC cells with a selective emitter, an alnealed rear thermal oxide and a thin thermal SiO_2/SiN front surface passivation where fabricated.

Results for the various cells are given in Table 6.5, where the cell results of Table 6.4 have also been included. Comparing the different cells to the standard processed all-SiN RP-PERC cell (cell T1), a number of observations can be made. Firstly, while cells with a full area rear contact (cells A1 and A2) show significantly lower V_{oc} than cell T1 (≈15mV less), they

Table 6.5. Calibrated measurements of RP PERC cells with different rear passivation schemes. The cells were fabricated using 0.3Ωcm FZ substrates and the emitter was defined using a masking oxide.

Cell	A1*	A2*	T1*	A3*	A4*
Front passivation	SiN	SiN	SiN	SiN	SiO_2/SiN
Rear passivation	none (Al)	Al-BSF	SiN	SiN (reg etched)	SiO_2
V_{oc} (mV)	641	642	655.6	666	684
J_{sc} (mA/cm^2)	36.5	37.0	36.8	37.7	38.6
Fill Factor (%)	76.3	79.4	76.9	78.3	80.7
η (%)	17.8	18.8	18.5	19.7	21.3

* Independently confirmed at NREL, Sandia National Laboratories or the Fraunhofer ISE

show very similar J_{sc}. It appears that under short-circuit conditions, the action of a parasitic shunt at the rear of an all-SiN passivated cell is almost equivalent to the recombination losses if the rear surface was unpassivated. This would be consistent with the interpretation of the rear induced junction collecting carriers generated by long wavelength light and annihilating them across the shunt.

A second comparison is between cell T1 and cell A3. These cells are essentially identical except for the etching of silicon inside the rear contact dots. It is clear that cell A3 shows superior performance with a 10mV increase in V_{oc}, a 0.9mA/cm^2 increase in J_{sc} and 1.4% increase in fill-factor, resulting in a conversion efficiency of 19.7%. This is amongst the highest efficiencies achieved for all-SiN passivated solar cells. The high V_{oc} of 666mV for cell A3 is essentially as high as that achieved for planar all-SiN passivated cells. Comparing cell A3 with the rear oxide passivated cell T2 (see Table 6.4), shows that the J_{sc} of the rear SiN passivated cell is almost as high as that of the rear oxide cell. When it is considered that the etching of the rear dots was not optimised, the difference in J_{sc} could probably be less than 0.6mA/cm^2 with proper optimisation.

Finally, the results for cell A4 indicate that a J_{sc} as high as 38.6mA/cm^2 should be possible based on the cell processing techniques used for these cells. The higher J_{sc} of cell A4 compared to the other cells is partially related to its selective emitter structure and the superior front surface passivation provided by the thin thermal SiO_2/SiN stack, particularly on textured surfaces. What is clear is that a much higher V_{oc} is achievable using the selective emitter structure, largely because of the significant amount of busbar that exists in the front finger design used for these cells. Literature values for the J_{sc} of RP-PERC type cells shows that currents around 40mA/cm^2 are possible [155], appreciably higher than the 38.6mA/cm^2 determined in these experiments. It appears that the front finger design of the cells in Table 6.5,

when compared to the finger design used at the Fraunhofer ISE for example, results in a relative J_{sc} loss of ~1mA/cm^2 due to increased reflection from the front surface (primarily off the metal). Furthermore, the use of less heavily doped wafers, say 0.5-0.6Ωcm rather than 0.3Ωcm, would also aid the J_{sc} due to their higher bulk lifetime.

6.3.3.5 Local BSF Type Rear Contact Without Photolithography

The above results and discussion indicate that when using a SiN layer for rear surface passivation, the maximum benefits to cell performance would occur when a local rear BSF or PERL type rear contact is used. That is, the V_{oc} would be significantly increased compared to a full area metal contact or Al-BSF, and the J_{sc} loss associated with the parasitic shunt is minimised due to the local p^+ diffusion separating the rear metal contact and the SiN induced inversion layer. The use of a PERL type rear structure also has the advantage that it allows higher resistivity material to be used for the base compared to a PERC type rear contact.

A novel method for forming a PERL type rear contact without photolithography has been investigated. It takes advantage of the relatively low temperatures used for the SiN deposition, and the much greater deposition rate of SiN onto a silicon surface compared to an aluminium surface. Cells were fabricated using planar, 300μm thick, 1.5Ωcm *p*-type FZ silicon. A tube based $POCl_3$ diffusion was used to form the n^+ emitter (~120Ω/□) and then high purity aluminium was evaporated onto the rear surface through a shadow mask consisting of 300μm diameter holes with a coverage fraction of ~10%. The aluminium was then alloyed at 900°C for 15mins in a nitrogen ambient to form a local Al-BSF. Stoichiometric SiN films were then deposited onto the front and rear surfaces for reflection control and surface passivation. A second aluminium layer is then evaporated over the entire rear surface and because the deposition rate of SiN onto the aluminium dots is so slow, the second aluminium layer actually contacts the local Al-BSF dots. The cells were completed by forming the front grid by liftoff, with subsequent sintering and Ag plating of the front fingers. Cells with a full area Al-BSF were fabricated for comparison.

Table 6.6 shows results for the best cells from a limited experimental effort. It can be seen that the use of the PERL type rear structure consisting of SiN and local Al-BSF has boosted the V_{oc} to 649mV, a 13mV increase compared to the case of a full area Al-BSF. Importantly, the J_{sc} has not decreased due to parasitic shunting at the rear surface, but, if anything has slightly increased due to the improved rear surface passivation and internal reflectance. Unfortunately the fill-factor is only 76.5% for the PERL type cell and so the efficiency of this cell was 17.7%, slightly less than the cell with a full area Al-BSF. It is not

Table 6.6. In-house measurements of cells incorporating a local Al-BSF at the rear surface with SiN passivation elsewhere. The rear surface structure was formed without photolithography. The cells were fabricated using 1.5Ωcm FZ silicon with a planar front surface. Cells with a full area Al-BSF are included for comparison.

Cell	R1	1Tb
Front passivation	SiN	SiN
Rear passivation	SiN/Al-BSF	Al-BSF
V_{oc} (mV)	649	636
J_{sc} (mA/cm^2)	35.6	35.4
Fill Factor (%)	76.5	79.6
η (%)	17.7	17.9

known if the lower fill-factor is due to a thin residual SiN layer between the alloyed Al dots and the second aluminium layer. Nevertheless, the experimental results certainly demonstrate the feasibility of this novel method for forming a PERL type rear contact using SiN and without photolithography, which appears very attractive. A significant amount of optimisation is still required for the process however, including factors such as the design of the rear Al dots (contact fraction and dot size), the thickness of Al evaporated to form the dots and possible variations of the contact sintering to improve the fill-factor.

Another attractive feature of this novel rear type contact is that it could easily be formed using screenprinted aluminium and therefore would be easily transferable to low cost industrial cells. It would also be highly suitable for bifacial cells, where the second aluminium evaporation would be eliminated. It is also very promising for cells fabricated on thin wafers where a full area Al-BSF is undesirable due to bowing of the wafers, while providing improved surface passivation. Obviously it would be possible to simply fire a screen-printed aluminium grid through a rear SiN layer and, as long as the aluminium alloyed with the silicon, then the same type of rear structure is formed. Critically though, the scheme introduced above does not rely on the SiN film maintaining it's excellent surface passivation during a high temperature firing step.

6.3.3.6 Conclusions

Simplified PERC cells involving PECVD SiN layers for front and rear surface passivation have been fabricated. High open circuit voltages of 665-670mV have been obtained using float-zone silicon substrates for cells with either a planar front surface or with random pyramid texturing. These high V_{oc}'s confirm the excellent surface passivation of the stoichiometric SiN films in actual devices. Conversion efficiencies upto 19.7% have been

achieved. Cells fabricated on gettered, multicrystalline substrates using only one high temperature step have produced open circuit voltages of 655-659mV and conversion efficiencies upto 17.3% with a planar front surface and a single layer anti-reflection coating.

Evidence of parasitic shunting at the rear of SiN passivated *p*-type PERC solar cells has been presented, which results in a loss of J_{sc} compared to other rear surface passivation schemes. The parasitic shunt arises from an inversion layer at the rear surface, due to a high fixed positive charge density in the SiN layer. It has been demonstrated that a simple way to reduce the impact of the parasitic shunt is to etch away some of the silicon at the rear contact dots. A novel method for forming a PERL type rear contact consisting of a local Al-BSF and SiN without photolithography has also been developed. This novel rear contact scheme appears to offer significant improvements to V_{oc}, due the SiN rear surface passivation, without any loss in J_{sc} from parasitic shunting. It is ideally suited to thin wafers as it does not result in wafer bowing and to bifacial cells.

6.4 n-type Cells with SiN Passivation

The use of well passivating stoichiometric SiN films to fabricate high V_{oc} and high efficiency *p*-type silicon solar cells has been demonstrated in the previous section. It is also interesting to apply stoichiometric SiN films to other devices. In particular, demonstrating that a high V_{oc} can also be achieved for all-SiN passivated solar cells fabricated from *n*-type silicon would be highly desirable, as this would confirm the low surface recombination velocities determined for the *n*-type Si/SiN interface in Chapter 4 in a real device. The lack of relevant data on such devices in the literature makes this investigation interesting, particularly considering the potential to use high lifetime *n*-type CZ wafers (see Chapter 3) which do not show the same light induced degradation observed in boron doped *p*-type CZ wafers.

The fabrication of an *n*-type solar cell with high V_{oc} relies on the formation of a high quality *p*-type emitter, while maintaining a high bulk lifetime, along with excellent surface passivation. Forming an ohmic contact to *n*-type silicon also requires a relatively high phosphorus concentration at the surface. The results of Chapter 5 show that the SiN films optimised in this study provide poor passivation of p^+ emitters. The bifacial cells of Figure 6.7 were therefore devised for this study, as they have only a small area of p^+ diffusions, and they also maximise the area of the *n*-Si/SiN interface, which is the recombination mechanism of interest.

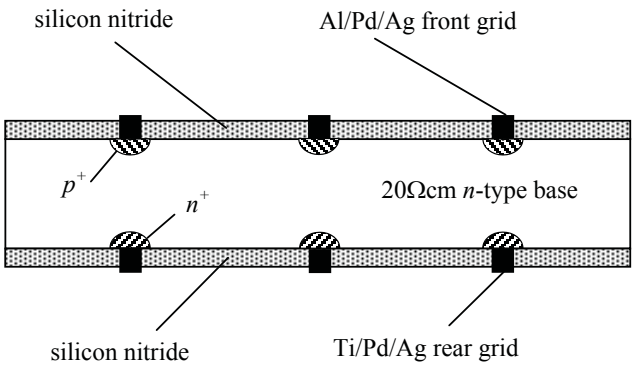


Figure 6.7. Schematic of the bifacial structure used for fabricating all-SiN passivated *n*-type solar cells.

The substrates used where <100> oriented, 200μm thick, 20Ωcm *n*-type float-zone silicon. Texturing was omitted for simplicity. An n^+ diffusion was performed on one side of the substrates at 880°C for 30mins using $POCl_3$ as the dopant source, to give a sheet resistance of 120Ω/□. A p^+ diffusion was then performed on the other side of the substrates at 965°C for 50mins using BBr_3 as the dopant source, to give a sheet resistance of 30Ω/□. Mesa-etching was used to define a finger grid on each side of the substrate and the surfaces where passivated with stoichiometric SiN. Metal contacts of Ti/Pd/Ag on the n^+ diffusion and Al/Pd/Ag on the p^+ diffusion where then formed by the liftoff technique and subsequently Ag plated.

Results for the two solar cells fabricated are given in Table 6.7 for both front and rear illumination. It can be seen that very high V_{oc} of 668mV to 675mV have been obtained for front and rear illumination, demonstrating the excellent surface passivation achieved at the *n*-type Si/SiN interface in real devices. Furthermore, the V_{oc} of 675mV achieved for cell 20nf under front illumination appears to be the highest ever measured for an all-SiN passivated solar cell regardless of the substrate type and resistivity. Importantly, these high V_{oc} have been achieved using high resistivity substrates, where the V_{oc} is much more sensitive to the surface passivation than for low resistivity substrates. Coincidentally, the values obtained for the V_{oc} on 20Ωcm *n*-type substrates are almost identical to the V_{oc} values obtained on 0.3Ωcm *p*-type substrates in section 6.3, but with an entirely different cell structure. It is important to point out that the cell structure used for the *n*-type cells is far from optimised in terms of the diffusion profiles, grid designs etc and higher V_{oc} are certainly obtainable.

The data in Chapters 3 to 5 can be used to estimate the limits imposed by recombination processes on the V_{oc} of these 20Ωcm all-SiN passivated *n*-type cells. Using Figure 5.7 for the J_{oE} of metallised emitters (assuming the curve applies to both n^+ and p^+ emitters), a contact fraction of 4% results in an emitter recombination of ~64fA/cm^2, which is mainly due to the

Table 6.7. Measurements for bifacial all-SiN passivated solar cells fabricated using planar 20Ωcm *n*-type substrates. The p^+ and n^+ diffusions where restricted to ~4% of the front and rear surface respectively to maximise the area of the *n*-type Si/SiN interface.

Cell	20nf		20ne	
Illumination	front (p^+ side)	rear (n^+ side)	front (p^+ side)	rear (n^+ side)
V_{oc} (mV)	675	674	669	668
J_{sc} (mA/cm^2)	30.8	31.8	30.3	30.2
Fill Factor (%)	77.0	72.9	73.5	73.8
η (%)	16.0	15.6	14.9	14.9

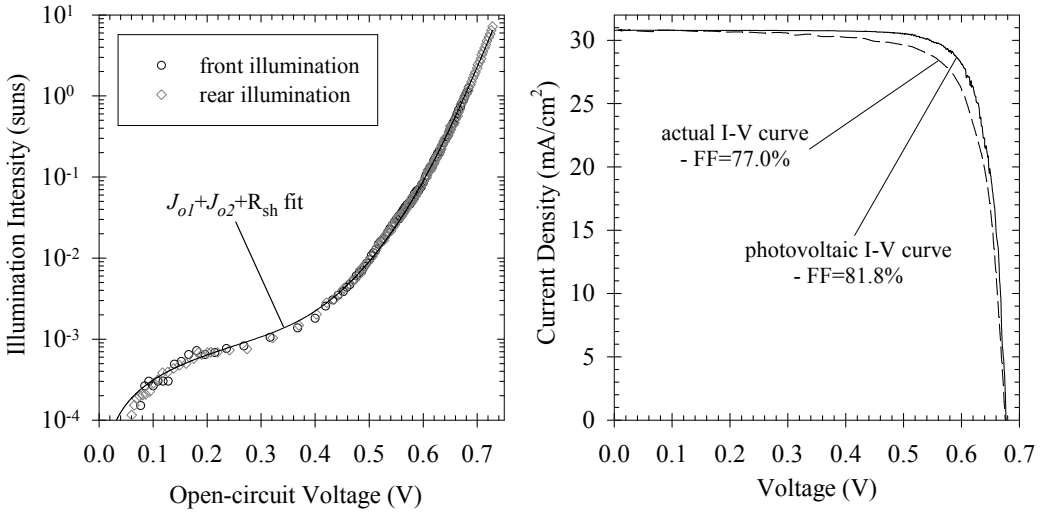


Figure 6.8. Illumination-Voltage characteristic and I-V curves for a planar, all-SiN passivated bifacial cell fabricated using 20Ωcm *n*-type silicon (cell 20nf in Table 6.6).

120Ω/□ n^+ emitter. In combination with bulk recombination (Chapter 3) and surface recombination at the Si/SiN interface (Chapter 4), the estimated V_{oc} would be 680mV for an assumed J_{sc} of 30.8mA/cm^2. This is in reasonable agreement with the measured V_{oc} and also indicates that reducing recombination at the n^+ diffusion, by using a lower sheet resistance, is highly desirable for increasing the V_{oc} of this cell structure. The estimated fill-factor and efficiency would be 82.7% and 17.3% respectively.

Comparison of the J_{sc} values for the cells in Table 6.7 shows that the J_{sc} seems to be as high, if not higher, under rear illumination (from the n^+ grid side) than under front illumination, that is, a bifaciality ≥ 100%. It is not clear if this is due to different reflection properties from the front and rear surfaces, say from different SiN film thicknesses, or if it is an electrical effect which results in a greater loss in J_{sc} under front illumination than under rear illumination. It should be pointed out that these J_{sc} values are in-house measurements only. The relative values

are believed to be correct but there is not an identical in-house reference for measuring *n*-type cells. The absolute values for the J_{sc} in Table 6.7 are relative to a *p*-type reference cell, which might result in a significant error.

The fill-factors for the cells in Table 6.7 are relatively poor, with the exception of cell 20nf under front illumination which gave a reasonable value of 77.0%. Significant problems with the adhesion of the metal fingers were experienced during the fabrication process, which resulted in the front fingers actually lifting off both cells during the Ag plating. The front fingers therefore had to be re-evaporated, which may partially explain the relatively poor fill-factors. Figure 6.8(a) shows the illumination-V_{oc} characteristics for cell 20nf under front and rear illumination. It can be seen that the cell's V_{oc} response is practically identical when illuminated from the different sides, which is consistent with a low S_{eff} at the Si/SiN interface. The resulting photovoltaic I-V curve is compared with the actual I-V curve in Figure 6.8(b). It can be seen that series resistance effects (including contact resistance) are quite severe for this cell as they have reduced the fill-factor from 81.8% down to 77.0%. Optimisation of the cell design in terms of diffusion profiles and grid spacing, with the possible inclusion of full area n^+ diffusions would likely improve the fill-factor.

The fill-factor and efficiency from the photovoltaic I-V (81.8% and 17.0%) are in reasonable agreement with the values estimated from the data in Chapter 3 to 5, which were 82.7% and 17.3% respectively. A standard diode analysis of the illumination-V_{oc} characteristic gives fit values of J_{o1} = 105fA/cm^2, J_{o2} = 13nA/cm^2 and R_{shunt} = 10500Ω, with the fit included in Figure 6.8(a). It is not known if the shunt arises because of the SiN surface passivation (in this case the SiN films would cause an accumulation of electrons near the surface), but the shunt certainly reduces the fill-factor of the photovoltaic I-V curve, partially explaining why it is not as high as the 82.7% expected. Possible degradation of the bulk lifetime during the boron diffusion, as was shown in section 5.3 (albeit at a low level), has also not been included in the modeled values.

Conversion efficiencies up to 16% have been achieved for these planar all-SiN passivated *n*-type cells, which is a reasonable result. This could obviously be improved by surface texturing. The high V_{oc} and bifaciality factors are, nevertheless, a strong proof of concept and indicate that *n*-type cells with SiN passivation are a very promising alternative to prevalent device structures.

6.5 Solar Cells with an Industrial Belt-Line Emitter Diffusion

The commercial application of PECVD SiN films for the front surface of multicrystalline silicon solar cells is becoming a reality [163, 178]. Typical commercial multicrystalline silicon solar cells are planar due to the lack of a suitable texturing method and are fabricated using simple processes such as a belt-line furnace for emitter formation and screen-printing for the metal contacts. It has already been shown in section 5.2.5 that stoichiometric SiN films can be used to obtain reasonable surface passivation for industrial, belt-line diffused emitters, which are characterised by a very high surface concentration of phosphorus atoms ($\sim 10^{21} cm^{-3}$). In this section, results are presented for solar cells fabricated in a commercial environment but incorporating stoichiometric SiN films on the front surface. Firstly, the performance levels that might be achieved using stoichiometric SiN passivation on the front surface are investigated by using high quality, planar float-zone silicon substrates processed partially in the laboratory and partially in BP Solar's factory. Secondly, standard BP Solar multicrystalline silicon cells where fabricated in the factory, with the exception that the TiO_2 anti-reflection coating was replaced with a stoichiometric SiN film. Finally, BP Solar multicrystalline silicon solar cells were fabricated in the factory but using a stoichiometric SiN film on the front surface in conjunction with a fire-through screen-printed metallisation. A novel, maskless, reactive-ion-etching technique developed at Sandia National Laboratories [166] was applied to some of these fire-through cells.

6.5.1 Large Area Planar Float-Zone Silicon Cells

Solar cells were fabricated on 4inch diameter, 300μm thick, 1.5Ωcm *p*-type float-zone substrates using two of BP Solar's diffusions, the standard production diffusion of 55Ω/□ and a lighter diffusion of 90Ω/□ (see section 5.2.5 for more information). Planar wafers were deliberately used as this is the typical surface condition of multicrystalline substrates. Following, the emitter diffusion at BP Solar, approximately 1.5μm of aluminium was evaporated onto the rear surface and alloyed in nitrogen at 900°C for 15mins to form an aluminium back-surface field. The open-circuit voltage limit imposed by the Al-BSF was independently measured on p^+pp^+ test structures to be ≈635mV, which is comparable to the V_{oc} limit imposed by the standard Al-BSF formed at BP Solar using a thick (~10μm) screen-printed aluminium layer [179]. A stoichiometric SiN film was then deposited on the front surface and the front grid of Ti/Pd/Ag fingers formed by liftoff with subsequent silver plating. The cells

Table 6.8. Calibrated measurements of cells incorporating a SiN passivated industrial belt-line n^+ emitter. The cells were fabricated using 1.5Ωcm FZ silicon with a planar front surface and a full area Al-BSF.

Cell	A*	B*
R_{sheet} (Ω/□)	90	55
n^+ diffusion	Belt-line	Belt-line
Cell area (cm^2)	46.2	46.2
V_{oc} (mV)	632	631
J_{sc} (mA/cm^2)	34.5	33.9
Fill Factor (%)	79.4	79.6
η (%)	17.3	17.0

* Independently confirmed at the Fraunhofer ISE

were isolated from the periphery of the wafer by a dicing saw, resulting in a cell size of 68mm x 68mm.

Performance data for the best two cells, independently measured at the Fraunhofer ISE, are given in Table 6.8. It is important to note that the V_{oc} for both cells (~632mV) are limited by the rear Al-BSF, explaining why the voltage of the two cells is the same despite the different emitter. The J_{sc} of cell A is $34.5mA/cm^2$, which is very satisfactory considering the surface is not textured and only has a single layer anti-reflection coating. The heavier diffusion of cell B (55Ω/□) produces a drop in current of $0.6mA/cm^2$ (1.8% in relative terms). The fill-factor of both cells is close to 0.8, which is also good considering the cells have a surface area of $46.2cm^2$. The resulting cell efficiencies are 17.3% and 17%. Comparison with the results for cell 1Tb (see Table 6.6), which had the same rear Al-BSF but was much smaller (~$4cm^2$) and had a laboratory processed n^+ emitter of 120Ω/□, shows that currents of $35.4mA/cm^2$ can be achieved with a higher quality laboratory emitter and reduced shading loss from the front grid.

To gain further insight into the surface passivation quality of the stoichiometric SiN films on the industrial emitters, spectral response measurements were performed. The internal quantum efficiency of cell A and cell B are shown in Figure 6.9. It can be seen that both cells have identical IQE for intermediate and long wavelengths, which indicates that the bulk lifetime and BSF are practically identical. As expected, cell A with its lighter emitter shows an improved blue response compared to cell B, with higher IQE for wavelengths <500nm. Importantly though, the short wavelength IQE for both cells is quite high (~80% at 350nm). This indicates that, in agreement with the J_{oE} measurements, that the emitters are indeed reasonably well passivated even for the high phosphorus concentration at the surface.

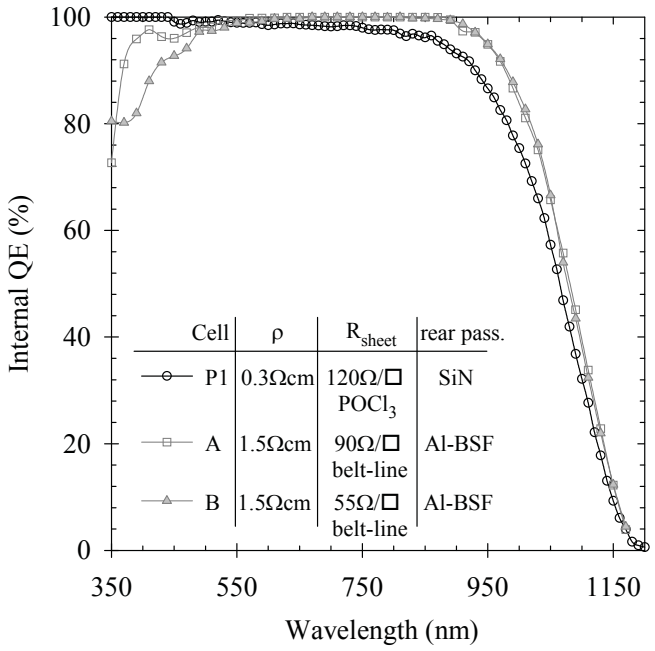


Figure 6.9. Comparison of the internal quantum efficiency of cells with SiN passivated n^+ emitters formed in an industrial belt-line furnace and a laboratory tube furnace.

It is interesting to compare the cell results in Table 6.8 with those of the planar PERC cells in section 6.3.3.1. Despite the planar PERC cells having open-circuit voltages that are 30-35mV higher, the efficiencies of the small area cells are not significantly different. This is because the PERC cells have much lower J_{sc}. Included in Figure 6.9 is the IQE for a planar PERC cell fabricated on 0.3Ωcm *p*-type FZ silicon. It can be seen that the PERC cell has the best blue response due to its better optimised emitter (laboratory processed, 120Ω/□), but a lower IQE for wavelengths >650nm. The lower long-wavelength IQE is partly due to the heavier doping of the substrates used to fabricate the PERC cells. However, because effective lifetimes greater than 170μs have been measured for these 0.3Ωcm substrates, the lower long-wavelength IQE is believed to be mainly due to the loss of current from the parasitic shunt at the rear surface of the PERC cells. Indeed, the efficiency of cell A, with a 90Ω/□ industrial emitter and being more than ten times the area, is almost as high as the best planar PERC cell which was 17.8%. This again stresses the importance of avoiding parasitic shunting of the rear induced junction for efficient rear SiN passivated solar cells.

6.5.2 Large Area Screen-Printed Multicrystalline Silicon Cells

Stoichiometric SiN films where next applied to commercial BP Solar multicrystalline solar cells. Two sets of fourteen matched multicrystalline substrates where chosen from commercial material (a total of 28 wafers) and processed using the standard industrial

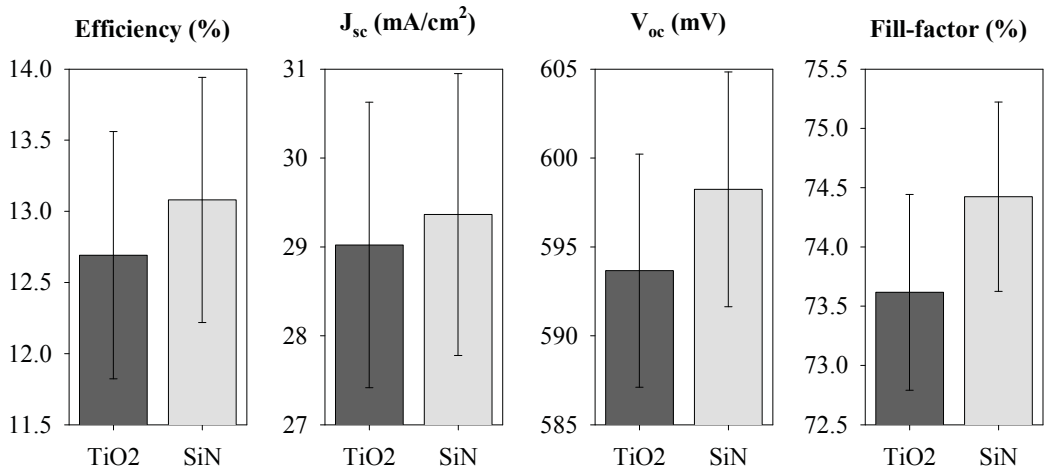


Figure 6.10. Electrical performance of SiN passivated, industrially processed large area multicrystalline cells and TiO_2 control cells.

fabrication sequence. The final production step involves depositing an APCVD TiO_2 anti-reflection coating, which one set of substrates received (the control set), while a stoichiometric SiN film was deposited on the front of the second set. As the SiN film was deposited as the last step, the potential for bulk passivation is reduced as there is no subsequent firing steps to release the hydrogen in the SiN film into the bulk of the multicrystalline wafer [178]. The cell dimensions where 11.4cm by 11.4cm.

The mean electrical performance of the two sets of cells are given in Figure 6.10. It can be seen that, on average, the SiN coated cells demonstrated modest improvements compared to the TiO_2 cells, with an absolute increase in efficiency of 0.39% (3.1% in relative terms), an increase in J_{sc} of 0.4mA/cm2 (1.2% relative), an increase in V_{oc} of 4.5mV (0.8% relative) and an absolute increase in fill-factor of 0.8% (1.1% relative). The best SiN coated cell had an efficiency of 14.2% compared to 13.8% for the best TiO_2 cell. These results suggest that replacing the TiO_2 coating with SiN film is advantageous, even when the process is not optimised to enhance bulk passivation. These results are further evidence of some degree of passivation of the industrial n^+ emitters.

6.5.3 Large Area Fire-Through Multicrystalline Silicon Cells

The use of a short, high temperature (~800°C) anneal for multicrystalline solar cells with a PECVD SiN coating on the front has been shown to be beneficial in improving the bulk lifetime of the multicrystalline silicon base [164]. It is believed that hydrogen in the SiN films is released during the anneal and then diffuses into the bulk of the substrate where it passivates various recombination centres. The use of this short temperature anneal to simultaneously fire

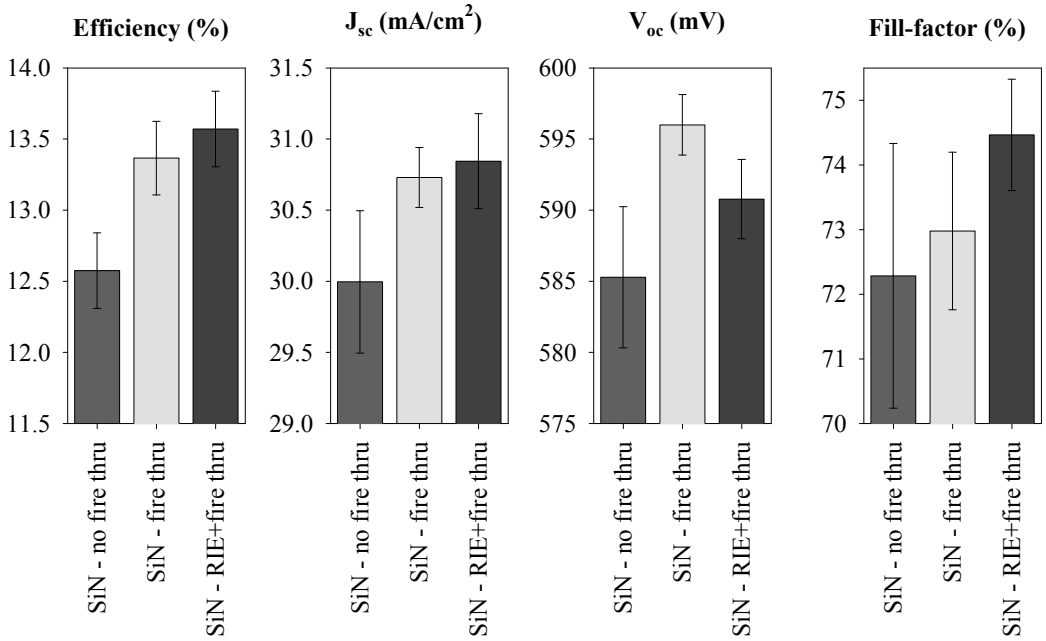


Figure 6.11. Electrical performance of SiN passivated, industrially processed large area multicrystalline cells. Cells with a planar surface and a mask-less RIE front texture were investigated, as well as firing the contacts through the SiN passivation.

screen-printed contacts has resulted in significant improvements to cell efficiency without increasing the processing complexity [165]. The potential for *bulk passivation* by using the stoichiometric SiN films optimised in Chapters 4 and 5 was investigated with the results reported in this section. Admittedly, the stoichiometric SiN films developed in this study where optimised for surface passivation and it does not follow that the same deposition parameters will be optimal for bulk passivation.

Three sets of eight matched multicrystalline substrates where chosen from commercial BP Solar material (24 wafers in total). The first set of wafers was processed using the standard industrial fabrication sequence, with the final step being the deposition of a stoichiometric SiN film on the front surface. The second and third sets of wafers where processed at BP Solar using a fire-through screen-print metallisation. The details of the fire-through parameters were developed by BP Solar and involves depositing the SiN film of the front surface before screen-printing the metal pastes and then firing the contacts. The second set of wafers had the conventional planar surface, while the third set where textured using a maskless reactive-ion-etching technique developed at Sandia National Laboratories [166] with a subsequent etch to remove the surface damage caused by the RIE. The cell dimensions where 11.4cm by 11.4cm.

The mean electrical performance of the three sets of cells are given in Figure 6.11, while data for the best cell from each set is given in Table 6.9. It can be seen from Figure 6.11, that

Table 6.9. Calibrated measurements of industrially fabricated multicrystalline solar cells incorporating a SiN passivated front passivation. Cells with a planar surface and a mask-less RIE front texture were investigated, as well as firing the contacts through the SiN passivation.

Cell	11*	1*	15*
Front surface	planar	planar	RIE texture
Fire thru	no	yes	yes
V_{oc} (mV)	585	596	595
J_{sc} (mA/cm^2)	29.4	30.8	31.8
Fill Factor (%)	73.8	75.3	75.1
η (%)	12.7	13.8	14.2

* Independently confirmed at Sandia National Laboratories

the planar fire-through cells show a significant improvement in performance compared to the standard cells. The average cell efficiency increased by 0.8% in absolute terms (6.3% in relative terms) due largely to an increased J_{sc} of 0.75mA/cm^2 and increased V_{oc} of 10.7mV. The RIE texture fire-through cells also showed significant improvement in comparison to the standard cells (a 1% gain in efficiency in absolute terms), but only small improvements compared to the planar fire-through cells (a 0.2% gain in efficiency in absolute terms). This indicates that it is the fire-through process that is responsible for the improvements, which is consistent with a bulk passivation mechanism.

The results for the best cells in Table 6.9 show that the best standard cell had an efficiency of 12.7%. This is significantly lower than for the substrates processed in section 6.5.2 using the same process sequence (η=14.2%) and is indicative of the variability in the quality of commercial multicrystalline substrates. It appears that the substrates used for these fire-through experiments where relatively poor. The best fire-through cells had reasonable efficiencies of 13.8% for a planar surface and 14.2% for an RIE textured surface, with the two cells having almost identical V_{oc} and fill-factor. The V_{oc} are relatively low however (~595mV) when compared to many other large area industrially fabricated multicrystalline solar cells, which are typically 610-625mV [165]. Reflectance measurements for the two fire-through cells showed the weighted front reflectance to be 11.3% and 7.1% for the planar and RIE textured cell respectively. However, as can be seen from the IQE measurements shown in Figure 6.12, while both the fire-through cells had identical intermediate and long wavelength response, the RIE textured fire-through cell had an inferior blue response compared to the planar fire-through cell. This is probably due to some residual damage at the front surface from the RIE. Therefore, while the RIE texturing was successful in reducing the reflectance, the full benefit of this could not be realised due to increased recombination at the front surface.

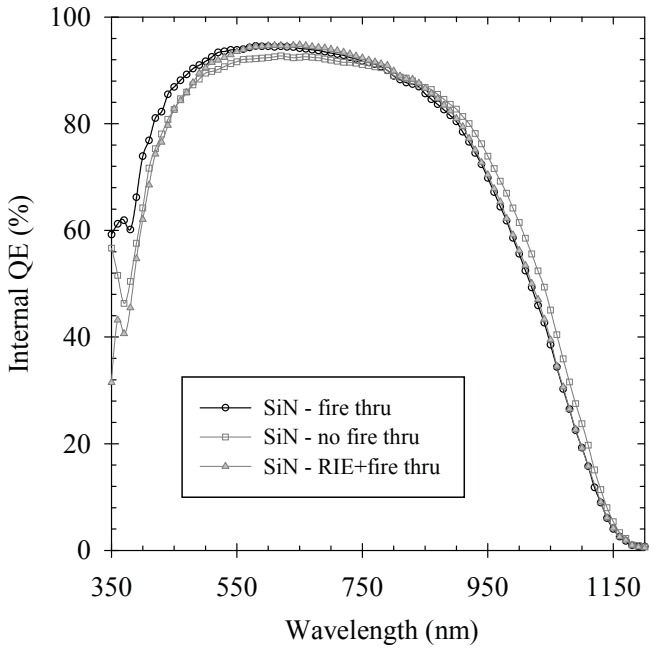


Figure 6.12. Comparison of the internal quantum efficiency of industrially fabricated multicrystalline solar cells incorporating a SiN passivated front passivation.

Comparison of the IQE for the standard cell and planar fire-through cell in Figure 6.12 shows that that the planar fire-through cell had a superior short wavelength response but an inferior long wavelength response. This indicates that bulk lifetime of the multicrystalline material (including the bulk of the n^+ diffused region) has been increased for the fire-through cell, at least near the front surface where light upto 850nm in wavelength are predominantly absorbed. This is presumably due to bulk passivation. It also suggests however, that the Al-BSF of the fire-through process is inferior to that of the standard process and more optimisation work is required at the rear surface of the fire-through cells. This is probably because the firing conditions for the rear surface are not the same for the two cells, as the fire-through process involves co-firing both the front and rear contact and the conditions are adjusted to suit this co-firing.

Finally, while it has been shown that bulk passivation occurs for these stoichiometric SiN film (at least towards the front surface), it is important to remember that the SiN films were optimised for their surface passivation properties. A re-optimisation for bulk passivation or ideally bulk and surface passivation could lead to further performance improvements.

6.5.4 Conclusions

Stoichiometric SiN films have been used to passivate the front surface of large area cells, where the n^+ emitter was fabricated in an industrial belt-line furnace. All the cells had a full area

Al-BSF which limited the V_{oc} to ~635mV. Cells fabricated on planar float-zone substrates with a photolithographically defined front gird demonstrated efficiencies up to 17.3% and reasonably high internal quantum efficiencies at short wavelengths (>80% at 350nm). Multicrystalline cells fabricated in a commercial production line demonstrated efficiencies upto 14.2% with screen-printed contacts. Planar multicrystalline cells fabricated on the same commercial production line but by firing the contacts through the front SiN film showed an absolute increase of 0.8% in cell efficiency compared to cells fabricated without the fire through process. Significant increases in both J_{sc} and V_{oc} were observed, presumably due to bulk passivation effects from the SiN layer. Inclusion of a mask-less RIE front texture resulted in a further modest 0.2% increase in cell efficiency, but resulted in a 5mV decrease in V_{oc} on average. Internal quantum efficiency measurements indicate that residual surface damage for the RIE texture cells reduces the gains provided by the lower reflection at the front surface.

6.6 Chapter Summary

The performance of silicon solar cells passivated with stoichiometric SiN films has been investigated in this chapter. Emphasis has been placed on demonstrating devices with a high V_{oc}, as this is the best indicator of the overall recombination rate within the cell, and demonstrates that the good surface passivation qualities provided by the SiN films can be maintained in real devices. High V_{oc}'s of 670mV have been obtained for all-SiN passivated simplified PERC cells fabricated on *p*-type float-zone silicon with either a planar or random pyramid textured front surface. Conversion efficiencies up to 19.7% have been achieved, amongst the highest for all-SiN passivated devices. Evidence of parasitic shunting at the rear of SiN passivated *p*-type PERC solar cells has been presented, which results in a loss of J_{sc}. It has been demonstrated that a simple way to reduce the impact of the parasitic shunt is to etch away some of the silicon from the rear contact dots. An alternative method is to have locally diffused p^+ regions under the rear contacts, and a novel method to form a rear structure consisting of a local Al-BSF with SiN passivation elsewhere, without using photolithography, has been demonstrated. Bifacial solar cells fabricated using planar, high resistivity *n*-type silicon have demonstrated V_{oc} up to 675mV, the highest ever reported for all-SiN passivated solar cells, and ~100% bifaciality factors. Small area cells fabricated on gettered, multicrystalline substrates have also demonstrated very high V_{oc} up to 659mV and conversion efficiencies up to 17.3%, with a planar front surface and a single layer anti-reflection coating. Stoichiometric SiN films have also been used to passivate the front surface of large area cells, where the n^+ emitter was formed in an industrial belt-line furnace. Reasonably high internal quantum efficiencies were

obtained at short wavelengths (>80% at 350nm), giving further evidence of the good passivation provided by the SiN films even for surfaces saturated with phosphorus. Multicrystalline cells fabricated in a commercial production line demonstrated efficiencies up to 14.2% with screen-printed contacts. Firing the contacts through the front SiN film showed an absolute increase of 0.8% in cell efficiency, with significant increases in both J_{sc} and V_{oc}, presumably due to bulk passivation effects from the SiN layer. Inclusion of a mask-less RIE front texture resulted in a further modest 0.2% increase in cell efficiency, but resulted in a 5mV decrease in V_{oc} on average. Internal quantum efficiency measurements indicate that residual surface damage for the RIE texture cells reduces the gains provided by the lower reflection at the front surface.

CHAPTER 7

Summary and Further Work

Recombination in silicon, both within the bulk and at its surfaces, has been investigated in this thesis. Special attention has been paid to the surface passivation achievable with PECVD SiN layers due to their potential for widespread use in silicon solar cells, particular in the context of a commercial drive towards using thinner substrates and requiring higher cell efficiencies. The accurate evaluation of surface recombination processes relies on accurate knowledge of bulk recombination rates. The intrinsic recombination rate within both *n*-type and *p*-type silicon has therefore been studied as a function of injection level for a large range of dopant densities, and a general parameterisation for the intrinsic recombination rate in crystalline silicon at 300K developed. This new parameterisation formed the basis for studying surface recombination at the Si/SiN interface. Optimised PECVD deposition parameters where determined using ammonia and dilute silane (4.5% silane in nitrogen) as the process gases. Importantly, the resulting optimised SiN films offer excellent surface passivation but are *stoichiometric* in composition rather than being silicon rich. The injection level dependence of the surface recombination velocity has been comprehensively studied for silicon passivated with these optimised SiN films for both *n*-type and *p*-type silicon and compared to silicon passivated with thermally grown SiO_2 (FGA and alnealed). The passivation of n^+ and p^+ emitters with optimised SiN films and thermal SiO_2 has also been extensively studied in this thesis over a large range of emitter sheet resistances. Finally, the optimised SiN films where implemented into a number of cell designs, incorporating *n*-type and *p*-type FZ silicon and *p*-type

multicrystalline silicon, to demonstrate their excellent surface passivation properties in finished devices. While the modeling work in this thesis has focused on silicon solar cells, the data provided for surface, emitter and bulk recombination in silicon is intended for broader application in general silicon semiconductor device modeling and analysis.

7.1 Measuring Recombination in Crystalline Silicon

Injection-level dependent lifetime measurements have been extensively used throughout this thesis to quantify the recombination rate in silicon. New techniques for interpreting the effective lifetime in terms of device characteristics have been introduced, based on the physical concept of a net photogeneration rate. The converse relationships for determining the effective lifetime from measurements of the V_{oc} under arbitrary illumination have also been introduced, thus establishing the equivalency of the photoconductance and voltage techniques, both quasi-static and transient, by allowing similar possibilities for all of them. Together, the photoconductance and voltage techniques form a powerful set of characterisation tools that can be applied at the wafer level and to finished devices, not only for scientific studies of recombination processes, but also for process optimisation and control as well as other diagnostic purposes.

Further Work: The quasi-steady-state methodology can be extended to develop new characterisation techniques, which are complementary to the existing tools. Possibilities include spectrally resolved measurements of the photoconductance or the open-circuit voltage, allowing recombination to be spatially resolved within the device in the same way as quantum efficiency measurements are based on short-circuit currents. Obviously the short-circuit current of finished devices could also be measured under quasi-steady-state conditions to further study recombination processes. The possibility of doing combined illumination-V_{oc} and illumination-J_{sc} measurements exist, which in principle would allow the separation of bulk and surface recombination mechanisms. Furthermore, analysing capacitive effects in samples measured under a time-varying illumination would improve the QssV_{oc} method in the low voltage range.

The adoption of lifetime monitoring within an industrial environment is also a challenging prospect. Significant economic benefits could be realised by greatly improved process control and optimisation, from the crystal growth and wafering stages right through to the solar cell fabrication. The development of simple, robust hardware with high throughput and little user intervention is required. Techniques for sorting wafers that show a relatively uniform lifetime across each wafer, especially for inhomogeneous material like multicrystalline and

ribbon silicon, without compromising throughput are also required. Methods for dealing with the variable surface conditions found on wafers, be it an as-cut condition, alkaline etched or textured etc, also need to be developed, especially as manufacturers are likely to be resistant, from a cost perspective, to having dedicated steps to passivate the wafers surfaces that would allow the lifetime to be measured more easily.

7.2 Lifetime and Efficiency Limits of Silicon Solar Cells

The rate of intrinsic recombination in crystalline silicon, particularly Auger recombination, is of fundamental importance. It ultimately determines the limiting performance of many silicon devices, including solar cells, and is typically a dominant recombination mechanism in heavily doped regions such as emitters. Record values for the effective lifetime, up to 32ms for high resistivity silicon, have been measured in this thesis for high quality *n*-type and *p*-type silicon with dopant densities up to ~$5x10^{16}cm^{-3}$. Importantly, the wafers where commercially sourced and had undergone significant high temperature processing. A new, general parameterisation has been proposed for band-to-band Auger recombination in crystalline silicon at 300K, which accurately fits the experimental lifetime data for arbitrary injection level and arbitrary dopant density, for both *n*-type and *p*-type dopants. The efficiency of crystalline silicon solar cells limited by intrinsic recombination has been re-evaluated using the newly developed parameterisation, where the effects of photon recycling have been included. The impact of *p*-type and *n*-type doping of the silicon has been studied, with a efficiency limit of 28.6% determined for 1Ωcm *p*-type silicon.

Further Work: Effective lifetimes higher than those achieved in this thesis may be ultimately obtained, particularly for high resistivity silicon. Close collaboration between growers of float-zone silicon and groups with expertise in surface passivation and lifetime measurements appears a sensible pathway to facilitating this. Improved methods of surface passivation, compared to the alnealed SiO_2 films used in this study, could also lead to improved lifetimes and amorphous silicon appears to be a potential candidate. Detailed experiments, based on wafer thinning could also be performed using the high lifetime wafers and surface passivation techniques of this study to separate the bulk and surface recombination rates.

The largest scatter in the experimental lifetime data appears to be for dopant densities in the range $10^{17}cm^{-3}$ to $5x10^{18}cm^{-3}$ and for injection levels between $10^{17}cm^{-3}$ to $10^{19}cm^{-3}$. Further work to clarify the intrinsic recombination limits in these ranges would be valuable, particularly for verifying if a transition in the intrinsic recombination rate occurs at the Mott density. Not all

lifetime measurement techniques are accurate in these ranges of dopant density and injection level, and methods based on free-carrier absorption using infra-red illumination appear to be the most suitable. Finally, a more accurate assessment of the radiative recombination rate in silicon appears warranted. Dependencies on the dopant density and injection level should be considered to investigate possible effects of Coulomb enhancement. The last evaluations of the radiative recombination rate in silicon appear to have occurred in the 1970's and the higher quality silicon and improved surface passivation techniques available today should allow improvements on these previous studies.

7.3 Passivation of *n*-type and *p*-type Silicon with PECVD Silicon Nitride

Surface recombination processes in silicon solar cells are becoming progressively more important as industry drives towards thinner substrates and higher cell efficiencies. The surface recombination properties of well-passivating SiN films on *p*-type and *n*-type silicon have been comprehensively studied in this thesis, with S_{eff} values as low as 1cm/s being unambiguously determined. The SiN films optimised in this thesis are unique in that they are stoichiometric in composition, rather than being silicon rich, a property which is attributed to the use of dilute silane as a process gas. A simple physical model, based on recombination at the Si/SiN interface being determined by a high fixed charge density within the SiN film (even under illumination), has been proposed to explain the injection-level dependent S_{eff} for a variety of differently doped wafers. The passivation obtained with the optimised SiN films has been compared to that obtained with high temperature thermal oxides (FGA and alnealed) and the limits imposed by surface recombination on the efficiency of SiN passivated solar cells investigated. Additional properties of the optimised stoichiometric SiN films were also investigated. This included demonstrating their negligible absorption of UV photons from the solar spectrum and their high etch rates in buffered HF, which allows them to be patterned by photolithography and therefore makes them attractive for fabricating high V_{oc} and high efficiency solar cells.

Further Work: The concentration of the silane bearing process gas appears to be critical in determining the composition of the optimised SiN films. The use of pure silane can result in well-passivating silicon rich SiN films, while, as shown in this thesis, the use of dilute silane (4.5% silane in nitrogen) can result in well-passivating stoichiometric SiN films. While both stoichiometric and silicon-rich SiN films offer very good surface passivation, their other properties, such as absorption coefficients, etchability, thermal stability etc, are distinctly

different. A more detailed study of the role of the silane gas concentration on the recombination, electrical and physical characteristics of well-passivating PECVD SiN films is therefore appropriate. Such a study has the potential to allow the surface recombination properties of the SiN films to be separately optimised from other physical properties such as the optical constants (refractive index and absorption coefficient). This could be extremely important for industrial applications of SiN films, as it would in effect allow the front surface reflection (and therefore the J_{sc}) to be optimised, while still maintaining good surface passivation. In addition, different types of SiN films might be more suitable for the rear surface than for the front surface depending on a combination of their optical properties and thermal stability.

The addition of other process gases, in particular hydrogen would also be interesting to study. PECVD SiN films typically contain a large amount of atomic hydrogen, which is normally sourced from the ionized silane and ammonia species. The addition of extra hydrogen gas might increase the atomic hydrogen content of the films even further, potentially resulting in improved surface passivation or, more importantly, improved bulk passivation, particularly after firing the films.

In the context of the SiN films optimised in this thesis, the investigation of higher deposition temperatures would be extremely interesting. It was shown that the effective lifetime of SiN/Si/SiN test samples was very sensitive to the deposition temperature and was increasing strongly with temperature, even at the maximum deposition temperatures that could be obtained using our PECVD chamber (400°C). Additional fundamental studies of the physical mechanisms responsible for the passivation of *p*-type and *n*-type silicon surfaces using these stoichiometric SiN films also seems warranted. Small pulse DLTS and C-V measurements could be used to determine the energy dependence of the interface trap density and the capture cross-sections along with the fixed charge density. It should be noted the well-passivating stoichiometric SiN films optimised in this study represent a unique opportunity for such DLTS and C-V measurements, as the MIS capacitors required for the measurements have small leakage currents. MIS capacitors fabricated with silicon rich SiN films typically exhibit leakage currents that are too large.

7.4 Passivation of Diffused Surfaces

The recombination properties of n^+ and p^+ emitters passivated with optimised SiN films and thermal SiO_2 have been extensively studied in this thesis over a large range of emitter sheet resistances. Both planar and random pyramid textured surfaces were studied for n^+ emitters,

where the optimised SiN films were again found to be stoichiometric in composition. The optimised SiN films provided good passivation of the heavily doped n^+-Si/SiN interface, with the surface recombination velocity increasing from 1400cm/s to 25000cm/s as the surface concentration of electrically active phosphorus atoms increased from $7.5x10^{18}cm^{-3}$ to $1.8x10^{20}cm^{-3}$. The optimised SiN films also provided reasonable passivation of industrial n^+ emitters formed in a belt-line furnace. It was found that the surface recombination properties of SiN passivated p^+ emitters was poor and was worst for sheet resistances of ~150Ω/□. The hypothesis that recombination at the Si/SiN interface is determined by a high fixed charge density within the SiN films was extended to explain the dependence of the SiN passivation of the p^+ emitters on their sheet resistance. For sheet resistances of ~150Ω/□, it is believed that the competing actions of the p^+ doping profile and the positive charges in the SiN film result in the silicon surface being in deep depletion, which maximises the surface recombination rate. At higher sheet resistances the surface is weakly inverted, while at lower sheet resistances the surface is weakly depleted and so the surface recombination rate is lower than the deep depletion case. The efficiency potential of SiN passivated n^+p cells has been investigated with a sheet resistance of 80-100Ω/□ and a base resistivity of 1-2Ωcm found to be optimal. Open-circuit voltages of 670-680mV and efficiencies up to ~20% and ~23% appear possible for SiN passivated planar and textured cells respectively, based on assumed short-circuit current densities of $35mA/cm^2$ and $40mA/cm^2$. The recombination properties measured for emitters passivated with SiO_2, both n^+ and p^+, were consistent with other studies and found to be superior to those obtained with SiN passivation.

Further Work: As discussed in section 7.3, further investigations into the effect of the process gases, in particular the composition of the silane carrying process gas, would also be appropriate for passivated n^+ emitters. Likewise, the effect of including additional process gases, specifically hydrogen, would also be interesting to study in the context of n^+ emitter passivation, as would investigating deposition temperatures above 400°C. A complete re-optimisation of the PECVD deposition parameters for passivating p^+ emitters with SiN would also be interesting. If SiN films that provide good passivation of heavily doped p^+ surfaces could be identified, then they would probably have very different properties than the stoichiometric SiN films studied throughout this thesis and they may indeed by more suitable for passivating the rear surface of solar cells fabricated with *p*-type silicon.

More general studies of oxide passivated p^+ emitters also seem warranted. There is little information available on the passivation of textured p^+ emitters, nor does there seem to be a great deal of consistent processing information on how to obtain well passivated p^+ emitters, which do not subsequently degrade and without reducing the quality of the bulk silicon.

7.5 Solar Cell Structures Passivated with PECVD SiN

Stoichiometric SiN films were used to passivate the front and rear surfaces of various solar cell structures. Emphasis was placed on demonstrating devices with high V_{oc} as this is the best indicator of the overall recombination rate within the cell, and therefore demonstrates that the good surface passivation qualities of the SiN films can be maintained in real devices. Simplified PERC cells fabricated on 0.3Ωcm *p*-type silicon, with either a planar or random pyramid textured front surface, produced high V_{oc}'s of 665-670mV and conversion efficiencies up to 19.7%, which are amongst the highest obtained for SiN passivated solar cells. Bifacial solar cells fabricated on planar, high resistivity *n*-type substrates (20Ωcm) have demonstrated V_{oc}'s up to 675mV, the highest ever reported for an all-SiN passivated cell, and excellent bifaciality factors. Planar PERC cells fabricated on gettered, 0.2Ωcm multicrystalline silicon have also demonstrated very high V_{oc}'s of 655-659mV and conversion efficiencies up to 17.3% using a single layer anti-reflection coating. Short-wavelength internal quantum efficiency measurements confirmed the excellent passivation achieved with the optimised stoichiometric SiN films on n^+ emitters, while long-wavelength measurements show that there is a loss of J_{sc} at the rear surface of SiN passivated *p*-type cells due to parasitic shunting. The parasitic shunt arises from an inversion layer at the rear surface, which forms due to the high fixed charge (positive) density in the SiN layers. It has been demonstrated that that a simple way to reduce the impact of the parasitic shunt is to etch away some of the silicon from the rear contact dots. An alternative is to have locally diffused p^+ regions under the rear contacts, and a novel method to form a rear structure consisting of a local Al-BSF with SiN passivation elsewhere, without using photolithography, has been demonstrated. Large area solar cells fabricated with a planar front surface and an industrial n^+ emitter (characterised by a surface saturated with phosphorus atoms) demonstrated efficiencies up to 17.3%. Reasonably high internal quantum efficiencies were obtained at short wavelengths (>80% at 350nm), further demonstrating the good passivation of the SiN films on industrial emitters. Large area multicrystalline cells with the front contacts fired through a SiN film produced efficiencies up to 14.2%. This was an absolute increase of 0.8% in cell efficiency compared to cells without fired contacts, and demonstrates bulk passivation effects form the SiN layer.

Further Work: The fabrication of all-SiN passivated solar cells with efficiencies in excess of 21% appears feasible. A PERL type cell structure seems most appropriate as the passivated rear dot contacts helps to minimse any parasitic shunting of the rear surface. Less heavily doped *p*-type silicon can also be used compared to a PERC type cell, which aids in increasing the J_{sc}. Importantly, because the well-passivating stoichiometric SiN films developed in this thesis can be patterned using standard photolithography, the fabrication of PERL type cells, which require

aligned photolithography steps, is feasible. The same cannot be said of well-passivating silicon rich SiN films. Numerous other high efficiency solar cell features could also be applied to improve the efficiency of the all-SiN passivated cells fabricated in this thesis. A redesign of the front finger grid to reduce the size of the busbar is required, or preferentially, a picture-frame type front grid could be used to improve both V_{oc} and J_{sc}, where the cell busbar is outside the illuminated cell area and does not actually touch the underlying silicon. The use of a selective emitter structure to passivate the front contacts would be desirable to improve V_{oc}, as would using inverted pyramids to texture the front surface rather than random pyramids. Improvements to J_{sc} could be obtained by using a double-layer anti-reflection coating, possibly using PECVD SiO_2 as the second layer. High aspect ratio front fingers would also reduce grid shading, where the Ag plating is performed into a thick layer of photoresist to cause the fingers to be taller and thinner.

Many of the above cell improvements could also be applied to improve the efficiency of the all-SiN passivated multicrystalline silicon solar cells fabricated in this thesis. Keeping in mind the desire to minimise the number of high temperature steps, the most attractive cell improvements would be the redesign of the front finger grid to reduce shading losses and recombination under the busbar; the introduction of a front surface texture consisting of isotropically etched "tubs" formed using a PECVD SiN mask; and a double-layer anti-reflection coating.

The continued development of SiN passivated solar cells fabricated on *n*-type silicon is also an attractive option. As only planar devices where considered in this thesis, an obvious first step is to include surface texturing along with many of the cell improvements mentioned above (DLAR, grid design etc). A better optimisation of the sheet resistance of the n^+ and p^+ doped regions used under the metal grids would be appropriate, particularly for the n^+ diffusion, which was too light. The use of a light n^+ diffusion over the entire rear side of the cell (the n^+ grid side) might also be beneficial to cell fill-factor. Monofacial design rather than bifacial operation might also be better due to the improved rear surface reflector and associated light trapping benefits. The use of high quality *n*-type CZ wafers as a lower cost alternative to *n*-type FZ wafers is also a very attractive possibility, as well as many other potential cell designs including point-contact solar cells, etc.

The novel method introduced for forming a local rear Al-BSF with SiN passivation elsewhere, without using photolithography, requires significant further development. Its potential to be transferred to commercial production of both single crystal and multicrystalline silicon solar cells, using screenprinted aluminium, makes it an interesting prospect, particularly

for thin wafers. Indeed, the concept can also be extended in a number of ways such as for forming the collecting junction on the rear surface of *n*-type cells.

List of Publications

Publications arising from the work in this thesis

Refereed journal paper

[1] M. J. Kerr, P. Campbell, and A. Cuevas, "Limiting Efficiency of Crystalline Silicon Solar Cells due to Coulomb-Enhanced Auger Recombination" *Prog. Photovolt.*, submitted for publication, (2002).

[2] M. J. Kerr and A. Cuevas, "General parameterization of Auger recombination in crystalline silicon" *J. Appl. Phys.*, **91** (4), pp. 2473-2480, (2002).

[3] M. J. Kerr, A. Cuevas, and R. A. Sinton, "Generalized analysis of quasi-steady-state and transient decay open circuit voltage measurements" *J. Appl. Phys.*, **91** (1), pp. 399-404, (2002).

[4] M. J. Kerr and A. Cuevas, "Recombination at the interface between silicon and stoichiometric plasma silicon nitride" *Semi. Sci. and Tech.*, **17** , pp. 166-172, (2002).

[5] M. J. Kerr and A. Cuevas, "Very Low Bulk and Surface Recombination in Oxidized Silicon Wafers" *Semi. Sci. and Tech.*, **17** , pp. 35-38, (2002).

[6] M. J. Kerr, J. Schmidt, A. Cuevas, and J. H. Bultman, "Surface recombination velocity of phosphorus-diffused silicon solar cell emitters passivated with plasma enhanced chemical vapor deposited silicon nitride and thermal silicon oxide" *J. Appl. Phys.*, **89** (7), pp. 3821-3826, (2001).

[7] J. Schmidt, M. J. Kerr, and A. Cuevas, "Surface passivation of silicon solar cells using plasma-enhanced chemical-vapour-deposited SiN films and thin thermal SiO_2/plasma SiN stacks" *Semi. Sci. and Tech.*, **16** , pp. 164-170, (2001).

[8] J. Schmidt and M. J. Kerr, "Highest-quality surface passivation of low-resistivity *p*-type silicon using stoichiometric PECVD silicon nitride" *Sol. En. Mat. and Sol. Cells*, **65** , pp. 585-591, (2001).

[9] M. J. Kerr, J. Schmidt, and A. Cuevas, "Comparison of the Open Circuit Voltage of Simplified PERC Cells Passivated with PECVD Silicon Nitride and Thermal Silicon Oxide" *Prog. Photovolt.*, **8** , pp. 529-536, (2000).

[10] J. Schmidt, M. J. Kerr, and P. P. Altermatt, "Coulomb-enhanced Auger recombination in crystalline silicon at intermediate and high-injection densities" *J. Appl. Phys.*, **88** (3), pp. 1494-1497, (2000).

[11] A. Cuevas, M. Stocks, D. Macdonald, M. Kerr, and C. Samundsett, "Recombination and Trapping in Multicrystalline Silicon" *IEEE Trans. Elec. Dev.*, **ED-46** (10), pp. 2026-2034, (1999).

Refereed papers presented at international conferences

[12] M. J. Kerr and A. Cuevas, "Comprehensive Study of the Doping and Injection-Level Dependence of Stoichiometric Plasma Silicon Nitride Passivation for Silicon Solar Cells," *29th IEEE Photovoltaic Specialists Conference*, New Orleans, to be presented, (2002).

[13] M. J. Kerr, P. Campbell, and A. Cuevas, "Lifetime and Efficiency Limits of Crystalline Silicon Solar Cells," *29th IEEE Photovoltaic Specialists Conference*, New Orleans, to be presented, (2002).

[14] M. J. Kerr and A. Cuevas, "Low Recombination in Oxidized Silicon Wafers," *ISES 2001*, Adelaide, Australia, (2001).

[15] M. J. Kerr and A. Cuevas, "Generalisation of the Illumination Intensity vs. Open-Circuit Voltage Characteristics of Solar Cells," *17th European Photovoltaic Solar Energy Conference*, Munich, Germany, (2001).

[16] M. J. Kerr and A. Cuevas, "Record High Minority Carrier Lifetimes in Processed Silicon Wafers," *17th European Photovoltaic Solar Energy Conference*, Munich, Germany, (2001).

[17] M. J. Kerr, J. Schmidt, and A. Cuevas, "Surface Passivation of Silicon Solar Cells Using Plasma Silicon Nitride Films and Thermal Silicon Oxide/Plasma Silicon Nitride Stacks," *Solar 2000*, Brisbane, Australia, (2000).

[18] M. J. Kerr, J. Schmidt, and A. Cuevas, "Simplified PERC Solar Cells Passivated with PECVD Silicon Nitride," *16th European Photovoltaic Solar Energy Conference*, Glasgow, Scotland, (2000).

[19] M. J. Kerr, J. Schmidt, and A. Cuevas, "Comparison of High Quality Surface Passivation Schemes for Phosphorus Diffused Emitters," *16th European Photovoltaic Solar Energy Conference*, Glasgow, Scotland, (2000).

[20] P. P. Altermatt, J. Schmidt, M. J. Kerr, G. Heiser, and A. G. Aberle, "Exciton-Enhanced Auger Recombination in Crystalline Silicon Under Intermediate and High Injection Conditions," *16th European Photovoltaic Solar Energy Conference*, Glasgow, Scotland, (2000).

[21] J. Schmidt and M. J. Kerr, "Highest-Quality Surface Passivation of Low-Resistivity *p*-type Silicon using Stoichiometric PECVD Silicon Nitride," *Technical Digest of the 11th International Photovoltaic Science and Engineering Conference*, Sapporo, pp. 581-582, (1999).

Other related publications

Refereed journal paper

[22] P. P. Altermatt, J. O. Schumacher, A. Cuevas, S. W. Glunz, M. J. Kerr, R. R. King, G. Heiser, and A. Schenk, "Numerical modeling of highly doped Si:P smitters based on Fermi-Dirac statistics and self-consistent material parameters" *J. Appl. Phys.*, submitted for publication, (2002).

[23] A. Cuevas, R. A. Sinton, M. J. Kerr, D. H. Macdonald, and H. Mackel, "A contactless photoconductance technique to evaluate the quantum efficiency of solar cell emitters" *Sol. En. Mat. and Sol. Cells*, **71** , pp. 295-312, (2002).

[24] D. Macdonald, M. J. Kerr, and A. Cuevas, "Boron-related minority-carrier trapping centers in *p*-type silicon" *Appl. Phys. Lett.*, **75** (11), pp. 1571-1573, (1999).

Refereed papers presented at international conferences

[25] D. Macdonald, A. Cuevas, M. Kerr, C. Samundsett, D. Ruby, S. Winderbaum, and A. Leo, "Texturing Industrial Multicrystalline Silicon Solar Cells," *ISES 2001*, Adelaide, Australia, (2001).

[26] D. Macdonald, A. Cuevas, M. Kerr, C. Samundsett, and A. Sloan, "Characterisation of a Commercial Multicrystalline Silicon Solar Cell Fabrication Process," *Solar 2000*, Brisbane, Australia, (2000).

[27] A. Cuevas, D. Macdonald, M. J. Kerr, C. Samundsett, A. Sloan, A. Leo, M. Mrcarica, S. Winderbaum, and S. Shea, "Evidence of Impurity Gettering by Industrial Phosphorus Diffusion," *28th IEEE Photovoltaic Specialists Conference*, Anchorage, Alaska, (2000).

[28] A. Cuevas, M. Kerr, and D. Macdonald, "Emitter Quantum Efficiency from Contactless Photoconductance Measurements," *28th IEEE Photovoltaic Specialists Conference*, Anchorage, Alaska, (2000).

[29] A. Cuevas, M. Stocks, D. Macdonald, M. Kerr, and C. Samundsett, "Multicrystalline Silicon Research at the Australian National University," *Proc. of World Renewable Energy Congress*, Perth, Australia, (1999).

Bibliography

[1] P. Maycock, in *PV News*, (2001).

[2] M. Schmela, "PV in the fast lane" in *Photon International*, **3**, pp. 32-35, (2001).

[3] L. L. Kazmerski, "The Solar-Electric Decades: Opportunities and Expectations 2001-2010," *Technical Digest of the 12th International Photovoltaic Science and Engineering Conference*, Jeju, Korea, pp. 11-14, (2001).

[4] M. Schmela, "We have a vision of growing to 100MW by 2007" in *Photon International*, **2**, pp. 14-16, (2001).

[5] M. Schmela, "Sharp plans almost a doubling of production capacity" in *Photon International*, **2**, pp. 24, (2001).

[6] James&James, "BP announce plans to increase its Spanish PV production fivefold" in *Renewable Energy News*, **4**, (2001).

[7] A. Kreutzmann and M. Schmela, "Highlights unrecognized" in *Photon International*, **6**, pp. 14-16, (2001).

[8] P. Maycock, "The world PV market 2000 - Shifting from subsidy to "fully economic"?" in *Renewable Energy World*, **4**, pp. 59-74, (2000).

[9] T. Bruton, G. Luthardt, K. D. Rasch, K. Roy, I. A. Dorrity, B. Garrard, L. Teale, J. Alonso, U. Ugalde, K. Declerq, J. Nijs, J. Szlufcik, A. Rauber, W. Wettling, and V. A., "A Study of The Manufacturing at 500MWp p.a. of Crystalline Silicon Photovoltaic Modules," *14th European Photovoltaic Solar Energy Conference*, Barcelona, pp. 11-16, (1997).

[10] M. A. Green, "Third Generation Photovoltaics: Ultra-high Conversion Efficiency at Low Cost" *Prog. Photovolt.*, **9** , pp. 123-135, (2001).

[11] M. A. Green, "Silicon Solar Cells: At the Crossroads" *Prog. Photovolt.*, **8** , pp. 443-450, (2000).

[12] P. Sims, A. Barnett, E. DelleDonne, A. Ingram, R. Jonczyk, J. Rand, and J. Yaskoff, "Thin Silicon-on-Cermaic Solar Cells," *17th European Photovoltaic Solar Energy Conference*, Munich, Germany, (2001).

[13] G. Cook, L. Billman, and R. Adcock, *Photovoltaic Fundamentals*: U.S. Department of Energy, (1995).

[14] M. A. Green, "The Future of Crystalline Silicon Solar Cells" *Prog. Photovolt.*, **8** , pp. 127-139, (2000).

[15] C. Berge, R. B. Bergmann, T. J. Rinke, and J. H. Werner, "Monocrystalline Silicon Thin Film Solar Cells by Layer Transfer," *17th European Photovoltaic Solar Energy Conference*, Munich, Germany, (2001).

[16] K. J. Weber, A. W. Blakers, and K. R. Catchpole, "The Epilift technique for Si solar cells" *Appl. Phys. A*, **69** (2), pp. 195-199, (1999).

[17] R. Hezel and R. Schroner, "Plasma Si nitride - A promosing dielectric to achieve high-quality silicon MIS/IL solar cells" *J. Appl. Phys.*, **52** (4), pp. 3076-3079, (1981).

[18] R. F. Pierret, *Advanced Semiconductor Fundamentals*, vol. VI: Addison-Wesley, (1989).

[19] A. G. Aberle, P. P. Altermatt, G. Heiser, S. J. Robinson, A. Wang, J. Zhao, U. Krumbein, and M. A. Green, "Limiting loss mechanisms in 23% efficienct silicon solar cells" *J. Appl. Phys.*, **77** (7), pp. 3491-3504, (1995).

[20] D. H. Macdonald, "Recombination and Trapping in Multicrystalline Silicon Solar Cells" in *Engineering*. Canberra: Australian National University, pp. 210, (2001).

[21] D. K. Schroder, *Semiconductor Material and Device Characterization*, 2nd ed: John Wiley and Sons, (1998).

[22] T. Tiedje, E. Yablonovitch, G. D. Cody, and B. G. Brooks, "Limiting Efficiency of Silicon Solar Cells" *IEEE Trans. Elec. Dev.*, **ED-31** (5), pp. 711-716, (1984).

[23] W. Michaelis and M. H. Pilkhun, "Radiative recombination in silicon p-n junctions" *Phys. Stat. Sol. A*, **36** (1), pp. 311-319, (1969).

[24] H. Schlangenotto, H. Maeder, and W. Gerlach, "Temperature Dependance of the Radiative Recombination Coefficient in Silicon" *Physica Status Solidi*, **21a** , pp. 357-367, (1974).

[25] M. A. Green, *Silicon Solar Cells: Advanced Principles and Practice*, Sydney: UNSW, (1995).

[26] A. G. Aberle, *Crystalline Silicon Solar Cells - Advanced Surface Passivation and Analysis*, Sydney: University of New South Wales, (1999).

[27] J. W. Parks, K. F. Brennan, and A. W. Smith, "Two-dimensional model of photon recycling in direct gap semiconductor devices" *J. Appl. Phys.*, **82** (7), pp. 3493-3498, (1997).

[28] A. Hangleiter and R. Hacker, "Enhancement of Band-to-Band Auger Recombination by Electron-Hole Correlations" *Physical Review Letters*, **65** (2), pp. 215-218, (1990).

[29] M. S. Tyagi and R. Van Overstraeten, "Enhancement of Band-to-Band Auger Recombination by Electron-Hole Correlations" *Solid State Electronics*, **26** (6), pp. 577-579, (1983).

[30] J. Dziewior and W. Schmid, "Auger coefficients for highly doped and highly excited silicon" *Appl. Phys. Lett.*, **31** (5), pp. 346-348, (1977).

[31] R. A. Sinton and R. M. Swanson, "Recombination in Highly Injected Silicon" *IEEE Trans. Elec. Dev.*, **ED-34** (6), pp. 1380-1389, (1987).

[32] P. P. Altermatt, J. Schmidt, G. Heiser, and A. G. Aberle, "Assessment and parameterisation of Coulomb-enhanced Auger recombination coefficients in lowly injected crystalline silicon" *J. Appl. Phys.*, **82** (10), pp. 4938-4944, (1997).

[33] M. A. Green, *Silicon Solar Cells: Operating Principles, Technology and System Applications*, Sydney: UNSW, (1982).

[34] W. Shockley and W. T. Read, "Statistics of the Recombinations of Holes and Electrons" *Phys. Rev.*, **87** , pp. 835-842, (1952).

[35] R. N. Hall, "Electron-Hole Recombination in Germanium" *Phys. Rev.*, **87** , pp. 387, (1952).

[36] D. K. Schroder, *Semiconductor Material and Device Characterization*: John Wiley and Sons, (1990).

[37] W. D. Eades, "Characterization of Silicon-Silicon Dioxide Interface Traps Using Deep Level Transient Spectroscopy" in *Electrical Engineering*. Stanford: Stanford, pp. 137, (1985).

[38] R. B. M. Girisch, R. P. Mertens, and R. F. DeKeermaecker, "Determination of Si-SiO2 Interface Recombination Parameters Using a Gate-Controlled Point-Junction Diode Under Illumination" *IEEE Trans. Elec. Dev.*, **35** (2), pp. 203-222, (1988).

[39] S. W. Glunz, D. Biro, S. Rein, and W. Warta, "Field-effect passivation of the SiO2-Si interface" *J. Appl. Phys.*, **86** (1), pp. 683-691, (1999).

[40] P. Lolgen, "Surface and Volume Recombination in Silicon Solar Cells" : University Utrecht, pp. 152, (1995).

[41] D. E. Kane and R. M. Swanson, "Measurement of the Emitter Saturation Current by a Contactless Photoconductivity Decay Method," *18th IEEE Photovoltaic Specialists Conference*, Las Vegas, pp. 578-585, (1985).

[42] S. C. Jain and R. Muralidhan, "Effect of emitter recombination on the open circuit voltage decay of a junction diode" *Solid-State Electr.*, **24** , pp. 1147, (1981).

[43] A. B. Sproul, "Dimensionless solution of the equation describing the effect of surface recombination on carrier decay in semiconductors" *J. Appl. Phys.*, **76** (5), pp. 2851-2854, (1994).

[44] A. Cuevas, "The effect of emitter recombination on the effective lifetime of silicon wafers" *Sol. En. Mat. and Sol. Cells*, **57** , pp. 277-290, (1999).

[45] M. J. Stocks, A. Cuevas, and A. W. Blakers, "Process monitoring of multicrystalline silicon solar cells with quasi-steady state photoconductance," *26th IEEE Photovoltaic Specialists Conference*, Anaheim, CA, (1997).

[46] R. A. Sinton, "Possibilities for Process-Control Monitoring of Electronic Material Properties during Solar Cell Manufacture," *9th Workshop on the Role of Impurities and Defects in Silicon Device Processing*, Breckenridge, pp. 67-73, (1999).

[47] A. Cuevas and R. A. Sinton, "Prediction of the Open-circuit Voltage of Solar Cells from the Steady-state Photoconductance" *Prog. Photovolt.*, **5** , pp. 79-90, (1997).

[48] J. Schmidt and A. G. Aberle, "Accurate method for the determination of bulk minority-carrier lifetimes of mono- and multicrystalline silicon wafers" *J. Appl. Phys.*, **81** (9), pp. 6186-6199, (1997).

[49] A. Cuevas, M. Stocks, D. Macdonald, M. Kerr, and C. Samundsett, "Recombination and Trapping in Multicrystalline Silicon" *IEEE Trans. Elec. Dev.*, **ED-46** (10), pp. 2026-2034, (1999).

[50] R. A. Sinton and A. Cuevas, "Contactless determination of current-voltage characteristics and minority-carrier lifetimes in semiconductors from quasi-steady-state photoconductance data" *Appl. Phys. Lett.*, **69** (17), pp. 2510-2512, (1996).

[51] M. Bail and R. Brendel, "Seperation of Bulk and Surface Recombination by Steady State Photoconductance Measurements," *16th European Photovoltaic Solar Energy Conference*, Glasgow, Scotland, (2000).

[52] A. Cuevas, R. A. Sinton, M. J. Kerr, D. H. Macdonald, and H. Mackel, "A contactless photoconductance technique to evaluate the quantum efficiency of solar cell emitters" *Sol. En. Mat. and Sol. Cells*, **71** , pp. 295-312, (2002).

[53] H. Nagel, C. Berge, and A. Aberle, "Generalized analysis of quasi-steady-state and quasi-transient measurements of carrier lifetimes in semiconductors" *J. Appl. Phys.*, **86** (11), pp. 6218-6221, (1999).

[54] J. Krausse, *Solid-State Electronics*, **15** , pp. 1377, (1972).

[55] F. Dannhauser, *Solid-State Electronics*, **15** , pp. 1371, (1972).

[56] R. Brendel and M. Wolf, "Differential and Actual Surface Recombination Velocities," *13th European Photovoltaic Solar Energy Conference*, Nice, France, (1995).

[57] J. Schmidt, "Measurement of Differential and Actual Recombination Parameters on Crystalline Silicon Wafers" *IEEE Trans. Elec. Dev.*, **ED-46** (10), pp. 2018-2025, (1999).

[58] R. A. Sinton and A. Cuevas, "A Quasi-Steady-State Open-Circuit Voltage Method for Solar Cell Characterization," *16th European Photovoltaic Solar Energy Conference*, Glasgow, Scotland, pp. 1152-1155, (2000).

[59] J. E. Mahan and D. L. Barnes, "Depletion Layer Effects in the Open-Circuit-Voltage-Decay Lifetime Measurement" *Solid-State Electronics*, **24** (10), pp. 989-994, (1981).

[60] R. Hacker and A. Hangleiter, "Intrinsic upper limits of the carrier lifetime in silicon" *J. Appl. Phys.*, **75** (11), pp. 7570-7572, (1994).

[61] A. G. Aberle, S. W. Glunz, and W. Warta, "Impact of illumination level and oxide parameters on Shockley-Read-Hall recombination at the Si-SiO_2 interface" *J. Appl. Phys.*, **71** (9), pp. 4422-4431, (1992).

[62] E. Yablonovitch and T. Gmitter, "Auger recombination in silicon at low carrier densities" *Appl. Phys. Lett.*, **49** (10), pp. 587-589, (1986).

[63] T. F. Ciszek and T. H. Wang, "Silicon Defect and Impurity Studies Using Controlled Samples," *14th European Photovoltaic Solar Energy Conference*, Barcelona, pp. 396-399, (1997).

[64] R. R. King, "Studies of Oxide-Passivated Emitters in Silicon and Applications to Solar Cells" in *Electrical Engineering*. Stanford: Stanford, pp. 200, (1990).

[65] J. D. Plummer, M. D. Deal, and P. B. Griffin, *Silicon VLSI Technology - Fundamentals, Practice and Modeling*, New Jersey: Prentice Hall, (2000).

[66] S. K. Pang and A. Rohatgi, "Record high recombination lifetime in oxidized magnetic Czochralski silicon" *Appl. Phys. Lett.*, **59** (2), pp. 195-197, (1991).

[67] S. W. Glunz, S. Rein, W. Warta, J. Knobloch, and W. Wettling, "On the degredation of CZ-silicon solar cells," *2nd World Conference on Photovoltaic Energy Conversion*, Vienna, pp. 1343-1346, (1998).

[68] D. J. Roulston, *Bipolar Semiconductor Devices*: McGraw-Hill, (1990).

[69] D. B. Laks, G. F. Neumark, and S. T. Pantelides, "Accurate interband-Auger-recombination rates in silicon" *Physical Review B*, **42** (8), pp. 5176-5185, (1990).

[70] A. Haug, "Carrier density dependence of Auger recombination" *Solid-State Electronics*, **21** (11-12), pp. 1281-1284, (1978).

[71] P. T. Landsberg, "Trap-Auger recombination in silicon of low carrier densities" *Appl. Phys. Lett.*, **50** (12), pp. 745-747, (1987).

[72] J. del Alamo, S. Swirhun, and R. M. Swanson, "Simultaneous Measurement of Hole Lifetime, Hole Mobility and Bandgap Harrowing in Heavily Doped n-type Silicon," *International Electron Devices Meeting Technical Digest*, Washigton, pp. 290-293, (1985).

[73] S. E. Swirhun, Y. H. Kwark, and R. M. Swanson, "Measurement of Electorn Lifetime, Electorn Mobility and Bandgap Harrowing in Heavily Doped p-type Silicon," *International Electron Devices Meeting Technical Digest*, Washigton, pp. 24-27, (1986).

[74] S. E. Swirhun, "Characterization of Majority and Minority Carrier Transport in Heavily Doped Silicon" in *Electrical Engineering*. Stanford: Stanford, pp. 318, (1987).

[75] P. Jonsson, H. Bleichner, M. Isberg, and E. Nordlander, "The ambipoar Auger coefficient: Measured temperature dependence in electron irradiated and highly injected n-type silicon" *J. Appl. Phys.*, **81** (5), pp. 2256-2262, (1997).

[76] P. P. Altermatt, J. Schmidt, M. J. Kerr, G. Heiser, and A. G. Aberle, "Exciton-Enhanced Auger Recombination in Crystalline Silicon Under Intermediate and High Injection Conditions," *16th European Photovoltaic Solar Energy Conference*, Glasgow, Scotland, (2000).

[77] P. P. Altermatt, R. A. Sinton, and G. Heiser, "Improvements in numerical modelling of highly injected crystalline silicon solar cells" *Sol. En. Mat. and Sol. Cells*, **65** , pp. 149-155, (2001).

[78] J. Schmidt, M. J. Kerr, and P. P. Altermatt, "Coulomb-enhanced Auger recombination in crystalline silicon at intermediate and high-injection densities" *J. Appl. Phys.*, **88** (3), pp. 1494-1497, (2000).

[79] D. A. Clugston and P. A. Basore, "PC1D Version 5: 32-bit Solar Cell Simulation on Personal Computers," *26th IEEE Photovoltaic Specialists Conference*, Anaheim, CA, (1997).

[80] L. Huldt, N. G. Nilsson, and K. G. Svantesson, "The temperature dependence of band-to-band Auger recombination in silicon" *Appl. Phys. Lett.*, **35** (10), pp. 776-777, (1979).

[81] I. V. Grekhov and L. A. Delimova, "Auger recombination in silicon" *Sov. Phys. Semicond.*, **14** , pp. 529-533, (1980).

[82] Y. Vaitkus and V. Grivitskas, "Dependence of the rate of interband Auger recombination on the carrier density in silicon" *Sov. Phys. Semicond.*, **15** , pp. 1102-1110, (1981).

[83] K. Misiakos, J.-S. Park, and A. Neugroschel, "Carrier lifetimes in highly injected silicon" *J. Appl. Phys.*, **67** (5), pp. 2576-2582, (1990).

[84] B. C. Forget, D. Fournier, and V. E. Gusev, "Auger recombination in modulated photoreflectance characterization of silicon wafers" *Appl. Phys. Lett.*, **61** (19), pp. 2341-2343, (1992).

[85] S. G. Svantesson and N. G. Nilsson, "The temperature dependence of the Auger recombination coefficient of undoped silicon" *Journal of Physics C: Solid State Physics*, **12** (23), pp. 5111-5120, (1979).

[86] M. G. Grimaldi, P. Baeri, and E. Rimini, "Laser-induced free-carrier absorption in Si single crystal" *Applied Physics A - Solids and Surfaces*, **A33** (2), pp. 107-111, (1984).

[87] P. Baeri, M. A. Harith, G. Russo, E. Rimini, A. Giuletti, and M. Vaselli, "Free carrier dynamics and energy transfer to the Si lattice during pico and nanosecond Nd laser pulse excitation" *Physica Status Solidi B - Basic Research*, **130** (1), pp. 225-233, (1985).

[88] N. G. Nilsson, "Band-to-band Auger recombination in silicon and germanium" *Physica Scripta*, **8** (4), pp. 165-176, (1973).

[89] A. W. Stephens, A. G. Aberle, and M. A. Green, "Surface recombination velocity measurements at the silicon-silicon dioxide interface by microwave-detected photoconductance decay" *J. Appl. Phys.*, **76** (1), pp. 363-370, (1994).

[90] A. Cuevas, M. Stocks, S. Armand, M. Stuckings, A. W. Blakers, and F. Ferrazza, "High minority carrier lifetime in phosphorus-gettered multicrystalline silicon" *Appl. Phys. Lett.*, **70** (8), pp. 1017-1019, (1997).

[91] H. Nagel, J. Schmidt, A. G. Aberle, and R. Hezel, "Exceptionally high bulk minority-carrier lifetimes in block-cast multicrystalline silicon," *14th European Photovoltaic Solar Energy Conference*, Barcelona, pp. 762-765, (1997).

[92] D. Macdonald and A. Cuevas, "Trapping of minority carriers in multicrystalline silicon" *Appl. Phys. Lett.*, **74** (12), pp. 1710-1712, (1999).

[93] W. Shockley and H. J. Queisser, "Detailed Balance Limit of Efficiency of p-n Junction Solar Cells" *J. Appl. Phys.*, **32** , pp. 510-519, (1961).

[94] C. B. Honsberg, R. C. Corkish, and S. P. Bremner, "A New Generalized Detailed Balance Formulation to Calculate Solar Cell Efficiency Limits," *17th European Photovoltaic Solar Energy Conference*, Munich, Germany, (2001).

[95] M. A. Green, "Limits on the Open-Circuit Voltage and Efficiency of Silicon Solar Cells Imposed by Intrinsic Auger Processes" *IEEE Trans. Elec. Dev.*, **ED-31** (5), pp. 671-678, (1984).

[96] M. A. Green, "Limiting Efficiency of Bulk and thin-film Silicon Solar Cells in the Presence of Surface Recombination" *Prog. Photovolt.*, **7** , pp. 327-330, (1999).

[97] Y. H. Tang, X. M. Dai, J. Zhao, A. Wang, S. R. Wenham, and C. B. Honsberg, "Rear Surface Passivation in Buried Contact Solar Cells," *26th IEEE Photovoltaic Specialists Conference*, Anaheim, (1997).

[98] J. Zhao, A. Wang, and M. A. Green, "24.5% Efficiency Silicon PERT Cells on MCZ Substrates and 24.7% Efficiency PERL Cells on FZ Substrates" *Prog. Photovolt.*, **7** , pp. 471-474, (1999).

[99] A. Wang, J. Zhao, S. R. Wenham, and M. A. Green, "21.5% Efficient Thin Silicon Solar Cell" *Prog. Photovolt.*, **4** , pp. 55-58, (1996).

[100] R. R. King, R. A. Sinton, and R. M. Swanson, "Doped surfaces in one sun, point-contact solar cells" *Appl. Phys. Lett.*, **54** (15), pp. 1460-1462, (1989).

[101] K. Kawamoto, T. Nakai, T. Baba, M. Taguchi, H. Sakata, S. Tsuge, K. Uchihashi, M. Tanaka, and S. Kiyama, "A High-Efficiency HIT Solar Cell (21.0% ~100cm^2) with Excellent Interface Properties," *Technical Digest of the 12th International Photovoltaic Science and Engineering Conference*, Korea, (2001).

[102] A. G. Aberle, S. J. Robinson, A. Wang, J. Zhao, S. R. Wenham, and M. A. Green, "High-efficiency Silicon Solar Cells: Fill Factor Limitations and Non-ideal Diode Behaviour Due to Voltage-dependent Rear Surface Recombination Velocity" *Prog. Photovolt.*, **1** , pp. 133-143, (1993).

[103] A. W. Blakers, A. Wang, A. M. Milne, J. Zhao, and M. A. Green, "22.8% Efficient Silicon Solar Cells" *Appl. Phys. Lett.*, **55** (13), pp. 1363-1365, (1989).

[104] R. R. King, R. A. Sinton, R. M. Swanson, and T. Ciszek, "Low Surface Recombination Velocities on Doped SIlicon and Their Implications for point Contact Solar Cells," *19th IEEE Photovoltaic Specialists Conference*, New Orleans, pp. 1168-1173, (1987).

[105] M. Taguchi, K. Kawamoto, S. Tsuge, T. Baba, H. Sakata, M. Morizane, K. Uchihashi, N. Nakamura, S. Kiyama, and O. Oota, "HIT Cells - High-Efficiency Crystalline Si Cells with Novel Structure" *Prog. Photovolt.*, **8** , pp. 503-513, (2000).

[106] U. Rau, N. Jensen, and J. H. Werner, "Electronic Transport in Amorphous/Crystalline Silicon Heterojunction Solar Cells," *11th Workshop on Crystalline Silicon Solar Cell Materials and Processes*, Golden, Colorado, pp. 49-56, (2001).

[107] C. Leguijt, P. Lolgen, P. A. Eikelboom, P. H. Amesz, R. A. Steeman, W. C. Sinke, P. M. Sarro, L. A. Verhoef, P.-P. Michiels, Z. H. Chen, and A. Rohatgi, "Very low surface recombination velocities on 2.5 Ωcm Si wafers, obtained with low-temperature PECVD of Si-oxide and Si-nitride" *Sol. En. Mat. and Sol. Cells*, **34** , pp. 177-181, (1994).

[108] Z. Chen, A. Rohatgi, and D. Ruby, "Silicon Surface and Bulk Defect Passivation by Low Temperature PECVD Oxides and Nitrides," *1st World Conference on Photovoltaic Energy Conversion*, Hawaii, pp. 1331-1334, (1994).

[109] T. Lauinger, J. Schmidt, A. G. Aberle, and R. Hezel, "Record low surface recombinatin velocities on 1Ωcm *p*-silicon using remote plasma silicon nitride" *Appl. Phys. Lett.*, **68** (9), pp. 1232-1234, (1996).

[110] J. Schmidt and M. J. Kerr, "Highest-quality surface passivation of low-resistivity *p*-type silicon using stoichiometric PECVD silicon nitride" *Sol. En. Mat. and Sol. Cells*, **65** , pp. 585-591, (2001).

[111] H. Mackel and R. Ludemann, "Detailed study of the composition of hydrogenated SiNx layers for high-quality silicon surface passivation" *J. Appl. Phys.*, to be published, (2002).

[112] I. Martin, M. Vetter, A. Orpella, J. Puigdollers, A. Cuevas, and R. Alcubilla, "Surface Passivation of p-type Crystalline Silicon by PECVD Amorphous Silicon Carbide" *Appl. Phys. Lett.*, **79** (14), pp. 2199-2201, (2001).

[113] T. Lauinger, A. G. Aberle, and R. Hezel, "Comparison of Direct and Remote PECVD Silicon Nitride Films for Low Temperature Surface Passivation of P-type Crystalline

Silicon," *14th European Photovoltaic Solar Energy Conference*, Barcelona, pp. 853-856, (1997).

[114] T. Lauinger, J. D. Moschner, A. G. Aberle, and R. Hezel, "Optimization and characterization of remote plasma-enhanced chamical vapor deposition silicon nitride for the passivation of p-type crystalline silicon surfaces" *J. Vac. Sci. Technol. A*, **16** (2), pp. 530-543, (1998).

[115] P. Doshi, G. E. Jellison, and A. Rohatgi, "Characterization and optimization of absorbing plasma-enhanced chemical vapor deposited antireflection coatings for silicon photovoltaics" *App. Opt.*, **36** (30), pp. 7826-7837, (1997).

[116] J. Schmidt, T. Lauinger, A. G. Aberle, and R. Hezel, "Record low surface recombination velocities on low-resistivity silicon solar cell substrates," *25th IEEE Photovoltaic Specialists Conference*, Washington, pp. 413-416, (1996).

[117] H. Nagel, A. G. Aberle, and R. Hezel, "Optimized Antireflection Coatings for Planar Silicon Solar Cells using Remote PECVD SIlicon Nitride and Porous Silicon Dioxide" *Prog. Photovolt.*, **7** , pp. 245-260, (1999).

[118] J. R. Elmiger and M. Kunst, "Investigation of the silicon-plasma silicon nitride interface with insitu transient photoconductivity measurements" *App. Surf. Sci.*, **103** , pp. 11-18, (1996).

[119] J. R. Elmiger and M. Kunst, "Investigation of charge carrier injection in silicon nitride/silicon junctions" *Appl. Phys. Lett.*, **69** (4), pp. 517-519, (1996).

[120] J. Schmidt and A. G. Aberle, "Carrier recombination at silicon-silicon nitride interfaces fabricated by plasma-enhanced chemical vapor deposition" *J. Appl. Phys.*, **85** (7), pp. 3626-3633, (1999).

[121] A. G. Aberle, T. Lauinger, J. Schmidt, and R. Hezel, "Injection-level dependent surface recombination velocities at the silicon-plasma nitride interface" *Appl. Phys. Lett.*, **66** (21), pp. 2828-2830, (1995).

[122] J. Schmidt, "private communication" , (2001).

[123] S. Dauwe, A. Metz, and R. Hezel, "A Novel Mask-Free Low-Temperature Rear Surface Passivation Scheme Based on PECVD Silicon Nitride for High-Efficiency Silicon Solar Cells," *16th European Photovoltaic Solar Energy Conference*, Glasgow, Scotland, (2000).

[124] J. R. Elmiger, R. Schieck, and M. Kunst, "Recombination at the silicon nitride/silicon interface" *J. Vac. Sci. Technol. A*, **15** (4), pp. 2418-2425, (1997).

[125] R. A. Sinton, Y. Kwark, S. Swirhun, and R. M. Swanson, "Silicon Point Contact Concentrator Solar Cells" *IEEE Electron Device Letters*, **EDL-6** (8), pp. 405-407, (1985).

[126] A. W. Blakers, A. Wang, A. M. Milne, J. Zhao, X. Dai, and M. A. Green, "22.6% Efficient Silicon Solar Cells," *4th International Photovoltaic Science and Engineering Conference*, Sydney, pp. 801-806, (1989).

[127] F. Duerinckx and J. Szlufcik, "Defect passivation of industrial multicrystalline solar cells based on PECVD silicon nitride" *Sol. En. Mat. and Sol. Cells*, **72** , pp. 231-246, (2002).

[128] M. Maeda and M. Itsumi, "Thermal dissociation process of hydrogen atoms in plasma-enhanced chemical vapor deposited silicon nitride films" *J. Appl. Phys.*, **84** (9), pp. 5243-5247, (1998).

[129] J. Mandelkorn and J. H. Lamneck Jr., "A new electric field effect in silicon solar cells" *J. Appl. Phys.*, **44** (10), pp. 4785-4787, (1973).

[130] A. Luque, A. Cuevas, and J. Eguren, "Solar cell behaviour under variable surface recombination velocity and proposal of a novel structure" *Solid-State Electronics*, **21** , pp. 793-794, (1978).

[131] R. R. King, R. A. Sinton, and R. M. Swanson, "Studies of Diffused Phosphorus Emitters: Saturation Current, Surface Recombination Velocity, and Quantum Efficiency" *IEEE Trans. Elec. Dev.*, **ED-37** (2), pp. 365-371, (1990).

[132] A. Cuevas, P. A. Basore, G. Giroult-Matlakowski, and C. Dubois, "Surface recombination velocity of highly doped n-type silicon" *J. Appl. Phys.*, **80** (6), pp. 3370-3375, (1996).

[133] A. W. Blakers and M. A. Green, "20% efficieny silicon solar cells" *Appl. Phys. Lett.*, **48** (3), pp. 215-217, (1986).

[134] J. Zhao, A. Wang, P. P. Altermatt, S. R. Wenham, and M. A. Green, "24% Efficient Silicon Solar Cells," *1st World Conference on Photovoltaic Energy Conversion*, Hawaii, pp. 1477-1480, (1994).

[135] D. S. Ruby, W. L. Wilbanks, and C. B. Fleddermann, "A Statistical Analysis of the Effect of PECVD Deposition Parameters on Surface and Bulk Recombination in Silicon Solar Cells," *1st World Conference on Photovoltaic Energy Conversion*, Hawaii, pp. 1335-1338, (1994).

[136] A. Cuevas, P. A. Basore, G. Giroult-Matlakowski, and C. Dubois, "Surface Recombination Velocity and Energy Bandgap Narrowing of Highly Doped N-type Silicon," *13th European Photovoltaic Solar Energy Conference*, Nice, France, pp. 337-342, (1995).

[137] S. W. Glunz, S. Sterk, R. Steeman, W. Warta, J. Knobloch, and W. Wettling, "Emitter Dark Saturation Currents of High-Efficiency Solar Cells with Inverted Pyramids," *13th European Photovoltaic Solar Energy Conference*, Nice, France, pp. 409-412, (1995).

[138] L. Cai, S. Han, G. May, S. Kamra, T. Krygowski, and A. Rohatgi, "Optimization of saturation current density of PECVD SiN coated phosphorus diffused emitters using neural network modelling" *Journal of Electronic Materials*, **25** (11), pp. 1784-1789, (1996).

[139] B. Lenkeit, T. Lauinger, A. G. Aberle, and R. Hezel, "Comparison of Remote Versus Direct PECVD Silicon Nitride Passivation of Phosphorus-Diffused Emitters of Silicon Solar Cells," *2nd World Conference on Photovoltaic Energy Conversion*, Vienna, pp. 1434-1437, (1998).

[140] J. D. Moschner, P. Doshi, D. S. Ruby, T. Lauinger, A. G. Aberle, and A. Rohatgi, "Comparison of Front and Back Surface Passivation Schemes for Silicon Solar Cells," *2nd World Conference on Photovoltaic Energy Conversion*, Vienna, pp. 1894-1897, (1998).

[141] P. P. Altermatt, J. O. Schumacher, A. Cuevas, S. W. Glunz, R. R. King, G. Heiser, and A. Schenk, "The Extraction of the Surface Recombination Velocity of Si:P Emitters Using Advanced Silicon Models," *16th European Photovoltaic Solar Energy Conference*, Glasgow, Scotland, (2000).

[142] J. Snel, "The Doped Si/SiO_2 Interface" *Solid-State Electronics*, **24** , pp. 135-139, (1981).

[143] J. Zhao, A. Wang, and M. A. Green, "24% Efficient PERL Structure Silicon Solar Cells," *21st IEEE Photovoltaic Specialists Conference*, Kissimimee, pp. 333-335, (1990).

[144] R. R. King and R. M. Swanson, "Studies of DIffused Boron Emitters: Saturation Current, Bandgap Narrowing, and Surface Recombination Velocity" *IEEE Trans. Elec. Dev.*, **ED-38** (6), pp. 1399-1409, (1991).

[145] A. Cuevas, M. Stuckings, J. Lau, and M. Petravic, "The Recombination Velocity of Boron Diffused Silicon Surfaces," *14th European Photovoltaic Solar Energy Conference*, Barcelona, pp. 2416-2419, (1997).

[146] A. M. Slade, C. B. Honsberg, and S. R. Wenham, "Impact and options for boron diffusions in buried contact solar cells" *Sol. En. Mat. and Sol. Cells*, **66** , pp. 11-15, (2001).

[147] J. Zhao, A. Wang, M. Keevers, and M. A. Green, "High Efficiency PERT Cells on SEH p-type Si Substrates and PERT Cells on SEH n-Type Si Substrates," *Solar 2000*, Brisbane, Australia, (2000).

[148] A. Wang, J. Zhao, and M. A. Green, "24% Efficient Silicon Solar Cells" *Appl. Phys. Lett.*, **57** (6), pp. 602-604, (1990).

[149] J. Knobloch, A. Noel, E. Schaffer, U. Schubert, F. J. Kamerewerd, S. Klussmann, and W. Wettling, "High-Efficiency Solar Cells from FZ, CZ and MC Silicon Material," *23rd IEEE Photovoltaic Specialists Conference*, New York, pp. 271-276, (1993).

[150] A. M. Slade, C. B. Honsberg, and S. R. Wenham, "Processing and Characterisation of Boron Diffused Surface Fields in Mono- and Bifacial Buried Contact Solar Cells," *16th European Photovoltaic Solar Energy Conference*, Glasgow, Scotland, (2000).

[151] A. Cuevas and D. Russell, "Co-optimisation of the Emitter Region and the Metal Grid of Silicon Solar Cells" *Prog. Photovolt.*, **8** , pp. 603-616, (2000).

[152] A. Hübner, A. G. Aberle, and R. Hezel, "20% Efficient Bifacial Silicon Solar Cells," *14th European Photovoltaic Solar Energy Conference*, Barcelona, pp. 92-95, (1997).

[153] S. Muramatsu, T. Uematsu, H. Ohtsuka, Y. Yazawa, T. Warabisako, H. Nagayoshi, and K. Kamisako, "Effect of Hydrogen Radical Annealing for SiN Passivation of c-Si Solar Cells," *Technical Digest of the 11th International Photovoltaic Science and Engineering Conference*, Sapporo, pp. 583-584, (1999).

[154] R. Preu, S. W. Glunz, S. Schaefer, R. Ludemann, W. Wettling, and W. Pfleging, "Laser Ablation - A New Low-Cost Approach for Passivated Rear Contact Formation in Crystalline Silicon Solar Cell Technology," *16th European Photovoltaic Solar Energy Conference*, Glasgow, Scotland, (2000).

[155] S. W. Glunz, R. Preu, S. Schaefer, E. Schneiderlochner, W. Pfleging, R. Ludemann, and G. Willeke, "New Simplified Methods for Patterning the Rear Contact of RP-PERC High-Efficiency Solar Cells," *28th PVSC*, Anchorage, Alaska, (2000).

[156] E. Schneiderlochner, R. Preu, R. Ludemann, S. W. Glunz, and G. Willeke, "Laser-Fired Contacts (LFC)," *17th European Photovoltaic Solar Energy Conference*, Munich, Germany, (2001).

[157] S. W. Glunz, J. Dicker, D. Kray, J. Y. Lee, R. Preu, S. Rein, E. Schneiderlochner, J. Solter, W. Warta, and G. Willeke, "High-Efficiency Cell Structures for Medium-Quality Silicon," *17th European Photovoltaic Solar Energy Conference*, Munich, Germany, (2001).

[158] S. Schaefer, R. Preu, R. Ludemann, and S. W. Glunz, "Plasma Etched PERC and Buried Base Contact Solar Cells," *16th European Photovoltaic Solar Energy Conference*, Glasgow, Scotland, (2000).

[159] S. Dauwe, L. W. Mittelstadt, A. Metz, and R. Hezel, "Experimental Evidence of Parasitic Shunting in Silicon Nitride Rear Surface Passivated Solar Cells" *Prog. Photovolt.*, in press, (2002).

[160] A. Metz and R. Hezel, "Easy to Fabricate 20% Efficient Large Area Silicon Solar Cells," *Technical Digest of the 11th International Photovoltaic Science and Engineering Conference*, Sapporo, pp. 587-588, (1999).

[161] C. Hampe, A. Metz, and R. Hezel, "Experimental evidence of very high open-circuit voltages of inversion-layer silicon solar cells" *Sol. En. Mat. and Sol. Cells*, **65** , pp. 331-337, (2001).

[162] K. Fukui, K. Okada, Y. Inomata, H. Takahashi, S. Fujii, Y. Fukawa, and K. Shirasawa, "Surface and bulk-passivated large area multicrystalline silicon solar cells" *Sol. En. Mat. and Sol. Cells*, **48** , pp. 219-228, (1996).

[163] S. Fujii, Y. Fukawa, H. Takahashi, Y. Inomata, K. Okada, K. Fukui, and K. Shirasawa, "Production technology of large-area multicrystalline silicon solar cells" *Sol. En. Mat. and Sol. Cells*, **65** , pp. 269-275, (2001).

[164] F. Duerinckx, A. Noppe, P. Choulat, J. Szlufcik, J. F. Nijs, and B. Habraken, "Advanced Industrial Processes for Large Area Screen Printed Multicrystalline Silicon Solar Cells," *16th European Photovoltaic Solar Energy Conference*, Glasgow, Scotland, (2000).

[165] F. Duerinckx, L. Frisson, P. P. Michiels, P. Choulat, and J. Szlufcik, "Towards Highly Efficient Industrial Cells and Modules from Multicrystalline Silicon," *17th European Photovoltaic Solar Energy Conference*, Munich, Germany, (2001).

[166] D. S. Ruby, S. H. Zaidi, and S. Narayanan, "Plasma-Texturization for Multicrystalline Silicon Solar Cells," *28th IEEE Photovoltaic Specialists Conference*, Anchorage, Alaska, (2000).

[167] A. Rohatgi, Z. Chen, P. Sana, J. Crotty, and J. Salami, "High efficiency multicrystalline silicon solar cells" *Sol. En. Mat. and Sol. Cells*, **34** , pp. 227-236, (1994).

[168] J. H. Bultman, A. R. Burgers, J. Hoornstra, R. Kinderman, M. Koppes, W. J. Soppe, and A. W. Weeber, "Ideal Single Diffusion Step Selective Emitters: A Comparison Between Theory and Practice," *17th European Photovoltaic Solar Energy Conference*, Munich, Germany, (2001).

[169] W. Soppe, A. W. Weeber, H. de Moor, W. C. Sinke, T. Lauinger, R. Auer, B. Lenkeit, and A. G. Aberle, "Cost-Effective MC-Si Processing by Screenprinting on Remote-PECVD Layers," *2nd World Conference on Photovoltaic Energy Conversion*, Vienna, (1998).

[170] B. F. von Finckenstein, H. Horst, P. Fath, and E. Bucher, "Thin mc-Si Low Cost Solar Cells with 15% Efficiency," *28th IEEE Photovoltaic Specialists Conference*, Anchorage, Alaska, (2000).

[171] L. Mittelstadt, S. Dauwe, A. Metz, and R. Hezel, "Highly Efficient All Silicon Nitride Passivated Multicrystalline Silicon Solar Cells," *17th European Photovoltaic Solar Energy Conference*, Munich, Germany, (2001).

[172] A. Ebong, M. Hilali, A. Rohatgi, D. Meier, and D. S. Ruby, "Belt Furnace Gettering and Passivation of n-Web Silicon for High-Efficiency Screen-Printed Front-Surface-Field Solar Cells" *Prog. Photovolt.*, **9** , pp. 327-332, (2001).

[173] A. Hübner, C. Hampe, and A. G. Aberle, "A simple fabrication process for 20% efficient silicon solar cells" *Sol. En. Mat. and Sol. Cells*, **46** , pp. 67-77, (1997).

[174] J. Knobloch, S. W. Glunz, D. Biro, W. Warta, E. Schaffer, and W. Wettling, "Solar Cells With Efficiencies Above 21% Processed From Czochralski Grown Silicon," *25th IEEE Photovoltaic Specialists Conference*, Washington, pp. 405-408, (1996).

[175] J. Zhao, A. Wang, and M. A. Green, "19.8% Efficient Multicrystalline Silicon Solar Cells with Honeycomb Textured Front Surface," *2nd World Conference on Photovoltaic Energy Conversion*, Vienna, (1998).

[176] M. J. Stocks, A. J. Carr, and A. W. Blakers, "Texturing of polycrystalline silicon" *Sol. En. Mat. and Sol. Cells*, **40** , pp. 33-42, (1996).

[177] S. R. Wenham, S. J. Robinson, X. Dai, J. Zhao, A. Wang, Y. H. Yang, A. Ebong, C. B. Honsberg, and M. A. Green, "Rear Surface Effects in High Efficiency Silicon Solar Cells," *1st World Conference on Photovoltaic Energy Conversion*, Hawaii, (1994).

[178] J. F. Nijs, J. Szlufcik, J. Poortmans, S. Sivoththaman, and R. P. Mertens, "Advanced Manufacturing Concepts for Crystalline Silicon Solar Cells" *IEEE Trans. Elec. Dev.*, **ED-46** (10), pp. 1948-1969, (1999).

[179] A. Cuevas, D. Macdonald, M. J. Kerr, C. Samundsett, A. Sloan, A. Leo, M. Mrcarica, S. Winderbaum, and S. Shea, "Evidence of Impurity Gettering by Industrial Phosphorus Diffusion," *28th IEEE Photovoltaic Specialists Conference*, Anchorage, Alaska, (2000).

Typographical Corrections

abstract On the fifth last line of the abstract, the word "that" is incorrectly repeated.

p.6 On the twelfth line, the word "where" should replaced with "were".

p. 87 On the fourth line of section 3.4, the word "where" should replaced with "were".

p. 110 The caption of Figure 4.10 should read:

> Measured effective lifetimes for *p*-type silicon passivated with optimised stoichiometric SiN films. A clear maximum in the effective lifetime can be observed when the minority carrier injection level is close to the dopant density. The injection level dependence of the effective lifetime is nearly flat for more heavily doped material and becomes progressively stronger as the resistivity increases. A maximum effective lifetime of 9.6 ms has been measured.

p. 152 Replace point 4 of section 5.3.1 with:

> 4. Self-doping aluminium screen-printed contacts could possibly be used to form a selective emitter structure.

p. 172 The references in Table 6.1 should read:

Rear contact patterning	Plasma Etching [158]	Laser Ablation [154]	Laser Fired Contacts [156]	Mechanically Scribed [123]

p.175 Some of the text in Figure 6.2 printed incorrectly. The completed text is:

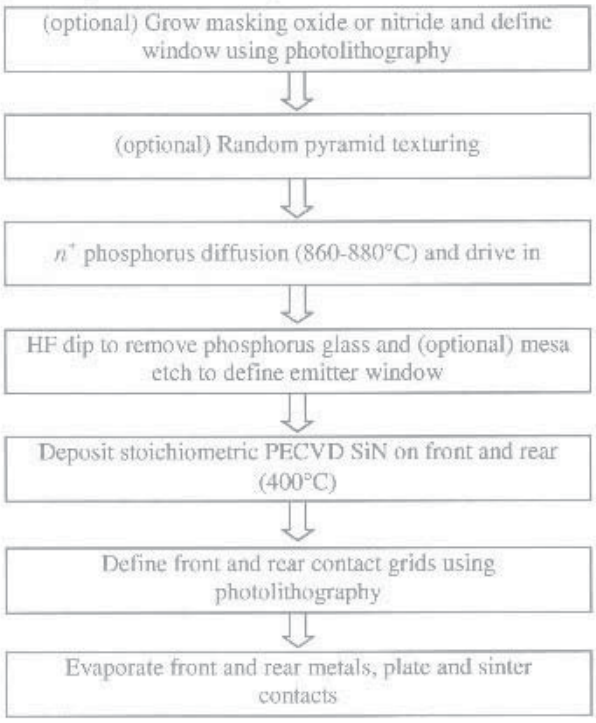


Figure 6.2. Processing sequence used for fabricating simplified PERC cells passivated with stoichiometric SiN.

p. 203 Replace the third sentence of section 7.2 with:

> Record values for the effective lifetime, up to 32ms for high resistivity silicon, have been measured in this thesis for high quality *n*-type and *p*-type silicon. Dopant densities up to ~5×10^{16}cm^{-3} were investigated.

p. 203 On the sixth line of section 7.2, the word "where" should replaced with "were".

general It is explicitly stated in the thesis when and where the program PC1D has been used for cell modelling. Other modelling results are based on in-house code using the equations given in the thesis.